

DISSERTATION  
SUBMITTED TO THE  
COMBINED FACULTY OF  
NATURAL SCIENCES AND MATHEMATICS  
OF THE  
RUPERTO-CAROLA-UNIVERSITY OF HEIDELBERG,  
GERMANY  
FOR THE DEGREE OF  
DOCTOR OF NATURAL SCIENCES

PUT FORWARD BY

DIPL. PHYS. PHILIPP GIRICHIDIS  
BORN IN: AACHEN, GERMANY

ORAL EXAMINATION: 27 JUNE 2012



IMPORTANCE OF THE INITIAL CONDITIONS FOR  
STAR FORMATION

REFEREES:

PROF. DR. ROBI BANERJEE

PROF. DR. HENRIK BEUTHER



*Für meine Eltern und Ines*



## Zusammenfassung

Die folgende Arbeit befasst sich mit dem Einfluss der Anfangsbedingungen auf die Sternentstehung im heutigen Universum. Mit Hilfe numerischer Simulationen wird der gravitative Kollaps dichter Molekülwolken und die resultierende Entstehung von protostellaren Objekten untersucht. Es wird analysiert, wie sich Variationen der anfänglichen Turbulenz sowie der Dichteverteilung des Gases während der Kontraktion auf wesentliche Kenndaten der Sternentstehung auswirken. Dazu gehören die Morphologie der kollabierenden Wolke, die Entstehungszeit sowie der -ort der Sterne, die energetische Entwicklung der Wolke, die Bildung von Sternhaufen sowie deren interne Struktur, das Akkretionsverhalten und die Massenverteilung der Sterne. Die Morphologie der Wolke sowie die Anzahl der Sterne zeigen eine besondere Empfindlichkeit gegenüber dem anfänglichen Dichteprofil und der Art der Turbulenz. Die Ergebnisse reichen von unveränderten Dichtestrukturen und einem einzigen Stern bis hin zu stark deformierten Wolken mit hunderten von Sternen und lokal entkoppelten Sternhaufen. Einen leichten systematischen Einfluss der Anfangskonfiguration findet sich in der internen Struktur der Sternhaufen. Bei der Akkretionsrate im Inneren dieser Sternhaufen zeigt sich hingegen ein sehr universelles Bild, nahezu unabhängig von den Anfangsbedingungen. Ähnliches lässt sich in Bezug auf die dynamische Entwicklung der Sternhaufen sagen. Die hier vorgestellten Rechnungen wurden mit Hilfe des gitterbasierten Codes FLASH der Universität Chicago durchgeführt.

## Abstract

This thesis investigates the impact of the initial conditions on present-day star formation. Using numerical simulations, we follow the gravitational collapse of dense molecular clouds under different initial turbulent motions and initial density distributions. Our analysis focuses on the morphology of the cloud, the time and location of the formation of stars, the energetics during the collapse, the formation of clusters including their internal structure, their accretion behaviour as well as their mass distribution. The morphology of the cloud and the total number of stars are strongly influenced by the initial type of turbulence and the initial density profile. The results range from almost unperturbed cores with a single star to strongly filamentary cores with hundreds of stars in disconnected clusters. The internal structure of protostellar clusters is systematically but not significantly influenced by the initial conditions. Concerning the accretion rates as well as the dynamical interactions of stars within the clusters, we observe a fairly uniform behaviour, not reflecting the large variations in the initial conditions. The simulations

presented in this thesis were performed using the grid-based code FLASH, developed mainly at the University of Chicago.

## List of publications

The following publications are partially presented in this thesis

1. **Girichidis, P.**; Federrath, C.; Banerjee, R.; Klessen, R.: Importance of the initial conditions for star formation - I. Cloud evolution and morphology, 2011, MNRAS 413, 2741
2. Walch, S.; Whitworth, A. P.; **Girichidis, P.**: The influence of the turbulent perturbation scale on pre-stellar core fragmentation and disc formation, 2012, MNRAS 416, 760
3. **Girichidis, P.**; Federrath, C.; Banerjee, R.; Klessen, R.: Importance of the initial conditions for star formation - II. Fragmentation-induced starvation and accretion shielding, 2012, MNRAS 420, 613
4. **Girichidis, P.**; Federrath, C.; Allison, R.; Banerjee, R.; Klessen, R.: Importance of the initial conditions for star formation - III. Statistical properties of embedded protostellar clusters, 2012, MNRAS 420, 3264



# Contents

<b>1</b>	<b>Introduction</b>	<b>1</b>
1.1	Motivation . . . . .	1
1.2	The formation of stars . . . . .	2
1.2.1	From dissipative to collisionless systems . . . . .	2
1.2.2	The dynamics of star forming regions . . . . .	3
1.2.3	Stellar interiors and nuclear fusion . . . . .	3
1.2.4	Stellar feedback . . . . .	4
1.2.5	Stellar masses . . . . .	7
1.3	The sites of contemporary star formation . . . . .	7
1.3.1	Properties of molecular clouds . . . . .	8
1.3.2	Turbulence . . . . .	9
1.4	Objectives of star-formation theory . . . . .	10
<b>2</b>	<b>Star formation theory</b>	<b>13</b>
2.1	Gravity . . . . .	13
2.1.1	Self-gravity . . . . .	13
2.1.2	Virial theorem . . . . .	14
2.1.3	Gravitational instability . . . . .	15
2.1.4	Core life time . . . . .	16
2.2	Conservation laws . . . . .	17
2.2.1	Hydrodynamic limit . . . . .	17
2.2.2	Conservation of mass . . . . .	19
2.2.3	Conservation of momentum . . . . .	20
2.2.4	Conservation of energy . . . . .	21
2.2.5	Closure relations . . . . .	21
2.2.6	Overview of the equation . . . . .	22
2.3	Thermo- & chemodynamic processes . . . . .	22
2.3.1	Equation of state . . . . .	23
2.3.2	Dust . . . . .	23
2.3.3	Chemistry . . . . .	24
2.3.4	Cosmic rays . . . . .	25

2.3.5	Heating and cooling	26
2.3.6	Jeans mass	27
2.4	The formation process	28
2.4.1	The formation of the first core	28
2.4.2	Kelvin-Helmholtz contraction	29
2.4.3	Collapse and contraction time scale	29
2.5	Accretion processes	30
2.5.1	Monolithic collapse	31
2.5.2	Bondi-Hoyle accretion	31
2.5.3	Free-fall accretion	32
2.5.4	Dynamical models	37
2.5.5	Remark on the dynamical models	38
2.6	Magnetic fields	38
<b>3</b>	<b>Turbulence</b>	<b>43</b>
3.1	Introduction	43
3.1.1	Reynolds number	43
3.1.2	From laminar to turbulent flows	44
3.2	Mathematical concept	47
3.2.1	Symmetries and conservation laws	47
3.2.2	Kolomorov and Burgers turbulence	49
3.2.3	Compressible and incompressible modes	50
3.3	Astrophysical turbulence	51
3.3.1	Historical note	51
3.3.2	Power spectrum	52
3.3.3	Power sources for interstellar turbulence	52
3.4	Numerical realisation of turbulence	53
3.4.1	Self-consistent turbulence driving	53
3.4.2	Fourier transformed turbulence fields	54
3.4.3	Spatial and dynamical ranges	54
<b>4</b>	<b>Topic of the thesis</b>	<b>57</b>
4.1	Overview	57
4.2	Considered scales and processes	57
4.2.1	Global simulation parameters	58
4.3	Initial turbulence	59
4.3.1	Power spectrum of the turbulence	59
4.3.2	Mach numbers	60
4.3.3	Sound crossing time and turbulence crossing time	60
4.4	Numerical methods	61
4.4.1	Equations to solve	61

4.4.2	Operator splitting . . . . .	61
4.4.3	Grid-based numerical scheme . . . . .	62
4.4.4	Numerical diffusion . . . . .	64
4.4.5	Numerical code . . . . .	64
4.5	Resolution limits . . . . .	65
<b>5</b>	<b>Cloud structure and morphology</b>	<b>69</b>
5.1	Introduction . . . . .	69
5.2	Initial conditions . . . . .	71
5.2.1	Initial density profiles . . . . .	71
5.2.2	Runs . . . . .	76
5.3	Cloud structure and morphology – results . . . . .	77
5.3.1	Analysis of the TH profile . . . . .	85
5.3.2	Analysis of the BE profile . . . . .	87
5.3.3	Analysis of the PL15 profile . . . . .	88
5.3.4	Analysis of the PL20 profile . . . . .	92
5.4	Cloud structure and morphology – discussion . . . . .	96
5.5	Cloud structure and morphology – conclusions . . . . .	98
<b>6</b>	<b>Accretion behaviour</b>	<b>101</b>
6.1	Introduction . . . . .	101
6.2	Accretion behaviour – results . . . . .	103
6.2.1	Overview . . . . .	103
6.2.2	Limiting accretion effects . . . . .	105
6.2.3	Disc-like accretion mode . . . . .	107
6.2.4	Filamentary accretion mode . . . . .	114
6.2.5	Mass evolution of all runs . . . . .	116
6.3	Accretion behaviour – discussion . . . . .	125
6.4	Accretion behaviour – summary and conclusions . . . . .	128
<b>7</b>	<b>Tidal effects</b>	<b>129</b>
7.1	Introduction . . . . .	129
7.2	Initial conditions . . . . .	130
7.2.1	Initial density profiles . . . . .	130
7.2.2	Mach numbers and turbulence crossing time . . . . .	134
7.2.3	Runs . . . . .	134
7.3	Analytical estimates . . . . .	134
7.3.1	Free-fall analysis . . . . .	134
7.3.2	Tidal forces . . . . .	137
7.4	Tidal effects – results . . . . .	139
7.4.1	Overview and cloud evolution . . . . .	139

7.4.2	Turbulence without central collapse . . . . .	141
7.4.3	Turbulence with central collapse . . . . .	144
7.5	Tidal effects – summary and conclusions . . . . .	155
<b>8</b>	<b>Cluster properties</b>	<b>159</b>
8.1	Introduction . . . . .	159
8.2	Cloud and cluster analysis . . . . .	161
8.2.1	Energy analysis . . . . .	161
8.2.2	Subclustering . . . . .	162
8.2.3	Mass segregation . . . . .	164
8.3	Cluster properties – results . . . . .	165
8.3.1	Overview . . . . .	165
8.3.2	Energy evolution of the global cloud . . . . .	167
8.3.3	Global cluster properties . . . . .	175
8.3.4	Properties of the reduced clusters . . . . .	181
8.3.5	Mass segregation . . . . .	181
8.4	Cluster properties – discussion . . . . .	184
8.5	Cluster properties – summary and conclusions . . . . .	189
<b>9</b>	<b>Conclusion and outlook</b>	<b>193</b>
9.1	Summary . . . . .	193
9.2	Main conclusions . . . . .	193
9.3	Extensions and outlook . . . . .	195
9.3.1	Magnetic fields . . . . .	195
9.3.2	Stellar feedback . . . . .	196
<b>A</b>	<b>Resolution Study</b>	<b>199</b>
A.1	Resolution study . . . . .	199
A.1.1	BE profile . . . . .	199
A.1.2	PL20 profile . . . . .	200
A.2	Tidal forces . . . . .	201
<b>B</b>	<b>Angular Momentum</b>	<b>203</b>
B.1	Angular momentum . . . . .	203
<b>C</b>	<b>Gravitational Softening</b>	<b>205</b>
C.1	Gravitational force softening . . . . .	205

# Chapter 1

## Introduction

### 1.1 Motivation

Stars play an important role in astrophysics. On the one hand, they are used as tracers to investigate the dynamics and infer masses and other properties in distant galaxies. On the other hand, they actively influence their local environment with mechanical and radiative feedback as well as the long-term chemical evolution of the universe by fusing hydrogen to heavier elements and redistributing them into the evolutionary cycle via winds and supernovae. Most effects from stars like winds, radiation, and chemical enrichment strongly depend on the stellar mass, which emphasises the importance of the distribution function of stellar masses on different scales and over time. Observationally, there is clear evidence for a universal mass distribution in the local universe, which seems to break only for very extreme conditions, e.g., close to the Galactic centre. Theoretically, this universality is not fully understood. The question, to what extent the stars form with a particular mass in the first place or gain their mass via accretion processes can not be answered conclusively. In particular, the formation of high-mass stars comprises major uncertainties.

In order to understand and quantify the impact of stars on their immediate and remote environment via different individual processes, we need to strongly improve the understanding of the formation mode of stars under certain circumstances. We need to pin down, what physical processes abet or retard the formation of stars, change the mass distribution within a stellar cluster, determine the feedback from stars, and trigger or suppress the formation of subsequent stars in the neighbourhood of star-forming regions. The formation process of stars is strongly influenced by the temperature of the gas in the cloud, the dynamical state, the chemical composition, and

many other parameters, i.e., star formation strongly depends on the initial conditions provided by the environment. Unfortunately, the early stages of star formation that could betray the initial conditions of the cloud immediately before the collapse are difficult to observe. The gas is very dense and opaque to visible light, so many details of the initial conditions are hidden.

## 1.2 The formation of stars

The formation of stars viewed from a large-scale perspective like the entire galaxy with billions of stars seems to be a relatively simple problem and can indeed be described empirically by relatively few key parameters like the stellar initial mass function. In contrast, a closer look at the actual formation process involves a huge variety of different physical processes acting on different spatial and dynamical ranges. The formation of stars covers more than 10 order of magnitude in size from giant molecular clouds (100 pc) down to the stellar radius ( $10^6$  km), 13 orders of magnitude in time from the dynamical time of a giant molecular cloud ( $10^6$  yr) down to minutes or seconds for chemical reactions and radiative processes, roughly 20 orders of magnitude in density from the diffuse gas with  $\rho \sim 10^2 - 10^3 \text{ cm}^{-3}$  up to  $\rho \sim 10^{22} \text{ cm}^{-3}$ , and similar ranges for various kinds of energies. These ranges are extremely challenging to cover at once. Therefore, the investigation of star formation processes is split into several parts and reduced to the most relevant physical interactions for the scale under consideration.

### 1.2.1 From dissipative to collisionless systems

In a galactic context, the formation of stars is a by-product of dynamical interactions of diffuse gas in the interstellar medium and the resulting gravitational instability that leads to a collapse on different scales. The complex interplay between various mechanical, thermal, and chemical processes can be abstracted by the transition from highly dissipative interactions to a collisionless system. Initially the gas in the interstellar medium is diffuse with very small mean free paths of the atoms and molecules relative to the spatial extend of the gas cloud. Consequently, collisions and large scale relative motions between clouds result in collisions of the atoms and a conversion of ordered kinetic motions into random thermal motions and the gas heats up. If the cloud is optically thin, this thermal energy can be radiated away which allows the cloud to cool. Due to the highly inelastic and dissipative process, the initial bulk kinetic energy of the cloud is converted into entropy and is therefore irreversibly lost.

The onset of gravitational instabilities lead to the formation of local condensations and locally collapsing regions, in which the gas is compressed into small cores. The details of this collapse depend on the properties of the area in question as well as on many individual physical processes during the different stages of the collapse. Overall, the collapse of a cloud changes the system from a volume filling one to a very sparse ensemble of relatively compact objects whose collisions get less and less frequent. Eventually, the final ensemble of stars has mean free paths that exceed its spatial extent by far, which turns it into a collisionless system.

This transition between opposite global properties is independent of the detailed properties of the collapsed objects. The newly formed system of compact objects will be collisionless regardless of, e.g., the mass distribution or the radiative feedback properties. Of course, the contraction from gas to stars, which ignite nuclear fusion and make a separate contribution to the thermodynamics and the heat balance, changes the *details* of the collapse and the formation *time scale*. But it can not maintain the overall dissipative character of the system.

### 1.2.2 The dynamics of star forming regions

The collapse of a cloud and the change from a gaseous structure to a conglomeration of compact objects generally happens far from quiescence. Collisions of clouds, shear flows, and various kinds of thermal and dynamical instabilities result in an environment with turbulent motions and a complex structure. First collapsing condensations constitute the seeds for the formation of stars. During the strong gravitational interactions, these initial seeds significantly gain mass via accretion of the surrounding gas. The mass of the object is the main parameter that controls the further evolution of the star itself as well as the impact on the surroundings. Understanding the accretion behaviour and the resulting distribution of masses in an ensemble of stars is therefore crucial to understand the long term evolution of the system. In order to emphasise the importance of the stellar mass, the following sections present important physical processes that strongly depend on the stellar mass.

### 1.2.3 Stellar interiors and nuclear fusion

Although stars with different masses have significantly different evolutionary tracks, all stars start their life as a star by igniting nuclear fusion of hydrogen ( $^1\text{H}$ ) into helium ( $^4\text{He}$ ) in their core, once gravitational contraction and the resulting compression lead to sufficiently dense and hot conditions (temperature  $T \gtrsim$  a few million degrees, density  $\rho$  of order of  $1 - 100 \text{ g cm}^{-3}$ ). The two

main ways how to convert hydrogen into helium are the proton-proton (pp) chains and the carbon-nitrogen-oxygen (CNO) cycles. For the most part, the first process is a simple sequence starting with single protons and fusing them gradually to a helium nucleus. The second process uses C, N, and O as catalysts to convert  $^1\text{H}$  to  $^4\text{He}$ . Depending on which process is the dominant one, the released energy

$$\epsilon = \epsilon_0 \rho^\lambda T^\nu \quad (1.1)$$

differs significantly for the pp chain ( $\lambda = 1$ ,  $\nu \approx 4$ ) and the CNO cycle ( $\lambda = 1$ ,  $\nu \approx 15$ ). This strongly influences the fusion rate and finally the total time scale over which the star can maintain the fusion process before the fuel is exhausted. For stars up to roughly a solar mass, the pp chain is dominant, more massive stars burn their fuel via the CNO cycle. Overall, this means that the mass of the star that leads to the compressional heating in the first place is the most important parameter for the energy conversion and the total nuclear fusion time scale.

### 1.2.4 Stellar feedback

Once stars form, they influence their surroundings thermally and dynamically in almost all evolutionary stages. During their formation, magnetically driven jets and outflows collimate accreted material and feed it back into the interstellar medium with high velocities, inducing turbulent motions in the directions of the flow. Having entered the main sequence phase, the radiation emitted from the atmosphere heats the surrounding gas in a mostly spherically symmetric manner. Similarly, winds that are expelled from the star via radiation dynamically interact with the environment and, in addition, reduce the stellar mass over its life time, strongly dependent on the initial stellar mass. At the end of a star's life, massive stars undergo a supernova explosion, which both thermally and dynamically alter the environmental conditions.

#### Jets and outflows

During the formation of stars, rotating cores collapse while conserving angular momentum. This leads to the formation of a centrifugally supported disc with sizes of a few hundred AU ([Andrews and Williams, 2007](#); [Kitamura et al., 2002](#)). The contraction of the system, coupled with angular momentum transport and mass accretion drives powerful winds and jet-like outflows with observed velocities of  $v \gtrsim 100 \text{ km s}^{-1}$  ([Shepherd and Churchwell, 1996](#); [Arnett, 1996](#); [Beuther et al., 2002](#); [Wu et al., 2004](#)). These outflows are likely to be driven by magnetic fields ([Blandford and Payne, 1982](#); [Pudritz](#)

and Norman, 1983; Spruit, 1996; Pudritz, 2004) rather than by radiation (Lada, 1985).

## Radiation

An important feedback mechanism from protostars and stars is radiative feedback that heats or even ionises the surrounding medium (see, e.g., review by McKee and Ostriker, 2007). During the early phases of star formation, the majority of radiation originates from the conversion of potential to thermal energy during the accretion phase. Once a star starts to burn and reaches a mass of  $\sim 8 M_{\odot}$ , the radiation that diffuses from the burning core to the envelop starts to dominate over accretion effects.

During the star formation process in large and dense clouds with complex interior structure, the first stars can heat the immediate surrounding gas and may prevent it from undergoing gravitational collapse (For details, see chapter 2.1.3). This means that the first stars in a cluster influence the subsequent formation of other stars in their neighbourhood, in particular in the case of high-mass stars (see, e.g., Yorke and Sonnhalter, 2002; Krumholz et al., 2007; Peters et al., 2010a). The amount of radiated energy from the stellar surface depends on the energy conversion via accretion in the early phases of star formation and via nuclear fusion in the core of a star at a later stage. For both processes, the mass of the star is a crucial parameter.

In addition to the heating effect on the surrounding gas, the radiation pressure from high-mass stars may be high enough to prevent gas from being accreted onto the star (see review by, e.g., Zinnecker and Yorke, 2007). The luminosity in this case exceeds the Eddington limit, which corresponds to the balance of gravitational attraction and radiative expulsion. A spherically symmetric analysis therefore sets upper limits on the mass of an accreting star. However, in dynamical models and simulations the limits can be bypassed by radiation shielding and funneled accretion flows onto the star.

## Winds

During their entire life stars expel electrons and atoms from their surface, known as stellar winds. For small stars like our sun, the ejected particles are mostly electrons and protons and almost no heavy elements. The low radiation pressure and low surface temperature of low-mass stars do not allow heavy elements to escape. In contrast, O-B stars have a significantly higher surface temperature and radiation pressure and can eject heavier elements like nitrogen and oxygen (Castor et al., 1975). Whereas the total mass of low-mass stars is not significantly affected by stellar winds, high-mass stars can

lose a remarkable fraction of their initial mass (see, e.g., [Chiosi and Maeder, 1986](#); [Meynet et al., 1994](#)). Apart from the consequences for the further stellar evolution, the large amount of ejected material provides mechanical energy to blow bubbles into the interstellar medium and sweep up material for potential subsequent star formation as well as chemical enrichment that alters the chemical processes in the surrounding area. In particular carbon and oxygen undergo important chemical reactions for star formation.

## Supernovae

Depending on the initial mass of the star, the stellar fate also differs remarkably (e.g., [Iben, 1967](#); [Hansen et al., 2004](#)). Whereas most low-mass stars end their lives quietly, the more massive stars ( $M \gtrsim 8 M_{\odot}$ ) eventually undergo a core collapse and explode in a gigantic supernova explosion (see, e.g., [Heger et al., 2003](#)). During the burning of nuclear fuel, the numerous hydrogen atoms are fused to large nuclei – mostly iron nuclei in a stable nuclear burning. The total number of nuclei reduces during this phase significantly which leads to a loss in stabilising pressure against gravitational forces in the centre of a star. This goes along with a further contraction of the central region of the star until the core can not supply enough stabilising pressure and collapses. The remaining material can then ignite an unstable thermonuclear ignition of outer layers which disrupts the star and ejects thermal as well as mechanical feedback into the surrounding medium. This in turn has a strong impact on the subsequent formation of stars in the immediate surrounding. Whereas regions close to the supernova are likely to be disrupted entirely, the expanding shock wave may also sweep up enough material for a new cycle of star formation. Perhaps the most important contributions of supernovae are the injected turbulence, determining the dynamics of new star-forming regions, and the chemical enrichment, influencing the thermal properties of the gas. As turbulence is an important aspect of star formation it is discussed in detail in [chapter 3](#). In contrast to stellar winds that mostly eject light nuclei into the interstellar medium, supernovae supply their environment with *all* heavy elements. These elements cover both the ones that form during the stellar phase in thermonuclear fusion, i.e., elements up to iron, as well as heavier elements that form via pyconuclear reactions during the explosion. Consequently, star formation in the immediate proximity to a supernova proceeds differently than in an low-metallicity environment.

### 1.2.5 Stellar masses

All together, an equally simple but significant key property of a star is its mass. A complex combination of differently massive collapsing areas and further accretion processes onto the first forming cores finally shapes the distribution function of stellar masses. The mass function obtained from observations shows an astonishingly uniform shape in the present-day universe. For most regions, the so-called *initial mass function* (IMF),  $\phi$ , of stars can be described by a piece-wise defined power-law distribution. The first person to derive an IMF was [Salpeter \(1955\)](#). He fitted the observational data for stars with masses ranging from  $0.4 - 10 M_{\odot}$  with a power-law function

$$\phi(M) dM \propto M^{-2.35} dM. \quad (1.2)$$

Today, stars with lower masses than  $0.4 M_{\odot}$  can be observed, which show a significant departure from the Salpeter equation. The IMF is usually fitted with different power-laws for three main mass ranges,

$$\phi(M) dM \propto M^{-2.3} dM : M \gtrsim 0.5 M_{\odot} \quad (1.3)$$

$$\phi(M) dM \propto M^{-1.3} dM : 0.5 M_{\odot} \gtrsim M \gtrsim 0.08 M_{\odot} \quad (1.4)$$

$$\phi(M) dM \propto M^{-0.3} dM : 0.08 M_{\odot} \gtrsim M \gtrsim 0.01 M_{\odot}, \quad (1.5)$$

where the Salpeter slope still holds for high masses. The above fits for the IMF are only one popular possibility. Many models have been developed to explain the details of the distribution in different mass regimes. For a discussion on the shape of the IMF, see the review by [Bastian et al. \(2010\)](#).

Although the IMF shows universality in many regions of the present-day universe, its shape is expected to differ perceptibly in the early universe. The lack of heavy elements and the resulting less efficient cooling possibilities of the interstellar medium is likely to affect the IMF in favour of more massive stars. As this epoch of star formation is inaccessible observationally, there are only theoretical models for the IMF in the early universe. Due to large uncertainties in the thermal and dynamical processes of low-metallicity gas, no conclusive shape for the IMF of the first stars has been established so far.

## 1.3 The sites of contemporary star formation

Stars form in the densest parts of molecular clouds. These clouds are concentrated in the disc of galaxies, in particular in the spiral arms. Examples of star-forming regions in the Milky Way are Taurus, Orion, W3, and W49. Most stars if not all form in a clustered environment rather than in isolation

(e.g., [Lada and Lada, 2003](#)). Even among observed field stars there is a decisive fraction that is likely to originate from a cluster. However, the term *cluster* in this context is hard to define. Some stars form in small ensembles of only 10, other clusters count as many as  $10^7$  members. An additional complication arises from the complex substructure in clusters. Nonetheless, in both observations and simulations of star-forming regions, only very few stars form in complete isolation.

One special type of star-forming regions are OB associations, named after the significant number of O and B stars they contain. They are unbound, which allows them to grow in size over time, contain  $10^3 - 10^5$  stars, and have sizes of 10 – 200 pc. Their formation is linked to star formation in large molecular cloud complexes like Orion, Upper Scorpius and Upper Centaurus-Lupus. After the most massive stars in an OB association have burned out, the area is largely dispersed due to the strong impact of the massive stars on their environment and hard to discern. Most OB associations can be subdivided into smaller groups, of which the youngest star-forming regions are the most embedded areas, surrounded by a dense, opaque cloud of gas. For electromagnetic waves up to wave lengths in near and mid infrared, the clouds are opaque, which justifies their name *infrared dark clouds* (see, e.g., review by [Bergin and Tafalla, 2007](#)).

### 1.3.1 Properties of molecular clouds

Molecular clouds have size of a few tens of parsecs and contain up to  $10^5$  solar masses of gas. Observations reveal that their structure is filamentary and that the medium in the cloud is turbulent with supersonic velocities (rms Mach numbers of  $\mathcal{M} = 5 - 20$ , [Zuckerman and Evans \(1974\)](#)). These clouds are cold with temperatures of the order of 10 K. With an average number density of  $100 \text{ cm}^{-3}$  and a low temperature, the gas is mainly molecular rather than in an atomic phase. This leads to a difficulty in the visibility of the processes in the cloud. The  $\text{H}_2$  molecule, which is by far the most abundant one, does not have a dipole moment and the rotational and vibrational modes of  $\text{H}_2$  are too energetic to be excited by collisions in this cold environment. Therefore, the clouds are dark. Observations of the interior structure are only possible via other tracer molecules like CO,  $\text{NH}_3$  or HCN. As the abundances of these molecules are sensitive to the environment and the dynamics of the cloud, and the opacity can vary strongly within the cloud, observations of the interior of molecular clouds are challenging. A more robust tracer for observations is dust because the gas-to-dust ratio of about 100 seems to be roughly constant throughout the cloud ([Lilley, 1955](#); [Predehl and Schmitt, 1995](#)). As dust extinction measurements are indepen-

Table 1.1: Key properties of dark clouds, clumps, and cores

	Clouds	Clumps	Cores
Mass ( $M_{\odot}$ )	$10^3 - 10^4$	50 – 500	0.5 – 5
Size (pc)	2 – 15	0.3 – 3	0.03 – 0.2
Mean density ( $\text{cm}^{-3}$ )	$10^3 - 10^4$	$10^4 - 10^5$	50 – 500
Velocity extent ( $\text{km s}^{-1}$ )	2 – 5	0.3 – 3	0.1 – 0.3
Crossing time (Myr)	2 – 4	$\approx 1$	0.5 – 1
Gas temperature (K)	$\approx 10$	10 – 20	8 – 12
Examples	Taurus, Oph, Musca	L1709, B213	L1544, L1498, B68

dent of the dust temperature and directly proportional to the optical depth and thus the column density, dust can be used to estimate the gas content of the cloud (Lada et al., 1994; Alves et al., 1998; Lombardi and Alves, 2001).

With increasing density the size of the structures shrinks going from *clouds* to *clumps* and *cores*, whose central density reaches  $10^4 - 10^5 \text{ cm}^{-3}$ . Typical values for the structures are shown in table 1.1, taken from Bergin and Tafalla (2007). The dynamical state changes from the overall highly supersonic molecular cloud to transsonic dense cores. Although a classification of the individual structures is difficult, cores with a diameter of  $d \lesssim 0.2 \text{ pc}$  are assumed to be the actual sites of star formation.

### 1.3.2 Turbulence

There is observational evidence for complex gas motions within a molecular cloud, which can not be explained by unordered thermal motions and is associated with turbulence. Turbulent motions are characterised by locally ordered motions following eddies of different sizes. A key number that distinguishes between laminar and turbulent flow is the Reynolds number

$$\text{Re} = \frac{\rho v l}{\mu}, \quad (1.6)$$

where  $\rho$  is the density,  $v$  the velocity,  $l$  the lengths of the area in question, and  $\mu$  the viscosity of the gas or fluid. This ratio can also be expressed as the ratio of inertia force over viscous force or total momentum transfer over molecular momentum transfer. Above a critical Reynolds number, small perturbations in the ordered laminar flow can grow, the flow becomes unstable, and turbulent eddies develop. Averaged over several eddies in a turbulent flow again yields an isotropic pattern, which appears like an additional turbulent pressure term. Observations of molecular lines in star-forming regions

show line widths that are too broad to be explained by thermal motions with the inferred temperature. Thus, this additional line broadening is associated with turbulent contributions. Empirically, the size of a gaseous structure and its dynamical state are linked via a simple functional relation. [Larson \(1981\)](#) found the velocity dispersion and the size to be connected by a power-law function

$$\frac{\sigma}{\sigma_0} = \left( \frac{L}{L_0} \right)^n, \quad (1.7)$$

the so-called *Larson's law*, where  $n \approx 0.5$  and  $\sigma_0 \approx 1 \text{ km s}^{-1}$  for  $L_0 = 1 \text{ pc}$ .

The thermal line broadening can be estimated with the velocity dispersion  $\sigma_T = (kT/m)^{1/2}$ , where  $k$  is the Boltzmann constant,  $T$  the temperature, and  $m$  the mean molecular weight of the atoms and molecules. The total effect of line broadening is given by  $\sigma_0^2 = \sigma_T^2 + \sigma_{NT}^2$ , where  $\sigma_{NT}^2$  is the non-thermal contribution. How dominant the non-thermal broadening is, depends on the kinematics of the region, which is empirically connected to its size. Observationally, one finds that for cores above a size of  $0.01 - 0.1 \text{ pc}$ ,  $\sigma_{NT}^2$  is the dominant term. However, as the dynamics on small scales is inherited from the dynamical cascade of motions from large to small scales during the collapse of a region, the structure of the turbulent motions still plays an important role in regions where the thermal line broadening is comparable to or even larger than the turbulent contribution. A detailed discussion of the effects of turbulence is presented in [chapter 3](#).

## 1.4 Objectives of star-formation theory

Many aspects of star formation are still a matter of debate, in particular because many stages can not be observed directly. During the formation process, the young stellar object is deeply embedded into a dense environment that obscures the interior processes. In addition, the individual star-forming regions that we are able to observe with current methods differ remarkably so that a direct comparison is impossible. Therefore, many aspects of present-day star formation can only be answered in a statistical manner, if averaged over a large ensemble of objects. Some of the main objectives of theoretical investigations are listed below (adapted from [Ward-Thompson and Whitworth, 2011](#)).

### 1. Is there a threshold surface density or volume density for star formation to occur?

A disc tends to be stable against fragmentation unless the *Toomre*

parameter (Toomre, 1964)

$$Q \equiv \frac{c_s \kappa}{\pi G \Sigma} < 1, \quad (1.8)$$

where  $c_s$  is the speed of sound,  $\kappa$  is the epicyclic frequency in the disc,  $G$  is the Gravitational constant, and  $\Sigma$  is the surface density of the disc. This threshold criterion has been applied primarily in the Galactic disc. On small scales there are idealised theoretical thresholds like the *Jeans criterion* (Jeans, 1902) for a thermal instability or the critical *mass-to-flux ratio* in magnetised environments (Mestel and Spitzer, 1956; Mestel, 1965; Mouschovias and Spitzer, 1976). However, these estimates only use global quantities like the total energy of the region under consideration and might not precisely describe the real processes.

## 2. What determines the efficiency of star formation?

Once star formation sets in, what are the processes and conditions that eventually stop it. In a simple gravitational picture of an unstable cloud without any stellar feedback, the star formation efficiency will eventually reach 100 percent because all gas in the cloud can either collapse to form numerous individual stars or is accreted onto the existing ones. Observations, however, reveal that the formation of stars is rather inefficient with a fraction of only a few percent of gas that is converted into stars. Radiative feedback is certainly one important aspect in terminating further fragmentation of the surrounding gas, but current theoretical and numerical work suggests that radiation feedback does not prevent ongoing accretion.

## 3. What causes the IMF?

If measured a large ensemble of stars, the stellar mass distribution shows evidence for universality. However, there is no conclusive theoretical theory describing the shape of the IMF. Is there a precise interplay between turbulence, gravitational collapse and dynamical accretion that shapes the IMF? Is this complex interplay a self-regulating process? Do specific scale-dependent processes set the pivotal key properties? How important are local processes before the immediate formation of a stars in comparison to the initial conditions on large scales, i.e., at what point during the star formation process is the structure of the IMF determined.

## 4. What fraction of stars is born in clusters/in isolation?

It is fairly established that most stars form in a clustered environment. But how large is that fraction precisely? Are there only a few individual

stars that are accidentally born in isolation or is there a different star formation mode that produces isolated stars? Are there perhaps more stars that form in isolation that quickly merge with a clustered stellar structure? What type of star is mostly born in isolation? Does an IMF for isolated stars look the same as the universal IMF?

**5. What determines the cluster structure?**

Stellar ensembles form with very different masses, number of members, and energetic states. What determines the number of stars that form in a group and how bound the system is. Is there a universal principle behind the substructure of these ensembles?

**6. What is the binary statistics?**

Many stars form binary systems with very different binary properties like ratio of masses, orbital period, and eccentricity. The observed values for these binary parameters cannot be explained by theoretical models. In particular it is still unclear when and how these binary systems form.

**7. How do these aspects depend on environmental factors?**

This aspect focuses on the impact of large scale phenomena. How do galaxy mergers change the star formation process. What is the influence of UV radiation or cosmic rays? How important are chemical abundances and the temperature of the surrounding gas, i.e., to what extent does star formation differ in the early universe?

# Chapter 2

## Star formation theory

This chapter covers some important physical aspects that need to be taken into account for present-day star formation theory. We discuss self-gravity and gravitational instability as the main driver for star formation, the hydrodynamic limit and resulting conservation laws, and the relevant thermodynamics for the investigated clouds. We also review the individual phases of the gravitational collapse and the accretion processes that control the dynamical mass growth during the collapse. The aspects of turbulent motions that play an important role on almost all scales are not described in this chapter but are presented in detail in chapter 3.

### 2.1 Gravity

Although gravity is only one force for all sort of objects, there is a significant difference between *external forces* acting on a collapsing subsystem and the effects resulting from *self-gravity* of the subsystem. External fields lead to global acceleration, large scale rotation and tidal effects. Self-gravity supports a subsystem to collapse to the local centre of mass. In this work, We concentrate on the effects of tidal fields onto small overdensities and the effects of self-gravity in the investigated clouds. Within the complex interplay between thermal, kinetic, and gravitational energy, the onset of gravitational instabilities play a major role in the formation of individual stars and nascent clusters.

#### 2.1.1 Self-gravity

For the given mass and density ranges of star formation, the Newtonian description ([Newton, 1687](#)) of gravity is sufficient for our calculations. In

this limit, gravity can be described as a conservative scalar potential  $\Phi$ . A self-consistent description of the gravitational potential with the mass distribution is given by the Poisson equation,

$$\Delta\Phi = 4\pi G\rho. \quad (2.1)$$

Taken into account the boundary condition that the potential  $\Phi$  needs to vanish at infinity, one can solve this elliptical partial differential equation.

### 2.1.2 Virial theorem

In general, the virial theorem states that the temporal average of the kinetic,  $E_{\text{kin}}$ , and the potential energy,  $U$ , are related as (see, e.g., [Scheck, 1990](#))

$$2\langle E_{\text{kin}} \rangle - \left\langle \sum r_i \cdot \nabla_i U \right\rangle = 0. \quad (2.2)$$

If the potential is a homogeneous function of order  $k$  in the arguments  $r_i$  the above equation simplifies to

$$2\langle E_{\text{kin}} \rangle - k\langle U \rangle = 0. \quad (2.3)$$

For the Newtonian description of gravity,  $k = -1$ , yielding a virialised system for the condition

$$\alpha = \frac{\langle E_{\text{kin}} \rangle}{\langle U \rangle} = \frac{1}{2}, \quad (2.4)$$

where  $\alpha$  is called the *virial parameter*. Note that this is a necessary, but not sufficient criterion for equilibrium.

During the formation process of stars, starting from the earliest phase in overdense regions of molecular clouds to the main sequence star, the virial parameter,  $\alpha$ , changes. Molecular clouds with sizes of the order of parsecs tend to be super-virial, i.e.,  $\alpha > 0.5$ . In contrast, local overdense regions within the cloud may be in a sub-virial state, which may cause the region to collapse.

As the virial parameter only relates the total kinetic energy to the total potential energy, it does not necessarily indicate whether the region under consideration is gravitationally stable or collapsing. Further information about the thermal properties of the gas and the direction of the gas motions is needed in order to determine whether a cloud is going to collapse.

Associated with the virial analysis, there is the virial mass and a virial velocity, which are both direct consequences of the virial theorem. Given the total kinetic energy as

$$E_{\text{kin}} = \frac{Mv^2}{2} \quad (2.5)$$

and a total potential energy of a spherically symmetric mass distribution

$$U = -\frac{GM^2}{R}, \quad (2.6)$$

the virial theorem states

$$Mv^2 = \frac{GM^2}{R}, \quad (2.7)$$

which can be solved for the mass and the velocity, respectively, yielding

$$M_{\text{vir}} = \frac{Rv^2}{G} \quad (2.8)$$

for the virial mass and

$$v_{\text{vir}} = \sqrt{\frac{GM}{R}} \quad (2.9)$$

for the virial velocity.

### 2.1.3 Gravitational instability

For a basic investigation of the fragmentation behaviour we need to discuss the occurrence of gravitational instabilities and the main parameter associated with them. A simple estimate of the collapse condition can be done by equating the stabilising accelerations due to thermal pressure and the contracting acceleration due to self-gravity. This analysis is known as the Jeans instability (Jeans, 1902). Consider uniform density in three-dimensional space with small density fluctuations. For symmetry reasons, an infinite uniform medium does not develop expanding or collapsing regions, because the internal pressure and the gravitational potential are uniform. In the presence of fluctuations, in contrast, the question is whether these fluctuations can grow and contract or disperse due to internal pressure.

The pressure term is  $\nabla P/\rho$ , which can be approximated in an isothermal case with  $\nabla P \sim P/r$  and  $P = c_s^2\rho$ , yielding

$$\frac{\nabla P}{\rho} \sim \frac{c_s^2}{r}. \quad (2.10)$$

The contribution due to gravity is given by  $-GM/r^2$  and reduces to

$$-\frac{GM}{r^2} \sim -\frac{G\rho_0}{r}, \quad (2.11)$$

using  $M = \rho_0 r^3$ . Adding both effects, the net acceleration is given by

$$\ddot{r} \approx \frac{c_s^2}{r} - \frac{G\rho_0}{r}. \quad (2.12)$$

For a contraction,  $\ddot{r}$  needs to be negative, yielding the threshold condition,  $\ddot{r}(r = \lambda_J) = 0$ ,

$$\lambda_J = \frac{c_s}{(G\rho)^{1/2}}. \quad (2.13)$$

Here,  $\lambda_J$  is called the *Jeans length*, which marks the minimum initial radius for a spherically symmetric cloud of uniform gas with density  $\rho_0$  and isothermal sound speed  $c_s$  to collapse under its own weight. A different derivation of the Jeans length can be done via perturbation theory, leading to  $\lambda_J = \sqrt{\frac{\pi c_s^2}{G\rho}}$  with a slightly different numerical prefactor. Both formulas are used in the literature.

The Jeans length and the given density yield a corresponding mass, the *Jeans mass*,

$$M_J = \frac{4\pi}{3} \left(\frac{\lambda_J}{2}\right)^3 \rho \quad (2.14)$$

$$= \frac{\pi c_s^3}{6\sqrt{G^3\rho_0}}, \quad (2.15)$$

defined as a sphere with a diameter of a Jeans length. This definition of the volume is not universally used in the literature. One other commonly found definition of the Jeans mass is based on a box, where the length of the edge is set to the Jeans length. Using the isothermal sound speed of an ideal gas,  $c_s = \sqrt{kT/(\mu m)}$ , gives

$$M_J \propto \frac{T^{3/2}}{\rho^{1/2}}, \quad (2.16)$$

indicating a strong dependence of the Jeans mass on the temperature. Figure 2.1 shows the Jeans mass as a function of density for different temperatures.

### 2.1.4 Core life time

If a core is not in hydrostatic equilibrium its life time depends on the energy content and the exact dynamical processes. For an order of magnitude estimate, one can distinguish between a cloud that is strongly dominated by kinetic motions and one that is entirely dominated by gravity. In the first case, the dispersion time scale is given by

$$t_{\text{disp}} = \frac{R}{\sigma}, \quad (2.17)$$

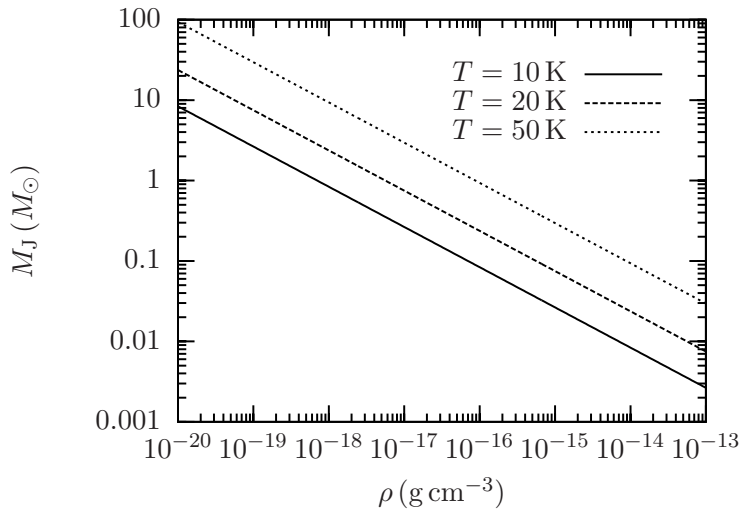


Figure 2.1: Jeans mass as a function of density for different temperatures.

where  $R$  is the radius of the cloud and  $\sigma$  is the velocity dispersion. In the opposite case, the collapsing time scale can be approximated by gas in free-fall yielding

$$t_{\text{ff}} = \left( \frac{3\pi}{32G\rho} \right)^{1/2}, \quad (2.18)$$

only depending on the density of the cloud,  $\rho$ , see figure 2.2.

## 2.2 Conservation laws

Conservation laws are perhaps the most powerful tools in physics. The conservation of a certain quantity sets major constraints on the available phase space for a physical system. For calculations in star formation, we use the first three moments of the *Boltzmann transport equation* to describe the conservation of mass, momentum, and energy in the hydrodynamic limit.

### 2.2.1 Hydrodynamic limit

The conservation of physical quantities like mass, momentum, and energy can be done in many different ways, depending on the framework, in which the equations are formulated. The evolution of a large number of gas particles can be done using collisional invariants of the Boltzmann transport equation, which predicts an irreversible increase of the entropy of a thermally isolated

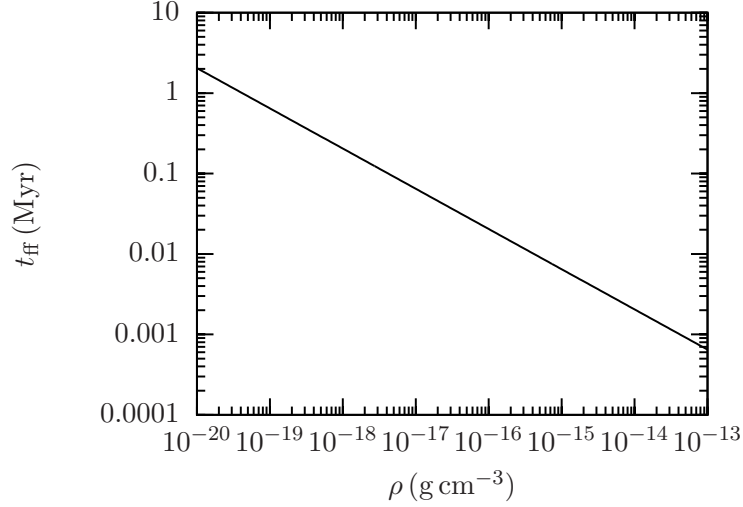


Figure 2.2: Free-fall time as a function of density.

gas

$$S \equiv -k \int f \ln f d^3x d^3p, \quad (2.19)$$

with  $k$  being Boltzmann's constant and  $f$  being the particles' distribution function. The integral is taken over the entire  $6N$ -dimensional phase space of the system. As in this approach it is difficult to obtain evolutionary equations for mass, momentum, and energy, the system is analysed with *moment equations*. Using the zeroth, first and second moment of  $f$  of the Boltzmann equation, we arrive at the following equation for mass, momentum, and energy

$$\begin{pmatrix} \rho \\ \rho \mathbf{u} \\ \rho E \end{pmatrix} \equiv \int \begin{pmatrix} m \\ m \mathbf{v} \\ m |\mathbf{v} - \mathbf{u}|^2 / 2 \end{pmatrix} f(\mathbf{x}, \mathbf{v}, t) d^3v, \quad (2.20)$$

where  $\rho$  is the density,  $m$  the total mass of the set of particles,  $\mathbf{u}$  the net motion of the set of particles,  $\mathbf{v}$  the motion of the individual particles, and  $E$  the kinetic energy about the mean motion.

One common way is to use the fluid approximation to follow the gas dynamics of a star-forming region. In order for the fluid approach to be valid, the mean free path of a gas molecule,  $l$ , needs to be much less than the size of a defined fluid element,  $L$ ,

$$l \ll L. \quad (2.21)$$

In this limit, the gas molecules can collisionally exchange kinetic and thermal energy. This condition is therefore equivalent to *local thermal equilibrium*.

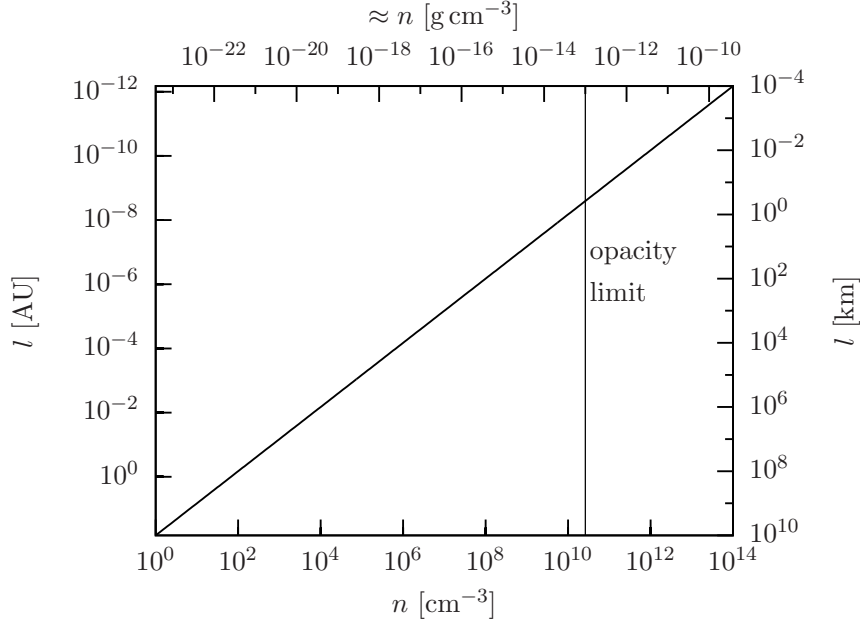


Figure 2.3: Mean free path for a gas molecule as a function of density.

The mean free path is given by  $l = (n\sigma)^{-1}$ , where  $n$  is the number density of typical collision partners and  $\sigma$  is the scattering cross section. Assuming a typical value of  $\sigma \sim 10^{-15} \text{ cm}^2$  gives the mean free path for gas molecules shown in figure 2.3. For the density ranges we are investigating in this work, the mean free path is significantly smaller than the size of a computational fluid element. The approach of a fluid is therefore justified.

In optically thin regions, the mean free path of photons is usually much larger than the computational cells. The fluid approach then breaks down and radiation generally needs to be treated differently. Only in very dense regions, where the gas is opaque, the mean free path of photons decreases perceptibly below the size of a computational cell and the fluid approach is also applicable for radiation fields.

### 2.2.2 Conservation of mass

From equation (2.20) we get the equation for the conservation of mass, also called *continuity equation*, which reads

$$\frac{\partial \rho}{\partial t} + \frac{\partial}{\partial x_k}(\rho u_k) = 0. \quad (2.22)$$

Apart from the pure information of mass conservation, this equation also contains the information that the density within a given volume changes in

a continuous fashion. A change in density within this volume is related to the mass flow through the surface of the volume. The equation can be written in vector notation like

$$\frac{\partial \rho}{\partial t} + \nabla \cdot (\rho \mathbf{u}) = 0. \quad (2.23)$$

### 2.2.3 Conservation of momentum

The *momentum equation* takes the form

$$\frac{\partial}{\partial t}(\rho u_i) + \frac{\partial}{\partial x_k}(\rho u_i u_k + P \delta_{ik} - \pi_{ik}) = -\rho \frac{\partial \Phi}{\partial x_i}. \quad (2.24)$$

Here, the  $i$ -th component of the momentum density is denoted  $\rho u_i$ . The momentum flux of the  $i$ -th component in the  $k$ -th direction consists of a mean part,  $\rho u_i u_k$ , and a random part, which is split into an isotropic component,  $P \delta_{ik}$ , and a non-isotropic and therefore traceless component,  $\pi_{ik}$ . The isotropic component is associated with the pressure of the gas, the non-isotropic one with viscous properties of the gas. The source term on the right hand side is the momentum density contribution due to the gravitational acceleration.

In astrophysical computations the viscous stresses  $\pi_{ik}$  are generally unimportant. The ratio of kinetic over viscous contributions to the momentum reads

$$\frac{\partial(\rho u_i u_k)/\partial x_k}{\partial \pi_{i,k}/\partial x_k} \sim \frac{\rho U^2/L}{\mu U/L^2} = \frac{UL}{\nu} =: \text{Re}, \quad (2.25)$$

with the typical flow speed  $U$ , the shear viscosity  $\mu$ , the kinematic viscosity  $\nu = \mu/\rho$ , and the Reynolds number  $\text{Re}$ . The shear viscosity can be estimated with the Chapman-Enskog procedure (see, e.g., [Shu, 1992](#))

$$\mu \sim \frac{m v_T}{\sigma}, \quad (2.26)$$

where  $v_T$  is the thermal speed  $(kT/m)^{1/2}$  and  $\sigma$  is the collision cross section. This simplifies the kinematic velocity to  $v_T l$ , where  $l$  is the mean free path. The Reynolds number is then

$$\text{Re} \sim \frac{UL}{v_T l} \gg 1, \quad \text{for } U \sim v_T. \quad (2.27)$$

For astrophysical flows in the transsonic or supersonic regime, the Reynolds number are therefore usually large and viscous stresses can be neglected in numerical computations, which we also do in this work.

### 2.2.4 Conservation of energy

The second moment of the Boltzmann equation finally leads to the energy equation

$$\begin{aligned} \frac{\partial}{\partial t} \left( \frac{\rho}{2} |\mathbf{u}^2| + \rho\varepsilon \right) + \frac{\partial}{\partial x_k} \left[ \frac{\rho}{2} |\mathbf{u}^2| u_k + u_i (P\delta_{ik} - \pi_{ik}) + \rho\varepsilon u_k + F_k \right] \\ = -\rho u_k \frac{\partial \Phi}{\partial x_k}. \end{aligned} \quad (2.28)$$

The total energy density  $\rho E$  is the sum due to bulk motion,  $\rho |\mathbf{u}^2|$ , and random motion, i.e., internal energy,  $\rho\varepsilon$ :  $E = \varepsilon + |\mathbf{u}|^2/2$ . The energy flux in direction  $k$  is given by the translation of the bulk kinetic energy,  $(\rho |\mathbf{u}^2|/2) u_k$ , plus the flux of enthalpy,  $(\rho\varepsilon + P) u_k$ , plus a viscous contribution,  $-u_i \pi_{ik}$ , plus the conductive flux,  $F_k$ . The source term on the right-hand side,  $\rho u_k \partial \Phi / \partial x_k$ , is the contribution due to gravitational acceleration. The conductive term,  $F_k$ , is, like  $\pi_{ik}$ , also not considered here because the ratio of the advection of heat over the conduction of heat (see, e.g., [Shu, 1992](#)),

$$\frac{\partial[(\rho\varepsilon + P)u_k]/\partial x_k}{\partial F_k/\partial x_k} \sim \text{Re}, \quad (2.29)$$

is of the order of the Reynolds number and generally high in the considered environments.

The energy equation can be rewritten as a function of total energy density as follows,

$$\frac{\partial}{\partial t} (\rho E) + \frac{\partial}{\partial x_k} [(\rho E + P) u_k] = -\frac{\partial F_k}{\partial x_k} + \pi_{ik} \frac{\partial u_i}{\partial u_k} - \rho u_k \frac{\partial \Phi}{\partial x_k}. \quad (2.30)$$

### 2.2.5 Closure relations

The three equations shown above describe the conservation of mass, momentum, and energy with various terms that describe the properties of the gas. However, the three equations do not form a closed system just by themselves. The total number of variables is larger than the number of equations: There are thirteen variables, density (1), velocity (3), pressure (1), viscous stress tensor (5 for a symmetric traceless tensor), and conductive flux (3). In contrast, the number of equations is only five. Therefore, for a self-consistent combination of them, we need closure relations that connect the thirteen variables. Depending on the environment, in which we want to use the equations, the dominating physical processes and the resulting closure relations will differ.

Relating the density to the pressure via an equation of state yields the so called *Navier-Stokes* equations, the limit of negligible viscous stresses and conductive heat reduces the Navier-Stokes equation to the *Euler equations*.

### 2.2.6 Overview of the equation

As we neglect viscous stresses as well as heat conduction, we only solve the Euler equations in this work. With an ideal equation of state, we arrive at the following set of equations:

$$\frac{\partial \rho}{\partial t} + \nabla \cdot (\rho \mathbf{u}) = 0, \quad (2.31)$$

$$\frac{\partial \rho \mathbf{u}}{\partial t} + \nabla \cdot (\rho \mathbf{u} \mathbf{u}) + \nabla P = \rho \mathbf{g}, \quad (2.32)$$

$$\frac{\partial \rho E}{\partial t} + \nabla \cdot [(\rho E + P) \mathbf{u}] = \rho \mathbf{u} \cdot \mathbf{g} \quad (2.33)$$

with the equation of state

$$E = \varepsilon + \frac{1}{2} |\mathbf{u}|^2, \quad (2.34)$$

$$P = (\gamma - 1) \rho \varepsilon \quad (2.35)$$

that is described in more detail in the following section. A description of the numerical solution of the equations is given in section [4.4](#).

## 2.3 Thermo- & chemodynamic processes

The conditions, when and where stars start to form strongly depends on the behaviour of the material that stars form from. The major constituent by mass for all stars and all star-forming environments is hydrogen gas. However, the dynamical, chemical, and thermal behaviour can be strongly influenced by catalysts of various kinds that trigger chemical reactions or radiative transitions and change the properties of the gas. Some important elements with a significant impact are various oxygen and carbon species and dust particles. In this section we describe the main processes that heat or cool the gas in star-forming regions and eventually determine its thermal state in the investigated environment.

### 2.3.1 Equation of state

The simplest assumption for a gaseous medium is an ideal gas, obeying the relation

$$PV = NkT, \quad (2.36)$$

with the pressure,  $P$ , the volume,  $V$ , the total number of gas particles,  $N$ , the Boltzmann constant,  $k$ , and the temperature,  $T$ . As the total volume and total number of particles are less convenient, we can relate them to the density,  $\rho$ ,

$$\rho = \frac{N\mu m_p}{V}, \quad (2.37)$$

where  $\mu$  is the molecular weight and  $m_p$  is the mass of a proton. Then the equation of an ideal gas finally reads

$$P = \frac{\rho kT}{\mu m_p}. \quad (2.38)$$

The temperature of the gas can be related to the internal energy,  $\varepsilon$ , yielding for the pressure

$$P = (\gamma - 1)\rho\varepsilon, \quad (2.39)$$

with  $\gamma$  being the ratio of the specific heats. In the limit of an isothermal temperature, the ratio  $P/\rho$  is a constant

$$\frac{P}{\rho} = \frac{kT}{\mu m_p} = c_s^2, \quad (2.40)$$

which is the square of the isothermal sound speed. In contrast, the adiabatic equation of state relates the pressure to the density like

$$P = K\rho^\gamma, \quad (2.41)$$

with  $K$  being a constant and  $\gamma$  being the ratio of the specific heats at constant pressure,  $c_p$ , and constant volume,  $c_V$ .

Despite the simplicity, these two approaches hold for a remarkably large range in density, not reflecting the complex physical processes and interactions that occur during the dynamical interactions of the gas.

### 2.3.2 Dust

Dust in the interstellar medium mostly consists of carbon and silicon compounds with a total mass fraction of roughly one percent. The grains usually have sizes of sub-micron scale. Although small, dust grains are compounds

with a relatively large number of atoms, so that their interactions are not observable in single emission and absorption lines like energy transitions in atoms, but rather in a large range of wave lengths with a well defined temperature. In order to describe the radiative processes of dust, it is therefore appropriate to use blackbody continuum radiation.

Calculating radiative transfer processes can be simplified by introducing the optical depth,  $\tau_\nu$ , along a path,  $l$ ,

$$\tau_\nu(l) = \int_{s=0}^{s=l} \kappa_\nu(s) ds, \quad (2.42)$$

where  $\kappa_\nu$  is the frequency dependent opacity of the grains. From observations, the empirical relation

$$\tau_\nu = \left( \frac{\nu}{\nu_c} \right)^\beta \quad (2.43)$$

relates the frequency  $\nu$  to the critical frequency  $\nu_c$ , defined where the optical depth is unity,  $\tau_\nu = 1$ . The measured power-law index is in the range of  $1 \leq \beta \leq 2$  (e.g., [Draine and Lee, 1984](#); [Mathis, 1990](#)). Hence, the longer the wave length the lower the optical depth. As a result, radiation with higher frequencies is trapped within a dense dusty cloud. Consequently, the dust properties and the abundance of dust particles have a significant impact on the cooling efficiency via radiation.

### 2.3.3 Chemistry

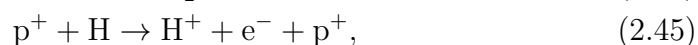
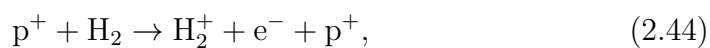
The presence of various chemical species and their transitions between different phases and energetic states influence the thermal and dynamical evolution of a gas cloud. The most important effect of chemistry in the ISM is the modification of the cooling ability of the gas. Although dominated in mass by hydrogen, the present-day interstellar medium contains other elements like carbon and oxygen and various combinations of which CO is the most abundant today. One has to distinguish between the gas phase chemistry on the one hand, and grain surface chemistry on the other hand. The latter provides a heat sink for the excess energy and a momentum buffer during a collision and thus accelerates chemical reactions. In contrast the chemical reactions in the gas phase are much more difficult because of the smaller cross section and encounters with other single atoms and small molecules. In most atomic collisions in the gas phase, the atoms simply bounce off instead of undergoing a chemical reaction.

Chemical reactions have a direct influence on the star formation process in various ways:

- Chemistry influences the ionisation levels of atoms. The resulting net charge of the atoms changes their ability to couple to magnetic fields via the Lorentz force. As magnetic fields tend to retard the collapse of the cloud, the coupling of the gas to the field has a significant impact on the star formation time scale.
- Elements and molecules change the optical properties of dust grains. If covered with water or CO ice, the grains have a significantly different optical behaviour. The assumed optical properties in the analysis of observations and the inferred physical properties of the observed region, therefore rely on the chemical processes.
- Chemical species serve as observational aids. As H<sub>2</sub> lines are difficult to observe, the transition lines of different molecules and metals are used to trace the gas in different regimes. Consequently, the formation and destruction of molecules as a function of density and temperature is crucial to properly interpret observations.
- Chemistry affects the micro-physics and thus the ability of the gas concerning to response to the changes in density and temperature. A change in the equation of state directly leads to changes in the hydrodynamic evolution.

### 2.3.4 Cosmic rays

Cosmic rays mainly consist of relativistic protons and light nuclei. They originate from mainly extragalactic sources and cover a large range in energy from  $10 - 10^{14}$  MeV (see, e.g., review by [Beatty and Westerhoff, 2009](#)). The energy spectrum is nearly a power-law distribution  $\Phi \propto E^{-q}$ , with  $q = 2.7 - 2.8$ , depending on the energy ([Nagano et al., 1992](#); [Abraham et al., 2008](#); [Abbasi et al., 2008](#)). Few astrophysical objects are capable of accelerating particles up to  $\sim 10^{20}$  eV. One scenario predicts the acceleration via magnetic fields in active galactic nuclei (AGN), radio galaxy lobes and hot spots, highly magnetised neutron stars, and accretion shocks within clusters of galaxies (see, e.g., [Hillas, 1984](#)). In another scenario cosmic rays are produced by the decay of long-lived supermassive relic particles from the big bang ([Hill et al., 1987](#); [Bhattacharjee et al., 1992](#)). Cosmic rays interact with the interstellar medium via the ionisation of atomic and molecular hydrogen,



which heats up the gas and couples the charged current to the ambient magnetic field. Additional heating comes from the collision of cosmic rays with protons and a subsequent formation of a  $\pi^0$  meson that decays into two photons.

### 2.3.5 Heating and cooling

During the contraction of a cloud the temperature mainly determines the evolution, in particular the ability of the cloud to fragment and form stars. Contracting gas naturally heats up and reduces the possibility for gravitational fragmentation. Due to collisional excitations and subsequent emission, the gas can cool and radiate away the increasing thermal energy due to the gravitational compression. The principal mechanism is the excitation of oxygen and carbon fine structure lines in collisions with dust particles. Thanks to cosmic rays and background UV radiation, carbon atoms are singly ionised (CII). With  $\tau_{\text{CR}}$  being the optical depth for cosmic rays and hard radiation, the rates for molecular cloud cooling can be combined to (Larson, 1973; Goldsmith and Langer, 1978; Bisnovatyi-Kogan, 2011)

$$\Lambda_{\text{CII}} = 9.0 \times 10^{19} \exp(-\tau_{\text{CR}}) \rho \exp(-92/T) \text{ erg g}^{-1} \text{ s}^{-1} \quad (2.46)$$

$$\Lambda_{\text{OI}} = 2.5 \times 10^{20} \rho T^{0.33} \exp(-228/T) \text{ erg g}^{-1} \text{ s}^{-1} \quad (2.47)$$

$$\Lambda_{\text{d}} = 1.1 \times 10^{14} \rho T^{1/2} (T - T_{\text{d}}) \text{ erg g}^{-1} \text{ s}^{-1} \quad (2.48)$$

where  $\Lambda_{\text{CII}}$ ,  $\Lambda_{\text{OI}}$ , and  $\Lambda_{\text{d}}$  are the cooling rates of CII, OI and dust, and  $T_{\text{d}}$  is the dust temperature. Here, the temperatures are measured in  $K$ , 1/10th of the carbon is assumed to be in the gas phase, and the opacity of cosmic rays is taken to be  $\kappa_{\text{CR}} = 300 \text{ cm}^2 \text{ g}^{-1}$ . The dust temperature  $T_{\text{d}}$  is calculated as equilibrium between dust heating by gas ( $\Lambda_{\text{d}}$ ) and thermal cooling by the radiation flux

$$j = 2.3 \times 10^{-4} k_p T_{\text{d}}^4 \text{ erg m}^{-2} \text{ s}^{-1} \quad (2.49)$$

from their surface. The dust grains are assumed to have a radius of  $r_{\text{d}} = 2 \times 10^{-5} \text{ cm}$  and the number density of dust grains per gram of gas is  $n_{\text{d}} = 2 \times 10^{11}$ . The mean Planck opacity is

$$k_P = 3 \times 10^{-5} T_{\text{d}}^3 \text{ cm}^2 \text{ g}^{-1}. \quad (2.50)$$

In contrast the heating due to cosmic rays and adiabatic contraction in free-fall are

$$\Gamma_{\text{CR}} = 2.0 \times 10^{-3} \exp(-\tau_{\text{CR}}) \text{ erg g}^{-1} \text{ s}^{-1} \quad (2.51)$$

$$\Gamma_{\text{ff}} = 3.8 \times 10^4 \rho^{1/2} T \text{ erg g}^{-1} \text{ s}^{-1}. \quad (2.52)$$

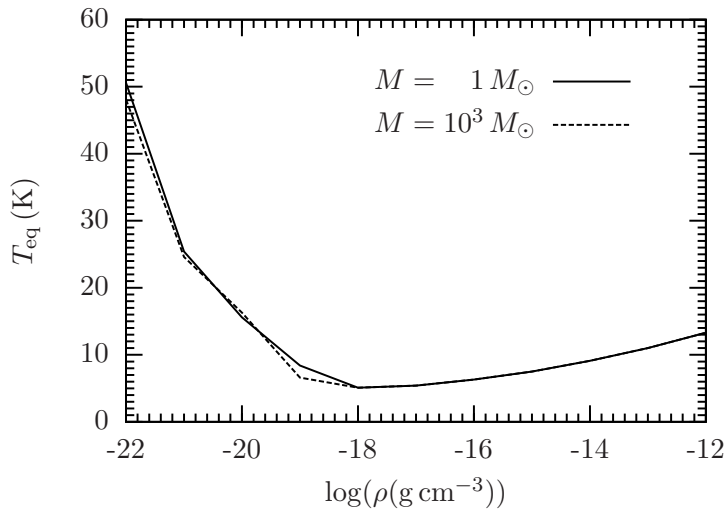


Figure 2.4: Equilibrium temperature for an optically thin gas cloud, see equation (2.53).

The equilibrium temperature can be found by solving the balance equation

$$\Gamma_{\text{CR}} + \Gamma_{\text{ff}} = \Lambda_{\text{CII}} + \Lambda_{\text{OI}} + \Lambda_{\text{d}}, \quad \Lambda_{\text{d}} = j. \quad (2.53)$$

The resulting temperature (Kolesnik, 1973) for two different cloud masses of  $M = 1 M_{\odot}$  and  $M = 1000 M_{\odot}$  is shown as a function of density in figure 2.4. For the density from  $\rho \sim 10^{-20} \text{ g cm}^{-3}$  up to  $10^{-12} \text{ g cm}^{-3}$ , the temperature shows perceptibly little variation. The contraction of a cloud within this density regime can thus be assumed isothermal.

Whereas regions of low-mass star formation have a temperature of roughly 10 K, observations of high-mass star-forming regions reveal a slightly higher equilibrium temperature of roughly 20 K (see, e.g., Beuther et al., 2007). Nonetheless, the temperature variations are still very small for increasing densities, and high-mass star-forming regions are also roughly isothermal within this density regime.

### 2.3.6 Jeans mass

In section 2.1.3 we have seen that the Jeans mass strongly depends on the temperature,  $M_{\text{J}} \propto T^{3/2}$ , which emphasises the importance of the equilibrium temperature for gravitational collapse. The Jeans mass for the calculated equilibrium temperature as a function of density is shown in figure 2.5. Below a density of roughly  $10^{-18} \text{ g cm}^{-3}$  the Jeans mass decreases due to the

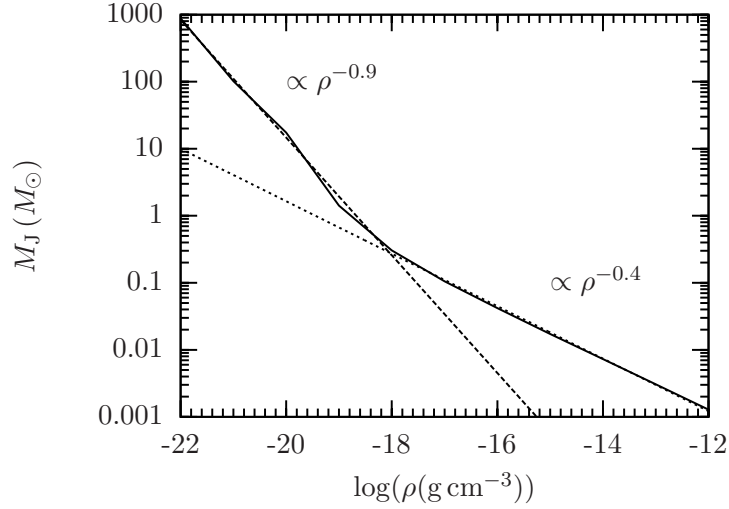


Figure 2.5: Jeans mass (equation (2.14)) for the calculated equilibrium temperature (equation (2.53)) as a function of gas density.

decrease in temperature, scaling with  $\rho^{-0.9}$ . Above  $10^{-18} \text{ g cm}^{-3}$  the almost isothermal conditions lead to a scaling with  $\rho^{-0.4}$ .

## 2.4 The formation process

Viewed from large scales, protostars are just a source of gravity and a sink of mass that accretes the surrounding gas. In the central region of the nascent star, different physical processes determine the first collapse, the formation of the first core, the subsequent contraction and the formation of the second core. The initially molecular gas dissociates and becomes ionised during the formation process before the stars enters the main sequence and starts nuclear fusion. The surrounding gas and the impact of accretion determine to what extent the thermodynamics of the young protostar can influence the surrounding region via radiative and mechanical feedback. In addition, the formation of gaseous discs provide a reservoir of gas for further accretion and marks the birthplace of planetary systems.

### 2.4.1 The formation of the first core

The first phase of the protostellar collapse proceeds in an isothermal manner. Once the cold cloud of gas ( $T \sim 10 \text{ K}$ ) becomes Jeans unstable, the still diffuse matter contracts in nearly free fall. As the optical depth of the cloud is

very low, the gained internal energy due to compression can be radiated away very efficiently, keeping the gas at the cold background temperature. This phase continues until the gas reaches densities of the order of  $10^{-13} \text{ g cm}^{-3}$ , at which the increasing optical depth prevents the internal energy to be radiated away (e.g., Larson, 1969). The central temperature increases and provides additional thermal pressure that acts against the gravitational pressure. The central contraction therefore slows down significantly and slowly reaches a state of nearly hydrostatic balance. This hydrostatic objects is called the *first core*.

### 2.4.2 Kelvin-Helmholtz contraction

The further contraction of the hydrostatic core is also called Kelvin-Helmholtz contraction and proceeds slowly. The energy balance of the core is close to virial equilibrium, which allows a temperature estimate of the centre of the core,

$$T \approx \frac{\mu}{3\mathcal{R}} \frac{GM}{R} \quad (2.54)$$

$$\approx 850 \text{ K} \left( \frac{M}{5 \times 10^{-2} M_{\odot}} \right) \left( \frac{R}{4 \text{ AU}} \right)^{-1}, \quad (2.55)$$

where  $\mu$  is the mean molecular weight, which is roughly 2.4 for interstellar gas,  $\mathcal{R}$  is the gas constant,  $G$  is Newton's constant, and  $M$  and  $R$  are the protostellar mass and radius. Continuous accretion of gas from the envelope causes the core to further contract and the core density gradually increases. Once the protostar reaches a density of  $10^{-10} \text{ g cm}^{-3}$ , the central temperature has risen to roughly 2000 K. Due to the increasing frequency of thermal collisions, the  $\text{H}_2$  molecules dissociate. This endothermal transition causes the temperature to increase slower than in the previous contraction phase. A temperature of 2000 K corresponds to a thermal energy of 0.74 eV, the dissociation temperature of  $\text{H}_2$  is 4.48 eV, which is significantly higher. All excess energy from the compression of the system can thus be efficiently converted into internal energy without a significant increase in temperature. The ongoing increase in mass due to accretion and continuous contraction eventually pushes the core above the critical density for a second Jeans instability. The core then collapses again to form the so-called *second core*.

### 2.4.3 Collapse and contraction time scale

During the first phase of gravitational collapse, the gas collapses in nearly free-fall which is solely determined by the average density of the collapsing

region

$$t_{\text{ff}} = \sqrt{\frac{3\pi}{32G\rho}}. \quad (2.56)$$

Inserting typical densities in star-forming regions, this time scale ranges from roughly 1 Myr for a density of the order of  $10^{-20} \text{ g cm}^{-3}$  down to 1 kyr for the density of  $10^{-13} \text{ g cm}^{-3}$  at the opacity limit.

After the formation of the first core, the protostellar condensation is close to hydrostatic equilibrium. Further contraction results in a rise in temperature, which increases the inner thermal pressure support. The contraction of the core is therefore related to the ability of the core to radiate away the converted potential energy via radiation. The *Kelvin-Helmholtz time* estimates the contraction time of the core by equating the luminosity  $\mathcal{L}$  with the change in potential energy  $-dW/dt$ .

$$\mathcal{L} = \frac{-dW}{dt} \approx \frac{GM^2}{R} \left( \frac{dR/dt}{R} \right). \quad (2.57)$$

Assuming a constant luminosity over time defines a characteristic e-folding time for the decrease in radius, the Kelvin-Helmholtz time,

$$t_{\text{KH}} \approx \frac{GM^2}{R}. \quad (2.58)$$

Expressed in solar units, the equation reads

$$t_{\text{KH}} \approx 10^7 \left( \frac{M}{M_{\odot}} \right)^2 \left( \frac{\mathcal{L}}{\mathcal{L}_{\odot}} \right)^{-1} \left( \frac{R}{R_{\odot}} \right)^{-1} \text{ yr}, \quad (2.59)$$

which varies significantly for different masses of the contracting core.

Overall, the contraction time scale tends to be significantly longer than the free-fall time. Consequently, the important distribution process of masses is the first fragmentation phase and mass accretion phase during the collapse of the cloud. In particular the accretion process in the nascent protostellar cluster and the resulting protostellar mass distribution determines the further evolution of the stars. For high-mass stars with  $\sim 10 M_{\odot}$ , the contraction time reduces significantly and the stars are likely to start nuclear fusion and enter the main sequence phase while still accreting gas from the outer envelopes of a cloud. In contrast, low-mass objects might remain in the protostellar stage throughout the active collapse and accretion process.

## 2.5 Accretion processes

Between the onset of the gravitational collapse and the ignition of hydrogen burning in the centre of the star, the mass of the collapsing condensation is

primarily determined by the surrounding medium and the amount of mass that the condensation can accrete during that period. In particular in dense environments, where many protostars form, the distribution of available mass onto the nascent stars is a difficult and highly non-linear process. Besides three simplified analytical models that describe the accretion onto single objects, two dynamical processes are presented, which describe the accretion dynamics in a cluster environment with many protostars.

### 2.5.1 Monolithic collapse

The apparent similarity in the distribution function of dense cores and stars, i.e., the similar shape of the *core mass function* (CMF) and the *initial stellar mass function* (IMF) (Testi and Sargent, 1998), suggests a simple collapse and accretion model, in which every dense core collapses to one or at most a few objects. In this monolithic collapse model (McKee and Tan, 2002, 2003), the mass of a dense core and the mass of the final star are directly related without the need of complex accretion processes, in which multiple protostars compete with one another for the available gas. The core mass function, which is shifted to higher masses by a factor of a few, only needs to be rescaled by an efficiency factor in order to match the stellar initial mass function. However, there are several weak points in this simple collapse modes. First of all, the simple collapse of individual cores with different masses and average densities leads to a time scale problem (Clark et al., 2007). In addition, observations and numerical simulations suggest, that the collapse of a core into one of two objects only occurs in very few cases. Observations by Bontemps et al. (2010), for instance, show high resolution observations of massive dense star-forming cores with sizes of only about 2000 – 5000 AU that may still hide further fragmentation in their central region. Similarly, most collapse simulations show a complex collapse and fragmentation structure, which suggests that cores form clusters rather than single objects or binary stars.

### 2.5.2 Bondi-Hoyle accretion

A powerful analytic accretion model was developed by Bondi (1952). The model assumes a star with a mass much smaller than the Jeans mass,

$$M_* \ll M_J \sim \frac{c_s^3}{\sqrt{G^3 \rho_0}}, \quad (2.60)$$

placed in an infinitely extended stationary background with density  $\rho_0$ , temperature  $T_0$ , and isothermal sound speed  $c_s$ . Furthermore, the gas is assumed

to be non-self-gravitating and reacts isothermally while being accreted. The star is at rest with respect to the surrounding gas, so the accretion is spherically symmetric. The accretion flow is then dominated by the central point mass and one can derive a steady state solution for the accretion flow that only depends on position, but not on time, i.e., the accretion flow is constant if the mass of the star is growing sufficiently slow, so that the increase in mass does not change the dynamics of the flow. The physically meaningful solution of the mathematical formulation yields for the accretion rate

$$\dot{M}_* = \frac{\rho_0 G^2 M_*^2}{c_s^3} \quad (2.61)$$

and a characteristic accretion radius of

$$R_B = \frac{2GM_*}{c_s^2}. \quad (2.62)$$

This model was extended by Bondi and Hoyle ([Bondi and Hoyle, 1944](#)) to also cover stars that are moving with respect to the surrounding gas. The modified Bondi-Hoyle radius for a relative velocity of  $v$  is given by

$$R_B = \frac{2GM_*}{c_s^2 + v^2} \quad (2.63)$$

and decreases for increasing relative velocities. This behaviour is expected as the effective gravitational cross section for the moving star decreases.

### 2.5.3 Free-fall accretion

In contrast to Bondi-Hoyle accretion, where the accreting star is not the dominant mass in the system, one can derive analytical accretion rates for systems, in which the accreting objects gravitationally dominates the system ([Whitworth and Ward-Thompson, 2001](#)). In this case the gravitational attraction of the star is much stronger than the pressure forces within the gas,

$$\nabla P \ll -\rho \nabla \Phi. \quad (2.64)$$

Assume a sphere of material with the total mass

$$M(R) = 4\pi \int_0^R r^2 \rho(r) dr \quad (2.65)$$

at time  $t = t_0$  that collapses in free-fall without mixing the material from inner to outer parts. Then the mass inside that free-falling sphere with radius

$R$  will be constant during the collapse. The outer boundary of the sphere  $R$  will be a function of time  $R(t)$  where  $R$  and  $t$  are connected via the free-fall time

$$t_{\text{ff}} = \frac{\pi R^{3/2}}{\sqrt{8GM(R, t = t_0)}}. \quad (2.66)$$

The total mass that is accreted onto the star as a function of time can therefore be expressed as the total mass inside  $R$  as a function of the time-dependent radius  $R(t)$  with the density distribution at  $t = t_0$  ( $\rho(r, t = 0) = \rho_0(r)$ )

$$M(t) = M(R(t)) = 4\pi \int_0^{R(t)} r^2 \rho_0(r) dr. \quad (2.67)$$

In order to find the radius at  $t$ , one has to solve the equation for the free-fall time of  $R$ , which cannot be done in general in a closed form, because the mass  $M(R)$  also depends on the radius and does not necessarily take a simple analytic form. That means one has to search for the radius and the corresponding mass, which yield the desired time  $t$  as free-fall time. Analytic solutions for simple density profiles are shown below.

The accretion rate can be approximated by the mass difference between  $t_0$  and  $t_1$

$$\dot{M}(t_x) = \frac{\Delta M}{\Delta t} = \frac{M(t_1) - M(t_0)}{t_1 - t_0} \quad (2.68)$$

$$= \frac{4\pi}{t_1 - t_0} \left[ \int_0^{R(t_1)} r^2 \rho_0(r) dr - \int_0^{R(t_0)} r^2 \rho_0(r) dr \right] \quad (2.69)$$

$$= \frac{4\pi}{t_1 - t_0} \int_{R(t_0)}^{R(t_1)} r^2 \rho_0(r) dr, \quad (2.70)$$

which reduces the computation to the search for the two radii  $R(t_0)$  and  $R(t_1)$ .

### Ideal and realistic cases

If the objects that accretes material is already a star, its radius is generally much smaller than the extension of the cloud that supplies the gas. Therefore in many cases it is appropriate to neglect the radius of the star and follow the accretion onto the centre at  $R = 0$ . However, this assumption faces some problems, in particular with density profiles that have a flat core region around the central object. Assuming a constant density  $\rho_c$ , the mass of the

sphere reads  $M(R) = 4/3 \pi \rho_c R^3$  and the free-fall time is a constant

$$t_{\text{ff}} = \left( \frac{3\pi}{32G\rho_c} \right)^{1/2}. \quad (2.71)$$

In this approach, the entire mass hits the centre at once and the mass of the central accreting object is described by a step function at  $t_{\text{ff}}$  with infinite accretion rate. If one allows the central object to have finite size, the radius in the equation for the free-fall time has to be reduced by the radius of the central object, as the free-falling distance is shorter

$$t_{\text{ff}} = \frac{\pi(R - R_*)^{3/2}}{\sqrt{8GM(R)}}. \quad (2.72)$$

If one initially allows for an empty hole inside of  $R_*$  the mass has to be modified as well yielding again equation 2.71. If the centre is initially filled with gas at the same uniform density the mass does not change. In this case, the equations for the total accreted mass and the accretion rate as a function of time read

$$M(t) = \frac{4}{3}\pi\rho_c R_*^3 \left( 1 - \left( \frac{32G\rho_c t^2}{3\pi} \right)^{1/3} \right)^{-3} \quad (2.73)$$

and

$$\dot{M}(t) = -\frac{8}{3}\pi\rho_c R_*^3 \left( \frac{32G\rho_c}{3\pi} \right) \left( 1 - \left( \frac{32G\rho_c t^2}{3\pi} \right)^{1/3} \right)^{-4} t^{-1/3} \quad (2.74)$$

### Special functions for power-law density distributions

For a general mass distribution it is not possible to give closed functions for the accreted mass. However, if closed functions for the total mass as a functions of radius are available, the above equations can be solved without numerically solving for the free-fall time.

Let the density be described by a power-law profile of the form

$$\rho(r) = \rho_c \left( \frac{R_c}{r} \right)^p, \quad (2.75)$$

where  $\rho_c$ ,  $R_c$  and  $p$  are fixed parameters. The density  $\rho_c$  and  $R_c$  can be combined in one parameter, but it is more convenient to keep them into two parameters with simple physical meaning. With this profile the mass can be

computed explicitly,

$$M(R) = 4\pi \int_0^R r^2 \rho_c \left( \frac{R_c}{r} \right)^p dr \quad (2.76)$$

$$= 4\pi \rho_c R_c^p \int_0^R r^{2-p} dr \quad (2.77)$$

$$= 4\pi \rho_c R_c^p \left[ \frac{r^{3-p}}{3-p} \right]_0^R \quad (2.78)$$

$$= \frac{4\pi \rho_c R_c^p}{3-p} R^{3-p} \quad (2.79)$$

for  $p \neq 3$ . This equation for the mass can now be inserted in the equation for the free-fall time yielding

$$t_{\text{ff}} = \frac{\pi R^{3/2}}{\sqrt{8G}} \left( \frac{3-p}{4\pi \rho_c R_c^p R^{3-p}} \right)^{1/2} \quad (2.80)$$

$$= \sqrt{\frac{\pi(3-p)}{32G\rho_c}} \left( \frac{R}{R_c} \right)^{p/2} \quad (2.81)$$

and solved for the radius

$$R = \left( \frac{32G\rho_c}{\pi(3-p)} \right)^{1/p} R_c t^{2/p}. \quad (2.82)$$

Combining the radius and the total mass equation finally gives for the total accreted mass as a function of time

$$M(t) = \frac{4\pi \rho_c R_c^p}{3-p} \left( \frac{32G\rho_c}{\pi(3-p)} \right)^{(3-p)/p} R_c^{3-p} t^{2(3-p)/p}. \quad (2.83)$$

The accretion rate can now be easily computed by differentiating

$$\dot{M} = \frac{\partial M}{\partial t} \quad (2.84)$$

$$= \frac{2(3-p)}{p} \frac{4\pi \rho_c R_c^p}{3-p} \left( \frac{32G\rho_c}{\pi(3-p)} \right)^{(3-p)/p} R_c^{3-p} t^{3(2-p)/p}. \quad (2.85)$$

For the self-similar collapse of an isothermal sphere with an initial power-law density profile with  $p = 2$  the accretion rate is constant (Shu, 1977), which can be seen in the vanishing exponent of the time.

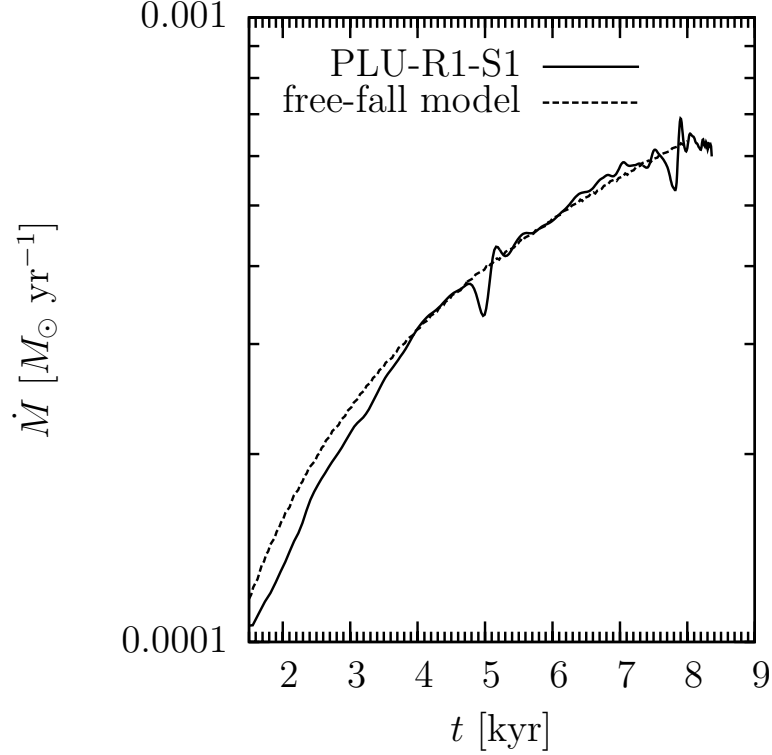


Figure 2.6: Comparison of the accretion rate for a numerical simulation and the theoretical model for the Plummer-like profile, equation (2.86).

### Comparison to numerical simulations

The important question is whether the influence of the pressure term in the Euler equations can really be neglected. Figure 2.6 shows the accretion rate for a star in a three-dimensional hydrodynamical simulation and the reduced one-dimensional free-fall model. The density profile that is used is a Plummer-like density profile of the form

$$\rho = \rho_c \left( \frac{R_c}{(R_c^2 + r^2)^{1/2}} \right)^\eta \quad (2.86)$$

with the following parameters:  $\rho_c = 2.79207 \times 10^{-14} \text{ g cm}^{-3}$ ,  $R_c = 2.992 \times 10^{14} \text{ cm}$  and  $\eta = 1.5$ , see also chapter 7 for a detailed description of the density profile. Taking into account that the numerical simulation also has turbulent motion that may disturb the radial symmetry of the collapsing cloud, the free-fall model gives comparable results.

For power-law profiles with slope  $p = 1.5$  and  $p = 2$  the results are shown in figure 2.7, see also chapter 5 for a detailed description of the setup. In

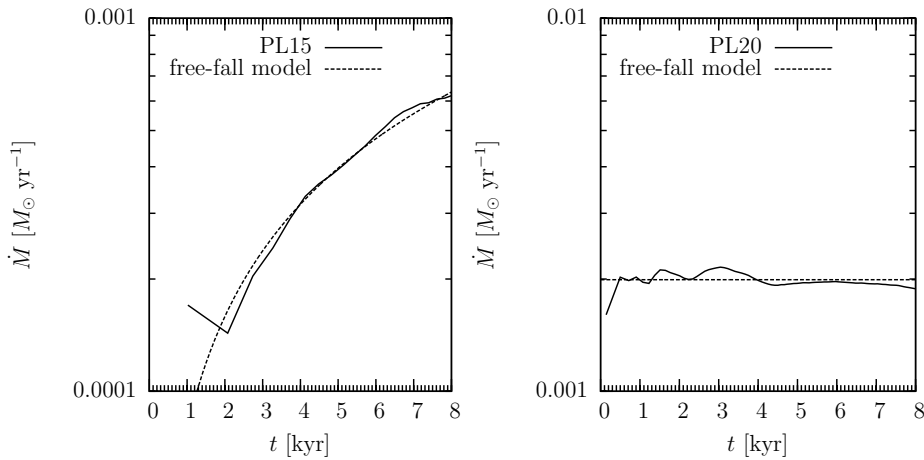


Figure 2.7: Comparison of the accretion rate for the numerical simulation and the theoretical model for power-law profiles with  $p = 1.5$  and  $p = 2$ .

both cases the free-fall results are acceptable. The calculated value from the model is  $1.95 \times 10^{-3} M_{\odot} \text{yr}^{-1}$ , the results by [Shu \(1977\)](#) differ by roughly 5%.

#### 2.5.4 Dynamical models

In stellar clusters the accretion processes are much more complicated than the analytical estimates shown above. Gas and nascent stars form a complex dynamical system, in which the stars compete for the available gas. A simple analytic description of the accretion rates for individual stars is therefore not possible because the accretion rates depend on too many parameters: the mass of the star, the distance to the nearest competing neighbour, the position within the cluster, the distance to the largest accretion flow that might be determined by the global cluster position within the ISM, and whether the gas is bound to the star in question. Dynamical models are therefore only accessible through statistical averages or numerical simulations. Concerning the accretion in clusters, there are two extreme models, namely *Competitive accretion* and *Fragmentation-induced starvation* or *Accretion shielding*.

##### Competitive accretion

The competitive accretion model ([Bonnell et al., 2001a,b](#); [Bonnell and Bate, 2002](#); [Bate and Bonnell, 2005](#)) is based on the position of the stars within the cluster. The closer the stars are located to the centre of the cluster, the more they can profit from the deep gravitational potential, which helps the stars

to accrete more material at a higher rate. The gas is funneled from larger distances into the central region of the cluster, passing the stars that are located in the outskirts of the cluster. The central stars therefore have the highest accretion rate. This model implies that the stars at larger radii do not have enough gravitational attraction to stop the gas from being passed by and transported to the centre.

### Accretion shielding

Fragmentation-induced starvation (Peters et al. 2010b, see chapter 6) describes the opposite effect to the competitive accretion model. The gas flow is still dominated by the global potential of the cluster. In contrast to competitive accretion as described above, the material cannot be funneled to the central regions, because it is accreted by the stars in the outskirts of the cluster. The stars that surround the cluster therefore shield the accretion flow to the centre. In the case of subsequent star formation, the first star can accrete gas at a high rate up to the point, when further stars form at larger distances from the centre and start to shield the innermost area of the cluster.

### 2.5.5 Remark on the dynamical models

Both dynamical models describe opposite accretion effects. However, they do not exclude each other. Depending on the key properties of the cluster like the density distribution, the total mass of the cluster, the amount of available gas for accretion and the number of stars, either one or the other effect can be more prominent. During the evolution phase of the cluster it might also be possible for a cluster to go through both accretion phases. However, so far, there is no conclusive theory that can predict the accretion mode within a cluster. A detailed discussion of the models is given in chapter 6.

## 2.6 Magnetic fields

Observations reveal that magnetic fields are ubiquitous in the interstellar medium. Their strengths differ significantly between large scale fields in the Galaxy and small scale fields in the star-forming regions, so does their spatial structure. It is unclear where these magnetic fields originate from. Cosmological seed fields might serve as a possible source, however, the initial source fields are relatively weak (see, e.g., Grasso and Rubinstein, 2001; Widrow, 2002). The exact strength is still a matter of debate, but cosmological fields

do not seem to be stronger than  $10^{-6}$  G. In galaxies, the field is observed to follow a large scale structure with a strength of the order of  $10 \mu\text{G}$  (see, e.g., Beck, 2009), which is assumed to be generated by the mean field dynamo. On smaller scales like clouds and star forming cores, the magnetic field is significantly stronger, but varies strongly between low-mass and high-mass prestellar cores. In a highly conducting medium like the interstellar medium the magnetic field moves together with the gas. This so-called *flux freezing* connects the field strength with the density. Compressing a volume orthogonal to the magnetic field lines increases the field strength with  $B \propto 1/\text{volume}$ . Hence, the magnetic field scales as  $B \propto \rho$ . This relation qualitatively explains the difference between the field strength in low-mass regions ( $\sim 1 M_{\odot}$ ,  $\sim 0.05 \text{ pc}$ ) with  $B \sim 10 - 30 \mu\text{G}$  (see, e.g., Kirk et al., 2006) and massive cores ( $\sim 100 - 1000 M_{\odot}$ ,  $\sim 0.2 \text{ pc}$ ) with  $B \sim 10 \text{ mG}$  (see, e.g., Beuther et al., 2010). Apart from the field amplification due to gravitational compression, the interplay between small scale turbulent motions and a tangled field can lead to a very efficient magnetic field amplification via the small scale dynamo (see review by Brandenburg and Subramanian, 2005). The importance of this process for present-day star formation has not been investigated yet.

Besides the strength of the field, the detailed spatial structure is rather unclear. Whereas many early observations suggest a field on rather large scales, i.e., comparable to the size of the observed core (Goodman et al., 1990; Ward-Thompson et al., 2000; Crutcher et al., 2004), more recent observations with better resolution show evidence for a tangled structure. The structural difference in the field and its impact on the dynamics of the cloud is theoretically rather unexplored. In particular, the impact of the magnetic field structure on outflows and jets, which are magnetically supported, is likely to be relevant.

Generally, magnetic fields act against gravity and delay or even suppress a gravitational collapse. The critical quantity to determine the impact of magnetic fields is the ratio of the mass to the magnetic critical mass,  $M_{\Phi}$ , given by equating magnetic and gravitational energy. In magnetostatic equilibrium  $M_{\Phi}$  can be written in the form

$$M_{\Phi} = c_{\Phi} \frac{\Phi}{G^{1/2}}, \quad (2.87)$$

with  $\Phi$  being the magnetic flux threading the cloud and  $c_{\Phi}$  being a numerical constant, discussed below. In supercritical clouds ( $M > M_{\Phi}$ ), the magnetic field can not prevent gravitational collapse, whereas in the subcritical case  $M < M_{\Phi}$  gravity can not overcome the stabilising magnetic pressure. The

critical *mass-to-flux* ratio (Mestel and Spitzer, 1956; Mestel, 1965)

$$\left(\frac{M}{\Phi}\right)_{\text{cr}} \equiv \frac{M_{\Phi}}{\Phi} = c_{\Phi} G^{-1/2} \quad (2.88)$$

is a pivotal quantity in this context. The numerical constant  $c_{\Phi}$  depends on the density distribution in the cloud and on the structure of the magnetic field and takes values of  $c_{\Phi} \approx 0.16 - 0.18$  (Nakano and Nakamura, 1978; Tomisaka et al., 1988). The magnetic critical mass can also be written in terms of the mean density and the magnetic field in the cloud (Mouschovias and Spitzer, 1976)

$$\frac{M_B}{M} = \left(\frac{M_{\Phi}}{M}\right)^3, \quad (2.89)$$

where  $M_B$  is the equivalent to  $M_{\Phi}$  when  $\Phi$  is replaced by  $\pi R^2 \langle B^2 \rangle^{1/2}$  and  $R$  marks the radius of the cloud.

Observations by Heiles and Troland (2005) reveal that the magnetic field in the interstellar medium is strong enough to prevent the gas from gravitational collapse ( $M/M_{\Phi} < 0.16$ ), assuming sheet-like geometries for the gas structures. One central problem of star formation in magnetised environments is how this ratio can increase to values  $M/M_{\Phi} \gtrsim 2$  so that gravitational collapse readily occurs. In fact, the geometry of the region in question can significantly alter the result. The observational techniques require thorough assumptions of the real structure of the clouds and the magnetic field structure that are obscured by projection effects. Crutcher et al. (1999) and Heiles and Crutcher (2005) observed dense cores with structures that probably differ significantly from a sheet-like geometry, measuring supercritical values of  $M/M_{\Phi} = 1.65 \pm 0.02$ . Thus, a detailed inclusion of density structures and structure-forming turbulent motions is necessary for a well-grounded analysis of the effects of magnetic fields, so are the contributions of turbulent magnetic effects. Li et al. (2006) found that the energy of the magnetic field is comparable to the turbulent kinetic energy. On large scales, the turbulent magnetic energy is likely comparable to or larger than the mean magnetic energy, and the kinetic energy is at least as large as the magnetic energy. In virial equilibrium, this leads to  $M \gtrsim 2M_{\Phi}$  (McKee and Ostriker, 2007). On smaller scales, Nakano (1998) also found the cores to be magnetically supercritical and thus collapsing. Numerical simulations suggest that magnetic fields have little impact on the global star formation rate if the cloud is supercritical (Ostriker et al., 1999; Heitsch et al., 2001; Li et al., 2004; Vázquez-Semadeni et al., 2005a,b; Nakamura and Li, 2005). However, the details of the collapse of a magnetised cloud down small scales of the

actual star-formation process might significantly depend on the strength and structure of the magnetic field.

Although magnetic fields are an important ingredient in star formation theory, we do not explore their effects in this work. The inclusion of magnetic fields will be a follow-up project, where a focus on different strengths and magnetic field structures will shed light on how strongly the magnetic fields will influence the star-forming regions considered in this work.



# Chapter 3

## Turbulence

### 3.1 Introduction

Turbulent motions appear in a large variety in daily life, nature, engineering, and also astrophysical processes. Although the systems, in which turbulence appears, are very different, the statistical key properties of turbulent flows have strong similarities. The way how turbulence occurs, how energy is transported, and how turbulent systems evolve is very complicated if followed in detail in local areas of the medium. However, in a statistical description using global structure and energy parameter, turbulence seems to be a universal process.

In a turbulent medium it is not possible to predict individual motions and the behaviour of a local region for a long period of time. This is due to the non-linear evolution of the flow. Nevertheless, the system itself is deterministic. A turbulent medium thus shows deterministic chaotic motions.

The main equation to describe the onset and effects of turbulence is the Navier-Stokes equation. As the mathematical description of turbulence is very complicated, a comprehensive theory only exists for incompressible fluid, but not for compressible media like gas (see, e.g., book by [Frisch, 1995](#)). Therefore, the incompressible model of turbulence also serves as a starting point in investigations of compressible systems with remarkable success considering the fundamentally different fluid properties.

#### 3.1.1 Reynolds number

The turbulent flow can be described efficiently by the Reynolds number as the main control parameter,

$$\text{Re} = \frac{\rho v l}{\mu}, \quad (3.1)$$

where  $\rho$  is the density,  $v$  the velocity,  $l$  the lengths of the area in question, and  $\mu$  the viscosity of the gas or fluid. Expanding the equations shows that the Reynolds number is equivalent to the ratio of inertia force over viscous force or total momentum transfer over molecular momentum transfer. This already suggests that the viscosity and therefore molecular properties determine characteristic properties of the flow. Small Reynolds numbers indicate laminar flow, above a critical value of a few hundred, the flow starts being turbulent. This chapter shows how the dissipation scale enters the description of turbulence and what that means for numerical simulations of turbulence.

### 3.1.2 From laminar to turbulent flows

Consider a laminar flow along the  $x$  axis around an infinite cylinder with the symmetry axis pointing into the  $z$ -direction like in figure 3.1. For very slow motions of the fluid, the system shows two symmetries in the  $x - y$  plane (upper part, A). The flow pattern shows mirror symmetry with respect to  $y = 1.5$  as well as to  $x = 0$ . This is due to the fact that the non-linear term in the Navier-Stokes equation can be neglected. If the flow velocity increases and the non-linear term becomes non-negligible, the flow becomes slightly asymmetric and the  $x = 0$  symmetry breaks (lower part, B). Apart from the spatial symmetries, the flow pattern is constant over time, which gives a temporal symmetry.

Further increase of the Reynolds number leads to a change in topology. The area behind the cylinder starts developing recirculating eddies, which still preserve the mirror symmetry with respect to  $y$ . Even larger Reynolds numbers finally result in a true loss of symmetry. Bifurcations appear in the flow as well as time variations and oscillations in the formation of eddies, the so-called Karman vortex street (see figure 3.2).

Increasing the Reynolds number further results in complicated transition from connected existing spatial and temporal symmetries to unstable bifurcations that lead to chaotic advection. This happens around a Reynolds number of a few hundreds and is not precisely known. Within the chaotic regime, the flow patterns turn into a homogeneous and isotropic dynamical structure in a statistical sense. That means that locally the flow does not follow symmetries, but the structure of the overall chaotic flow does not seem to change under translations and rotations. A closer look at the structure of the eddies also shows a statistical scale-invariance, i.e., a fractal picture of self-similar patterns.

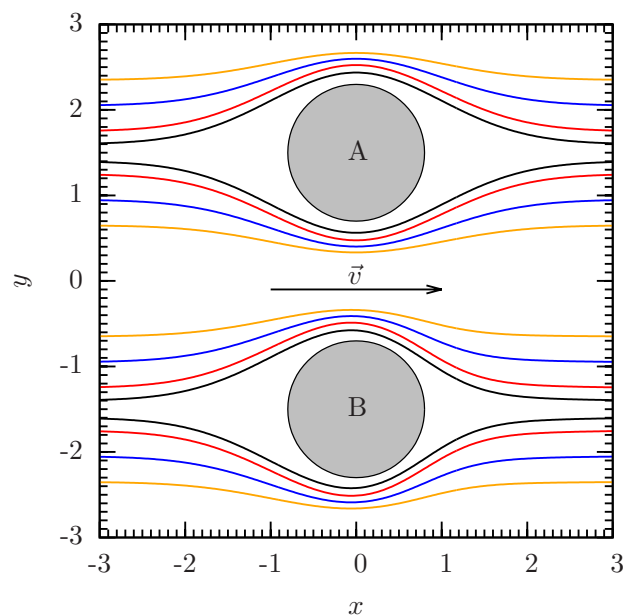


Figure 3.1: Laminar flow around a cylinder. The upper part (A) shows the flow for very low fluid velocities. The non-linear term in the Navier-Stokes equation can therefore be neglected and the flow pattern preserves mirror symmetry with respect to the  $x = 0$  and  $y = 1.5$ . The upper part shows the flow pattern for faster flow. In this case the symmetry with respect to  $y = -1.5$  still holds whereas the symmetry with respect to  $x = 0$  is broken.

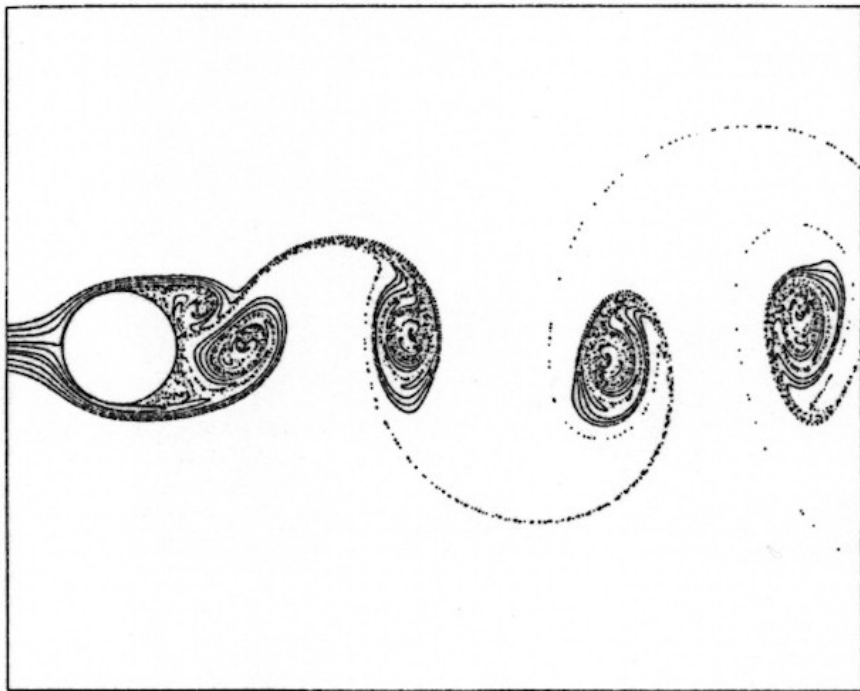


Figure 3.2: Appearance of alternating and growing eddies. The flow pattern is called the Karman vortex street (courtesy to Professor Changhong Hu, Kyushu University).

## 3.2 Mathematical concept

### 3.2.1 Symmetries and conservation laws

The main equation to investigate the evolution of turbulent flows is the Navier-Stokes equation

$$\partial_t v_i + v_j \partial_j v_i = -\partial_i p + \nu \partial_{jj} v_i, \quad (3.2)$$

where  $p$  and  $\nu$  denote the pressure and viscosity. The derivatives are abbreviated with

$$\partial_t = \frac{\partial}{\partial t}, \quad \partial_i = \frac{\partial}{\partial x_i}, \quad \partial_{ij} = \frac{\partial^2}{\partial x_i \partial x_j}. \quad (3.3)$$

The ideal configuration for the theoretical model is to assume an infinitely large box. However, this is not practical, therefore one chooses periodic boundary conditions

$$v(x + nL_x, y + mL_y, z + qL_z) = v(x, y, z), \quad (3.4)$$

$\forall n, m, q \in \mathbb{Z}$ .  $L_{x,y,z}$  is the period in direction  $x, y, z$ , which in most practical calculations is set to the same value. Using periodic boundaries allows to fully describe the turbulent motions within the area  $0 \leq x < L_x$ ,  $0 \leq y < L_y$ ,  $0 \leq z < L_z$ .

Symmetries and conservation laws are linked via Noether's theorem (Noether, 1918) stating that there is a conservation law for each symmetry in a conservative system describable with a Lagrangian function. In order to find the conserved quantities for a turbulent flow, the symmetries of the Navier-Stokes equation are listed:

$$\text{space-translations} \quad g_s : t, \vec{r}, \vec{v} \rightarrow t, \vec{r} + \vec{s}, \vec{v} \quad \vec{s} \in \mathbb{R}^3 \quad (3.5)$$

$$\text{time-translations} \quad g_\tau : t, \vec{r}, \vec{v} \rightarrow t + \tau, \vec{r}, \vec{v} \quad \tau \in \mathbb{R} \quad (3.6)$$

$$\text{Galilean transf.} \quad g_{\vec{U}} : t, \vec{r}, \vec{v} \rightarrow t, \vec{r} + \vec{U}t, \vec{v} + \vec{U} \quad \vec{U} \in \mathbb{R}^3 \quad (3.7)$$

$$\text{Parity} \quad \mathbf{P} : t, \vec{r}, \vec{v} \rightarrow t, -\vec{r}, -\vec{v} \quad (3.8)$$

$$\text{Rotations} \quad g_A : t, \vec{r}, \vec{v} \rightarrow t, A\vec{r}, A\vec{v} \quad A \in \text{SO}(\mathbb{R}^3) \quad (3.9)$$

$$\text{Scaling} \quad g_\lambda : t, \vec{r}, \vec{v} \rightarrow \lambda^{1-h}t, \lambda\vec{r}, \lambda^h\vec{v} \quad \lambda \in \mathbb{R}_+, h \in \mathbb{R} \quad (3.10)$$

From these symmetries the following conservation laws can be derived.

- Conservation of momentum

$$\frac{d}{dt} \langle \vec{v} \rangle = 0 \quad (3.11)$$

- Conservation of energy

$$\frac{d}{dt} \left\langle \frac{1}{2} v^2 \right\rangle = -\frac{1}{2} \nu \left\langle \sum_{ij} (\partial_i v_j + \partial_j v_i)^2 \right\rangle = -\nu \langle |\vec{\omega}|^2 \rangle, \quad (3.12)$$

where  $\vec{\omega} = \nabla \times \vec{v}$ .

- Conservation of helicity

$$\frac{d}{dt} \left\langle \frac{1}{2} \vec{v} \cdot \vec{\omega} \right\rangle = -\nu \langle \vec{\omega} \cdot \nabla \times \vec{\omega} \rangle \quad (3.13)$$

Defining the mean energy density,

$$E = \left\langle \frac{1}{2} |\vec{v}|^2 \right\rangle, \quad (3.14)$$

allows to define the *energy dissipation rate*

$$\epsilon \equiv -\frac{dE}{dt}. \quad (3.15)$$

The energy equation above does not contain non-linear terms. It can be shown that the non-linearities redistribute energies among different scales while preserving the global energy budget. The different *scales* can be investigated with a Fourier transform of the real domain. The discrete transform of a periodic box is given by

$$\tilde{f}(\vec{k}) = \sum_r f(\vec{r}) \exp(-i\vec{k} \cdot \vec{r}), \quad \vec{k} \in \frac{2\pi}{L} \mathbb{Z}^3, \quad (3.16)$$

where  $\tilde{f}(\vec{k})$  describes the power of the field  $f(\vec{r})$  at scale  $\vec{k}$ . Assuming isotropy in the turbulent motions, the vector  $\vec{k}$  simplifies to its norm,  $k$ , and reduces the function  $\tilde{f}(\vec{k})$  to a function with a scalar argument  $\tilde{f}(k)$ . After a lengthy derivation one arrives at a *scale-by-scale* energy equation

$$\partial_t E_K = F_K - \Pi_K - 2\nu\Omega_K. \quad (3.17)$$

This shows that the rate of change down to  $l = K^{-1}$  is given by the injected energy ( $F_K$ ) minus the contributions due to dissipation ( $2\nu\Omega_K$ ) and the energy flux to different scales due to non-linear effects ( $\Pi_K$ ). At high Reynolds numbers, the energy is typically injected at large scales (*injection scale*) and cascades down to small scales (*inertial range*). At the smallest scales, where dissipative effects convert the turbulent motions into heat via

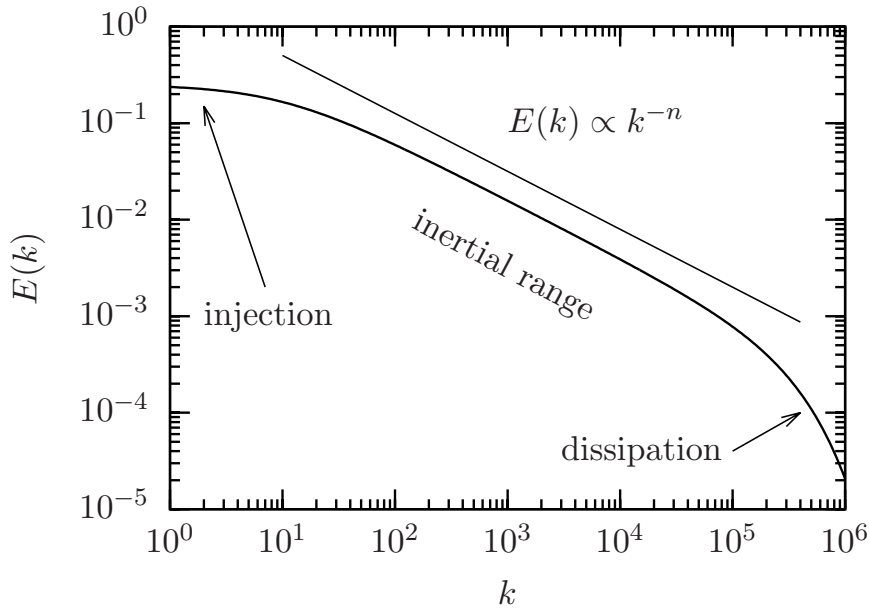


Figure 3.3: Schematic figure of the energy spectrum. The energy is injected at large scales (small  $k$ , *injection scale*), cascades down with a power-law shape (*inertial range*) and dissipates at small scales (*dissipation scale*).

friction processes, the cascade stops and no further energy is transported to smaller scales (*dissipation scale*). Over a large range the spatial energy spectrum,

$$E(k) \equiv \frac{dE_K}{dk}, \quad (3.18)$$

can be approximated by a power-law function

$$E(k) \propto k^{-n}. \quad (3.19)$$

An overview of the relevant parts of the energy spectrum is shown schematically in figure 3.3.

### 3.2.2 Kolomorov and Burgers turbulence

The Kolmogorov theory of turbulence (Kolmogorov, 1941) describes the energy cascade in incompressible media with a power spectrum  $E(k) \propto k^{-5/3}$  in the inertial range for an isotropic formulation of the power spectrum. This index,  $-5/3$ , is derived under the assumption of negligible fluid velocities compared to the thermal speed in the fluid. In isothermal systems this thermal speed is the sound speed  $c_s$ . In star-forming regions, however, this

condition is usually not fulfilled, i.e., the velocities of the gas or fluid exceed the sound speed and the Kolmogorov theory of the energy cascade does not need to be applicable. Instead of a conservative cascade of the energy, i.e., starting from large scale and consecutively passing all scales down to the dissipation scale, energy is dissipated directly via the interactions of strong shocks. In the limit of zero pressure ( $c_s \rightarrow 0$ ), the turbulent system consists of an ensemble of overlapping shocks, which referred to Burgers turbulence (Frisch and Bec, 2001) with a power spectrum  $E(k) \propto k^{-2}$ . Most astrophysical systems can not exactly be categorised in one or the other extreme but lie in between them. Depending on the scale and the major physical processes involved, the energy might not even be decaying on all scales with a constant spectral index for the entire inertial range. Instead the turbulence might be driven on a particular scale, reshaping the inertial range of the system as a whole.

### 3.2.3 Compressible and incompressible modes

The theory described so far is based on incompressible fluids and thus does not show any density fluctuations. The velocity field is purely divergence-free,  $\partial_i v_i = 0$ , also called *solenoidal*. This condition is pretty obvious as long as the fluid has incompressible character. However, in many turbulent environments, in particular if considering turbulent gas, the medium can be compressed strongly, making the problem much more complex. The characteristic behaviour of the gas concerning compressions is described by the equation of state, which does not need to be scale free within the considered dynamical range and may depend on several parameters. Not only do convergent and divergent regions appear, the ratio of compressible and solenoidal motions can in addition change over time. In a statistical average with random forcing of the turbulence, one expects 1/3 of the modes being compressible, corresponding to longitudinal modes, and 2/3 of the modes being solenoidal, corresponding to transversal modes, respectively. In order to analyse turbulence effects due to one or the other type of modes separately, one uses a decomposition of the modes, to achieve purely longitudinal or transversal modes. The *Helmholtz theorem* states that any vector field  $\mathbf{F}(\mathbf{r})$  can be decomposed into to fields  $\mathbf{F}_{\parallel}(\mathbf{r})$  and  $\mathbf{F}_{\perp}(\mathbf{r})$  such that

$$\mathbf{F}(\mathbf{r}) = \mathbf{F}_{\parallel}(\mathbf{r}) + \mathbf{F}_{\perp}(\mathbf{r}), \quad \text{with } \nabla \times \mathbf{F}_{\parallel}(\mathbf{r}) = 0, \quad \nabla \cdot \mathbf{F}_{\perp}(\mathbf{r}) = 0. \quad (3.20)$$

Transforming this identity into Fourier space translates the differential operators into multiplications by  $\mathbf{k}$ , yielding

$$\tilde{\mathbf{F}}(\mathbf{k}) = \tilde{\mathbf{F}}_{\parallel}(\mathbf{k}) + \tilde{\mathbf{F}}_{\perp}(\mathbf{k}), \quad \text{with } \mathbf{k} \times \tilde{\mathbf{F}}_{\parallel}(\mathbf{k}) = 0, \quad \mathbf{k} \cdot \tilde{\mathbf{F}}_{\perp}(\mathbf{k}) = 0. \quad (3.21)$$

The projection of the longitudinal field  $\tilde{\mathbf{F}}_{\parallel}$  can be obtained with

$$\frac{1}{k^2} \mathbf{k} \left( \mathbf{k} \cdot \tilde{\mathbf{F}}(\mathbf{k}) \right), \quad (3.22)$$

the perpendicular field  $\tilde{\mathbf{F}}_{\perp}$  is computed via the difference

$$\tilde{\mathbf{F}}_{\perp}(\mathbf{k}) = \tilde{\mathbf{F}}(\mathbf{k}) - \tilde{\mathbf{F}}_{\parallel}(\mathbf{k}). \quad (3.23)$$

### 3.3 Astrophysical turbulence

In an astrophysical environment, the description and investigation of turbulence faces many more difficulties than turbulent motions in an ideal incompressible fluid. The medium is highly compressible, changes the chemical composition depending on the density and temperature, is stirred on different scales by various mechanisms and experiences various forces that differ on different scales.

#### 3.3.1 Historical note

The first turbulent description of the interstellar medium was formulated by [von Weizsäcker \(1951\)](#) and has not changed fundamentally since then. The energy is deposited on large scales and cascades down to small scales via a hierarchy of structures. The energy dissipates by atomic viscosity. [von Hoerner \(1951\)](#) analysed the velocities of the Orion nebula and found a power-law dependence on spatial scales similar to the Kolmogorov energy cascade. The first statistical model for continuous and correlated gas distributions was developed by [Chandrasekhar and Münch \(1952\)](#). The discovery of power-law correlations between the size of molecular clouds and their velocity dispersion by [Larson \(1981\)](#) was an important confirmative step towards the acceptance of the turbulent structure of the ISM. The found slope of the power spectrum was consistent with the Kolmogorov model, which was supported by additional observations ([Myers, 1983](#); [Dame et al., 1986](#); [Solomon et al., 1987](#)). Remaining doubts concerning the turbulent nature were reduced by the onset of infrared observations of dark clouds that also revealed a filamentary structure following a comprehensive picture of a turbulent cascade.

The theoretical and observational description of the turbulent ISM were later supported by numerical simulations of various kinds of driven and decaying turbulent models (see e.g., reviews by [Vázquez-Semadeni et al. \(2000\)](#); [Mac Low \(2003\)](#); [Mac Low and Klessen \(2004\)](#)).

### 3.3.2 Power spectrum

The diagnostics of turbulent motions covers a wide range of different techniques like correlation functions, power spectra, and delta variance, just to name a few. The power spectrum of an observable  $Q$  is given by

$$P(\vec{k}) = \hat{Q}(\vec{k})\hat{Q}^*(\vec{k}) \quad (3.24)$$

for the Fourier transform  $\hat{Q}$  and its complex conjugate  $\hat{Q}^*$ . The one-dimensional energy spectrum of an isotropic observable  $Q$  is then

$$E(k) = P(k) dk^D, \quad (3.25)$$

where for the three-dimensional volume  $dk^3 = 4\pi k^2 dk$ . The Kolmogorov spectra are then  $P(k) \propto -11/3$  and  $E(k) \propto -5/3$ , respectively.

### 3.3.3 Power sources for interstellar turbulence

Observations of the ISM and comparisons with simulations suggest that turbulence in the ISM is driven on large scales. However, the origin of the driving force is still not well understood. The main sources for large scale motions are stars, galactic rotation, self-gravity, fluid instabilities, and galactic gravity (see, e.g. review by [Elmegreen and Scalo, 2004](#); [Mac Low and Klessen, 2004](#)). Stars may contribute in the form of protostellar winds, expanding HII regions, O star and Wolf-Rayet winds, supernovae, and through dynamics of superbubbles. Among these contributions, the impact of main-sequence winds can be neglected ([Mac Low and Klessen, 2004](#)), supernovae and resulting winds and superbubble clearly dominate on scales of the order of a few hundred parsecs. Galactic rotation results in shocks in the spiral arms or bars, leads to Balbus-Hawley instability [Balbus and Hawley \(1991\)](#) and causes gravitational scattering of cloud complexes. The total amount of available energy in galactic rotation is basically unlimited if compared to the turbulent energy in the ISM ([Fleck, 1981](#)). Self-gravity may lead to global contraction and causes accretion flows within the ISM. [Baumgardt and Klessen \(2011\)](#) investigated how much turbulent energy can be supplied due to accretion streams on different scales and concluded that overall accretion is capable of supporting the observed amount of turbulence. Gravity on Galactic scales deposits energy into the ISM by disk-halo interactions and galaxy-galaxy interaction.

## 3.4 Numerical realisation of turbulence

Many aspects in theoretical star formation can only be investigated using large scale numerical simulations. In many cases, three-dimensional hydrodynamic simulations are used to investigate the interplay between physical processes. It is therefore crucial to model turbulent motions in hydrodynamic simulations reasonably well. One major problem of astrophysical simulations is the restriction to a relatively small dynamic range. For instance, it is impossible to model the entire star formation process from the formation of giant molecular clouds where turbulent gas dynamics might begin down to solar radii where sufficiently large densities, the corresponding equations of state, and possible phase transitions mark the regime of dissipation. Therefore, the turbulence must be *created* at some scale that lies within the dynamic range of the simulation. There are two popular ways how to generate turbulence in a simulation. The first approach is to apply a random, time varying forcing on large scales, which mark the injection scale. The dissipative effects in the simulation, represented either by explicitly following dissipative effects in the gas or by dissipation in the numerical code (numerical viscosity), then populate energy levels on smaller spatial scales by the onset of the turbulent cascade. The turbulence thus forms self-consistently within the simulation from the given initial forcing. The second approach for creating turbulence uses empirically known characteristic energy spectra to directly generate a turbulent field. Whereas the first approach yields a naturally created shape of the energy spectrum, the second one uses an assumed spectrum as an initial condition. As each way of creating turbulence is controlled by different parameters and creates fields that are not identical, individual numerical setups are easier to combine with one or the other method. In the following, both ways are described.

### 3.4.1 Self-consistent turbulence driving

Creating a self-consistent turbulent velocity field invokes driving forces on the injection scales that last long enough for the cascade to fully populate the dynamical range. Although physically a proper *forcing* might be advantageous, in most simulations it is very impractical because of the resulting time scale problem in under-dense regions. A forcing field results in large accelerations in areas of low density and leads to very high velocities in dynamically unimportant regions of the computational domain. Therefore, one uses acceleration fields, assuring that the acceleration of a local area does not depend on the mass contained. One way of creating a time varying large scale field is using the *Ornstein-Uhlenbeck* process, which is described by the

stochastic differential equation

$$dq_t = \theta(\mu - q_t) + \sigma dW_t, \quad (3.26)$$

where  $\theta > 0$ ,  $\mu$ , and  $\sigma > 0$  are parameters and  $W_t$  denotes a Wiener process with a normal distribution of the fluctuations. This technique has been slightly reformulated with physical quantities by, e.g., [Eswaran and Pope \(1988\)](#) and [Schmidt et al. \(2006, 2009\)](#).

A major advantage of this method of creating turbulent motions is that the power spectrum builds up naturally. In case of compressible fluids like interstellar gas the density fluctuations that arise with the motions are also self-consistently created. However, as the power spectrum is an intrinsic property of the setup and can not be regulated, this method is disadvantageous if one is interested in the effects of different shapes of the power spectrum.

### 3.4.2 Fourier transformed turbulence fields

Instead of allowing the turbulence to develop self-consistently using a forcing or acceleration field, one can directly create turbulent motions with a Fourier transform. The most convenient way is to set up a random velocity field in  $\mathbf{k}$  space, as the power spectrum can be set explicitly. If desired, non-isotropic effects can also be set directly. Having set the appropriate amplitude of the velocity at a given scale  $|\mathbf{k}|$ , the random character of the field can be achieved by adding random phases in the complex  $\mathbf{k}$  cube. Applying a Fourier transform as the third step finally yields the velocity field with the desired power spectrum.

The realisation of compressive or solenoidal turbulence can be done easily by applying the projections described in section [3.2.3](#) between the applied random phases and the Fourier transform back to real space.

A major advantage of this method is the ability to precisely control at the same time the structure of the modes as well as the scale at which most of the energy is deposited.

### 3.4.3 Spatial and dynamical ranges

Turbulent processes in nature allow for a large inertial range, meaning that the scale of energy injection is many orders of magnitude larger than the dissipation scale. In particular in astrophysical processes the inertial range can easily span 10 orders of magnitude in space. With spectral indices of roughly  $-2$ , the energy range spans 20 orders of magnitude. These large ranges can

not be completely covered by current computing facilities. Adaptive techniques can span a couple orders of magnitude, but in particular the very small dissipation scales, which are set by molecular properties are way too small to be covered within a global astrophysical simulation. This means that the small scale limit in the energy cascade is determined by the numerical resolution. Once the energy cascaded down to the smallest resolution element, the numerical viscosity dissipates the energy. Depending on the numerical technique, the effects on the dissipation are different. Smoothed particle hydrodynamics does not have an intrinsic viscosity, which means that it has to be put into the equations artificially. Without artificial viscosity, the SPH particles can move around at arbitrarily small distances without dissipating energy. In contrast, grid-based codes have an intrinsic numerical viscosity. Once a turbulent eddy approaches the resolution limit, the rotating structure disappears within a computational cell and dissipates the energy of the eddy. The critical question of how much resolution is needed in order to fully follow the turbulent cascade is difficult to answer. Whereas in nature the dissipation scale is always the same (assuming the same gas properties within the region under consideration), the numerical diffusion scale depends on the local resolution. Even worse is the situation in adaptive mesh refinement codes, where the local cell size varies and with it the minimum resolution of the smallest resolvable eddy.

Depending on the type of numerical simulation, the problems concerning the resolution elements in grid-based codes are more or less severe. In simulations, where the gas crosses the box several times, it is numerically too expensive to refine the grid locally with very high resolution. The volume filling eddies would require a large percentage of the simulation box to be refined. Therefore, simulations of turbulent boxes are usually done on a uniform grid without adaptive refinement, which reduces the spatial and dynamical range. In contrast, simulations of collapsing regions often cover a much smaller dynamical evolution time scale. In star formation simulations, the simulation time is in most cases of the order of a free-fall time rather than several crossing times. This means that the cloud collapses to a very dense region in a small spatial range and only a small percentage of the total box needs to be refined in order to follow the dynamically dominant region, e.g., the central stellar cluster. Therefore, adaptive meshes with very high refinement levels, covering spatial ranges of 4 – 5 orders of magnitude, are achievable.



# Chapter 4

## Topic of the thesis

### 4.1 Overview

In this thesis, we investigate the impact of different initial conditions on the collapse of gravitationally unstable clouds, the formation of density structures in the cloud like filaments and central clumps, as well as the early formation history of protostellar clusters. This analysis is divided into four main parts:

- the collapse of the cloud and the morphology,
- the accretion processes in protostellar clusters,
- the impact of turbulent modes and the importance of tidal forces, and
- the energetics and dynamical state of embedded protostellar clusters.

### 4.2 Considered scales and processes

We simulate the collapse of dense, massive cores with densities of the order of  $10^6 \text{ cm}^{-3}$  (Bontemps et al., 2010; Beuther et al., 2007) and sizes of  $\sim 0.2 \text{ pc}$ . These cores contain many tens of Jeans masses and collapse in nearly free-fall with rapid star formation activity. Because of the high average densities, the collapse scenario is particularly interesting concerning the formation of massive stars. Although observations allow for rough estimates of the density distribution within the cores, the details of the mass distribution, which can easily predetermine the fragmentation of the core and thus the spatial distribution of stars, show significant uncertainties. Depending on the observed wave length, the cores show more or less fragmented structure. The question

of how massive these fragments are and how well they are dynamically connected to each other is unknown but crucial to understand the formation of massive objects.

After the formation of the first fragments, the accretion processes may significantly alter the initial masses of the protostars. Therefore, it is important not to exclusively follow the first collapse of the unstable regions, but also simulate the formation of multiple stars and the resulting accretion flows within the star-forming region.

A further complication is the dynamics of the cores. The gas motions in the cores are supersonic and shape the gas distribution according to converging and diverging flows. The complexity of motions lead to strong local concentrations of angular momentum, which may form discs and influence the accretion processes.

### 4.2.1 Global simulation parameters

We simulate the collapse of an initially spherical molecular cloud with a radius of  $R_0 = 3 \times 10^{17}$  cm  $\approx 0.097$  pc, centred in a cubic computational domain of length  $L_{\text{box}} = 8 \times 10^{17}$  cm. The gas with a mean molecular weight of  $\mu = 2.3$  is assumed to be isothermal at a temperature of 20 K. The isothermal sound speed is given by

$$c_s = \sqrt{\frac{k_B T}{\mu m_p}} = 0.268 \text{ km s}^{-1} \quad (4.1)$$

with the Boltzmann constant  $k_B$ , the temperature  $T$ , the molecular weight  $\mu$ , and the proton mass  $m_p$ . For all runs the total mass enclosed within this sphere is  $100 M_\odot$ . The resulting average density is  $\langle \rho \rangle = 1.76 \times 10^{-18}$  g cm $^{-3}$  or  $\langle n \rangle = 4.60 \times 10^5$  cm $^{-3}$ , leading to a free-fall time

$$t_{\text{ff}} = \sqrt{\frac{3\pi}{32 G \langle \rho \rangle}} \quad (4.2)$$

of  $1.58 \times 10^{12}$  s or 50.2 kyr. However, this global average time is not a good measure for the strongly concentrated density profiles, where star formation and gravitational collapse occurs on much shorter time scales. All of the initial spheres are gravitationally highly unstable. With the Jeans length

$$\lambda_J = \sqrt{\frac{\pi c_s^2}{G \langle \rho \rangle}} = 9264 \text{ AU} = 0.46 R_0 \quad (4.3)$$

Table 4.1: Physical parameters of all setups

Parameter		Value
cloud radius	$R_0$	$3 \times 10^{17} \text{ cm} \approx 0.097 \text{ pc}$
total cloud mass	$M_{\text{tot}}$	$100 M_{\odot}$
mean mass density	$\langle \rho \rangle$	$1.76 \times 10^{-18} \text{ g cm}^{-3}$
mean number density	$\langle n \rangle$	$4.60 \times 10^5 \text{ cm}^{-3}$
mean molecular weight	$\mu$	2.3
temperature	$T$	20 K
sound speed	$c_s$	$0.27 \text{ km s}^{-1}$
rms Mach number	$\mathcal{M}$	3.28 – 3.64
mean free-fall time	$t_{\text{ff}}$	$5.02 \times 10^4 \text{ yr}$
sound crossing time	$t_{\text{sc}}$	$7.10 \times 10^5 \text{ yr}$
turbulent crossing time	$t_{\text{tc}}$	$1.95 - 2.16 \times 10^5 \text{ yr}$
Jeans length	$\lambda_J$	$9.26 \times 10^3 \text{ AU} \approx 0.23 R_0$
Jeans volume	$V_J$	$1.39 \times 10^{51} \text{ cm}^3$
Jeans mass	$M_J$	$1.23 M_{\odot}$

the Jeans volume, given as a sphere with diameter  $\lambda_J$ , reads  $V_J = \pi \lambda_J^3 / 6$  and the Jeans mass of this sphere is  $M_J = V_J \langle \rho \rangle = 1.23 M_{\odot}$ . An overview of the physical parameters is given in table 4.1,

The simulated density range justifies an isothermal equation of state. However, the missing heating effect due to radiation leads to more collapsing regions than in non-isothermal simulations. We therefore over-estimate the number of formed protostars, and the presented stellar statistics should more be understood as a comparison between the runs rather than an exact measurement of the IMF.

## 4.3 Initial turbulence

### 4.3.1 Power spectrum of the turbulence

The turbulence is modelled with an initial random velocity field, originally created in Fourier space, and transformed back into real space. The power spectrum of the modes is given by a power-law function in wave number space ( $\mathbf{k}$  space) with  $E_{\mathbf{k}} \propto k^{-2}$ , corresponding to Burgers turbulence (the value for incompressible, Kolmogorov turbulence would be  $E_{\mathbf{k}} \propto k^{-5/3}$  in this notation), which is consistent with the observed spectrum of interstellar turbulence (e.g., Larson, 1981; Heyer and Brunt, 2004). The velocity field is dominated by large-scale modes due to the steep power-law exponent,  $-2$ ,

with the largest mode having the size of the simulation box. Thus, changing the slope of the power spectrum is not expected to affect the results significantly (see, [Bate, 2009b](#)). However, the random seed and the mixture of modes of the initial turbulence can potentially change the results more strongly, which we investigate in this study. Concerning the nature of the  $\mathbf{k}$  modes, compressive (curl-free) are distinguished from solenoidal (divergence-free) ones. The simulation uses three types of initial fields: pure compressive fields (c), pure solenoidal (s), and a natural (random) mixture (m) of both. These choices were motivated by the strong differences found in driven turbulence simulations using purely solenoidal and purely compressive driving of the turbulence ([Federrath et al. 2008, 2009, 2010b](#)). Note however that only decaying turbulence with compressive, mixed, and solenoidal modes are considered here. For each of these three types, two different random velocity seeds are created, leading to six different initial velocity fields in total (c-1, c-2, m-1, m-2, s-1, s-2), which are combined with the different density profiles.

No overall global rotation is imposed on the cloud. Due to the random nature of the turbulence, the net rotation, and the net angular momentum are not strictly zero. The ratio of rotational to gravitational energy is of the order of a few times  $10^{-3}$ .

### 4.3.2 Mach numbers

All setups have supersonic velocities. Due to different density concentrations and the resulting different refinement structure of the AMR grid, the rms velocities and their Mach number

$$\mathcal{M} = \frac{v_{\text{rms}}}{c_s} \quad (4.4)$$

differ slightly among the different density profiles. [Table 5.2](#) shows the Mach numbers for all the setups which vary from  $\mathcal{M} = 3.28 - 3.64$  with an average of  $\langle \mathcal{M} \rangle = 3.44$ .

### 4.3.3 Sound crossing time and turbulence crossing time

The sound crossing time through the entire sphere is

$$t_{\text{sc}}(R_0) = 7.10 \times 10^5 \text{ yr}, \quad (4.5)$$

about one order of magnitude higher than the global free-fall time. For the supersonic turbulence with an average gas velocity of  $\mathcal{M} = 3.44$ , the average

turbulence crossing time is

$$t_{\text{tc}}(R_0) = 2.06 \times 10^5 \text{ yr.} \quad (4.6)$$

The crossing times for the core region are  $t_{\text{sc}}^{\text{core}} = t_{\text{sc}}(\lambda_{\text{J}}) = 1.64 \times 10^5 \text{ yr}$  and  $t_{\text{tc}}^{\text{core}} = t_{\text{tc}}(\lambda_{\text{J}}) = 4.77 \times 10^4 \text{ yr}$ , which is close to the global free-fall time.

## 4.4 Numerical methods

### 4.4.1 Equations to solve

We solve Eulers equations for compressible gas dynamics in three spatial dimensions, neglecting the effects of viscosity. The equations then take the form (Fryxell et al. 2000, FLASH user guide, section 2.2)

$$\frac{\partial \rho}{\partial t} + \nabla \cdot (\rho \mathbf{u}) = 0 \quad (4.7)$$

$$\frac{\partial \rho \mathbf{u}}{\partial t} + \nabla \cdot (\rho \mathbf{u} \mathbf{u}) + \nabla P = \rho \mathbf{g} \quad (4.8)$$

$$\frac{\partial \rho E}{\partial t} + \nabla \cdot [(\rho E + P) \mathbf{u}] + \nabla P = \rho \mathbf{u} \cdot \mathbf{g} \quad (4.9)$$

with the fluid density,  $\rho$ , the velocity,  $\mathbf{u}$ , the pressure,  $P$ , the total energy per unit mass,  $E$ , (sum of kinetic and internal energy),

$$E = \varepsilon + \frac{1}{2} |\mathbf{u}^2|, \quad (4.10)$$

the gravitational acceleration due to self-gravity,  $\mathbf{g}$ , and the simulation time,  $t$ . The pressure is obtained from the energy density via

$$P = (\gamma - 1) \rho \varepsilon \quad (4.11)$$

with  $\gamma$  being the ratio of the specific heats. The gravitational acceleration is computed by solving the Poisson equation

$$\nabla^2 \Phi = 4\pi G \rho. \quad (4.12)$$

### 4.4.2 Operator splitting

Solving the above equations for the entire domain in a high-resolution simulation is challenging. In principle, there are *explicit* and *implicit* numerical schemes that can compute solutions for the Euler's equations. However, for

state-of-the-art resolutions, the implicit methods are too time consuming because they involve the inversion of a matrix containing the entire domain. Therefore, explicit schemes are used to advance the equations with given initial conditions. Depending on how many processes interact in the simulation, the coupling of the quantities in the equations further complicates the computation. An example is the gas density. The density field influences the evolution of equations via the gravitational source terms in equations (4.8) and (4.9). At the same time, the density changes with a change of  $\mathbf{u}$  in equation (4.7). Ideally, the Euler's equations are solved simultaneously with the Poisson equation (4.12), which is computationally not practical. Similar complications arise from additional physics like complicated thermodynamics. Practically, the time evolution of the equations is solved using *operator splitting*. Euler's equations are solved for half of the desired time step  $\Delta t$ , then the gravitational potential is updated with the solution of the Poisson equation, and after that the equations are advanced for the second half of the time step with the same sequence of computation. Additional physics can be added to the sequence analogously. The following pseudo-code demonstrates this recipe.

```
main time loop
{
  # first half of time step dt
  call hydro_euler_equations(dt/2, ...)
  call poisson_solver(dt/2, ...)
  call ...

  # second half of time step dt
  call hydro_euler_equations(dt/2, ...)
  call poisson_solver(dt/2, ...)
  call ...
}
```

### 4.4.3 Grid-based numerical scheme

The equations are solved on a cartesian grid, organised in blocks of  $8^3$  cells per block (see figure 4.1). As the total computational domain is distributed among multiple CPUs, a block is surrounded by so-called *guard cells* or *ghost cells*, shown in grey. They are used to communicate the information at the border of the block to the neighbouring CPU. Within one block, the cells have equal sizes in all three dimensions. In order to follow the interesting parts in a simulation with more accuracy and more spatial resolution, the grid, on which

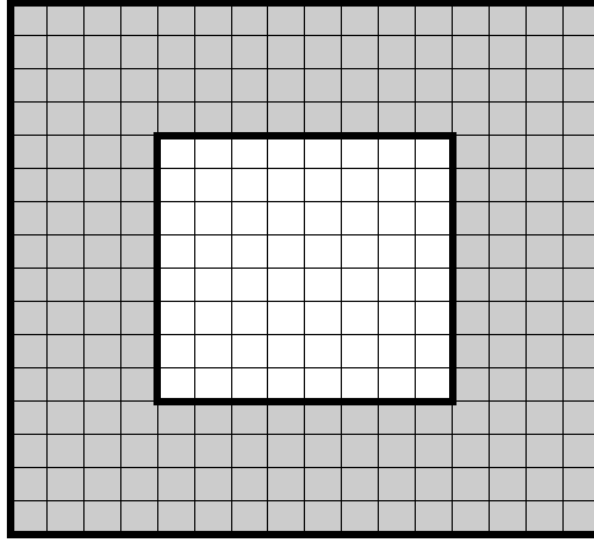


Figure 4.1: Computational block, consisting of  $8^3$  cells (white cells). A copy of the cells of the neighbouring block is stored in the *ghost cells*, shown in grey.

we compute the hydrodynamic equations needs to be refined locally. This so-called adaptive mesh refinement (AMR) is done in the simplest manner by splitting the cell in two equal parts in each dimension of the simulation, see figure 4.2. In a grid-based code the criteria for refinement can be defined and changed easily. Whenever a desired quantity exceeds a threshold value, the local grid cell can be split. The most common refinement criterion in a collapsing core is the density. In addition, the resolution of shocks can be increased locally by refining on a basis of the derivative of the density or the velocity, just to name two.

Two important aspects limit the applicability of hierarchical refinement, i.e., memory limits and time step limits, respectively. The former one is a simple result of the increasing number of computational elements that have to be stored in the memory of the computer. Obviously, the more computational cells a simulation contains, the more CPU time is needed to process them. The latter limit is connected to the stability of explicit numerical schemes. In order to assure numerical stability, the maximum evolutionary time step scales as  $\Delta t \propto \Delta x$ , which decreases with decreasing cell size, a pure result of the changing geometry. In addition the physical processes are likely to further reduce the time step for reasons of numerical stability. In most cases a local refinement follows dynamically active regions with high velocities and/or high temperatures, leading to significantly smaller time steps.

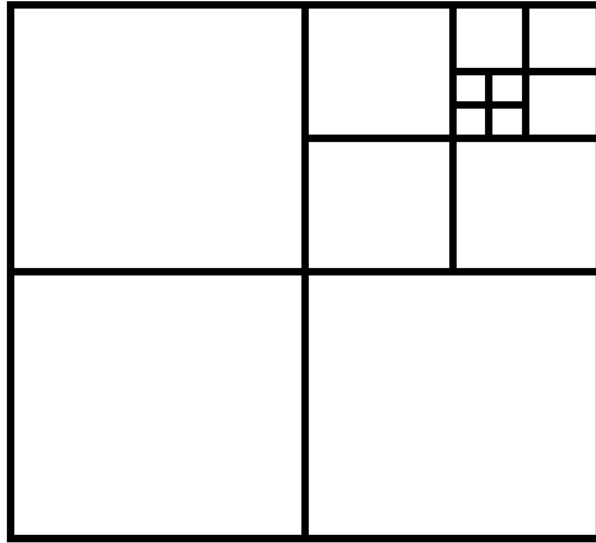


Figure 4.2: Illustration of the adaptive mesh refinement (AMR) in two dimensions. Local cells are split in half in each dimension of the domain.

#### 4.4.4 Numerical diffusion

Although not explicitly computed in the equations, the numerical scheme based on the grid is diffusive. Once motions on the smallest level of the refinement structure can not be resolved any more, the individual motions wash out and diffuse within one cell. This numerical diffusion dissipates energy not only on scales of the local minimum cell size, but already on larger scales, when the region is resolved with several cells. For turbulent motions the minimum resolution that is needed without being influenced by the numerical diffusion is roughly 30 cells ([Federrath et al., 2011](#)). One particular problem of an AMR grid is the varying diffusion scale in the domain and thus a varying energy range. Once a region is refined with more resolution, the kinetic motions can be followed to smaller scales, generally increasing the total kinetic energy in comparison to low-resolution regions. There are solutions to adequately compute the kinetic energy at the resolution limit via subgrid models of turbulent motions ([Braun and Schmidt, 2012](#)). But these methods have been developed fairly recently and are very difficult to include in a numerical scheme. They are therefore not implemented in this work.

#### 4.4.5 Numerical code

We investigate the collapse of the cores with three-dimensional hydrodynamic simulations using the grid based parallelised FLASH code in version 2.5

(Fryxell et al., 2000), which integrates the hydrodynamic equations with a piecewise-parabolic method (PPM) (Colella and Woodward, 1984). The code is parallelised using MPI. The computational domain is subdivided into blocks containing a fixed number of cells with an adaptive mesh refinement (AMR) technique based on the PARAMESH library (Olson et al., 1999). In order to accurately follow the physical processes in dynamically dominating high-density regions, the initial grid of blocks can be refined locally, controlled by different refinement criteria like the density, the velocity or derivatives of various quantities. In our setups we choose two refinement criteria, one based on the resolution of the Jeans length and one based on the second derivative of the velocity field.

## 4.5 Resolution limits

In order to avoid artificial fragmentation of the cloud, the Jeans length need to be resolved with at least 4 grid cells (Truelove et al., 1997). This implies higher refinement level and more cells in high-density regions. A side effect of the spatial refinement is the dropping incremental time step for the numerical integration scheme. As the solver for the hydrodynamic equations is an *explicit* scheme, the time step that the solution is advanced needs to be limited, in order to assure numerical stability. An important parameter in this context is the *Courant-Friedrichs-Lewy* number that can be regarded as the as the ratio of two speeds, namely the wave propagation speed  $a$  in the partial differential equation and the grid speed  $\Delta x/\Delta t$  defined by the discretisation of the domain (see, e.g. Toro, 2009),

$$\text{CFL} = \frac{a}{\Delta x/\Delta t} = \frac{a\Delta t}{\Delta x}, \quad (4.13)$$

which needs to be less than unity for numerical stability. Depending on the solver and the simulated physical system the CFL number varies. In our computations we used numbers in the range of 0.2 – 0.5.

Overall, further refinement decreases the numerical integration time steps and eventually stalls the simulation because of individual dense regions in the computational domain. Therefore the refinement of the domain needs to stop at a given maximum level to advance the computation with reasonable time steps. The resulting conflicts in dense regions at the highest level of refinement need to be solved with a sub-grid model that avoids artificial results.

One of the most popular sub-grid models in star formation simulations are *sink particles* (see e.g., Bate et al. 1995, Krumholz et al. 2004, Federrath et al.

2010a), that follow collapsing regions. If the Jeans length can not be resolved any more without further refinement, the gas in the cell is investigated for collapse criteria. The gas of the collapsing region is then removed from the grid cells and put into a Lagrangian particle, representing the collapsed point mass that does not interact hydrodynamically but only gravitationally.

The simulations were run with a maximum effective resolution of  $4096^3$  grid cells, corresponding to a smallest cell size of  $\Delta x \approx 13$  AU. In order to avoid artificial fragmentation, the Jeans length

$$\lambda_J = \sqrt{\frac{\pi c_s^2}{G \rho_{\max}}} \quad (4.14)$$

has to be resolved with at least 4 grid cells (Truelove et al., 1997). To resolve turbulence on the Jeans scale, however, a significantly higher number of cells is required. Federrath et al. (2011) find a minimum resolution of about 30 cells per Jeans length. Due to the high computational demand, we only use 8 cells in the current runs, so we likely miss some turbulent energy in our cores, which provides additional support against gravitational collapse. We might thus slightly overestimate the amount of fragmentation and underestimate the formation times of protostars. It must be noted, however, that this is a general limitation of all present star cluster formation calculations because resolving the Jeans length with more than 10–20 cells can be computationally prohibitive. Additionally, we use sink particles in the simulations. They are introduced at the highest level of the AMR hierarchy. A necessary but not sufficient criterion for the formation of sink particles is that the gas density needs to be higher than the threshold value

$$\rho_{\max} = \frac{\pi c_s^2}{4G(3\Delta x)^2} = 2.46 \times 10^{-14} \text{g cm}^{-3}. \quad (4.15)$$

If a cell exceeds this density, a spherical control volume with a radius of  $3\Delta x$  is investigated for gravitational collapse indicators. If the collapse criteria (Federrath et al., 2010a) are fulfilled, an accreting Lagrangian sink particle is formed. This sink particle is then identified as an individual protostar (Bate et al., 1995; Wuchterl and Klessen, 2001). Table 4.2 lists the simulation and resolution parameters.

Table 4.2: Numerical simulation parameters

Parameter		Value
simulation box size	$L_{\text{box}}$	0.26 pc
smallest cell size	$\Delta x$	13.06 AU
Jeans length resolution		$\geq 8$ (6*) cells
max. gas density	$\rho_{\text{max}}$	$2.46 \times 10^{-14} \text{ g cm}^{-3}$
max. number density	$n_{\text{max}}$	$6.45 \times 10^9 \text{ cm}^{-3}$
sink particle accretion radius	$r_{\text{accr}}$	39.17 AU

\* at highest level of refinement



# Chapter 5

## Cloud structure and morphology

This chapter is published in parts in Girichidis et al. 2011, MNRAS 413, 2741.

### 5.1 Introduction

The current paradigm of present-day star formation suggests that stars are born in molecular clouds, permeated by supersonic turbulence (Elmegreen and Scalo 2004, Mac Low and Klessen 2004, Ballesteros-Paredes et al. 2007). The cores have sizes of a few tenths of a parsec, are very dense with  $\langle n \rangle \sim 10^6 \text{ cm}^{-3}$  (Beuther et al., 2007), and in many cases they show large line widths, indicating supersonic, turbulent motions with a power-law spectral velocity distribution consistent with  $P(k) \propto k^{-2}$  (Zuckerman and Evans, 1974; Larson, 1981; Heyer and Brunt, 2004), and thus steeper than the Kolmogorov spectrum of turbulence,  $P(k) \propto k^{-5/3}$ . The steeper power-law exponent is a result of the compressible cascade of interstellar turbulence (Federrath et al., 2010b), in contrast to the incompressible cascade in Kolmogorov turbulence. The star-forming regions are observed to be fragmented with a filamentary, fractal-like structure (Scalo, 1990; Men'shchikov et al., 2010, and reference therein). Very dense cores that are supposed to form massive stars have higher temperatures ( $T \sim 20 \text{ K}$ ) in contrast to less dense clouds with 10 K (Beuther et al. 2007, Ward-Thompson et al. 2007).

Despite different fragmentation structures and different local environments, the overall interplay of physical processes that contribute to the formation of stars seems to be very robust in producing prestellar cores and finally stars with a mass distribution that does not show significant differ-

ences in most observed regions of our local universe. This mass distribution can be described by a universal initial mass function (IMF) (Scalo, 1986, 1998; Kroupa, 2001; Chabrier, 2003). Only under extreme circumstances, i.e. close to the Galactic Centre, may the initial mass function differ from the universal one. Whereas Löckmann et al. (2010) find that even there star formation is consistent with the canonical IMF, Bartko et al. (2010) clearly exclude a standard IMF in favour of a top-heavy mass function in the Galactic Centre stellar disks.

We know from observations that star formation is a complex interplay between a number of physical processes and ingredients: gravity, turbulence, rotation, radiation, thermodynamics, and magnetic fields. However, to what extent the various processes have a dominant impact on the evolution in comparison to the initial conditions of the molecular cloud is still unclear. Especially the impact of the initial conditions on the formation of massive stars, the spatial distribution of stars, and the mass evolution is unknown. Observations reveal that massive stars form early and with a tendency to be located at the centre of the cloud, whereas stars with lower masses form further out and at later times (Hillenbrand 1997; Hillenbrand and Hartmann 1998; Fischer et al. 1998; de Grijs et al. 2002; Sirianni et al. 2002; Gouliermis et al. 2004; Stolte et al. 2006; Sabbi et al. 2008).

Theoretical approaches reproduce consistent star formation key data with a variety of different numerical methods, initial setups, and physical processes (see review by Klessen et al., 2009). However, a systematic study of how the initial conditions influence the fragmentation process, the collapse of the gas into stars, the number of stars, and their accretion history is still missing. Especially how the formation of massive protostars depends on the interplay between initial density profile, turbulence, and accretion model needs to be studied systematically. The large variety of existing numerical simulations all with different initial conditions does not allow for a useful comparison. Bate et al. (2003), Bate and Bonnell (2005), Bate (2009a,b,c), Clark et al. (2008a), Bonnell et al. (2003, 2004), and Bonnell and Bate (2005) used uniform density distributions with solenoidal (divergence-free), decaying turbulent motions on different cloud scales. They use a turbulent power spectrum,  $P(k) \propto k^{-2}$ , consistent with supersonic turbulence, however, the influence of different mixtures of initial modes of the turbulence were never investigated. In particular, Bate (2009b) concluded from the similarity of their results with two different initial turbulence spectra,  $P(k) \propto k^{-2}$  versus  $P(k) \propto k^{-3}$ , that different turbulence in general has no major influence on star formation. However, both of the investigated spectra in Bate (2009b) are steep, such that the turbulence is dominated by the few large-scale modes (low  $k$ ) anyway. Different mixtures of solenoidal and compressive modes of

the initial turbulence are expected to have a much stronger influence on star formation, which we show here. [Krumholz et al. \(2007, 2010\)](#) favour concentrated density profiles with  $\rho \propto r^{-1.5}$ , referring to observations of dense cores. Their decaying turbulent velocities are based on a power spectrum of the form  $P(k) \propto k^{-2}$ , but not specifying the nature of the modes. In contrast, [Klessen \(2001\)](#) used driven turbulence on different scales to create dense cores self-consistently with a  $\rho \propto r^{-2}$  density profile in the outer region. [Offner et al. \(2008\)](#) compared driven and undriven turbulence with an initial flat power spectrum for the wave numbers  $3 \leq k \leq 4$ . [Federrath et al. \(2008, 2009, 2010b\)](#) investigated purely driven turbulence with the two limiting mixtures of turbulent modes: 1) fully solenoidal (divergence-free) and 2) fully compressive (curl-free), and found significantly different density distributions, with three times larger standard deviations of the density probability distribution function in the case of compressive compared to solenoidal driving (see also the follow-up studies by [Schmidt et al., 2009, 2010](#); [Seifried et al., 2011b](#); [Price et al., 2011](#)). Since such strongly different density fields are expected to lead to very different modes of star formation, we also investigate here three mixtures of the initial turbulence (compressive, mixed, and solenoidal). Here, however, we only apply the different turbulent modes as an initial condition, not continuously replenishing them by driving.

In this chapter, we investigate the fragmentation, the time scales, and the stellar distributions with a focus on how different initial conditions lead to different morphology and statistics of prestellar cores and stellar clusters. The chapter is structured as follows: section 5.2 describes the initial density profiles and the applied turbulent velocity fields for the simulations, as well as the numerical key parameters, and the usage of sink particles. In addition, a theoretical estimate of the accretion rate for the  $\rho \propto r^{-2}$  density profiles is calculated. In section 5.3 we present the results of the simulations, followed by a discussion in section 5.4. Here we concentrate on the cloud evolution and the global stellar properties. A detailed investigation of the spatial stellar distribution will be presented in chapter 8. Finally, in section 5.5 we summarise our results and conclusions.

## 5.2 Initial conditions

### 5.2.1 Initial density profiles

In the simulations the following four frequently used initial density profiles are applied:

1. Uniform density profile (Top-hat, TH)

2. Rescaled Bonnor-Ebert sphere (BE)
3. Power-law profile  $\rho \propto r^{-1.5}$  (PL15)
4. Power-law profile  $\rho \propto r^{-2.0}$  (PL20).

The profiles are motivated by the following reasonings. The TH just reflects the initial conditions in a uniform density environment with finite size. Neither initial density perturbations have been established nor does the sphere have a developed over-density. The BE profile is motivated by the theoretical calculation of an isothermal sphere in hydrostatic equilibrium confined by external pressure (Ebert 1955, Bonnor 1956). The PL20 profile is the limit of the collapsing BE sphere at the end of the evolution process. This density configuration of a singular isothermal sphere is widely applied because its collapse can be described by a self-similar solution with predictable in-fall and evolution properties (Shu (1977), section 5.2.1). So far studies with a singular isothermal sphere have only been done without turbulent velocity. Finally the PL15 profile, which is an intermediate evolutionary stage of the BE sphere before reaching the PL20 configuration, is motivated by observations. The outer region of collapsing clouds is observed to follow a density distribution of the form  $\rho \propto r^{-1.6}$  (Pirogov, 2009).

A comparison of the radial shape for all density profiles is shown in figure 5.1.  $\lambda_J$  marks the Jeans length for the average density  $\langle \rho \rangle$ . These four profiles are extreme setups that allow us to follow the influence on the central collapse and the fragmentation.

No initial density fluctuations were applied. The density of the surrounding gas in the cubic box around the spherical molecular cloud is set to  $10^{-2}$  times the gas density at the edge of the cloud at  $r = R_0$ . The initial temperature distribution is a step function with the temperature in the cloud envelope 100 times larger than in the inner isothermal collapsing cloud, which results in a continuous pressure at the boundary  $r = R_0$ .

### Top-hat

This density implementation is the simplest profile, describing the gas density as a step function

$$\rho = \begin{cases} \langle \rho \rangle & \text{for } r \leq R_0, \\ 0.01 \langle \rho \rangle & \text{for } r > R_0 \end{cases} \quad (5.1)$$

with

$$\langle \rho \rangle = \frac{M_{\text{tot}}}{V} = \frac{3M_{\text{tot}}}{4\pi R_0^3}. \quad (5.2)$$

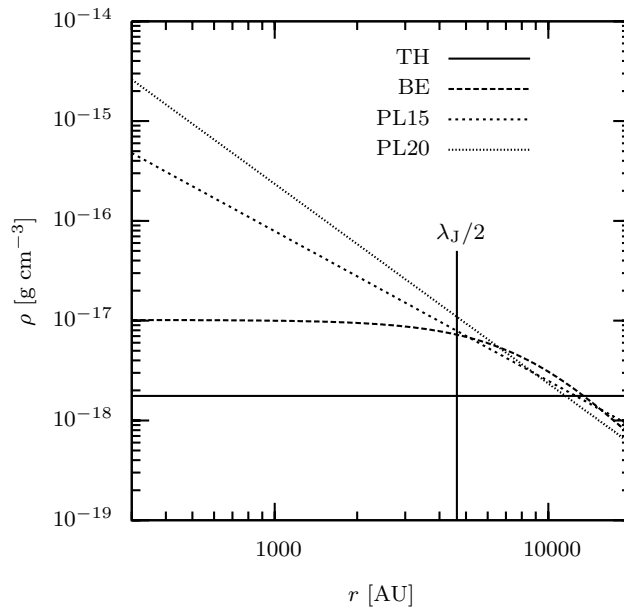


Figure 5.1: Comparison of the four initial density profiles adjusted to a total mass of  $100 M_{\odot}$  within a radius of 0.1 pc.  $\lambda_J$  marks the Jeans length for the average density  $\langle \rho \rangle$ .

### Rescaled Bonnor-Ebert sphere

In hydrostatic equilibrium the critical density profile is described by a Bonnor-Ebert sphere with normalised radius  $\xi = 6.41$  (Ebert 1955, Bonnor 1956). The only free parameter for this configuration is the central density  $\rho_0$ . In order to better compare this sphere with the other clouds, the central density was first chosen such that the outer radius of the sphere yielded the given size of 0.1 pc. Then the density at every point was rescaled to fit the total cloud mass of  $M_{\text{tot}} = 100 M_{\odot}$ .

### Power-law profiles

As the power-law profiles  $\rho \propto r^{-p}$  diverge in the centre of the cloud, an inner radius has to be defined below which the density follows a finite function. In these setups this part of the profile is described by a quadratic function:

$$\rho = \begin{cases} ar^2 + c & \text{for } 0 \leq r < r_1, \\ B \left( \frac{r}{R_0} \right)^{-p} & \text{for } r_1 \leq r \leq R_0. \end{cases} \quad (5.3)$$

The reason for this transition instead of a simple cut-off at the inner radius is to avoid artificial numerical effects at the boundary  $r_1$ . The value for  $r_1$  was

set to 3 (5) times the cell size at the highest level of refinement for  $p = 1.5$  ( $p = 2.0$ ). The choice for the values of  $a$  and  $c$  allow for a continuous transition for the density function value as well as for the derivative  $d\rho/dr$ . For  $p = 1.5$  the two values read  $a = 2.227 \times 10^{-44} \text{ g cm}^{-5}$  and  $c = 1.784 \times 10^{-14} \text{ g cm}^{-3}$ , the values for  $p = 2.0$  are  $a = 5.804 \times 10^{-44} \text{ g cm}^{-5}$  and  $c = 1.107 \times 10^{-13} \text{ g cm}^{-3}$ . The outer radius  $R_0$  was set to the radius of the cloud, the constant  $B$  scales the density profile to a total enclosed mass of  $M_{\text{tot}} = 100 M_{\odot}$ . Its value depends on the inner radius  $r_1$ . However, for small radii  $r_1$ , which is roughly three orders of magnitude smaller than  $R_0$  in the numerical setup,  $B$  converges to

$$\lim_{r_1 \rightarrow 0} B = \frac{M_{\text{tot}}(3-p)}{4\pi} \frac{1}{R_0^3}. \quad (5.4)$$

Depending on the effective resolution and therefore the parameter  $r_1$ , the maximum density changes significantly.

### Power-law profile $\rho \propto r^{-2}$ and self-similarity

Based on the analytic treatment of the collapse of a singular isothermal sphere by [Shu \(1977\)](#), the evolution of a density profile with the general form

$$\rho(r, t > 0) = \frac{c_s^2}{2\pi G} r^{-2}, \quad c_s^2 = \frac{k_B T}{\mu m_p} \quad (5.5)$$

can be described using the dimensionless similarity variable

$$x = \frac{r}{c_s t}, \quad (5.6)$$

where  $G$  is the gravitational constant. The density distribution, the mass accretion rate, and the in-fall velocity can be transformed to

$$\rho(r, t) = \frac{\alpha(x)}{4\pi G t^2} \quad (5.7)$$

$$\dot{M}_{\text{SIS}}(r, t) = \frac{c_s^3}{G} m(x) \quad (5.8)$$

$$u(r, t) = c_s v(x) \quad (5.9)$$

with  $\alpha(x) = x^{-2} dm/dx$  such that the collapse proceeds in a self-similar way. The two basic differential equations that have to be solved in order to find the values for  $\alpha$  and  $v$  read

$$[(x-v)^2 - 1] \frac{dv}{dx} = \left[ \alpha(x-v) - \frac{2}{x} \right] (x-v) \quad (5.10)$$

$$[(x-v)^2 - 1] \frac{1}{\alpha} \frac{d\alpha}{dx} = \left[ \alpha - \frac{2}{x} (x-v) \right] (x-v).$$

The initial density profile must have the form

$$\rho(r, t = 0) = \frac{c_s^2 A}{4\pi G} r^{-2} \quad (5.11)$$

with  $A > 2$ . This equation can be rewritten for the PL20 density setup as

$$\rho(r, t = 0) = q r^{-2} \quad \text{with} \quad q = 5.30 \times 10^{16} \text{ g cm}^{-1} \quad (5.12)$$

for a total enclosed mass of  $100 M_\odot$ . The constant  $A$  in this setup has the value

$$A = \frac{4\pi G q}{c_s^2} \approx 61.9. \quad (5.13)$$

Comparing the factor  $A$  to the number of Jeans masses in the cloud

$$M_J = \frac{\pi^{5/2}}{6} \frac{c_s^3}{G^{3/2} \rho^{1/2}}, \quad (5.14)$$

$$N_J = \frac{M_{\text{tot}}}{M_J} \quad (5.15)$$

it can be rewritten as follows to

$$A = \frac{4\pi^{8/3} q}{6^{2/3}} \frac{N_J^{2/3}}{\rho^{1/3} M_{\text{tot}}^{2/3}} \propto N_J^{2/3}. \quad (5.16)$$

In order to find the theoretical value for the accretion factor  $m_0 = m(r = 0, t = 0)$  equations (5.10) have to be integrated from a large  $x$  to a value close to zero. For a critical sphere with  $A = 2$  this factor is  $m_0 = 0.95$ , for  $A = 61.9$  it reaches a very high value of  $m_0 \approx 421$  (see figure 5.2). This finally gives a theoretical accretion rate of

$$\dot{M}_{\text{SIS}} = m_0 \frac{c_s^3}{G} \approx 1.89 \times 10^{-3} M_\odot \text{ yr}^{-1}. \quad (5.17)$$

The accretion factor  $m_0$  can be fitted with a power-law dependence

$$m_0 \propto A^{1.52} \quad (5.18)$$

(see right plot in figure 5.2) which in turn gives a theoretical accretion rate close to a linear dependence on the number of Jeans masses

$$m_0 \propto N_J^{1.01}. \quad (5.19)$$

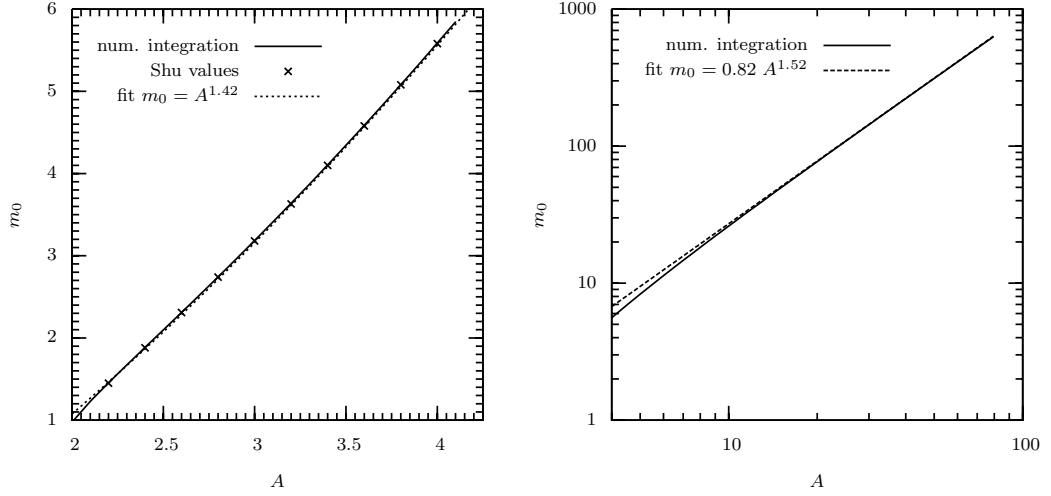


Figure 5.2: Accretion rates as a function of  $A$  from equations (5.10) and (5.11). In the left plot the values for small  $A$  are compared with the Shu values. The right plot shows the high- $A$  regime relevant for the simulation with the PL20 density profile.

### Properties of the central region

All of the initial spheres are gravitationally highly unstable. With the Jeans length

$$\lambda_J = \sqrt{\frac{\pi c_s^2}{G \langle \rho \rangle}} = 9264 \text{ AU} = 0.46 R_\odot \quad (5.20)$$

the Jeans volume, given as a sphere with diameter  $\lambda_J$ , reads  $V_J = \pi \lambda_J^3 / 6$  and the Jeans mass of this sphere is  $M_J = V_J \langle \rho \rangle = 1.23 M_\odot$ . The central region inside the Jeans volume is called the ‘core’ in the following. Accounting for the different masses inside the Jeans core due to different central mass concentrations  $M(r = \lambda_J/2) = M^{\text{core}}$ , it is useful to define the new average density ( $\rho^{\text{core}}$ ) and free-fall time ( $t_{\text{ff}}^{\text{core}}$ ) for the core region  $V_J$ . The core values for the different density profiles can be seen in table 5.1.

### 5.2.2 Runs

In order to systematically investigate the influence of the initial conditions, we follow a variety of combinations of turbulence and density profiles. Table 5.2 gives an overview of the combinations. The BE profiles as well as the PL15 profiles are combined with all turbulent fields. As the TH runs are computationally very expensive, only the turbulent fields with mixed modes

Table 5.1: Core properties of the different density distributions

setup	$M^{\text{core}} [M_{\odot}]$	$\rho^{\text{core}} [\text{g cm}^{-3}]$	$n^{\text{core}} [\text{cm}^{-3}]$	$t_{\text{ff}}^{\text{core}} [\text{kyr}]$	$t_{\text{tc}}^{\text{core}} / t_{\text{ff}}^{\text{core}}$
TH	1.25	$1.76 \times 10^{-18}$	$4.60 \times 10^5$	49.858	1.64
BE	5.84	$8.33 \times 10^{-18}$	$2.18 \times 10^6$	23.061	2.12
PL15	11.12	$1.59 \times 10^{-17}$	$4.16 \times 10^6$	16.707	2.92
PL20	23.02	$3.29 \times 10^{-17}$	$8.61 \times 10^6$	11.615	4.20

Core masses, densities, and free-fall times inside a sphere with diameter of a Jeans length ( $r^{\text{core}} = \lambda_{\text{J}}/2 = 7 \times 10^{16}$  cm). The free-fall time for the top-hat differs slightly from the theoretical value calculated by equation (4.2), because the data from this table are the numerical values taken from the simulation.

are applied. The PL20 density distribution has a very short central free-fall time and is expected to collapse and form a massive sink particle before the turbulent motions have an important impact on the cloud structure. Therefore 3 additional setups with compressive velocity field c-1 but higher rms Mach numbers (PL20-c-1b, PL20-c-1c & PL20-c-1d) were simulated. The velocities in PL20-c-1b are twice as high as the ones in PL20-c-1; runs PL20-c-1c and PL20-c-1d have velocities 4 and 6 times as high as PL20-c-1. The rms Mach numbers are:  $\mathcal{M}_{\text{c-1b}} = 6.57$ ,  $\mathcal{M}_{\text{c-1c}} = 13.1$ ,  $\mathcal{M}_{\text{c-1d}} = 19.7$  (see tab. 5.2).

### 5.3 Cloud structure and morphology – results

We followed the collapse to a star formation efficiency of 20%, i.e., until 20% of the initial cloud mass was captured in sink particles. The concentrated profile PL20 reached that stage quite quickly ( $\sim 11$  kyr). The PL15 runs show large differences in the simulation time, ranging from 25 – 36 kyr, which is similar to the time needed for the BE density setups (27 – 35 kyr). The longest time was needed for the TH setup with 45 – 48 kyr. Table 5.3 gives an overview of the total simulated time for all setups. Related to the core free-fall time, the TH and PL20 profiles just need roughly one  $t_{\text{ff}}^{\text{core}}$  to capture 20  $M_{\odot}$  in sink particles, whereas the BE runs need 1.2 – 1.5  $t_{\text{ff}}^{\text{core}}$ . The longest time was needed by the PL15 profiles with 1.4 – 2.1  $t_{\text{ff}}^{\text{core}}$ . A comparison of the captured mass in sink particles can be seen in figure 5.3 for all runs. The setups with the same density profile are plotted in the same line style in order to keep the plot readable.

Table 5.2: List of the runs and their main properties

density profile	turbulent modes	seeds	name	effective resolution	$\mathcal{M}$	total $\frac{E_{\text{kin}}}{ E_{\text{pot}} }$	total $\frac{E_{\text{thenn}}}{ E_{\text{pot}} }$	core $\left(\frac{E_{\text{kin}}}{ E_{\text{pot}} }\right)_c$	core $\left(\frac{E_{\text{thenn}}}{ E_{\text{pot}} }\right)_c$
TH	mix	1	TH-m-1	4096 <sup>3</sup>	3.3	0.075	0.047	0.027	0.038
TH	mix	2	TH-m-2	4096 <sup>3</sup>	3.6	0.090	0.047	0.111	0.038
BE	compr	1	BE-c-1	4096 <sup>3</sup>	3.3	0.058	0.039	0.073	0.028
BE	compr	2	BE-c-2	4096 <sup>3</sup>	3.6	0.073	0.039	0.055	0.028
BE	mix	1	BE-m-1	4096 <sup>3</sup>	3.3	0.053	0.039	0.018	0.028
BE	mix	2	BE-m-2	4096 <sup>3</sup>	3.6	0.074	0.039	0.082	0.028
BE	sol	1	BE-s-1	4096 <sup>3</sup>	3.3	0.055	0.039	0.057	0.028
BE	sol	2	BE-s-2	4096 <sup>3</sup>	3.5	0.074	0.039	0.072	0.028
PL15	compr	1	PL15-c-1	4096 <sup>3</sup>	3.3	0.056	0.038	0.067	0.025
PL15	compr	2	PL15-c-2	4096 <sup>3</sup>	3.6	0.068	0.038	0.042	0.025
PL15	mix	1	PL15-m-1	4096 <sup>3</sup>	3.3	0.050	0.038	0.013	0.025
PL15	mix	2	PL15-m-2	4096 <sup>3</sup>	3.6	0.071	0.038	0.072	0.025
PL15	sol	1	PL15-s-1	4096 <sup>3</sup>	3.3	0.053	0.038	0.052	0.025
PL15	sol	2	PL15-s-2	4096 <sup>3</sup>	3.5	0.069	0.038	0.061	0.025
PL20	compr	1	PL20-c-1	4096 <sup>3</sup>	3.3	0.042	0.029	0.046	0.017
PL20	compr	1	PL20-c-1b	1024 <sup>3</sup>	6.6	0.170	0.029	0.192	0.018
PL20	compr	1	PL20-c-1c	1024 <sup>3</sup>	13.1	0.682	0.029	0.768	0.018
PL20	compr	1	PL20-c-1d	1024 <sup>3</sup>	19.7	1.534	0.029	1.728	0.018

In order to increase the influence of the turbulence for the PL20 profile three more runs (PL20-c-1b, PL20-c-1c, PL20-c-1d) were carried out with the same structure of the velocity field as PL20-c-1, but with rescaled absolute values by factors of 2, 4, and 6, leading to rms Mach numbers  $\mathcal{M}_{c-1b} = 2\mathcal{M}_{c-1}$ ,  $\mathcal{M}_{c-1c} = 4\mathcal{M}_{c-1}$ ,  $\mathcal{M}_{c-1d} = 6\mathcal{M}_{c-1}$ . See table A.1 for resolution details.

Table 5.3: Overview of the simulation time and the sink particle properties

Run	$t_{\text{sim}}$ [kyr]	$t_{\text{sim}}/t_{\text{ff}}^{\text{core}}$	$t_{\text{sim}}/t_{\text{ff}}$	$N_{\text{sinks}}$	$M_{\text{max}}$
TH-m-1	48.01	0.96	0.96	311	0.86
TH-m-2	45.46	0.91	0.91	429	0.74
BE-c-1	27.52	1.19	0.55	305	0.94
BE-c-2	27.49	1.19	0.55	331	0.97
BE-m-1	30.05	1.30	0.60	195	1.42
BE-m-2	31.94	1.39	0.64	302	0.54
BE-s-1	30.93	1.34	0.62	234	1.14
BE-s-2	35.86	1.55	0.72	325	0.51
PL15-c-1	25.67	1.54	0.51	194	8.89
PL15-c-2	25.82	1.55	0.52	161	12.3
PL15-m-1	23.77	1.42	0.48	1	20.0
PL15-m-2	31.10	1.86	0.62	308	6.88
PL15-s-1	24.85	1.49	0.50	1	20.0
PL15-s-2	35.96	2.10	0.72	422	4.50
PL20-c-1	10.67	0.92	0.21	1	20.0
PL20-c-1b	10.34	0.89	0.21	2	20.0
PL20-c-1c	9.63	0.83	0.19	12	17.9
PL20-c-1d	11.77	1.01	0.24	34	13.3

The time of each simulation is given as the absolute time  $t_{\text{sim}}$ , the time in core free-fall times  $t_{\text{sim}}/t_{\text{ff}}^{\text{core}}$ , and the time in average free-fall times  $t_{\text{sim}}/t_{\text{ff}}$ .  $N_{\text{sink}}$  shows the number of sink particles at the end of the run,  $\langle M \rangle = 20 M_{\odot}/N_{\text{sink}}$  gives the average mass.

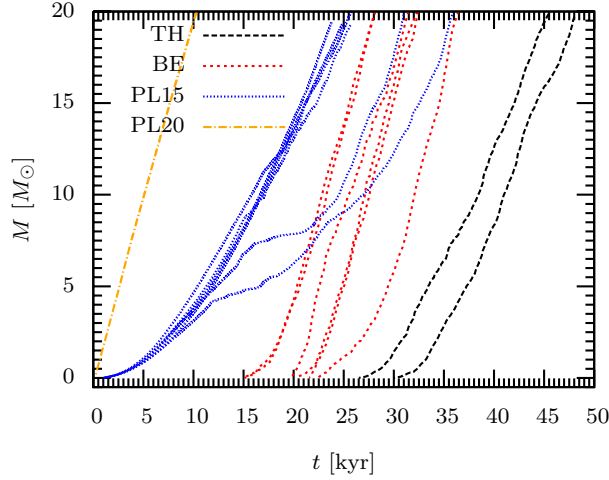


Figure 5.3: Comparison of the total mass in sink particles  $M$  for all simulations. All velocity realisations for one density profile are combined in one line style. A detailed discussion of each velocity field is given in the analysis section of each of the density profiles.

During the collapse of the cloud two different gravitational processes compete with each other. Firstly, the collapse toward the centre of mass and secondly the collapse of dense regions into filaments, induced by the turbulence. The different density profiles and turbulent fields lead to different cloud evolutions, fragmentation properties, and sink particle accretion rates. A column density plot at the end of each simulation is shown in figure 5.4 and 5.5. Figure 5.4 shows the column density plots for the density profiles TH, BE, and PL15 with the velocity field c-1, c-2, m-1, and m-2, as well as PL20-c-1. Each picture row shows simulations with the same initial turbulent velocity field, each column belongs to one density distribution. In the upper part of figure 5.5 we show the final column density for the BE and PL15 profile with the solenoidal fields. The lower part shows the PL20 profile with compressive turbulent modes for realisation 1. The four different plots belong to different initial kinetic energy variations (see table 5.2). All simulations show the formation of filamentary structures and sink particles. Depending on the initial density profile, the turbulent field, and the resulting total simulation time, the position of the filaments as well as the number of sink particles and their spatial distribution vary significantly. The TH profiles in figure 5.4 show locally disconnected filaments and subclusters of sink particles. The BE profiles also form many sink particles in extended filaments, but much more centrally concentrated and in stronger connected filaments. The initial mass concentration and the resulting faster central

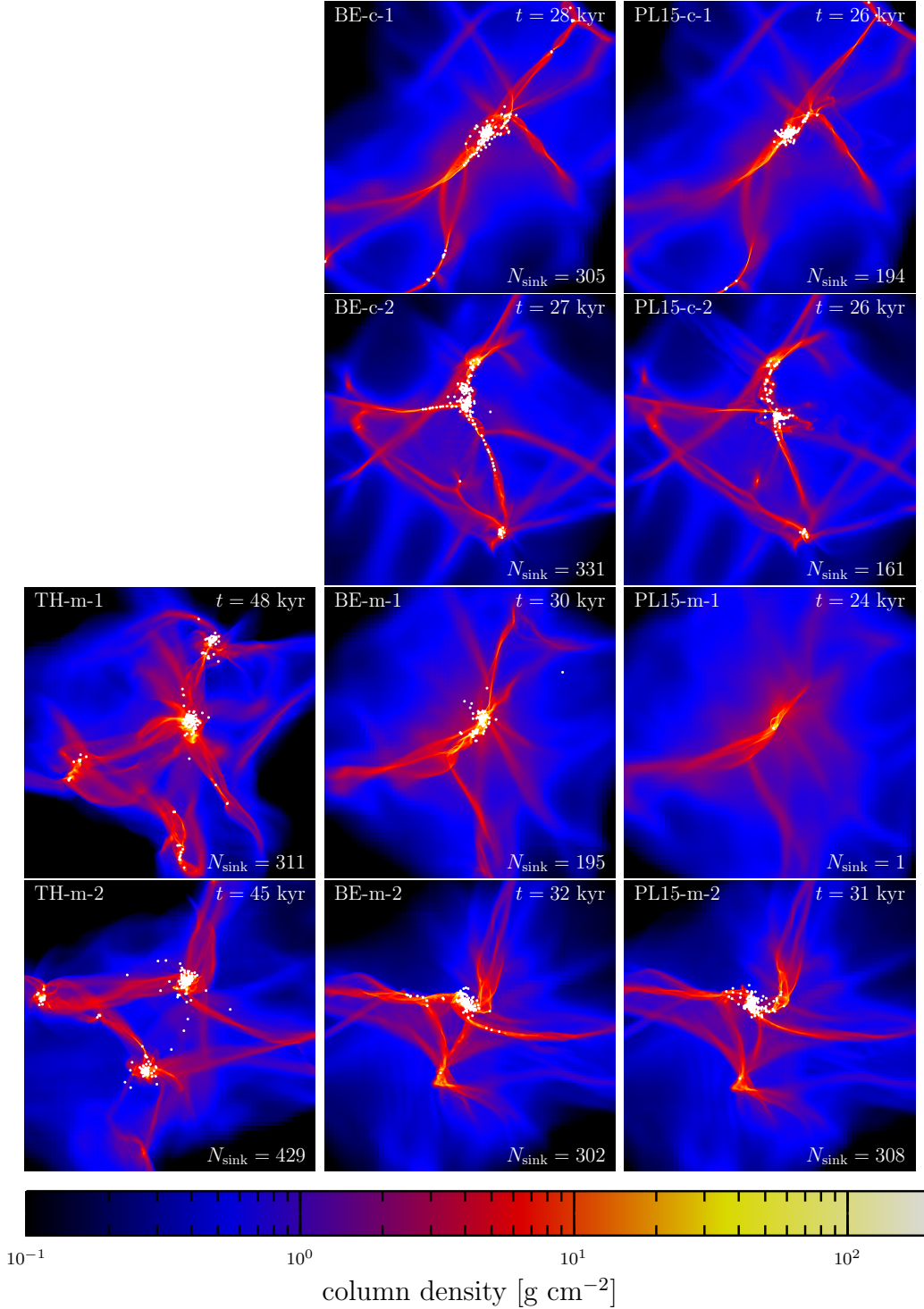


Figure 5.4: Column density plots for the TH, BE, and PL15 setups with velocity profiles c-1, c-2, m-1, and m-2 at the end of the simulation. The box in all cases spans 0.13 pc in both  $x$  and  $y$  direction. Each picture row corresponds to one velocity field, each column to a density profile. All setups show filamentary structures but differently spread in the box. Only the TH density runs form distinct subclusters.

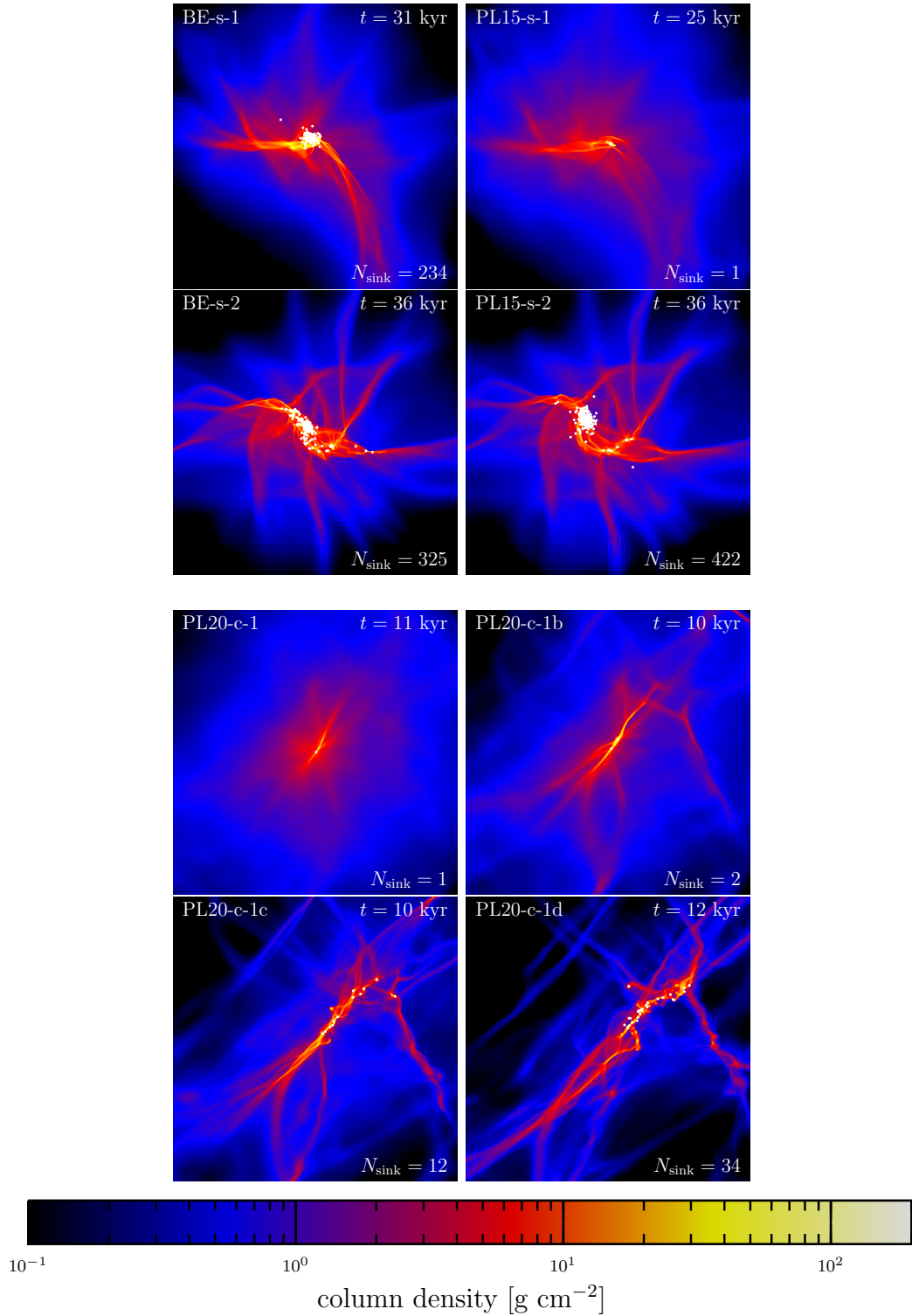


Figure 5.5: Column density plots for the BE and PL15 setups with velocity profiles s-1 and s-2 (upper part) as well as for the PL20 setup with turbulent field c-1, c-1b, c-1c, and c-1d (lower part). The box in all cases spans 0.13 pc in both  $x$  and  $y$  direction.

collapse suppress the formation of completely disconnected subclusters. The PL15 density profile shows in many cases a similar cloud evolution as the BE setups. However, the total number of sink particles varies strongly with different velocity realisations and the sink particles are located closer to the centre of mass. The influence of different initial kinetic energies of the turbulent motions can be seen in the PL20 setups. Higher velocities lead to much stronger substructures within the same simulated time.

A time evolution for turbulent field m-2 and the density profiles TH, BE, and PL15 is shown in figure 5.6. Each row shows the column density at the same simulation time. The columns correspond to the different density profiles. The much slower central collapse in the TH case allows the formation of two distinct over-dense regions, shown at  $t = 22$  kyr. At that time the BE profile has formed a few stars along the long main filament. The PL15 profile has already formed more than 50 sink particles very close to each other that interact very strongly and disturb the central filamentary structure. 3 kyr later the BE sphere formed more stars mainly along the outer arms of the main filament. Although the number of sink particles is larger than in the PL15 case at the previous time snapshot and the total mass captured in sink particles is roughly comparable, the cluster is not dominated by the gravitational attraction and  $N$ -body dynamics of the stars. The initial gas structure remains unperturbed. Another 3 kyr later the TH profile eventually developed collapsing regions in completely disconnected areas. By that time the BE cluster begins to show dynamical interactions. In the last time snapshot the overall cloud structure as well as SFE and the number of sink particles is comparable for the BE and the PL15 case.

Concerning the formation of sink particles, a clear distinction between the power-law profiles and the profiles with a flat core has to be made. The power-law profiles with their high density core form a sink particle very early due to the fast collapse of the central region. In the PL20 profile and in two of the PL15 profiles, this particle remains the only particle formed in the entire simulation time. PL15 runs with more than one sink particle form them with a large time gap after filamentary structures have formed and collapse. In the BE and TH profiles this central particle does not exist, and all particles form in filaments. This different behaviour can be seen in the mass evolution (figure 5.3). The runs with PL15 profile form a sink in the centre right after the start. The mass therefore evolves similarly at the beginning. For the BE sphere and the uniform density distribution, the different realisations of the turbulence lead to different filamentary structures and thus influence the point in time when sink particles are created. Therefore, the mass evolution of the different simulations show large offsets (figure 5.3).

In general, all setups result in high total accretion rates onto the sink

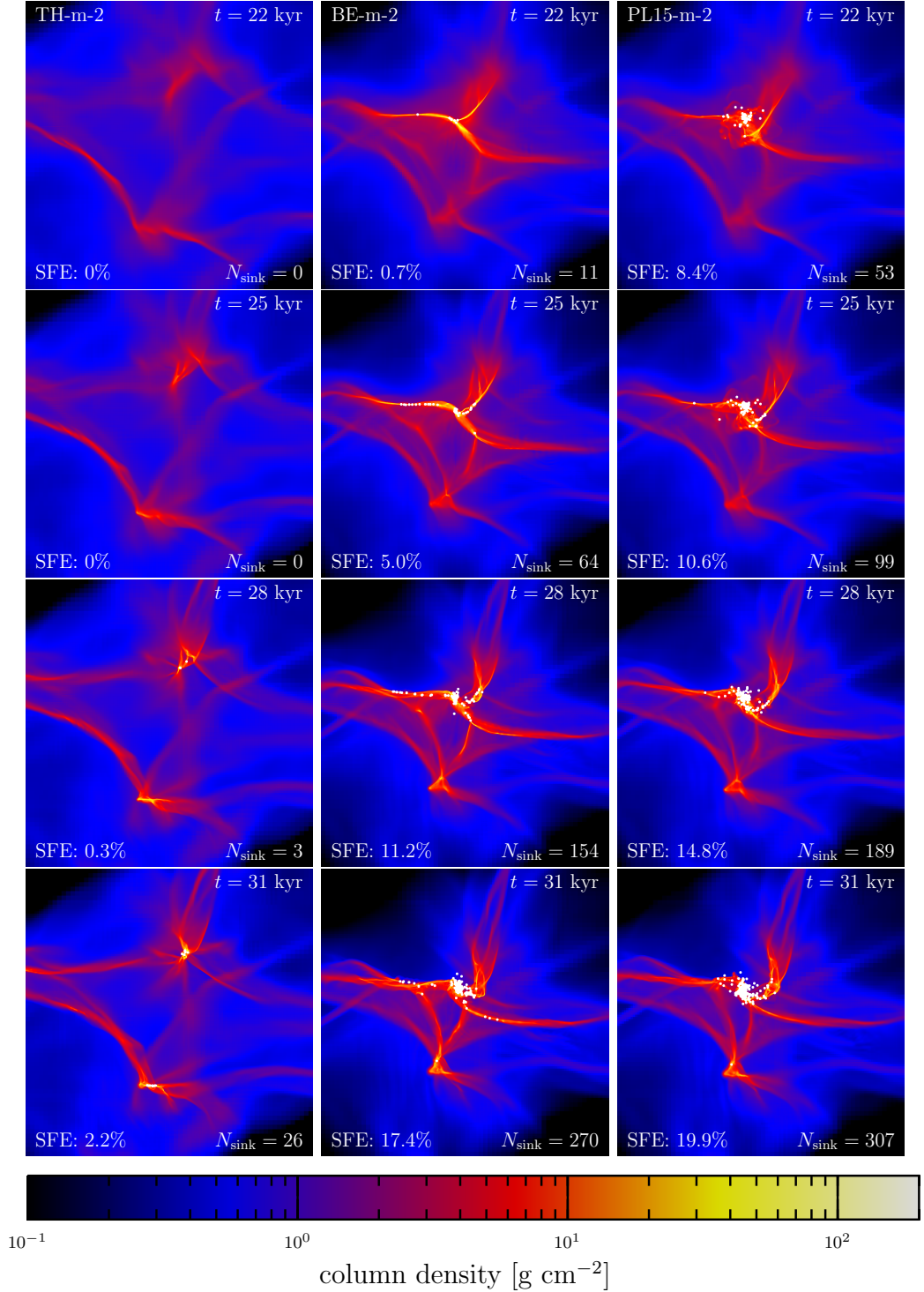


Figure 5.6: Column density plots for the TH, BE, and PL15 profile with the velocity field m-2 in a box of 0.13 pc in  $x$  and  $y$  direction. The TH-m-2 clearly develops two subclusters by the end of the simulation. The BE and PL15 runs show a similar general cloud structure that is dominated by central collapse. In the BE case the flatter initial density forms sink particles far away from the centre, whereas in the PL15 run the cluster is more compact.

particles of  $\dot{M} \sim 1 - 2 \times 10^{-3} M_{\odot} \text{ yr}^{-1}$ . Only PL15-m-2 and PL15-s-2 (see detailed discussion below) show somewhat smaller values of the accretion rate. The fluctuations around the mean value strongly depend on the number of particles, their positions, and the resulting particle-particle interactions as well as accretion shielding effects. The PL20 as well as two PL15 runs only form one sink particle and show a very smooth accretion rate with small fluctuations. The accretion rates in the TH and BE profiles are influenced by the particle movements but as the clusters are not that compact the interactions are less intense. The overall similarity of the accretion rates can also be seen in the similar slope of the mass function in the upper panel of figure 5.3.

### 5.3.1 Analysis of the TH profile

The uniform density distribution has much less mass within the core region compared to the concentrated profiles (see table 5.1), and its core free-fall time is longer. The initial supersonic velocity field has time to develop significant over-densities before the global collapse becomes dominant. Therefore the evolution of the cloud at the beginning of the simulation is dominated by the turbulent motion rather than the central collapse. The turbulence crossing time and the free-fall time of the core are similar ( $t_{\text{tc}}^{\text{core}}/t_{\text{ff}}^{\text{core}}=1.64$ ) which leads to the formation of over-dense regions all over the simulation box. These over-dense regions are very massive and evolve to locally collapsing filaments in which the first sink particles form. Filaments that are close to each other merge into sub-cores in which subclusters build up, before the central collapse sets in. After roughly one free-fall time, 20% of the mass is collapsed into sink particles.

The accretion rate for every single sink particle is a strongly varying function with time. However, the global rate for the sum of all sink particles quickly reaches a saturated value of  $\dot{M} \sim 10^{-3} M_{\odot} \text{ yr}^{-1}$  (figure 5.7), which can also be seen in the comparable slope of the total sink particle mass as a function of time. The number of sink particles is noticeably higher for TH-m-2.

The mass distribution of the sink particles follows an overall shape similar to the universal IMF (e.g. Kroupa, 2001; Chabrier, 2003), but shifted to lower masses by a factor of about 10 (see figure 5.8). A comparison with analytic models of the IMF (e.g., Padoan and Nordlund, 2002; Hennebelle and Chabrier, 2008) is planned in a future contribution. Here the main conclusion is that the formation of massive stars is very unlikely in a cloud with  $100 M_{\odot}$  and a uniform density distribution.

Since refinement is initiated in a very space-filling fashion for the uniform

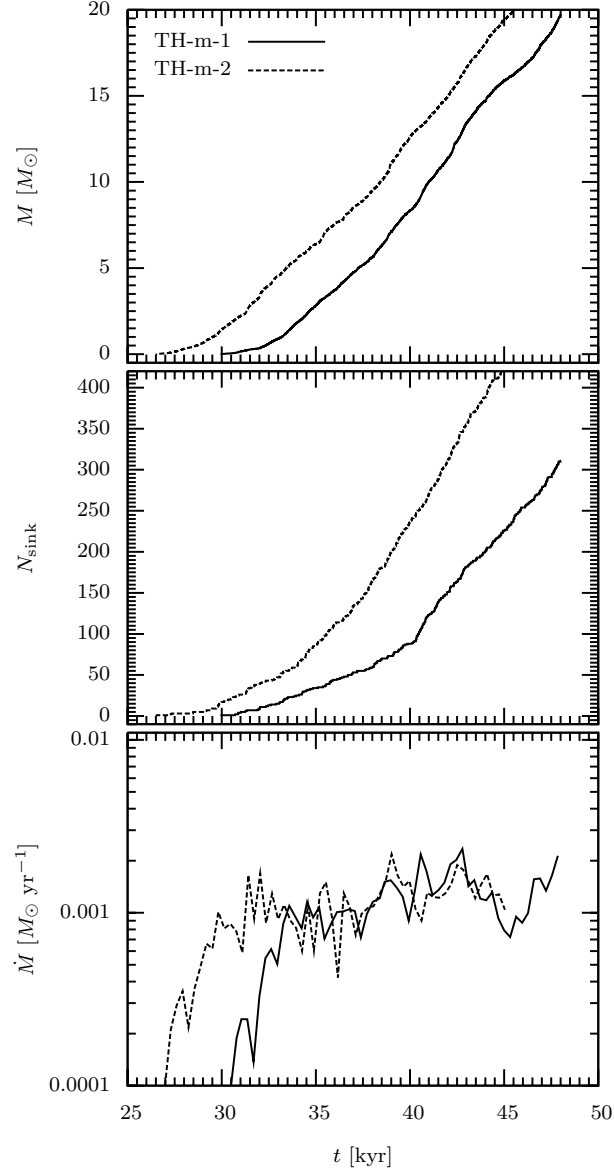


Figure 5.7: Sink particle evolution for the TH runs. Once sink particles have started to form the total accretion rate (lower plot) quickly reaches a value around  $\dot{M} \sim 10^{-3} M_{\odot} \text{ yr}^{-1}$ , fluctuating by a factor of roughly 2. Therefore the evolution of the mass captured in sink particles as a function of time looks very similar for both runs (upper plot), just shifted by 3 – 4 kyr.

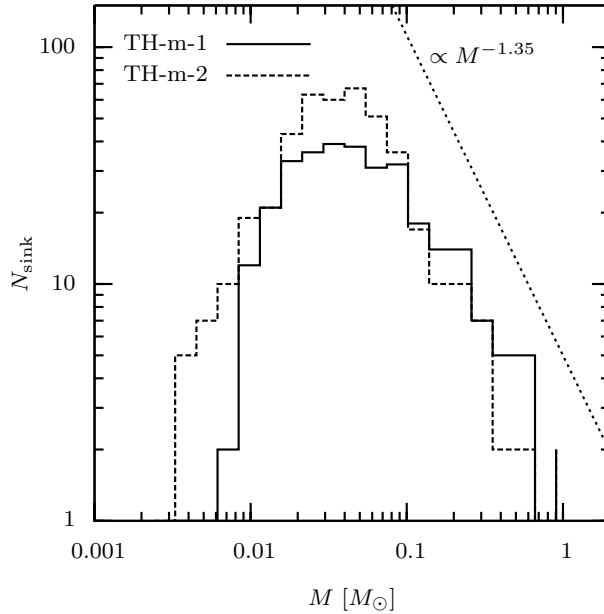


Figure 5.8: The mass distribution of the sink particles for the TH setup has an overall shape similar to the uniform IMF (Kroupa, 2001; Chabrier, 2003), but shifted to lower masses.

density distribution of the TH runs and thus computational cost became prohibitive, we only ran mixed turbulence runs with two different seeds. It should be noted, however, that the influence of the different mixtures (compressive versus solenoidal) of the turbulence has the biggest influence on the evolution and structure of the forming clusters and subclusters in the TH profiles, because TH profiles provide the most time for the turbulence to influence the cloud structure before the global collapse sets in..

### 5.3.2 Analysis of the BE profile

Here the cloud evolution at the beginning is similar to the collapse of the TH core. The turbulence can form strong filaments spread over large regions of the domain. However, the different radial mass distribution leads to low-mass filaments in the outer regions. This results in a stronger central acceleration, which causes the filaments to merge near the centre of mass. The formation of large subclusters is suppressed compared to the case of the uniform density distribution. By far, most of the sink particles, which are roughly as numerous as in the TH simulations, are formed in the core region. The time evolution of the cloud for different turbulent modes with the same random velocities can be seen in figure 5.9. The compressive modes lead

to sink particle formation about 25% earlier than the mixed and solenoidal modes.

The time evolution of the global sink particle properties are shown in figure 5.10. Although the random seed strongly determines the location and orientation of the filaments, the particle formation between BE-c-1 and BE-c-2 is almost indistinguishable. In the case of mixed and solenoidal modes the choice of the random seed significantly changes the time at which sink particles form. However, after the creation of sink particles has set in, the particle production rate with time as well as the total mass accretion rate is quite similar for all runs, not reflecting the structure of the initial turbulence at all. Only the BE-s-2 setup needs some more time until it reaches the asymptotic value of  $\dot{M} \sim 2 \times 10^{-3} M_{\odot} \text{ y}^{-1}$ . However, the accretion rate of individual sink particles varies strongly with time.

The mass distribution of the sink particles (figure 5.11) also shows a typical IMF structure like the TH runs, also shifted to much lower masses. This leads to the conclusion that the stronger central density concentration and the resulting stronger in-fall properties are still way too inefficient in forming massive stars.

### 5.3.3 Analysis of the PL15 profile

From the very beginning of the simulation, the PL15 profiles show a considerably different evolution compared to the TH and BE profiles. Due to the strong mass concentration, the first sink particle forms close to the centre very early, after roughly  $1 \text{ kyr} \approx 0.06 t_{\text{ff}}^{\text{core}}$ . The formation of this sink particle is not influenced by extended filaments, because the formation time of filaments is much larger than the time for central collapse. The central particle has a high and smooth accretion rate in all PL15 runs, which allows it to grow to the most massive sink particle in the simulation, while filaments in the outer regions start to form later (figure 5.12). Whether secondary sink particles form strongly depends on the random seed of the turbulence, as well as on the nature of the modes. All simulations with compressive modes lead to the formation of many sink particles in the filaments. On the other hand, mixed and solenoidal modes lead to either one (PL15-m-1 & PL15-s-1) or a few hundred particles (PL15-m-2 & PL15-s-2). A possible explanation for this dichotomy could be the influence of tidal forces, which can suppress the growth of the initial perturbations induced by the turbulence. In a density profile steeper than  $r^{-1}$  (see appendix A.2), tidal forces start to shear radial density fluctuations apart, thus reducing the chance of initial perturbations to grow by self-gravity. For the BE profile the central region of the cloud has a shallower density profile than  $r^{-1}$ , the PL15 profile a slightly steeper

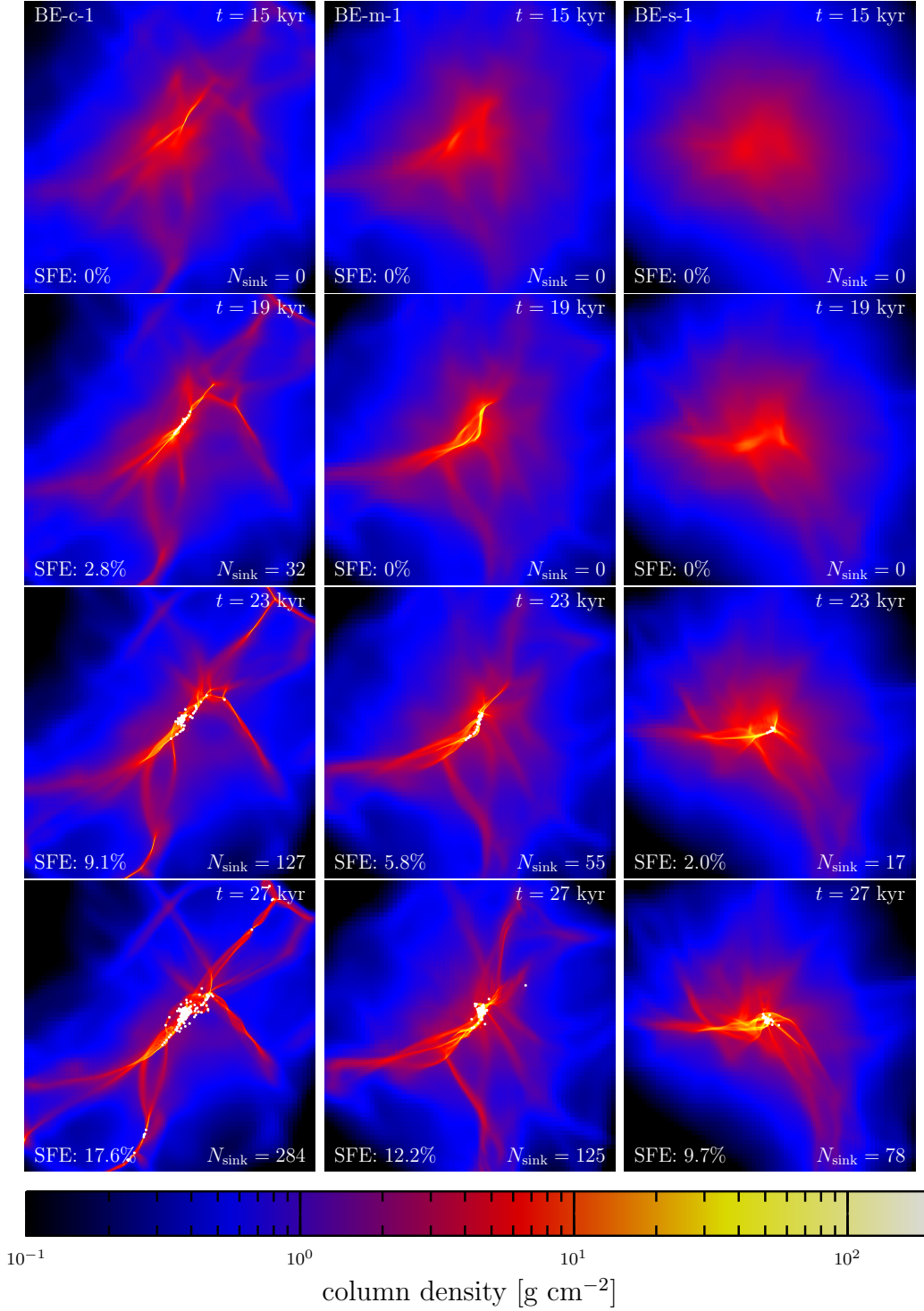


Figure 5.9: BE column density plots for the BE density profile and three different turbulent fields. The columns show snapshots with c-1, m-1, and s-1 velocities (from left to right) for the same physical time. The box shown spans 0.13 pc in  $x$  and  $y$  direction.

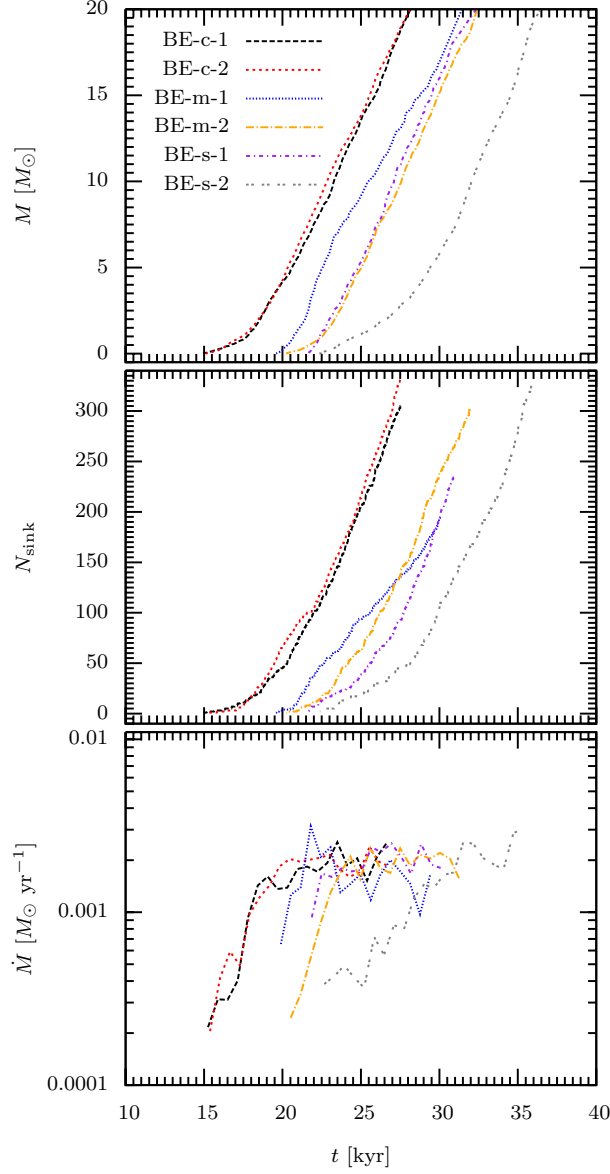


Figure 5.10: Sink particle evolution in the BE runs. The upper plot shows the total mass captured in sink particles. The compressive fields form sink particles first, the mixed and solenoidal velocity fields a few kyr later. After the formation of the first sink particle the accretion rate (lower plot) approaches a value of  $\sim 2 \times 10^{-3} M_{\odot} \text{ yr}^{-1}$ , independent of the initial turbulent field. The number of sink particles also shows a similar evolution for all setups (central plot).

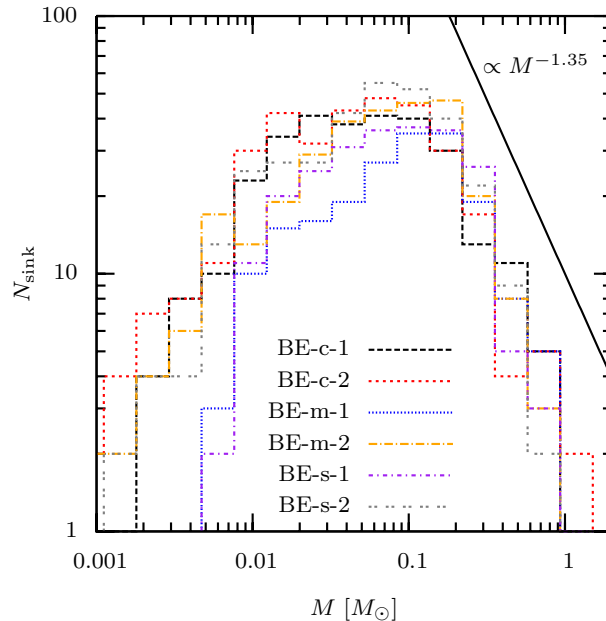


Figure 5.11: IMF for the BE setups. For all turbulent setups the IMF looks very similar. The distribution function mainly follows the general shape of a uniform IMF, but with lower average masses.

one. Over-dense regions that can marginally grow in the BE profile may be sheared apart in the corresponding PL15 profile with the same velocity field. However, the turbulence is supersonic and the density power-law exponent is not far from the critical one. This is why different locations and strengths of converging and diverging regions of the velocity field may easily overcome the shearing effect and cause the big differences between PL15-m-1/PL15-s-1 and PL15-m-2/PL15-s-2. Indeed, an analysis of the density-weighted divergence of the initial velocity fields shows that seed 2 produces stronger compressions in regions of high density than seed 1. Taken together with the fact that fragmentation into multiple objects always occurs for the purely compressive fields, this shows the importance of compressive modes for triggering the formation of dense fragments.

In the first 10 kyr, the evolution of all PL15 simulations is quite similar. During that time all simulations have only formed one central sink particle. As soon as other sink particles form, the situation changes significantly. In the case of multiple sink particles, their particle-particle interactions in the stellar cluster disturb the central in-fall and redirect the central gas velocities.

Although the total number of sink particles as a function of time is similar for PL15-c-1, PL15-c-2, PL15-m-2, and PL15-s-2, their spatial distribution

differs between the runs with compressive velocity field (PL15-c-1, PL15-c-2) and the runs PL15-m-2 and PL15-s-2 with mixed and solenoidal fields. In the former, the sink particles are located in filaments much farther away from the centre, resulting in weaker particle-particle interactions and allowing the particles to remain located in their dense parental filament. The runs PL15-m-2 and PL15-s-2 are dominated by the in-fall of less centrally located and hence less massive filaments. The local gravitational collapse inside these filaments is therefore delayed until the filament approaches the dense core. Sink particles show much lower mean separations which increases the strength and impact of particle-particle interactions. The induced cluster dynamics reduces the total mass accretion rate because individual sinks stop accreting if they are kicked out of the dense gas regions. This effect can also be seen in the IMF (figure 5.13). PL15-m-2 and PL15-s-2 have many more sink particles, but the final mass of the central one is lower than in the runs with compressive fields (see table 5.3). Hence, the accretion onto the central object is starved by the fragmentation around it (Peters et al., 2010a).

### 5.3.4 Analysis of the PL20 profile

For the PL20 density profile with the compressive turbulent field, only one sink particle was created already after 0.13 kyr which is only  $0.012 t_{\text{ff}}^{\text{core}}$ . As this velocity field is the most likely one to form more than one sink particle, the other turbulence realisations are not simulated entirely. This density profile is gravitationally too unstable for the turbulence to have an impact on the density evolution and the fragmentation of the gas sphere within a core free-fall time. As the turbulence crossing time is about 20 times longer than the core free-fall time, the small influence of the turbulence is expected. The accretion rates for all realisations of this setup are very similar (figure 5.14). Therefore only the setup with compressive mode 1 (PL20-c-1) was simulated up to a star formation efficiency of 20%. In conclusion, a  $\rho(r) \propto r^{-2}$  density profile does not reproduce a realistic IMF but helps to form massive stars.

In order to investigate the threshold turbulent energy that is needed to cause other regions to fragment and collapse besides the central region, three additional PL20 profiles with higher velocities were investigated (see tab. 5.2). The turbulence in PL20-c-1b, with twice as high velocities than our standard PL20 run, is still not strong enough to significantly alter the result. There is still only one sink particle created, accreting mass at a very high rate. For PL20-c-1c with velocities four times as high as in PL20-c-1 ( $\mathcal{M} = 13.1$ ), the situation changes. The stronger turbulence leads to the formation of other sink particles apart from the central one. However, the central particle in this run still contains 90% of the mass ( $M = 18 M_{\odot}$ ) at the end of the

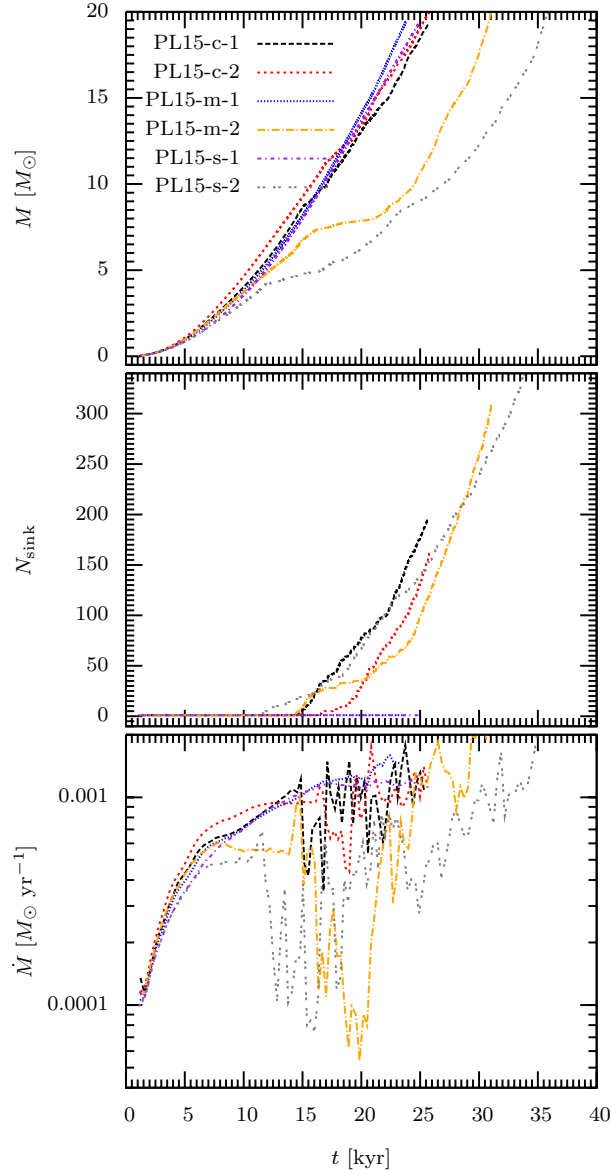


Figure 5.12: PL15 particle evolution. The upper plot shows the total mass captured in sink particles. Apart from the m-2 and s-2 velocity field, the mass evolution is very similar. This can also be seen in the lower plot, showing the accretion rate. In case of more sink particles, the accretion rate varies much more strongly with time. This is due to strong particle-particle interactions in the compact stellar cluster. If the cloud fragments and collapses in different regions the number of stars follows similar curves (central plot). However, the total number of particles differs much more than in other density setups.

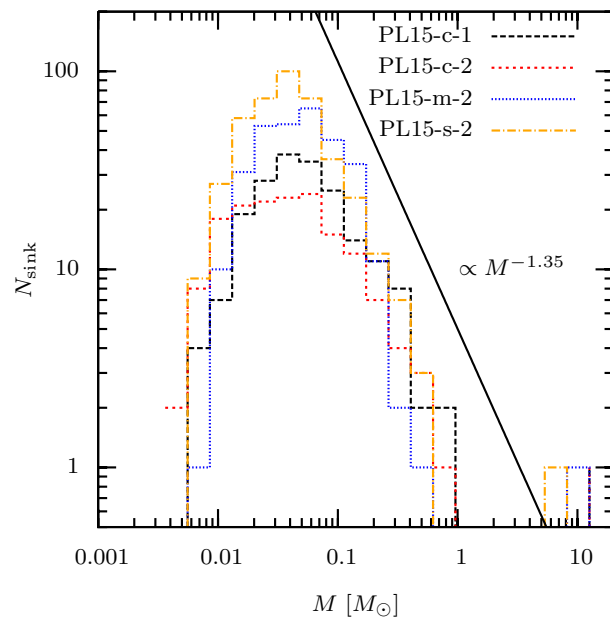


Figure 5.13: IMF for the PL15 runs. All runs form one very massive sink particle, which is by far the most massive one in the cluster, indicated by the single peak around  $10 M_{\odot}$ . The continuous set of low-mass particles below the mass gap shows similarities with the universal IMF, again shifted to almost 10 times lower masses as in the TH and BE profiles.

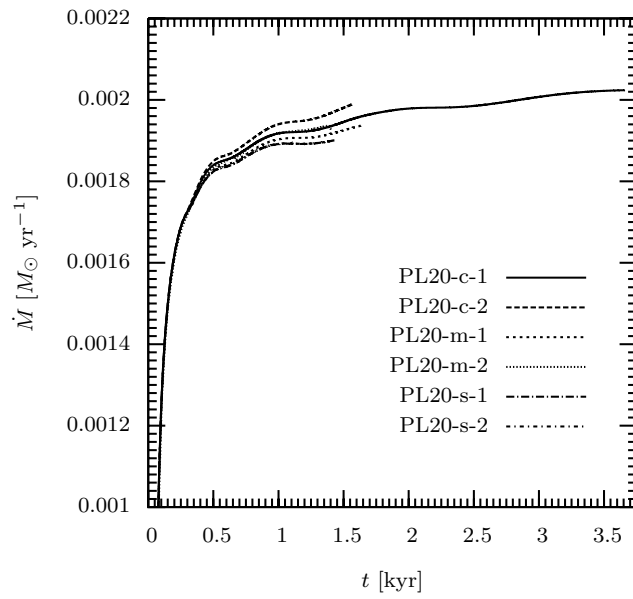


Figure 5.14: Comparison of sink particle accretion rate for the PL20 profile with different turbulent velocity fields. Note that the accretion rate is plotted in linear scale in order to see the small differences between the runs with different turbulence. In all cases only one sink particle is created over the whole simulation time.

simulation, and the second most massive particle is more than one order of magnitude less massive. Similar results are obtained from PL20-c-1d with a Mach number of  $\mathcal{M} = 19.7$ . More sink particles form, but still the central star is the most massive one with  $M = 13 M_{\odot}$ .

## 5.4 Cloud structure and morphology – discussion

Our results clearly show that diverse initial conditions lead to completely different cloud structures and collapse scenarios. However, the strong dependence of the simulation outcome on the initial conditions may be moderated by different input physics like radiation or magnetic fields and the effects due to rotation.

Our simulations indicate that massive stars can form without the aid of radiation and magnetic fields just from choosing centrally concentrated density profiles. In contrast, our isothermal cloud setups with flat density distributions fail to produce massive stars. We note that this result could change significantly if more massive clouds with more Jeans masses are used. We find in our simulations of isothermal gas that clouds with an initially uniform density distribution tend to overproduce low-mass proto-stars and have difficulty forming sufficient numbers of high-mass objects. This is in qualitative agreement with the simulations done by [Bate et al. \(2003\)](#) and [Bate and Bonnell \(2005\)](#). They used a uniform density distribution and solenoidal velocity fields, which seems to represent the conditions that inevitably lead to a large number of low-mass objects. This is also consistent with the calculations by [Offner et al. \(2008\)](#), [Klessen et al. \(1998\)](#), [Klessen and Burkert \(2000\)](#), [Klessen et al. \(2000\)](#), [Klessen \(2001\)](#), and [Heitsch et al. \(2001\)](#), who tested the influence of driven and decaying turbulence in a uniform density box. In order to suppress fragmentation and/or enhance the formation of massive stars in flat density profiles, more physics may help, which is addressed in three different approaches, namely radiation feedback, magnetic fields and stellar collisions. Concerning the first process, [Kratzer and Matzner \(2006\)](#) derived an analytical model to address the fragmentation process in massive discs. Indeed, [Bate \(2009b\)](#), [Krumholz et al. \(2009\)](#), [Peters et al. \(2010a,c,b\)](#) found reduced fragmentation in simulations. However, radiative feedback does not suppress fragmentation entirely. Alternatively, magnetic fields tend to reduce fragmentation. [Hennebelle and Teyssier \(2008\)](#), [Ziegler \(2005\)](#), and [Bürzle et al. \(2011\)](#) investigated the influence of magnetic fields in low-mass cores, [Banerjee et al. \(2009\)](#), [Peters et al. \(2011\)](#), and [Hennebelle](#)

et al. (2011) noted reduced fragmentation in high mass cores. But again, the fragmentation is not fully suppressed. The formation of massive stars by stellar collisions was proposed by Zinnecker and Yorke (2007). However, Baumgardt and Klessen (2011) showed that under realistic cloud conditions the contribution of stellar collisions can be neglected.

In earlier studies, the discussion about cloud fragmentation and the formation of massive stars is strongly focused on the physical processes, not taking heed of the importance of initial conditions. As the time scale for star formation is of the order of a few dynamical times (Ballesteros-Paredes et al., 1999; Elmegreen, 2000; Hartmann et al., 2001; Mac Low and Klessen, 2004; Elmegreen, 2007), the star-forming core has only little time to interact with the surrounding medium. The boundary and initial conditions are therefore decisive key properties for the collapse scenario and the star formation outcome. To fully understand the formation of a star cluster therefore requires knowledge of both the initial conditions for the cluster-forming cloud core (density profile, temperature, turbulent velocity content) as well as the time-dependent boundary conditions (as the core is connected to the overall turbulent cloud environment and may grow in mass by accumulation of gas at the stagnation points of larger-scale convergent flows).

Given the sensitivity of the dynamical evolution on the choice of the initial density profile, it is of pivotal importance to seek guidance from observations. On small scales ( $\ll 1$  pc) the observed cores clearly deviate from a uniform density (e.g., Pirogov, 2009; Könyves et al., 2010; Bontemps et al., 2010). The outer regions of molecular cloud cores can be described by a power-law with  $\rho \propto r^{-1.5}$ . In the centre of a dense core, however, the approach of a power-law function seems to be inconsistent with observations, which identify the central region of the core to be flat (Motte et al., 1998; Ward-Thompson et al., 1999). Starless cores may often be fitted with a critical Bonnor-Ebert sphere, cores with stars are often better fitted with supercritical ones (Teixeira et al., 2005; Kandori et al., 2005; Kirk et al., 2005). Krumholz et al. (2007, 2010) use very similar setups to our PL15 density profile, emphasising the importance of radiative feedback for the formation of massive stars. In this density profile the central region inevitably determines the collapse time scale and the formation of the first proto-stellar object. Our current analysis indicates that following a power-law profile to very small radii ( $< 10^3$  AU) introduces a bias towards forming a massive central object without much fragmentation around it. Adding radiative feedback does not change the outcome significantly in view of the very short central collapse time scales.

We can also look at the way ISM turbulence is treated in other numerical studies. Bate et al. (2003), Bate and Bonnell (2005), Bate (2009a,b,c),

Bonnell et al. (2003, 2004), and Bonnell and Bate (2005), for example, always used divergence-free, decaying turbulent fields. Clark et al. (2008b), Clark et al. (2008a), Offner et al. (2008), and Krumholz et al. (2007) do not specify the nature of the modes they select for their turbulence. As our results show that compressive, decaying modes lead to significantly earlier collapse and more elongated, shocked structures in the flat density profiles (TH and BE) than purely solenoidal turbulence, this is an important aspect of the star formation process that deserves further consideration. A systematic study of different modes of the turbulence was done by Federrath et al. (2008, 2009, 2010b) and Seifried et al. (2011b), but in a periodic box with driven turbulence and without gravity. These studies find the expected trend that compressive modes initiate faster collapse and higher accretion rates than purely solenoidal turbulence. However, the influence of the different modes is stronger in driven turbulence with self-gravity than in the decaying turbulence runs analysed here. Since dense cores are typically embedded in large-scale, turbulent molecular clouds, an effective driving of the internal turbulence from outside the core is expected (e.g., Klessen and Burkert, 2000; Federrath et al., 2010b).

## 5.5 Cloud structure and morphology – summary and conclusions

We performed a parameter study of the fragmentation properties of collapsing isothermal gas cores with different initial conditions. We combined four different density profiles (uniform, Bonnor-Ebert type,  $\rho \propto r^{-1.5}$ , and  $\rho \propto r^{-2}$ ) and six different turbulent, decaying velocity fields (compressive, mixed, and solenoidal, each with two different random seeds). For these simulations we neglected radiation, magnetic fields, and initial rotation, in order to study the direct influence of the initial density profile and the character of the turbulence. The cloud evolution as well as the star formation and their properties were examined. Here we list our main conclusions:

The density profile strongly determines the number of formed stars, the onset of star formation, the stellar mass distribution (IMF), and the spatial stellar distribution.

- Flat profiles (uniform density and Bonnor-Ebert profiles) produce many sink particles in elongated filaments. The formation of sink particles starts after slightly more than half of a core free-fall time for the uniform cloud and after roughly one core free-fall time for the Bonnor-Ebert setups. The runs with initially uniform density produce subclusters in

merging filaments in outer regions of the cloud. Even the relatively weak mass concentration in the centre of the Bonnor-Ebert setups suppresses the formation of subclusters. Both density profiles show an initial mass function with the high-mass end consistent with the Salpeter slope. In the case of initial compressive velocity fields, star formation sets in 25% earlier than in the solenoidal case. The mixed turbulent fields are in between the two extreme cases.

- The  $\rho \propto r^{-1.5}$  profiles always form one sink particle in the centre of the cloud at an early stage. This sink particle accretes gas at rate of  $\sim 10^{-3} M_{\odot} \text{ y}^{-1}$  and grows to the most massive particle by far. The formation of unstable filaments depends sensitively on the initial turbulent field. The formation of additional sink particles only occurs after a time delay of  $\sim 0.3 t_{\text{ff}}$ . The mass distribution of these sink particles shows a high-mass slope consistent with the Salpeter slope, but has a wide gap between this mass continuum and the central massive star of almost an order of magnitude in mass. The spatial distribution shows a compact structure around the centre of the cloud and no subclustering. The column density of the filamentary structure looks extremely similar for a  $\rho \propto r^{-1.5}$  run and the corresponding Bonnor-Ebert run with the same turbulent field, not reflecting the significantly different stellar properties.
- The  $\rho \propto r^{-2}$  density profile quickly leads to the formation of one single, central sink particle. The formation of other stars is strongly inhibited due to the rapid collapse compared to the time scale for filament formation. In this scenario further star formation can only be triggered by higher Mach numbers of the turbulence, if the ratio of turbulent energy to gravitational energy is increased to about unity.

The realisation of the turbulent velocity field has a major impact in the different morphology of the filamentary structure, their orientation, and shape.

- In the uniform density profile the random seed of the velocity determines the position of filaments from which stars form, and thus the location of the stellar subclusters. In addition, the number of sink particles generally depends on the random seed of the turbulence. Similar results are obtained for the BE profile.
- The  $\rho \propto r^{-1.5}$  profile, which marks the transition between one central massive sink particle and many low mass ones, is very sensitive to the

random seed. Different realisations may switch between one single star and several hundred. The formation time and location of the central, first sink particle, however, is not influenced by the random seed.

- The  $\rho \propto r^{-2}$  setups are not noticeably influenced by the turbulence. The short collapse time of the core compared to the turbulence crossing time does not allow for turbulence to strongly influence the evolution.

Our results suggest that massive stars predominantly form out of highly unstable cloud cores which are either strongly centrally concentrated or much more massive than modelled here, allowing stars to accrete from a larger mass reservoir. The density configuration with  $\rho \propto r^{-1.5}$  seems to be the most sensitive one concerning the number of collapsing fragments for different turbulent velocities.

Overall we conclude that the choice of the initial density profile is an extremely important, perhaps even the most important parameter determining the fragmentation behaviour of high-mass proto-stellar cores. Choosing an ideal simplified density profile strongly preordains the subsequent star cluster properties. This implies that the effects of different physical processes can only be reliably compared if the initial density profile is the same. In realistic star formation simulations, the formation of these cores needs to be taken into account and cores need to be formed self-consistently from larger clouds.

# Chapter 6

## Accretion behaviour

This chapter is published in parts in Girichidis et al. 2012, MNRAS 420, 613.

### 6.1 Introduction

The current paradigm of star formation suggests that most stars form in groups rather than in isolation (Lada et al., 2003). However, the fraction of stars that form in a bound clustered environment is still a matter of debate and varies between different models (Bressert et al., 2010). Whereas massive stars only seem to form in a dense environment, low-mass stars form in all observed star-forming regions. Numerical simulations suggest the formation of massive stars simultaneously with the formation of a cluster (Smith et al., 2009; Peters et al., 2010a,c,b). The spatial distribution of stars in the forming cluster shows a dependence on the stellar mass: more massive stars are located closer to the centre of the group, low-mass stars tend to populate the outer regions. Whether this mass segregation is primordial and therefore determined by the formation scenario or due to a dynamical relaxation process is still a matter of debate and might differ significantly among different clusters (see, e.g., the reviews by Mac Low and Klessen, 2004; McKee and Ostriker, 2007; Zinnecker and Yorke, 2007). Commonly found in observations as well as in numerical simulations is a universal distribution of masses (initial mass function, IMF, Scalo 1986, Scalo 1998, Kroupa 2001, Chabrier 2003, Bastian et al. 2010). Yet it is unclear, what is the influence of various physical processes and initial conditions on the initial mass distribution in star forming regions. Different physical processes like radiative feedback and magnetic fields are likely to have an impact on the collapse of gas clouds and the subsequent formation of a stellar cluster. Radiative feedback from

protostars can have two opposite effects. On the one hand, it heats the surrounding gas and thus contributes to stabilising the gas against collapse by increasing the Jeans mass. In case of massive protostars, the strong contribution in UV ionises the gas, forming HII regions. Hydrodynamic simulations of forming clusters show that radiative feedback tends to reduce the degree of fragmentation, but does not suppress it entirely (Krumholz et al., 2007; Bate, 2009a; Peters et al., 2010a,c,b). On the other hand, radiation pressure may indirectly enhance the formation of dense cores and the subsequent condensation into protostars. There are two different scenarios for this triggered star formation process. The first, "collect and collapse" (Elmegreen and Lada, 1977; Whitworth et al., 1994), appears where an expanding HII region pushes ambient gas into a shell, followed by fragmentation and collapse of the swept-up material. The other one is called "radiation driven implosion" (Bertoldi, 1989; Bertoldi and McKee, 1990) and depicts the UV-driven compression of a cloud core that is embedded into an HII region. Apart from radiation, magnetic fields have a noticeable impact on the evolution of a collapsing core. Magnetic pressure and tension forces counter the gravitational collapse and diminish fragmentation without completely inhibiting it (Ziegler, 2005; Banerjee and Pudritz, 2006; Price and Bate, 2007; Hennebelle and Teyssier, 2008; Hennebelle and Fromang, 2008; Hennebelle and Ciardi, 2009; Commerçon et al., 2010; Bürzle et al., 2011; Seifried et al., 2011a). Likewise, different initial conditions of the gas cloud strongly influence the star formation process, see chapter 5.

However, a clear universal formation picture of stellar systems in dense environments is still missing. Several formation and gas accretion processes have been proposed with different distribution scenarios of the gas onto the protostellar objects and different predictions concerning the more massive stars and the resulting IMF. The apparent similarity between the stellar mass function and the mass function of bound cores (Testi and Sargent, 1998) lead to the monolithic collapse model as a possible star formation scenario, in which every dense protostellar core collapses to a single star (McKee and Tan, 2002, 2003). However, this scenario lead to a time-scale problem, that can effectively destroy the similarity between IMF and the core mass function (Clark et al., 2007). Similar Problems hold for the proposal that massive stars form by collisions of low-mass stars (Zinnecker and Yorke, 2007), because the observed stellar densities are too low for this process to be important (Baumgardt and Klessen, 2011). As the formation process of a cluster in a dense environment is highly turbulent and dynamic, analytic estimates only give a vague idea of how accretion in this surroundings may work. With the help of simulations, two different cases have been proposed. In one scenario, which is called competitive accretion, the formation of the most massive stars is due

to a privileged position close to the centre of the stellar cluster, where the accretion rates are predicted to be highest throughout the simulation (Bonnell et al., 2001a,b). The other scenario is fragmentation induced starvation (Peters et al., 2010b), in which initially the central accretion rates are highest as well. However, subsequent fragmentation shows an increasing impact of the nascent protostars on the accretion behaviour of the central region, that gets starved of material by the surrounding companions.

In this study we investigate the accretion process in different initial density profiles and different turbulent velocity fields. Chapter 5 focused on the cloud structure and morphology. In this chapter we investigate the accretion processes in the formed clusters in detail.

## 6.2 Accretion behaviour – results

### 6.2.1 Overview

We follow the cloud collapse until 20% of the mass is accreted by sink particles. The simulation time, the number of formed protostars, and the mass of the most massive protostar are listed in table 6.1. A column density plot at the end of each simulation is shown in chapter 5 (figures 5.4 and 5.5).

The TH profile needs the longest time to form collapsing over-densities and confine  $20 M_{\odot}$  in sink particles. During this time of about 45 kyr, the turbulent motions can compress the gas in locally disconnected areas, leading to distinct subclusters of sink particles. The stronger mass concentration in the centre of the BE setups and the resulting shorter collapse and sink particle formation time suppresses the formation of disconnected subclusters in favour of one main central cluster. The corresponding PL15 profiles show very similar cloud structure to the BE runs, but significantly different stellar properties. Due to the much stronger gas concentration in the centre of the cloud, all PL15 setups form one sink particle very early in the simulation. This central sink particle accretes the surrounding gas at a high rate and can grow to a massive protostar before the turbulent motions eventually trigger the formation of collapsing filaments, which produce subsequent sink particles. Due to the stronger mass concentration, the clusters in the PL15 runs are more compact. In both cases (PL15 and BE), star formation can proceed from inside out. The central region, which is much denser in the PL15 case, forms collapsing filaments earlier. As time proceeds, the turbulence can continuously compress material in outer regions, and thus form sink particles at larger distances from the centre. The PL20 profile only forms one single sink particle due to the very strong mass concentration. It forms very early in

Table 6.1: List of the runs and their main simulation properties

$\rho$	mode and seed	name	$E_{\text{kin}}/ E_{\text{pot}} $	$t_{\text{sim}}$ [kyr]	$t_{\text{sim}}/t_{\text{ff}}$	$N_{\text{sink}}$	$M_{\text{mm}}$ [ $M_{\odot}$ ]
TH	mix-1	TH-m-1	0.075	48.01	0.96	311	0.86
TH	mix-2	TH-m-2	0.090	45.46	0.91	429	0.74
BE	com-1	BE-c-1	0.058	27.52	0.55	305	0.94
BE	com-2	BE-c-2	0.073	27.49	0.55	331	0.97
BE	mix-1	BE-m-1	0.053	30.05	0.60	195	1.42
BE	mix-2	BE-m-2	0.074	31.94	0.64	302	0.54
BE	sol-1	BE-s-1	0.055	30.93	0.62	234	1.14
BE	sol-2	BE-s-2	0.074	35.86	0.72	325	0.51
PL15	com-1	PL15-c-1	0.056	25.67	0.51	194	8.89
PL15	com-2	PL15-c-2	0.068	25.82	0.52	161	12.3
PL15	mix-1	PL15-m-1	0.050	23.77	0.48	1	20.0
PL15	mix-2	PL15-m-2	0.071	31.10	0.62	308	6.88
PL15	sol-1	PL15-s-1	0.053	24.85	0.50	1	20.0
PL15	sol-2	PL15-s-2	0.069	35.96	0.72	422	4.50
PL20	com-1	PL20-c-1	0.042	10.67	0.21	1	20.0

The table shows the setups with their turbulent modes, the random seed for the velocity field and their acronym used in further discussions. The ratio of kinetic to potential energy results from the applied scaling of the turbulent velocity and varies due to the random position of high- and low-velocity regions. The simulation time is given as total time in kyr and in units of the global free-fall time,  $t_{\text{sim}}/t_{\text{ff}}$ . The last two columns show the total number of sink particles  $N_{\text{sink}}$  and most massive particle  $M_{\text{mm}}$ , respectively.

the simulation and accretes gas at a constant rate of about  $2 \times 10^{-3} M_{\odot} \text{yr}^{-1}$ , extremely close to the analytical value of a highly unstable singular isothermal sphere (chapter 5). This results in a total simulation time of only 11 kyr, which is not enough for turbulent motions to form other filaments and further sink particles.

For the analysis of the accretion behaviour in a dense cluster environment, we only consider the setups with multiple sink particles. In order to understand the accretion process, especially during the early phases of a cluster, one has to distinguish between different star formation scenarios and the resulting cloud morphology around the accreting protostars. Here we discuss two extreme cases, an early disc-like structure around a central protostellar object and an initially filamentary structure that is not dominated by angular momentum. The first case is more pronounced in centrally concentrated density profiles where a net angular momentum with respect to the centre of mass is concentrated in a smaller and denser region. In contrast, initially flatter density structures allow the formation of very massive filaments and subsequently collapsing regions within these filaments out to larger distances from the centre of mass. The angular momentum with respect to the centre of mass may be of the same order as in the former case. However, due to the overall shallower density profile in the centre, the mass infall is slower and the timescale for the formation of a disc in the central region is larger than the timescale for turbulence to form filaments.

### 6.2.2 Limiting accretion effects

Before we discuss the two extreme cluster formation modes and their resulting accretion behaviour, we want to mention two effects that may limit the accretion in a cluster, namely the angular momentum barrier and accretion shielding by companion stars. In order to be accreted onto the surface of a protostar the gas needs to have a specific angular momentum that is lower than the Keplerian angular momentum with respect to the centre of the potential, given by  $j_{\text{Kepler}} = \sqrt{2GM_{\text{enc}}r}$ , where  $G$  is Newton's constant and  $M_{\text{enc}}$  is the enclosed mass within radius  $r$ . In a cluster and especially in disc-like environments, angular momentum can quickly be redistributed due to local instabilities, turbulent motions, and strong accretion streams. We analyse the angular momentum of the cloud with respect to the centre of the cluster and calculate the magnitude of the average angular momentum over thin spherical shells.

For the effects of accretion shielding by surrounding companion stars, we estimate how much of the infalling gas can be accreted by secondary cluster members before reaching the centre of the cluster and becoming accreted

by the primary cluster stars. Assuming a virialised cluster, one can derive the shielded fraction  $S$  using Bondi-Hoyle accretion (Bondi and Hoyle, 1944; Bondi, 1952). The Bondi-Hoyle radius can be written as

$$R_{\text{BH}} = \frac{2GM}{c_s^2 + v^2}, \quad (6.1)$$

where  $M$  is the mass of the accreting star,  $c_s$  is the speed of sound, and  $v$  is the relative velocity between the star and the immediate surrounding gas. In our analysis we investigate the gas within a radius  $r_{\text{surr}} = 100 \text{ AU}$  around each protostar. An application of the Bondi-Hoyle analysis to the accretion in clusters and the cluster dynamics can also be found in Bonnell et al. (2001a). The total shielded fraction of the gas falling onto a cluster with  $N$  stars, an average stellar mass  $M$ , and a cluster radius  $R_{\text{Cl}}$  can be estimated by the fraction of the shielded surface area

$$S = \frac{4\pi N R_{\text{BH}}^2}{4\pi R_{\text{Cl}}^2} = \frac{N}{R_{\text{Cl}}^2} \left( \frac{2GM}{c_s^2 + v^2} \right)^2. \quad (6.2)$$

In the case of high relative velocities between the stars and the gas, the  $c_s^2$  term can be neglected. Replacing  $v$  with the global virial velocity  $v_{\text{glob}}$  of the cluster,

$$v_{\text{glob}} = \left( \frac{GM_{\text{Cl}}}{R_{\text{Cl}}} \right)^{1/2} = \left( \frac{G N M}{R_{\text{Cl}}} \right)^{1/2}, \quad (6.3)$$

with  $M_{\text{Cl}} = NM$  being the cluster mass (assuming equal-mass stars for simplicity), yields

$$S \propto \frac{1}{N}. \quad (6.4)$$

In that case, the shielding is less efficient the more stellar objects there are in the cluster. Although this might sound counterintuitive, the assumption of virial velocities for the stars explains the strongly reduced Bondi-Hoyle radius with increasing number  $N$ . In the other extreme case of no relative velocity of the star to the surrounding gas, the shielding becomes

$$S = \frac{NR_{\text{BH}}^2}{R_{\text{Cl}}^2} \propto \frac{NM^2}{c_s^2 R_{\text{Cl}}}, \quad (6.5)$$

linearly increasing with  $N$ . In our simulations we observe stars forming inside filaments with initially no or very small relative velocity between them and the surrounding gas. The closer to the centre the stars form or migrate during the collapse of the cloud, the more they decouple dynamically from the gas forming a strongly interacting  $N$ -body system with a gaseous background.

We therefore expect the first case ( $S \propto 1/N$ ) to be more important in the central region of the cluster, whereas the latter effect ( $S \propto N$ ) is expected to be dominant in the outskirts of the cluster and in the filaments. An analysis of the simulation is shown below, separately for the two extreme formation modes.

### 6.2.3 Disc-like accretion mode

In the first case we discuss the accretion scenario in a disc-like structure, concentrating on simulation PL15-m-2 as an example. A global accretion history for all protostars is shown in figure 6.1, where we plot the total number of sink particles as well as the accretion rate and the total mass confined in sink particles. The middle panel shows the total accretion rate onto all sink particles  $\dot{M}_{\text{tot}}$ , the average accretion rate per protostar  $\langle \dot{M} \rangle = \dot{M}_{\text{tot}}(t)/N_{\text{sink}}(t)$ , as well as the accretion rate of the most massive protostar  $\dot{M}_{\text{mm}}$ , which happens to be the protostar located close to the centre of mass of the gas cloud and the cluster.

During the first 7 kyr, the turbulent motions do not have enough time to significantly disturb the cloud. The anisotropies formed so far can be neglected and the assumption of a spherically symmetric collapse holds. The first sink particle forms in the centre of the cloud and accretes material in nearly free-fall. The initial density profile results in a linearly increasing accretion rate (see also Klessen and Burkert, 2000; Schmeja and Klessen, 2004). At around  $t \sim 7$  kyr, the turbulent motions form a central filament whose colliding arms concentrate angular momentum in the gas around the central protostar and form a disc-like object. Thus, the spherically symmetric free-fall approximation does not hold any longer. For the time between  $7 \text{ kyr} \lesssim t \lesssim 14 \text{ kyr}$  the disc is stable and grows in mass and size by accretion from the filamentary arms. During that time, the angular momentum barrier prevents the accretion rate to increase further, resulting in a constant value of  $\dot{M} \approx 5 \times 10^{-4} M_{\odot} \text{ yr}^{-1}$ . At  $t \gtrsim 14$  kyr, the disc becomes unstable, forms spiral arms and fragments into multiple objects. The column density plots in figure 6.2 show a time sequence of this short period. After the formation of other protostars, the accretion rate onto the central sink particle drops dramatically, while the total accretion rate onto all sink particles increases. The gravitational interactions between the protostars in combination with further infalling gas from the filament disturb the initially disc-like structure and quickly destroy the disc. As a result, a more or less spherically symmetric cluster builds up. The average accretion rate  $\langle \dot{M} \rangle$  decreases by more than an order of magnitude after the formation of secondary stars. The fact that  $\dot{M}_{\text{mm}}$  is on average several orders of magnitude lower than  $\langle \dot{M} \rangle$  indicates that

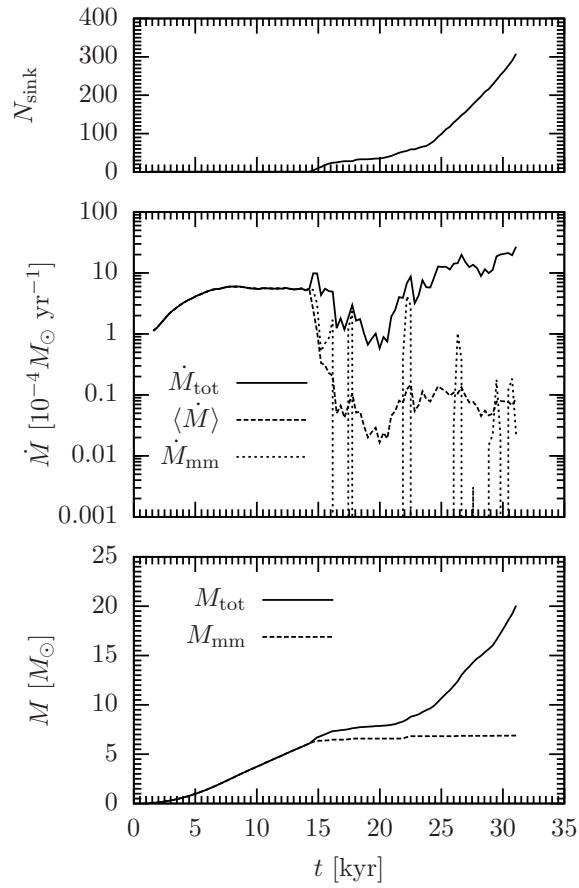


Figure 6.1: Mass evolution of the most massive, central sink particle in setup PL15-m-2. The upper panel shows the number of sink particles in the setup, the middle panel plots the accretion rate onto the most massive sink particle ( $\dot{M}_{\text{mm}}$ ) and onto all sink particles ( $\dot{M}_{\text{tot}}$ ). The bottom panel shows the mass.

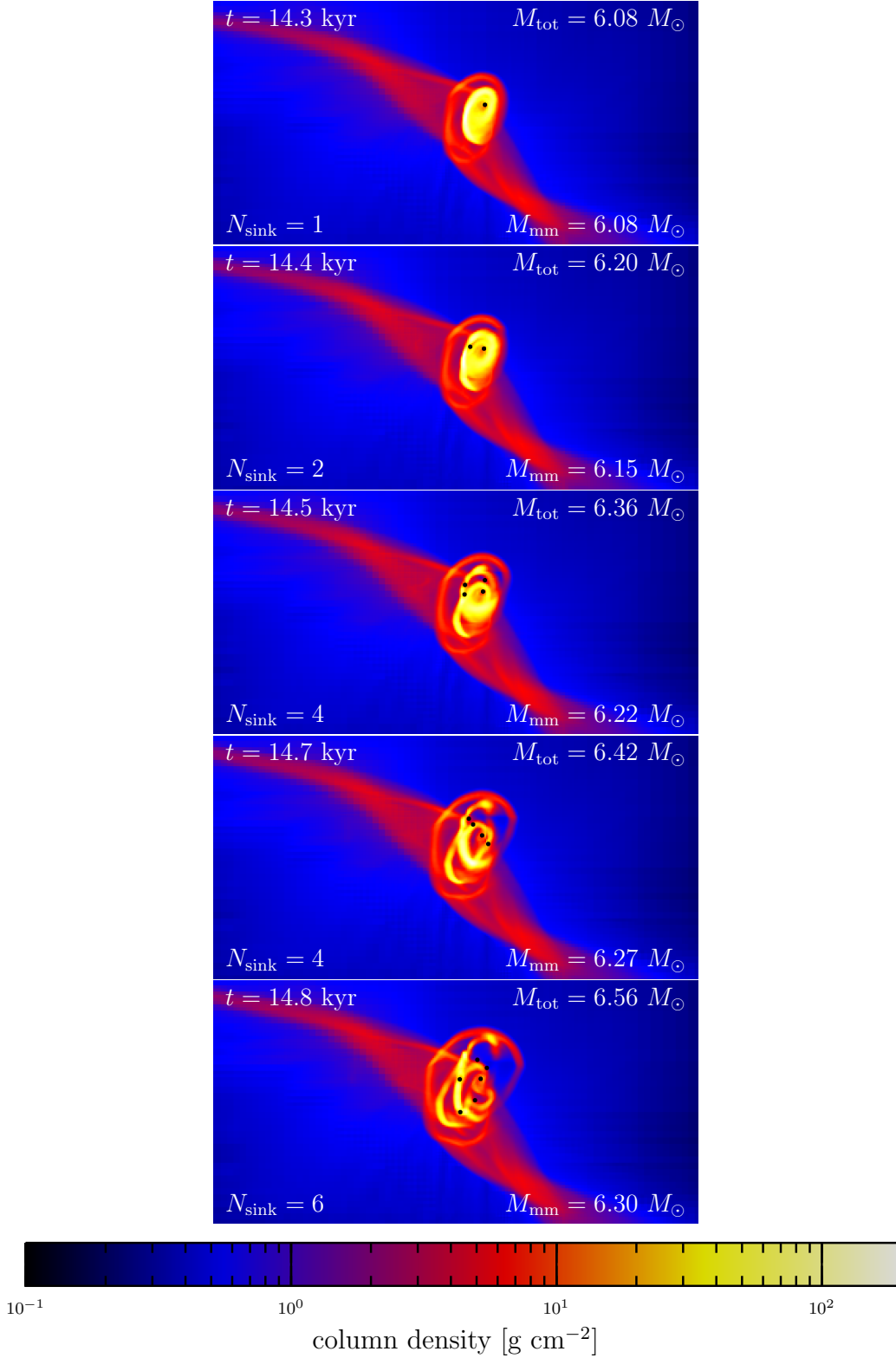


Figure 6.2: Column density plots of the central region with the disc around the most massive sink particle (subscript mm) in run PL15-m-2. The formation of secondary sink particles indicates the fragmentation into several objects, which quickly leads to the dissolution of the disc. Spiral arms develop and redirect the gas away from the central protostar, which gets starved of material. The images span roughly  $4000 \times 2000$  AU.

the available gas is not equally shared among the protostars but efficiently shielded from reaching the central region. This indicates that the process of fragmentation induced starvation, first described by Peters et al. (2010b) for disc-like structures, also works for more complex geometries. Small amounts of gas that can penetrate through the entire cluster and reach the centre can be seen as episodic accretion spikes.

We emphasise the influence of different geometrical shapes of the cluster. Whereas in Peters et al. (2010b) the angular momentum vector was well defined and the starvation effect was complete, the turbulent motions in our simulation allow for some accretion channels. The starvation effect can be understood by plotting the gas density around the central protostar (figure 6.3) and the accretion rate onto spherical shells around the central protostar (figure 6.4), including the net accretion onto gas shells as well as the accretion onto other sink particles. The gas density within a radius of  $r \sim 300$  AU around the central protostar first increases due to the global infall, forming a dense disc. Once other companions have formed, it decreases continuously, which starves the central object. The accretion rate as a function of radius supports this starvation picture. Before subsequent sink particles form, the accretion rate is roughly constant ( $\dot{M} \approx 5 \times 10^{-4} M_{\odot} \text{yr}^{-1}$ ). Immediately after the disc fragments, the accretion front moves outwards to larger radii, resulting in significantly smaller values around the central protostar. As the protostars in the cluster as well as the gas undergo strong dynamical interactions, the net accretion rate exhibits local fluctuations. The curves for  $t \geq 15.4$  kyr are therefore averaged over several thousand years. Phases that include an accretion spike (see second panel in figure 6.2) lead to positive values at  $r_{\text{sink}}$ , at other times the net accretion is negative, because some gas that is not bound to a protostar can enter and exit a spherical shell without being accreted onto any protostar. During the entire simulation time, but in particular after the formation of subsequent protostars, the specific angular momentum in the disc-like object (see figure 6.2) as well as in the later formed spherically symmetric cluster is lower than the Keplerian value for all radii (figure 6.5). Initially the ratio is close to unity indicating that gas motion in the disc-like object is affected by the angular momentum. This also leads to a deviation from the free-fall accretion rate for the simulation time  $t \in (7 - 14)$  kyr, which would further increase in case of no angular momentum. After the disc becomes unstable and further protostars form, the angular momentum is transferred efficiently resulting in a decreasing ratio. The low central accretion rates can therefore not be explained by an angular momentum barrier that inhibits the gas flow to smaller radii. A plot of the angular momentum of the gas as a function of enclosed mass for different times is shown in the appendix (figure B.1).

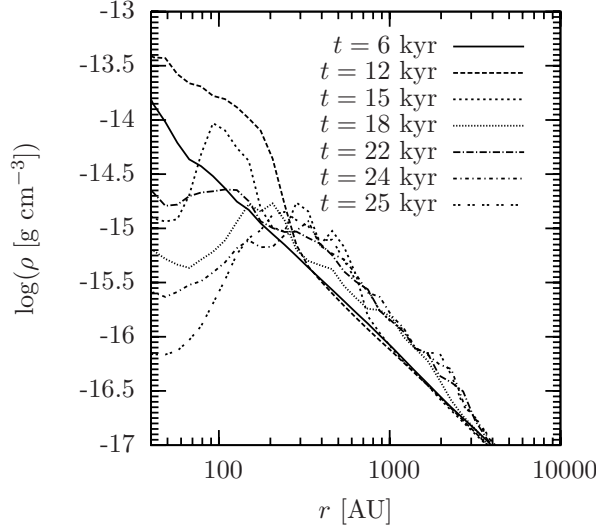


Figure 6.3: Radial density profile around the central protostar in run PL15-m-2. The gas density first increases in the immediate proximity of the protostar due to the global infall. At later times, the surrounding companions branch off most of the gas, leading to a continuous decrease of the central gas density.

In addition we analyse which accretion shielding is dominant in different regions of the cloud. In figure 6.6 we plot the relative velocity of the protostars to the surrounding gas within a radius of  $r_{\text{surr}} = 100 \text{ AU} = 2.5 r_{\text{accr}}$  around the protostar. For all times the velocities range from super-virial velocities in the centre of the cloud down to small relative velocities of the order of the speed of sound in the outskirts, indicating that the accretion shielding in the centre follows equation (6.4), whereas in the outskirts, it is better described by equation (6.5). As expected, both cases of the accretion shielding effects apply. In the central region, the shielding therefore becomes less efficient with an increasing number of protostars. In contrast, the protostars in the outskirts of the cluster are much more efficient in shielding the accretion flow. In addition to the larger shielded fraction, the shielding at larger distances from the centre becomes even more efficient, because the protostars form along the dense filaments that channel the accretion streams. The area of the strongest accretion flow then coincides with the position of the protostars that move with the gas flow. As a result, the total gas mass in the centre of the cluster is very small. Figure 6.7 shows the total enclosed mass (gas and protostars) as well as the enclosed gas mass as a function of radius. The gas mass is only a small fraction of the total mass and decreases

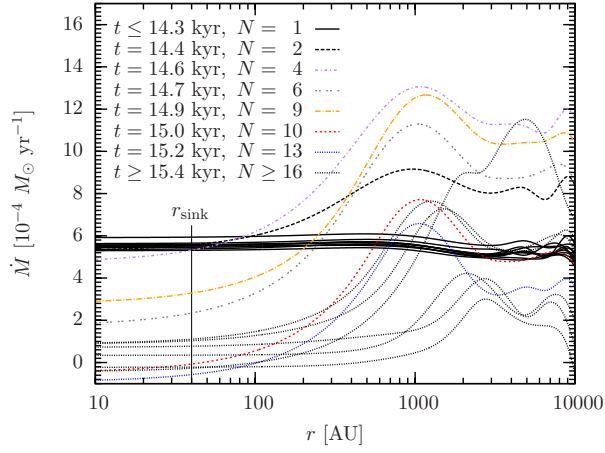


Figure 6.4: Accretion rate onto spherical shells around the central protostar in the cluster of setup PL15-m-2. The sink particle's accretion radius is indicated by  $r_{\text{sink}}$ . The plot shows several curves for  $t \leq 14.3$  kyr, where there is only one sink particle ( $N = 1$ ). Before the formation of secondary protostars, the accretion rate in the centre is roughly constant. Immediately after surrounding companions have formed, the accretion front moves to larger radii and starves the central object. At later simulation times ( $t \geq 15.4$  kyr) the accretion rate varies, but stays very small for all curves.

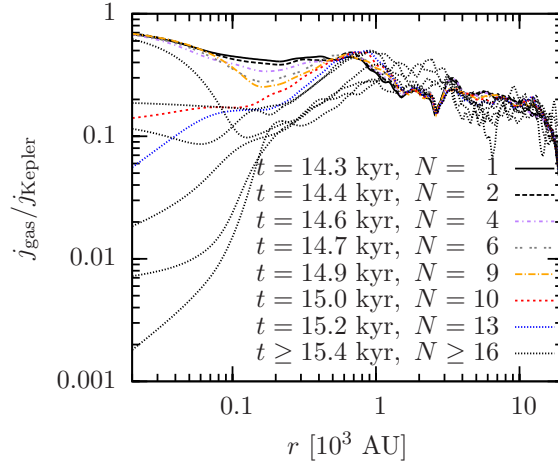


Figure 6.5: Ratio of specific angular momentum of the gas to the Keplerian value with respect to the centre of the cluster. For all times and all radii the ratio is smaller than unity, indicating that the gas is not prevented from moving inwards by angular momentum. After the formation of subsequent protostars the efficient angular momentum transport even lowers the ratio close to the centre.

strongly in the centre after the formation of multiple objects. Therefore the central accretion rate is low in spite of a less efficient accretion shielding. The gas is already accreted further out before it reaches the less shielded region.

Depending on the definition of the centre of the cluster (position of the most massive protostar, centre of mass of the protostars, centre of mass including protostars and gas), the most massive protostar is not located exactly at the centre of the cluster. In addition, the interaction with other protostars leads to small displacements during the simulation. Neglecting the fact, that only little mass is left in the centre of the cluster, it could be possible that the low accretion rates onto the protostars in the central region arise from these displacements, if the protostar escapes from a collimated accretion stream. In order to verify, that the central stars are really shielded, we need to analyse the motions of the central stars relative to the surrounding gas. We calculate the relative velocity dispersion of the gas with respect to the most massive protostar within a radius of 1000 AU around it, covering the vast majority of the entire cluster. We find velocity dispersions ranging from  $\sigma/c_s = 5.4 - 10.6$ , resulting in a total time for the gas to reach the central star of 1.7 – 3.3 kyr after entering the sphere of 1000 AU. This time is only 5 – 10% of the simulated time. Given the low angular momentum in the centre of the cluster (figure 6.5), the available gas has enough time to

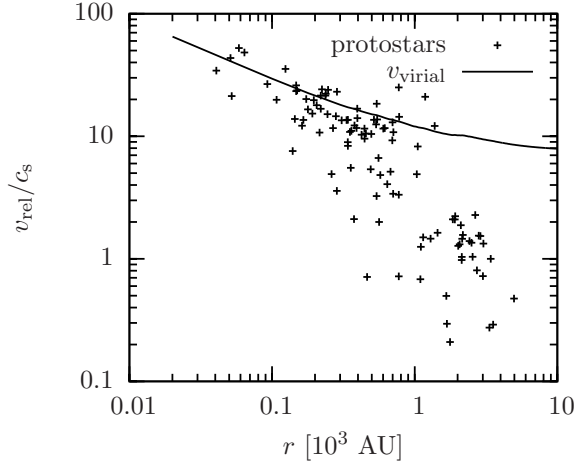


Figure 6.6: Relative velocity between the protostars and the surrounding gas within a radius of  $r_{\text{surr}} = 100$  AU around every protostar as a function of distance from the centre of the cluster  $r$  for one snapshot at  $t = 25$  kyr. The plots for different times look very similar. The relative velocity decreases for larger radii ranging from super-virial velocities in the centre down to sub-virial velocities of the order of the sound speed at large distances from the centre.

reach the most massive star regardless of displacements.

#### 6.2.4 Filamentary accretion mode

If the formation of a cluster is not dominated by a disc-like structure but by filaments, the formation scenario of protostars is different (see, e.g., [Banerjee and Pudritz, 2006](#)). The initial density profiles with a flat core need more time to form Jeans-unstable regions. During this time, the turbulence can form filaments in which protostellar condensations form next to each other along the densest part of the filament. The column density plots in figure 6.8 show a time evolution of the filamentary collapse. During their formation, the protostars inherit the motion of the parental filament and move with the gas flow. With increasing proximity to other protostars, their attraction as an  $N$ -body system becomes stronger than the force between protostars and gas. The protostars then dynamically decouple from the filaments and accumulate in the central region in a more spherically-symmetric configuration rather than in a flat or string-like structure. The initial filaments get dispersed in the central region, because the  $N$ -body system efficiently stirs the gas. The formation of the first protostars is shown in the column density plots in

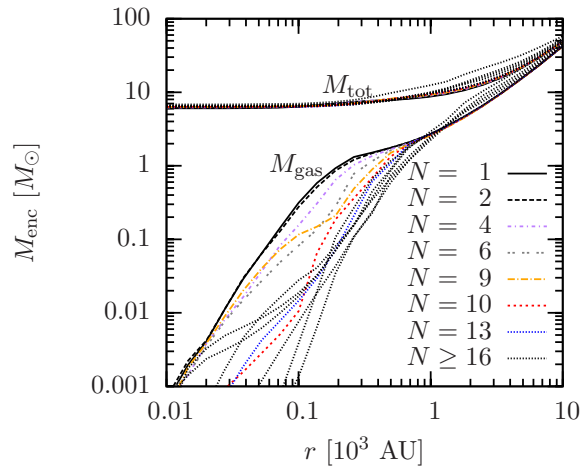


Figure 6.7: Enclosed masses as a function of radius for the total mass (gas and protostars) and the gas mass. The gas is only a small fraction of the total mass in the centre and decreases strongly after the formation of multiple protostars.

figure 6.8. The mass accretion in this formation mode is plotted in figure 6.9. Note that figure 6.8 only covers a small time range at the beginning of the cluster formation, whereas figure 6.9 covers the entire simulation time after the formation of sink particles.

During the first  $\sim 6$  kyr after the first protostar has formed, the accretion rate onto the most massive protostar stays roughly constant. About 100 sink particles form along the main filaments within this time. Initially, most protostars can accrete gas from both sides of the filamentary arm, resulting in a high accretion rate. Despite the fact that the total accretion rate increases by a factor of  $\sim 10$ , the average accretion rate gradually drops by about one order of magnitude, because this mass flow is distributed between  $\sim 100$  protostars. This is in contrast to the setup PL15-m-2, where the global accretion rate suddenly drops. As the setup is less concentrated, the Keplerian specific angular momentum of the gas with respect to the centre of the nascent cluster is significantly lower than in the PL15-m-2 case. Nonetheless, the ratio  $j_{\text{gas}}/j_{\text{Kepler}}$  (figure 6.5) is even smaller than in the disc-like accretion mode (figure 6.10), indicating that the gas motion is not restricted by the angular momentum barrier. A plot of the angular momentum of the gas as a function of enclosed mass for different times is shown in the appendix (figure B.2).

The lower central mass concentration allows for extended filaments and the formation of protostars at larger distances from the centre of the cluster. The relative velocity between the protostars and the surrounding gas

(figure 6.11) drops significantly for larger radii, but is closer to the virial velocity for this setup in comparison to the disc-like structure. The global cluster dynamics should therefore correspond to the shielding relation in equation (6.4). However, the relative velocities in the outskirts of the cluster are of the order of the speed of sound which marks the transition between the two extreme shielding cases. In addition, the gas distribution in the filamentary structure strongly deviates from spherical symmetry. The protostars in the outskirts of the nascent cluster move along the densest part of the filament and can therefore efficiently accrete a significant fraction of the filament mass before they dynamically decouple from the filament. As a consequence, the accretion shielding is more efficient, the more protostars form along the filaments. Similar to the disc-like case, the gas content in comparison to the total mass is very low in the central region of the cluster (figure 6.12). Overall, the more protostars accumulate in the central region forming a cluster, the more efficient is the accretion shielding effect. In the case of the most massive sink particle in BE-m-2, accretion is entirely shut off for  $t \gtrsim 27$  kyr.

### 6.2.5 Mass evolution of all runs

In general, the formation scenario of protostars in dense clusters will be a mixture of star formation in a disc and filaments, where the above examples are extremes. However, in all simulated cases, the formation of multiple protostars finally leads to a shielding effect in the formed cluster. Figure 6.13 shows the mass evolution of the most massive protostars of all clusters combined, figures 6.14–6.16 show the mass evolution of the 20 most massive sink particles for each simulations. In the case of an initially uniform density (TH, figure 6.14), the two main subclusters for each run (TH-m-1 and TH-m-2) were evaluated separately. The corresponding accretion plots for the most massive sink particle are very similar to the ones shown in figures 6.1 and 6.9. Despite different formation scenarios, all setups show very similar structures and emphasise the starvation effect on the most massive protostars, which are located preferentially closer to the centre of the cluster than low-mass companions.

Depending on the formation time, the formation location and the accretion rate over time, the mass of the most massive protostar in relation to the mass of the other objects or the entire ensemble of protostars in the cluster might differ for different setups and initial conditions. Figure 6.17 shows the mass of the most massive sink particle,  $M_{\text{mm}}$ , in relation to the total mass confined in sink particles,  $M_{\text{tot}}$ . The setups with strong initial mass concentrations (PL15) form an early protostar that stays the only sink particle for

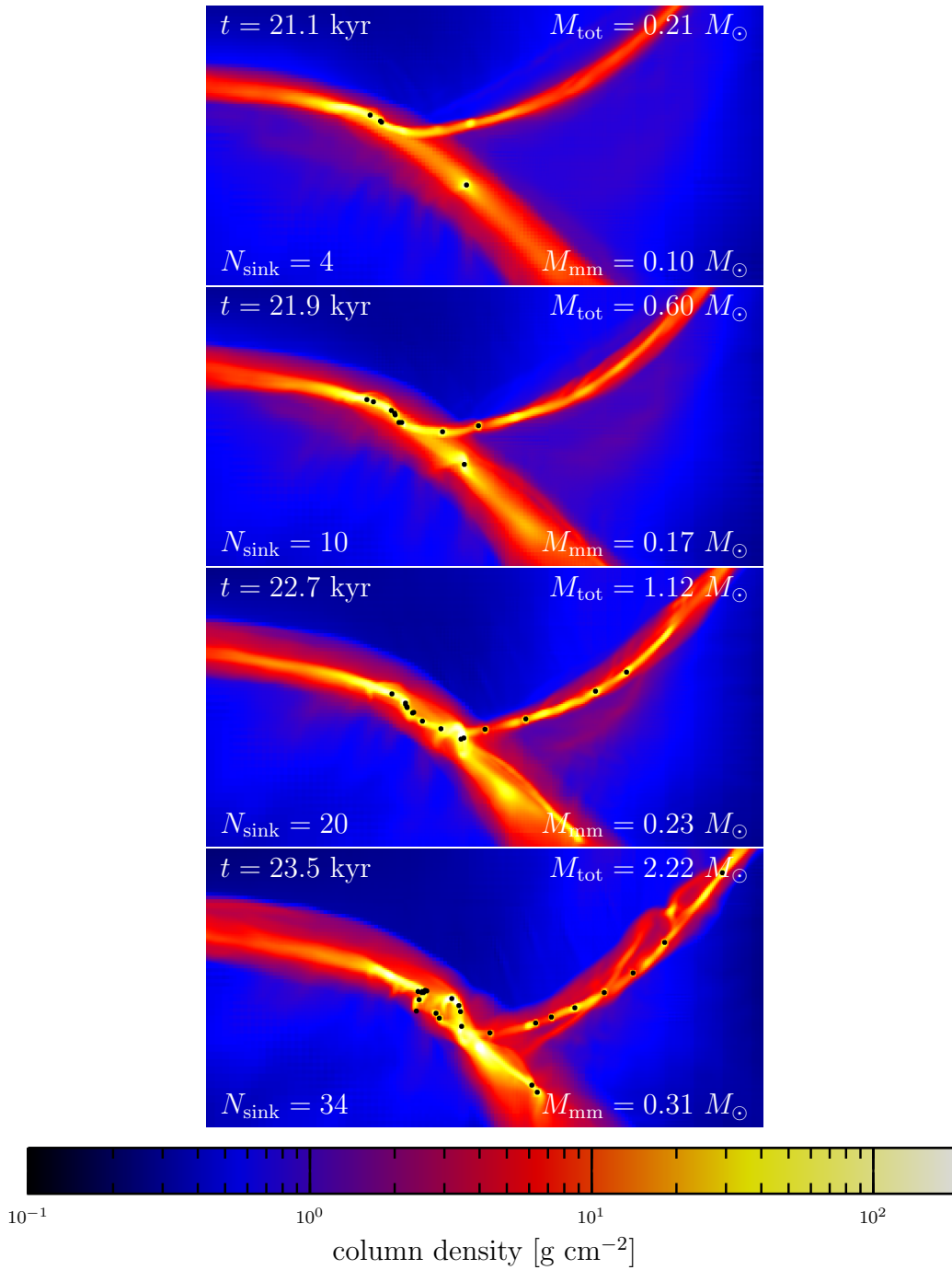


Figure 6.8: Column density plots of the central filament in BE-m-2. The sink particles form in the filament and remain there while converging to the centre of the cluster. The closer the protostars approach each other, the stronger decoupled is their motion from the motion of the filament. The images span roughly  $4000 \times 2000$  AU.

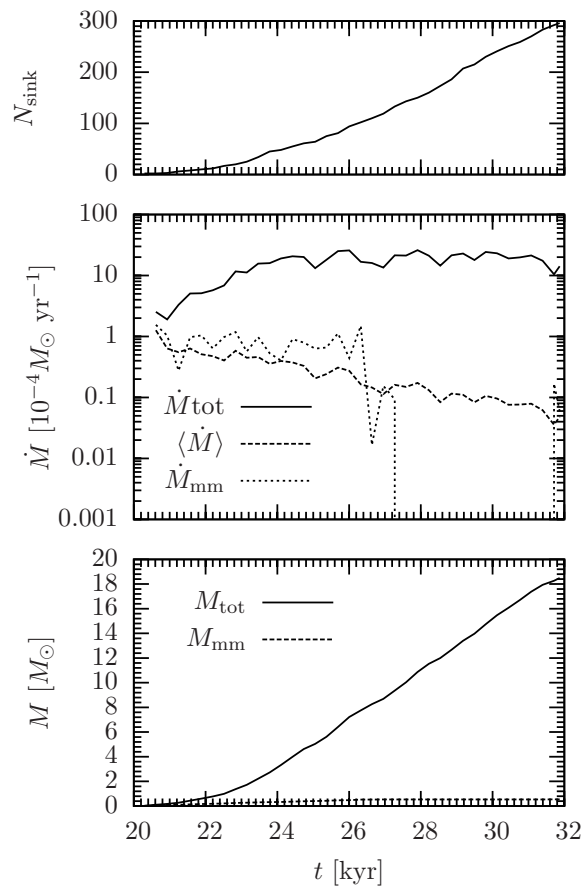


Figure 6.9: Same as figure 6.1 but for the simulation BE-m-2 (filamentary accretion).

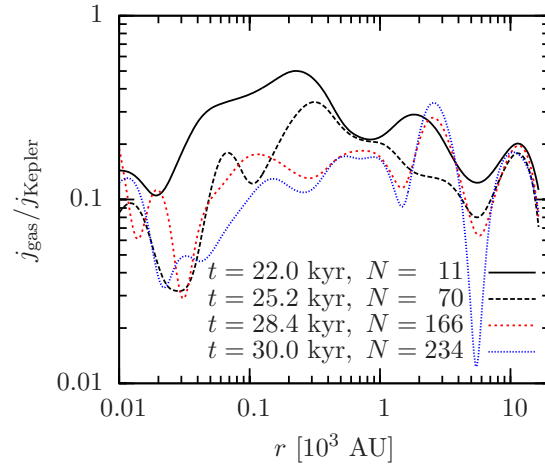


Figure 6.10: Same as figure 6.5 but for setup BE-m-2 (filamentary accretion).

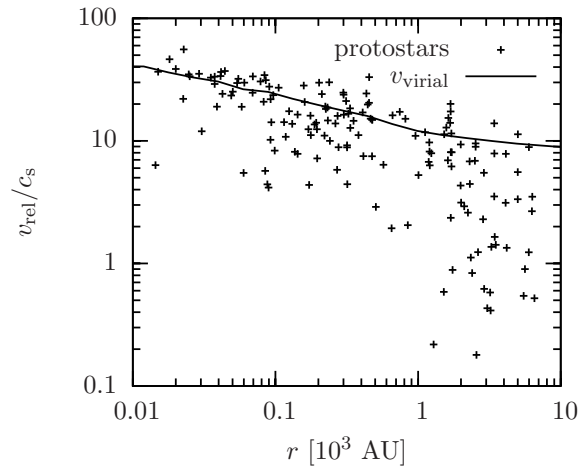


Figure 6.11: Same as figure 6.6 but for setup BE-m-2 (filamentary accretion) at  $t = 28$  kyr.

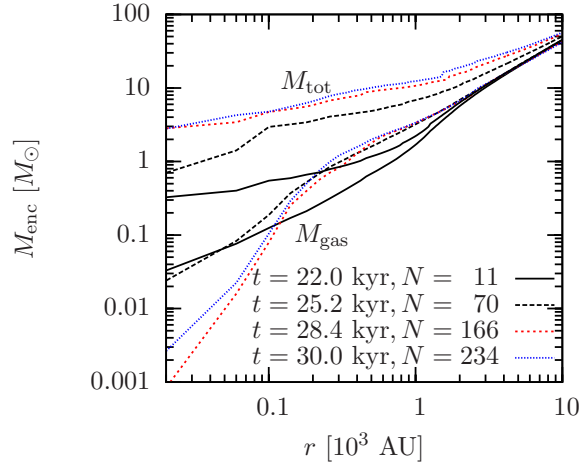


Figure 6.12: Same as figure 6.7 but for BE-m-2 (filamentary accretion).

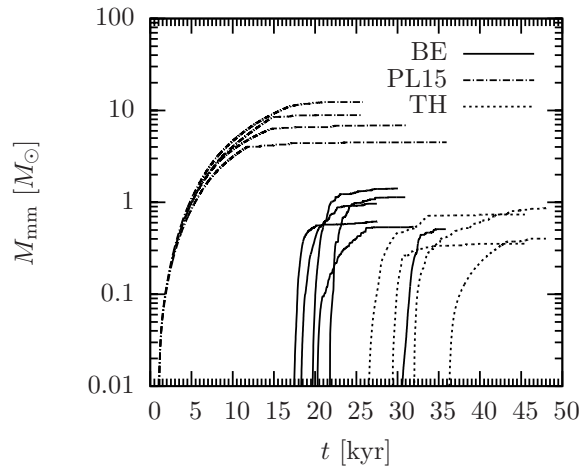


Figure 6.13: Mass evolution of the most massive protostar for all simulated clusters. In all cases the mass curves flatten significantly at the late-time evolution of the simulation. For a detailed mass analysis of each setup, see figures 6.14–6.16.

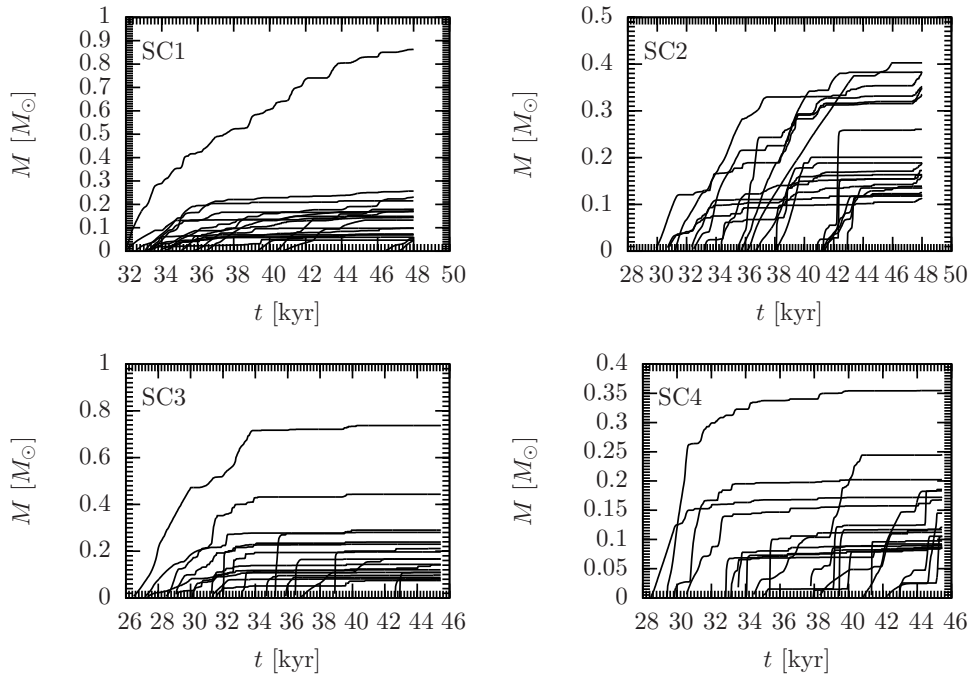


Figure 6.14: Mass evolution of each sink particle for the four main subclusters in the TH setups. The upper two plots correspond to the biggest subclusters (SC1, SC2) in run TH-m-1. The lower plots (SC3, SC4) are the main subclusters in TH-m-2, respectively. The most massive particles are located closer to the centre of mass and thus experience an efficient starvation effect, which can be seen in the low increase in mass.

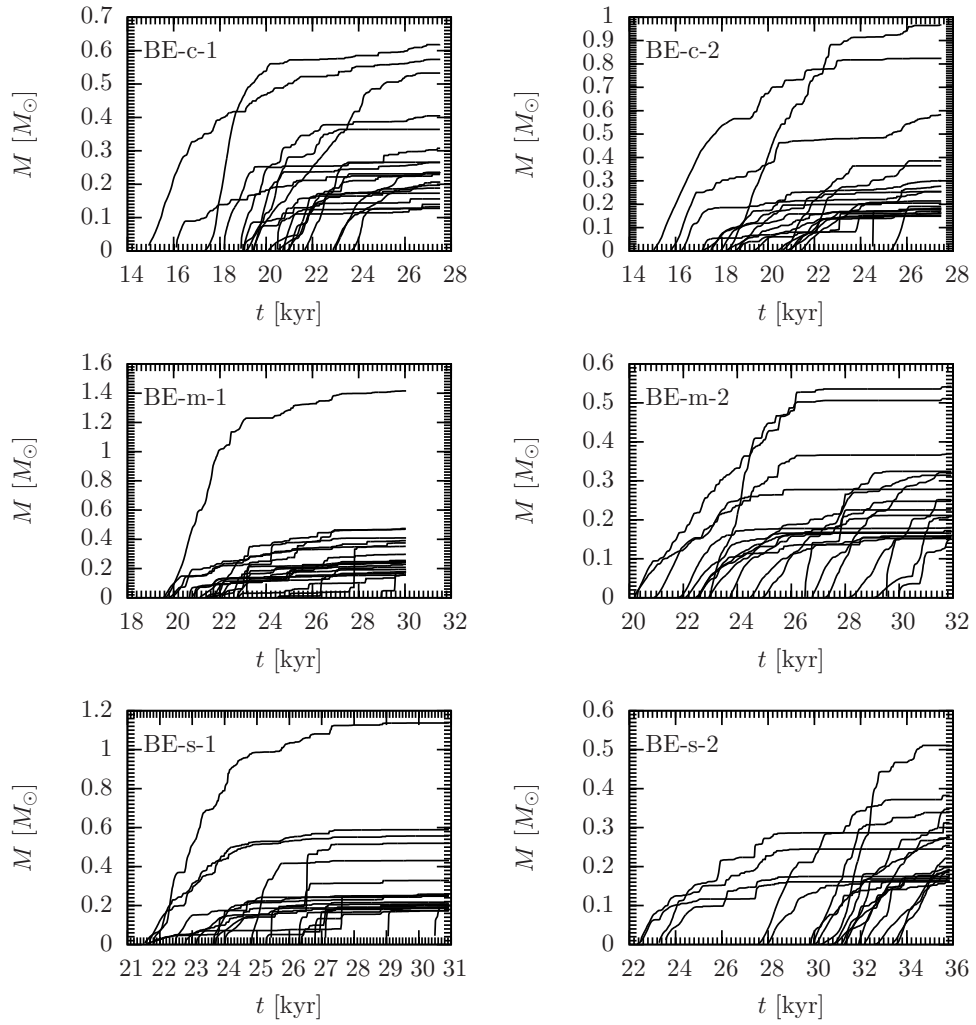


Figure 6.15: Same as figure 6.14 but for the BE setups.

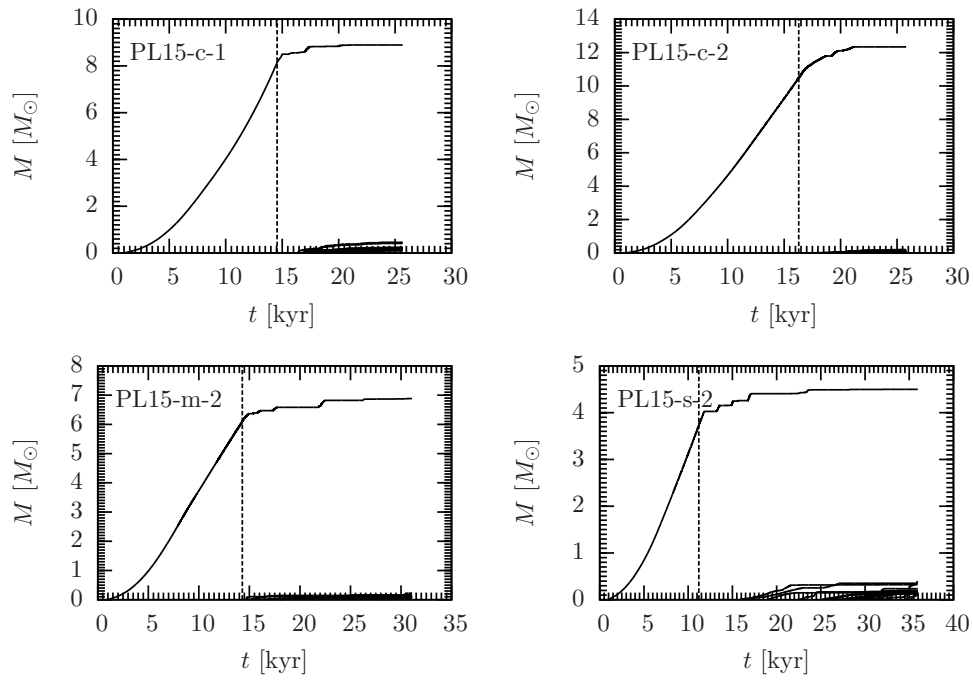


Figure 6.16: Same as figure 6.14 but for the PL15 setups. Note that the masses are plotted in linear scale in order to better see the starvation effect, which starts after the formation of the second sink particle (vertical lines).

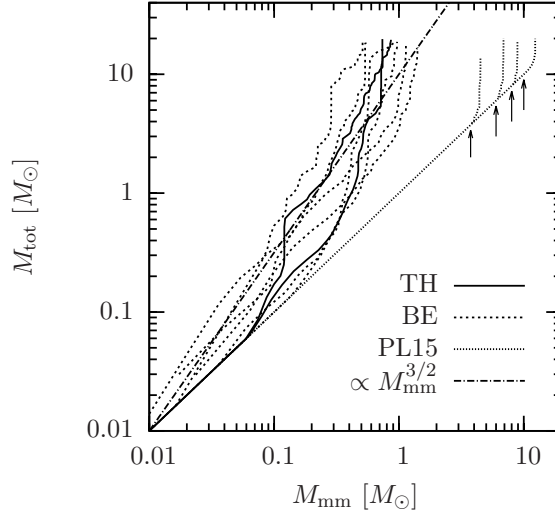


Figure 6.17: Relation of the most massive star in the cluster to the total cluster mass. Note that in the PL15 case, secondary sink particles form very late in the simulation (indicated by the arrows), which explains the large range in mass with a slope of unity.

a significant part of the total simulation. After the formation of subsequent protostars, the mass of the central massive one stays almost constant due to the starvation effect. The mass relations of all PL15 setups therefore bend upwards. In the setups with initially flat density distribution, the mass of the most massive protostar roughly follows a relation  $M_{\text{mm}} \propto M_{\text{tot}}^{2/3}$ , but with remarkable scatter. The fact that the difference in mass between the most massive and the other stars is much less, leads to a stronger impact of  $N$ -body interactions on the location of the most massive protostar within the cluster. While the very massive central stars in the PL15 runs remain within the accretion shielded area of the cluster, the most massive stars in the BE runs and in the subclusters of the TH setups follow larger orbits where they leave and reenter the shielded area alternately. Whenever the most massive sink particle gains further mass, either by leaving the accretion shielded area or experiencing episodic accretion, the curve flattens. Entering the accretion shielded volume of the cluster, the most massive object gets starved of material and its accretion stops. As the whole cluster continues to grow, the curves bend up.

## 6.3 Accretion behaviour – discussion

Two accretion models are widely discussed in the literature: 1) the monolithic collapse and 2) competitive accretion and fragmentation induced starvation, where mutual dynamical interactions of accreting protostars play a key role in shaping the final mass distribution. The monolithic collapse model is based on the apparent similarity of the core mass function (Motte et al., 1998; Johnstone et al., 2000, 2006; Lada et al., 2008) and the stellar initial mass function (Kroupa, 2002; Chabrier, 2003). It relies on a direct mapping of cores to stars with a constant efficiency factor for the collapse of a single core into a single stars or at most a binary system. A major caveat in this model is the collapse of very massive cores. The amount of turbulent energy deposited in these cores is likely to cause the core to fragment into many objects. This chapter and especially chapter 5 demonstrate that only strongly concentrated density profiles may prevent further fragmentation in an isothermal environment. Radiation feedback tends to reduce the degree of fragmentation, but still can not prevent the collapsing core from fragmenting into many protostars (Krumholz et al., 2007; Bate, 2009a; Peters et al., 2010a). Likewise magnetic fields support the agglomeration of larger masses. However, even magnetised cores fragment into smaller objects (Ziegler, 2005; Hennebelle and Teyssier, 2008; Banerjee et al., 2009; Bürzle et al., 2011; Peters et al., 2011; Hennebelle et al., 2011; Seifried et al., 2011a). The degree of fragmentation and the resulting dynamical accretion in our simulated dense clusters significantly differ from the monolithic collapse model. The fragmentation is suppressed only for highly concentrated density profiles and weak initial turbulent motions (chapter 5). Apart from the fragmentation of the gas, the assumption of a monolithic collapse leads to a time-scale problem that is likely to destroy the apparent similarity of the IMF and the core mass function (Clark et al., 2007; Smith et al., 2008).

In competitive accretion (Bonnell et al., 2001a,b; Bonnell and Bate, 2002; Bate and Bonnell, 2005), the cloud first fragments down to objects with masses close to the opacity limit, which then start to accrete and build up the initial mass function. The accretion rates are mainly determined by the position of the protostar in the cluster. The gravitational potential funnels gas to the centre of the cluster, leading to higher accretion rates onto the most central objects, located close to the centre of the potential well. Thus, central protostars can grow to the most massive ones. The more massive a star, the faster it can dynamically migrate to the centre of mass, continuously ensuring a gravitationally privileged position. Assuming a negligible impact of the surrounding protostars on the global mass accretion, the most massive stars continue to accrete at a higher accretion rate. As soon as the impact

of further fragmentation influences the global accretion process, the central accretion rates may vary significantly, as it is described in the fragmentation induced starvation model. In competitive accretion, the mass of the most massive star is related to the total stellar mass as  $M_{\text{mm}} \propto M_{\text{tot}}^{2/3}$  (Bonnell et al., 2004). This relation was assumed to be an indicator for this accretion model (Krumholz and Bonnell, 2009) and is in agreement with observations (Weidner and Kroupa, 2006; Weidner et al., 2010). However, as we discuss below, fragmentation induced starvation can lead to the same behaviour. This relation is therefore not a unique signpost of competitive accretion.

Intermediate scenarios between the two extreme models are also reported (e.g. Peretto et al., 2006; Wang et al., 2010), in which the formation model depends on the mass of the star. Low-mass objects form via local collapse, while massive protostars and their dense proximity accumulate gas from the global environment.

Recent numerical models of star cluster formation indicate that the competitive accretion model in its original flavour (Klessen and Burkert, 2000, 2001; Bonnell et al., 2001a,b; Bonnell and Bate, 2002; Bate and Bonnell, 2005) needs reinterpretation. The suggestion of higher central accretion rates due to the gravitationally privileged position changes once the formed fragments around the centre of the collapsing area have a significant impact on the global gas accretion process. The infalling gas may be branched off and either be accreted onto these objects or dynamically redirected before reaching the centre of the cluster. Peters et al. (2010b) found a strong impact of subsequent fragmentation on the accretion flow in a  $1000 M_{\odot}$  rotating core including radiative feedback, but without initial turbulence. The accretion rate onto the central object drops significantly. Instead of growing further, the central protostar is starved of material. Despite this significantly different accretion behaviour, they also found masses in the simulation in good agreement with the relation  $M_{\text{mm}} \propto M_{\text{tot}}^{2/3}$ , ruling out this relation as evidence for competitive accretion. As they do not apply turbulent motions, but only solid body rotation to the initial cloud, they focus on the starvation effect in disc-like conditions rather than in filamentary structures. Due to the missing turbulence, their disc-like structure does not evolve into a volume-filling cluster, but remains a flattened structure. A disc provides a smaller effective area through which gas can flow towards the centre. In a cluster with random protostellar trajectories, the effective accretion area is much larger. Therefore, from simple geometrical arguments, it is much more difficult to shield the central area from accretion flows.

However, we find that protostars in the outer region of the cluster form along the densest part of extended filaments, which allows them to accrete much more mass than in an idealised spherically symmetric setup. In ad-

dition to that, we observe significantly smaller relative velocities between the protostars and the immediate surrounding gas for protostars at larger distances from the centre of the cluster. This increases their geometrical accretion cross section, expressed by the Bondi-Hoyle accretion radius. Altogether, the accretion in the central region of the cluster is influenced by efficiently shielding protostars located at the position of the accretion flow. As a result, even a relatively small number of surrounding stars is sufficient to provide an efficient starvation effect in a volume-filling cluster environment.

One caveat of the presented simulations is the missing feedback from the stars that are formed first in the clusters. The gas stays isothermal and therefore tends to fragment much more quickly than with heating of the gas. Including this effect, the number of protostars is expected to be smaller. The starvation effect on the central objects in the protostellar cluster might thus be overestimated, especially in a turbulent volume-filling cluster, where gas can fall into the central region from all directions. However, [Peters et al. \(2010b\)](#) found that the number of protostars in simulations including radiative feedback is roughly half of the number of protostars in an isothermal calculation. As the total number of sink particles in our simulations is much larger than 100, and additionally, the starvation effect can already be seen with a relatively small number of competing protostars, we do not expect the shielding effect to completely vanish in the non-isothermal case. As long as there is some fragmentation, the fragments are likely to shield the central massive star from accretion, irrespective of whether radiation feedback is included or not. Likewise do magnetic fields tend to reduce the degree of fragmentation, but still do not prevent the cloud from fragmenting ([Hennebelle et al., 2011](#); [Peters et al., 2011](#)).

Finally, we want to point to recent studies by [Kruijssen et al. \(2012\)](#). They analysed the substructure within clusters as well as the dynamical state of the stellar cluster when gas expulsion becomes important, i.e., at a slightly later stage of the evolution of the cluster. Analysing the simulations of [Bonnell et al. \(2003, 2008\)](#), they find that the stellar system quickly reaches a globally virialised state if the gas potential is excluded and the stellar system is followed with pure  $N$ -body dynamics. Their results support the evolutionary picture of the formation of protostars that we see in our simulations. New protostars that form at larger radii from the centre of the cluster in gas-dominated regions have sub-virial velocities. As soon as they decouple from the gas motion and move to the central gas-poor environment, they quickly virialise.

## 6.4 Accretion behaviour – summary and conclusions

We performed simulations of collapsing molecular gas clouds with a total mass of  $100 M_{\odot}$  and a diameter of 0.2 pc. We varied the initial density profile as well as the turbulent supersonic velocity field and analysed the fragmentation process and the accretion onto nascent protostars. Most clouds, especially the ones with initially less centrally concentrated density profiles undergo fragmentation and form compact stellar clusters. We studied the accretion process in these clusters with the following conclusions:

- All clusters show strong and fast dynamical interactions between the protostars. During the formation time of the cluster, the protostars complete several orbits in the parental cluster. The mass accretion process can thus not be described by a monolithic collapse model.
- Fragmentation and formation of multiple protostars strongly influence the subsequent accretion flow in the entire cluster. Gas that falls towards the centre of the cluster is efficiently accreted onto protostars that are located at larger radii from the cluster centre. As a consequence, the central region is effectively shielded from further accretion and none of the central objects can sustain its initially high accretion rate. In all cases the observed decrease of the central accretion rate is due to the efficient shielding by secondary protostars. A significant starvation effect due to angular momentum and a resulting radial barrier can be excluded.
- In setups with initial flat density distributions, the mass of the most massive protostar,  $M_{\text{mm}}$ , scales with the total cluster mass,  $M_{\text{tot}}$ , like  $M_{\text{mm}} \propto M_{\text{tot}}^{2/3}$ , as originally proposed as a probe for competitive accretion. This relation is a common feature to both dynamical accretion models and cannot be used to distinguish between competitive accretion and fragmentation induced starvation, a conclusion that was already reached by [Peters et al. \(2010c\)](#).
- The accretion process does not differ between density profiles that form only one main cluster (power-law profiles, Bonnor-Ebert density distribution) and setups that form multiple subclusters (uniform density profile). In both, the central clusters as well as the disconnected subclusters, we find fragmentation induced starvation to work in the central region of the cluster.

# Chapter 7

## Tidal effects

### 7.1 Introduction

In the present-day universe, stars tend to form in strongly clustered environments (Lada and Lada 2003, Mac Low and Klessen 2004, McKee and Ostriker 2007, Bressert et al. 2010) with complex filamentary structures (Men'shchikov et al. 2010, Miville-Deschênes et al. 2010, Arzoumanian et al. 2011, Hill et al. 2011, Pineda et al. 2011). When averaged over a large number of stars, the stellar initial mass function shows evidence for a certain degree of universality (Salpeter 1955, Miller and Scalo 1979, Scalo 1986, 1998, Kroupa 2001, Chabrier 2003, Bastian et al. 2010). In particular, the high mass slope of the mass distribution for stars above  $\sim 1 M_{\odot}$  shows similar slopes in many different star-forming regions throughout the Galaxy. Exceptions may be found close to the Galactic centre (Nayakshin and Sunyaev 2005, Maness et al. 2007, Bartko et al. 2010), where clouds form more massive stars than in other regions. Overall the initial mass function seems to be relatively insensitive to the individual filamentary structure of collapsing clouds.

However, the formation of individual stars and small stellar clusters shows a strong dependence on the local conditions like the gas density distribution, the nature of turbulent motions, the thermal conditions in the gas (e.g., Peters et al., 2010a), and the structure and strength of magnetic fields (e.g., Seifried et al., 2011a), i.e., the local star formation process is strongly affected by the initial conditions.

During the collapse process two different time scales play an important role: the global time scale that the cloud needs to collapse, i.e., the free-fall time, and the time that filaments need to form and condense to form stars, i.e., the compressive impact of turbulence. In addition to that, the mass distribution in the cloud influences the speed at which filaments can form and

accrete enough mass to become Jeans-unstable. Initially flat density distributions lead to the formation of turbulence-induced filaments spanning the entire cloud. These filaments collapse to form distinct subclusters which are populated by preferentially low-mass stars. Central density enhancements and the accelerated central collapse coalesce the gas in the centre, suppressing the formation of multiple clusters in favour of a central single cluster. Strong central mass concentrations lead to the formation of a central star that accretes gas at high accretion rates before filaments and subsequent stars can form. The formation of filaments and the subsequent evolution are strongly influenced by the details of the turbulent motions like the nature of the modes, the local distribution of angular momentum and the positions of converging and diverging regions within the cloud.

In dense cores of high-mass star-forming regions the density profile and the turbulent motions lie within the regime where numerical work expects a strong sensitivity of the star formation rate, the number of formed stars, and the formation time scale on the local initial conditions. Apart from the initial density profile and the nature of turbulent modes, the realisation of turbulent motions with a slightly different spatial pattern of converging/diverging and rotating regions seems to significantly alter the outcome. In this chapter we want to further investigate the impact of slight changes in the initial conditions with a focus on tidal forces, the formation time and collapse of filaments, the positions of converging regions, and the concentration of angular momentum during the collapse of the cloud.

Beside these results for extreme initial conditions some questions concerning the collapse and the formation of central objects are still open. What initial configuration marks the threshold between a collapse that is dominated by central in-fall with a central star and a collapse that is dominated by turbulence induced fragmentation and the subsequent collapse of filaments? Does the central collapse support or suppress the formation of filaments close to the centre? Do tidal effects play a role? How does the mass concentration influence the time scale at which the filaments collapse? In the present study we address these questions with a two parameter study of different initial density profiles and different turbulence realisations.

## 7.2 Initial conditions

### 7.2.1 Initial density profiles

In chapter 5 we showed that the initial density profile has a strong impact on the formation time and formation mode of protostars. Centrally con-

centrated profiles lead to a massive central protostar whereas centrally flat density distributions tend to form low-mass objects in extended filaments. In particular, they found the transition between a dominant central protostar and numerous low-mass protostars between a rescaled Bonnor-Ebert sphere and a Power-law profile with  $\rho \propto r^{-1.5}$  as initial density profile. The simulations with these two extreme profiles are not described here, the radial density profiles are shown in the upper plot in figure 7.1, marked with BE for the Bonnor-Ebert sphere and PL15 for the power-law profile, respectively. The initial density profiles used in this calculation to investigate the transition between these two extreme cases are Plummer-like spheres of the form

$$\rho(r) = \rho_c \left( \frac{R_c}{(R_c^2 + r^2)^{1/2}} \right)^{3/2} \quad (7.1)$$

with 9 different values for a combination of  $R_c$  and  $\rho_c$ . The parameter  $\rho_c$  was adjusted such that the total mass inside the sphere is  $100 M_\odot$  for all simulations. Figure 7.1 shows the profiles with the parameters of table 7.1. The value  $M(R_c)$  denotes the mass inside the core radius  $R_c$ .

The density of the surrounding gas in the cubic box around the spherical molecular cloud is set to  $10^{-2}$  times the gas density at the outer edge of the cloud. The pressure at the boundary is continuous, resulting in a temperature step function with a temperature 100 times that of the isothermal collapsing cloud.

In preparation for further analytical analysis, we want to stress some properties of the applied density profiles. In the limiting case of a vanishing core radius  $R_c$  the Plummer-like distribution simplifies to a power-law  $\rho(r) = q r^{-3/2}$ . The average density inside  $r$  takes the simple form  $\langle \rho(r) \rangle = 2q r^{-3/2}$ , which results in a ratio of the density at radius  $r$  to the average density inside a sphere with radius  $r$  of

$$\frac{\rho(r)}{\langle \rho(r) \rangle} = \frac{1}{2}. \quad (7.2)$$

In the flat core regions of the Plummer-like profiles the density ratio is close to 1, yielding a range for the density ratio  $\rho(r)/\langle \rho(r) \rangle = (0.5; 1)$  as shown in figure 7.2, where the curves from left to right correspond to the radii R1 to R9 (table 7.1). Note that the choice of the exponent of 3/2 does not mark a special case concerning the density contrast. A distribution  $\rho(r) \propto r^{-p}$  generally has a constant density contrast of  $\rho(r)/\langle \rho(r) \rangle = 1 - p/3$ , for  $p < 3$ .

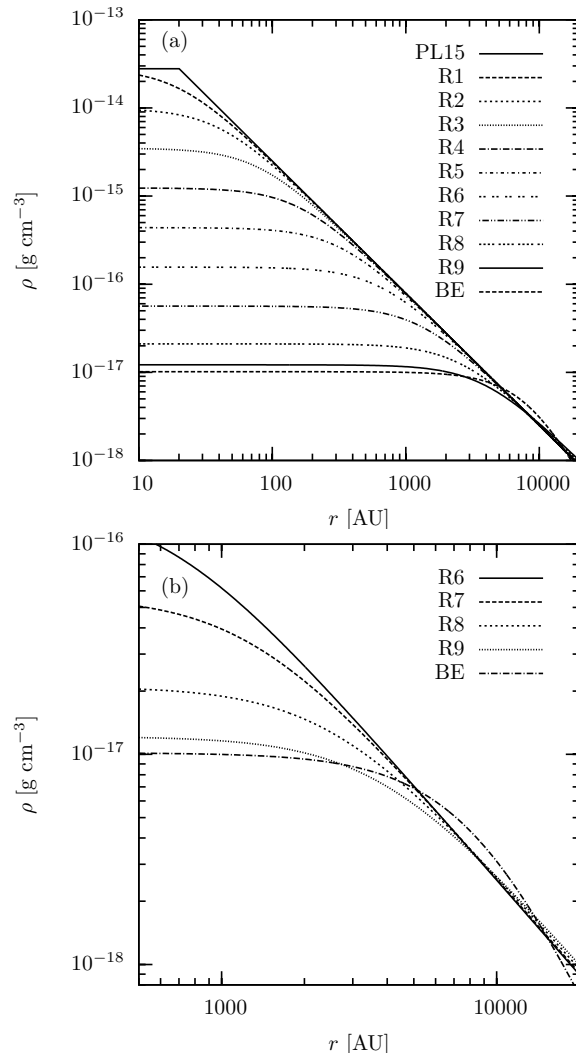


Figure 7.1: Comparison of the initial density profiles. Plot (a) shows all the profiles including the power-law profile (PL15) and the Bonnor-Ebert sphere (BE) profile from chapter 5. Plot (b) shows the outer wings for the density profiles  $R6 - R9$  in order to better distinguish between them and the BE profile. Details of the profile parameters are shown in table 7.1.

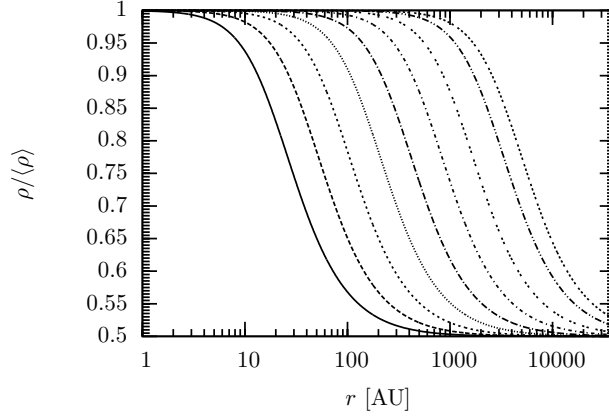


Figure 7.2: Density contrast for the Plummer density setups as a function of distance from the centre. The curves correspond to the different radii R1 to R9 from left to right (table 7.1).

Table 7.1: Plummer parameters

Profile	$R_c$ [AU]	$\rho_c$ [g cm <sup>-3</sup> ]	$t_{\text{ff}}(\rho_c)$ [kyr]	$M(R_c)$ [ $M_J$ ]
PLU-R1	20	$2.79 \times 10^{-14}$	0.40	0.000918
PLU-R2	40	$9.87 \times 10^{-15}$	0.67	0.00260
PLU-R3	80	$3.49 \times 10^{-15}$	1.13	0.00734
PLU-R4	160	$1.24 \times 10^{-15}$	1.89	0.0208
PLU-R5	320	$4.38 \times 10^{-16}$	3.18	0.0590
PLU-R6	640	$1.56 \times 10^{-16}$	5.33	0.168
PLU-R7	1280	$5.64 \times 10^{-17}$	8.87	0.486
PLU-R8	2560	$2.10 \times 10^{-17}$	14.5	1.45
PLU-R9	3840	$1.22 \times 10^{-17}$	19.1	2.83

Key parameters for the initial density profiles. The first column shows the name of the setup, the second and third column show the core parameters  $R_c$  and  $\rho_c$ , see equation 7.1. The last two columns show the free-fall time of the central density,  $t_{\text{ff}}(\rho_c)$  and the mass contained within the core radius  $R_c$ .

## 7.2.2 Mach numbers and turbulence crossing time

The gas motions are supersonic in all simulations. The volume weighted Mach number

$$\mathcal{M} = \frac{v_{\text{rms}}}{c_s} \quad (7.3)$$

differs slightly between the two random turbulent seeds. Table 7.2.2 gives an overview of the Mach numbers of the individual setups. The initial rms Mach numbers are  $\mathcal{M} = 3.32$  for seed 1 and  $\mathcal{M} = 3.63$  for seed 2, respectively. The runs indicated with suffix S1b have rescaled velocities to match the Mach number of the corresponding run with seed 2. The sound crossing time reads  $t_{\text{sc}}(2R_0) = 710 \text{ kyr} \approx 14 t_{\text{ff}}$ . The time needed for the gas to cross the entire cloud of  $2R_0$  is  $t_{\text{tc};1,2}(2R_0) = 214, 196 \text{ kyr}$ , respectively, about four times as large as the global free-fall time.

## 7.2.3 Runs

For every density profile we apply two different random velocity seeds, yielding 18 runs. In addition we perform three runs with turbulent seed 1 but rescaled velocities in order to match the Mach numbers of the corresponding runs with random turbulent seed 2. Table 7.2.2 gives an overview of the simulations, the initial kinetic properties and the main key properties at the end of the simulation. The density parameters are listed in table 7.1.

## 7.3 Analytical estimates

### 7.3.1 Free-fall analysis

Before investigating the details of the collapse, a simple analysis of the time scales for a collapse helps to appraise what effects to expect. The condition for free-fall to be a good approximation needs the pressure term in the force equation to be much smaller than the gravitational source term,  $\partial p / \partial r \ll -\rho g$ , which can be rewritten in the isothermal case ( $p = c_s^2 \rho$ ) as

$$\frac{c_s^2}{\rho} \partial_r \rho \ll -\frac{GM(r)}{r^2}. \quad (7.4)$$

For the applied Plummer-like spheres the free-fall approximation gets better for larger radii: if we exclude radii  $r < 40 \text{ AU}$  the gravitational term on the right hand side is 1.31 – 10.4 times as large as the pressure term on the left hand side at the beginning of the simulation, showing strong variations for the different density profiles. Considering radii larger than 100 AU from the

Table 7.2: Main parameters of the simulations

Name	$E_{\text{kin}}/ E_{\text{pot}} $	$\mathcal{M}$	$t_{\text{end}}$ [kyr]	$t_{\text{end}}$ [ $t_{\text{ff}}$ ]	$N_{\text{sink}}$	$M_{\text{mm}}$ [ $M_{\odot}$ ]	$t_1$ [kyr]	$\Delta t_{1,2}$ [kyr]
PLU-R1-S1	0.050	3.32	17.3	0.34	1	10.0	1.2	—
PLU-R2-S1	0.050	3.32	16.7	0.33	1	10.0	1.4	—
PLU-R3-S1	0.050	3.32	16.7	0.33	1	10.0	1.9	—
PLU-R4-S1	0.050	3.32	16.9	0.34	1	10.0	2.7	—
PLU-R5-S1	0.050	3.32	17.2	0.34	1	10.0	4.0	—
PLU-R6-S1	0.051	3.32	18.2	0.36	1	10.0	6.2	—
PLU-R7-S1	0.053	3.32	20.3	0.40	1	10.0	9.5	—
PLU-R8-S1	0.055	3.32	25.3	0.50	82	4.3	14.4	5.2
PLU-R9-S1	0.058	3.32	28.4	0.57	105	2.4	18.7	2.7
PLU-R3-S1b	0.079	3.63	16.8	0.33	1	10.0	1.9	—
PLU-R5-S1b	0.073	3.63	17.3	0.34	1	10.0	4.0	—
PLU-R7-S1b	0.073	3.63	21.6	0.43	19	9.3	9.3	10.3
PLU-R1-S2*	0.070	3.63	17.1	0.34	18	6.2	1.1	12.2
PLU-R2-S2	0.070	3.63	18.1	0.36	34	6.5	1.4	10.2
PLU-R3-S2**	0.071	3.63	17.1	0.34	25	7.0	1.8	12.8
PLU-R4-S2	0.071	3.63	18.2	0.36	28	6.7	2.7	11.6
PLU-R5-S2	0.071	3.63	20.8	0.41	34	6.7	4.0	11.6
PLU-R6-S2	0.072	3.63	25.0	0.50	126	5.3	6.1	8.7
PLU-R7-S2	0.073	3.63	25.6	0.51	124	4.3	9.2	7.6
PLU-R8-S2	0.075	3.63	28.0	0.56	152	1.6	14.5	4.3
PLU-R9-S2	0.078	3.63	30.8	0.61	176	0.9	19.5	2.9

Key properties of the runs. The name is composed of the radius (Rx) and the seed (Sx). The ratio of kinetic over potential energy as well as the Mach numbers are initial values. The Mach numbers are volume-weighted and therefore do not show differences for different density concentrations. The kinetic and potential energy depend on the mass concentration and vary. The simulation time is shown in kyr and in units of the global free-fall time. The sink particle data comprise the total number  $N_{\text{sink}}$ , the mass of the most massive sink particle  $M_{\text{mm}}$ , the formation time of the first sink particle  $t_1$ , and the time gap between the formation of the first and the second one  $\Delta t_{1,2}$ . (\* up to a SFE of 7%; \*\* up to a SFE of 8%)

centre of the cloud, gravity is 2.10 – 10.4 times as strong as pressure and for radii larger 300 AU the factor is 3.62 – 10.4 for the different Plummer-like spheres. At a radius of  $r = 1/3 R_0$  the gravitational term is at least 20 times larger than the pressure term for all setups. The free-fall approximation is therefore applicable, however, the estimates for the central region may be critical. Note that these numbers are taken from the initial profile. During the evolution of the cloud, in particular after the formation of the first protostars, gravity gets more and more dominant because the protostars contribute to the total mass and therefore the gravitational attraction but not to the pressure term. Applying the free-fall approximation leads to two different free-fall times for the spherical cloud: (1) the average free-fall time,  $t_{\text{ff}}(\langle \rho(r) \rangle)$ , i.e. the time that an object at radius  $r$  needs to fall to the centre and (2) the local free-fall time at radius  $r$ ,  $t_{\text{ff}}(\rho(r))$ , which is the time that an object with the local density  $\rho(r)$  needs to collapse itself. The ratio of these two free-fall times depends on the density profile and reads

$$\frac{t_{\text{ff}}(\rho(r))}{t_{\text{ff}}(\langle \rho(r) \rangle)} \in (1; \sqrt{2}), \quad (7.5)$$

where unity corresponds to the flat region in the centre and  $\sqrt{2}$  describes the ratio at the outskirts of the cloud ( $r \gg R_c$ ). The ratio shows that the time scale for a local collapse at  $r$  is slightly larger than the time scale needed to fall to the centre. Whether small gravitationally unstable regions collapse and form stars apart from the central one may sensitively depend on how good the free-fall approximation is throughout the cloud evolution and how the turbulent velocity disturbs the free-fall motions. A critical property of the velocity field is the converging or diverging character with respect to the centre. Converging flows towards the centre push the gas to the centre and thus decrease the average free-fall time by increasing the radial velocity towards the centre. Therefore, they do not leave enough time for outer regions to collapse themselves before reaching the central region and forming a central star or getting accreted onto an already existing central object. In contrast, diverging flows may easily increase the average free-fall time to a value larger than the local free-fall time at radius  $r$  which allows the region to collapse before reaching the centre. Therefore we expect large differences in the total number of condensations and stars between different turbulent velocity fields. As the two free-fall times have very similar values, we also expect the protostars to form close to the centre. A collapse of self-gravitating objects far from the central region requires either initially high densities at large radii or strong density enhancements due to the turbulent motions plus enough swept-up material. The first condition is not fulfilled by the applied density profiles. The latter condition needs either strong

turbulence or a sufficiently large total simulation time in order to allow for collapsing condensations at large radii. The complex interplay between the initial density profile, the resulting global collapse time and the formation of single or multiple subclusters has been investigated in detail in chapters 5, 6 and 8 for comparable setups. From these results we do not expect many protostars to form far away from the centre in distinct subclusters.

### 7.3.2 Tidal forces

Tidal forces are based on the different acceleration due to different distances from the attracting object. Assuming spherical symmetry, the tidal force at radius  $r$  from the centre with enclosed mass  $M$  is given by the difference between the acceleration at  $r \pm \Delta r$ ,

$$a_{\text{tidal}} = G M \left( \frac{1}{(r + \Delta r)^2} - \frac{1}{(r - \Delta r)^2} \right), \quad (7.6)$$

where  $G$  is the gravitational constant and  $\Delta r \ll r$  is sufficiently small so that the enclosed mass  $M$  can be assumed constant for  $r \pm \Delta r$ . With a simple density function of the form  $\rho(r) \propto r^{-p}$  the mass as a function of  $r$  is given by  $M(r) \propto r^{3-p}$  and the tidal acceleration scales as

$$a_{\text{tidal}}(r) \propto r^{1-p}. \quad (7.7)$$

The derivative with respect to  $r$ ,

$$\frac{\partial a_{\text{tidal}}}{\partial r}(r) \propto (1-p)r^{-p}, \quad (7.8)$$

changes sign at  $p = 1$ . For  $p < 1$ ,  $a_{\text{tidal}}$  increases with radius ( $\partial a_{\text{tidal}}/\partial r > 0$ ) and therefore compresses material at radius  $r$ . For  $p > 1$ ,  $\partial a_{\text{tidal}}/\partial r < 0$  and shears condensations apart. In regions with flat density profile, e.g. the flat core of the Plummer-like cloud, tidal effects lead to a compression of overdensities, whereas in the wings of the density distribution, where  $p = 1.5$ , condensations are more likely to be sheared apart.

The collapse of filaments in presence of a global collapse can be approximated by extending the tidal estimate to a simple model of two connected spheres. Assume a central spherical mass concentration  $M_1$  and an attached part of a filament  $M_2$  as shown in figure 7.3. In a simple approach without dynamic motions, the tidal forces can disrupt sphere 2 if the difference of the central acceleration  $\Delta a_c$  is larger than the acceleration of the local collapse

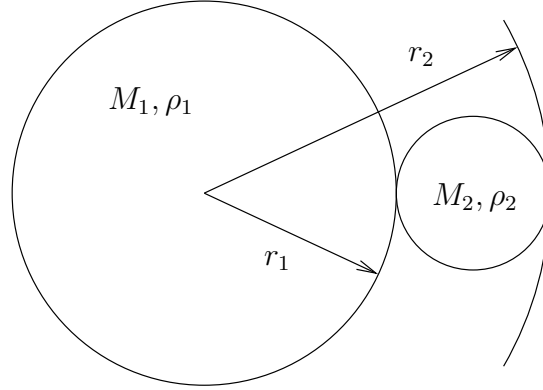


Figure 7.3: Simple model of the central mass  $M_1$  with average density  $\rho_1$  and an attached part of a filament with total mass  $M_2$  and a density  $\rho_2$ . Both masses are embedded in an environment with density  $\rho_0$  and a mass  $M_0$  between  $r_1$  and  $r_2$ . The size of the central mass depends on the position of  $M_2$ , the volume of  $M_2$  is determined by the resolution and the Jeans length at the given density.

of  $M_2$ , named  $a_{\text{fil}}$ . The first quantity is given by

$$\Delta a_c = a(r_1) - a(r_2) \quad (7.9)$$

$$= \frac{GM_1}{r_1^2} - \frac{G(M_1 + M_2)}{r_2^2}. \quad (7.10)$$

The collapsing accelerations for mass  $M_2$  is given by

$$a_{\text{fil}} = GM_2 \left( \frac{2}{r_2 - r_1} \right)^2. \quad (7.11)$$

Solving the inequality  $a_{\text{fil}} > \Delta a_c$  gives

$$\frac{M_2}{M_1} > \left( \frac{1}{r_1^2} - \frac{1}{r_2^2} \right) \left( \frac{4}{(r_2 - r_1)^2} + \frac{1}{r_2^2} \right)^{-1}, \quad (7.12)$$

further conversion of the ratio of masses  $M_i$  to the ratio of densities  $\rho_i$  yields

$$\frac{\rho_2}{\rho_1} > \frac{8r_1^3}{(r_2 - r_1)^3} \left( \frac{1}{r_1^2} - \frac{1}{r_2^2} \right) \left( \frac{4}{(r_2 - r_1)^2} + \frac{1}{r_2^2} \right)^{-1}, \quad (7.13)$$

which indicates the density contrast, at which a local collapse of a filamentary region is not impossible in presence of tidal forces. In the simulations presented here, the collapse radius of sphere 2  $r_{\text{coll}}$  is set to 3 times the cell

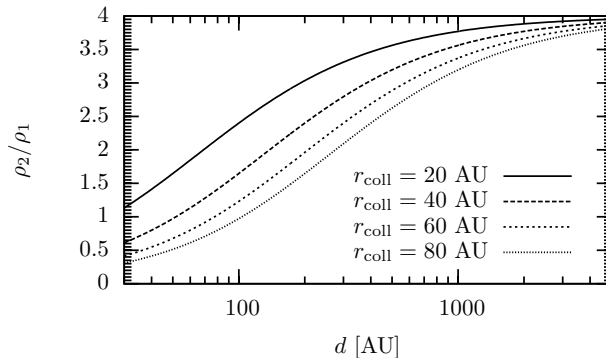


Figure 7.4: Density contrast for different sizes of collapsing regions as a function of distance from the centre. The collapse radius in this study is set to  $r_{\text{coll}} = (r_2 - r_1)/2 = 40$  AU.

size at the highest level of the AMR grid, which is equal to the accretion radius of a sink particle. Hence, equation (7.13) can be parameterised by only one radius  $r_1$  as we are tracing the formation of protostars at that fixed spatial scale. The resulting density contrast needed to prevent tidal disruption is plotted in figure 7.4, where  $r_{\text{coll}} = (r_2 - r_1)/2$ . In this simple model the density contrast needs to be less than 4 for all radii and sizes of the collapsing region.

In this model we do not take into account that both spheres may be embedded in a surrounding medium with  $\rho > 0$ . However, a detailed analysis shows that a surrounding medium decreases the density contrast. The simple model therefore marks an upper limit and realistic environments will be even less affected by tidal effects.

Combining the density contrast  $\rho(r)/\langle\rho(r)\rangle$  of the initial cloud (figure 7.2) with the highest density contrast needed to avoid tidal disruption (equation 7.13, figure 7.4) yields a total density contrast relative to the initial setup ranging from 0.2 to 8 as shown in figure 7.5.

## 7.4 Tidal effects – results

### 7.4.1 Overview and cloud evolution

We run most of the simulations until the total mass accreted onto protostars reaches  $10 M_{\odot} \hat{=} 10\%$  star formation efficiency (SFE). Some simulations have such compact clusters with highly dynamical interactions that the computational time step in the simulation decreased dramatically. These simulations are run only up to a SFE of 8%, which does not affect the final result of

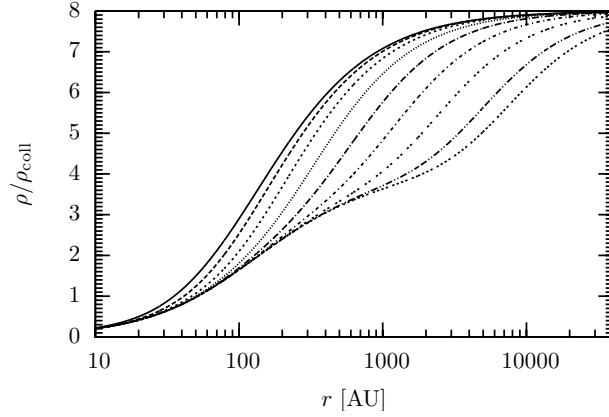


Figure 7.5: Density contrast for the initial Plummer spheres according to equation (7.13) that is needed for a collapse at radius  $r$ . The collapse radius is set to  $r_{\text{coll}} = 40$  AU. The curves correspond to the different radii R1 to R9 from left to right.

our conclusions. The most centrally concentrated density profiles (R1, R2) collapse in the centre forming a protostar after just  $\sim 1$  kyr  $\sim 0.02 t_{\text{ff}}(\langle\rho\rangle)$ . During this short period the turbulent velocities can not influence the cloud visibly. The turbulence with rms Mach numbers  $\mathcal{M} \approx 3$  needs roughly  $\sim 50$  kyr to cross the distance of a Jeans length, comparable to the global free-fall time. The larger the central flat region of the initial density profile, the longer it takes to accumulate enough mass and form Jeans-unstable regions. The runs with the lowest initial central density need roughly 19 kyr before the first protostar forms. During this time the turbulence can produce overdensities of various shapes and in extended regions of the cloud core. Figure 7.6 and 7.7 show column density plots of the central region during the early phase of the collapse for the density profiles R7, R8, and R9. These filaments can accumulate mass themselves and form subsequent gravitationally bound objects. The formation of protostars close to the centre is delayed with decreasing initial central density. If the time scales for the formation of a central protostar and the formation of protostars in filaments are comparable, the cloud and the resulting star cluster are not dominated by the central star, but by the substructures developed by turbulent motion. An overview of the key properties of the runs is shown in table 7.2.2. The total simulation time ranges from 17 – 31 kyr, the number of protostars from 1 to almost 200. The time between the formation of the first protostar and the formation of subsequent stars in filaments decreases for flatter initial density profiles. As the evolution of the cloud is a complex interplay between the global collapse of the cloud and the collapse of dense regions enhanced by turbulence, we

also numerically investigate the impact of the turbulence without the global collapse.

### 7.4.2 Turbulence without central collapse

Before we are able to answer how strongly the collapse of filaments is influenced by a central overdensity and the global collapse we have to investigate the evolution of turbulent gas without the side effects of non-uniform density profiles and central collapse. In order to do so, two separate runs were performed, in which the central collapse is switched off. This is realised by using a uniform density distribution and periodic boundary conditions for the calculation of the gravitational potential. The density in the box was set to the same average value as in the other setups,  $\langle \rho \rangle = 1.76 \times 10^{-18}$ . We then applied the same two turbulent random velocity fields (S1, S2).

Figure 7.8 shows column density plots for the two runs with turbulent random seed S1 and S2. The filaments form throughout the entire simulation box with similar strength everywhere. The second run with seed S2 forms distinct elongated overdensities earlier than the run with S1. The filaments start to form protostars after roughly 26 – 28 kyr, which is a bit more than half a free-fall time. The first protostars mostly form in the centre of a filament or at the intersections of filaments. Long dense filaments form multiple protostars along them yielding a line of objects.

A very important difference between the two setups are the positions of converging regions and voids. The turbulent field S1 shows a converging region in the centre whereas field S2 creates a void in the centre. Whereas the positions of knots and voids is unimportant in a periodic box with initially uniform density, they have a major impact of the evolution in a setup with concentrated density profile. The converging central region of field 1 accelerates the global collapse enough to prevent further fragmentation in the stronger concentrated density profiles PLU-R1–PLU-R7. Only the setups with the largest core radii can undergo additional fragmentation. On contrary, all setups with turbulent field S2 show multiple fragments because the diverging character of the field in the central region sufficiently retards the global collapse. The time scale for an overdensity to fall to the central region is pushed above the time scale needed for local collapse.

Figure 7.9 shows the key properties of the protostars. Plot (a), (b) and (c) show the number of protostars, the total mass of all protostars, and the global accretion rate onto all protostars as a function of time. The formation rate of objects in plot (a) increases slowly at the beginning when the first protostars form in the local centres of overdense regions. After  $t \sim 36 \text{ kyr} \approx 0.7 t_{\text{ff}}$  the formation rate increases significantly when the extended arms of the filaments

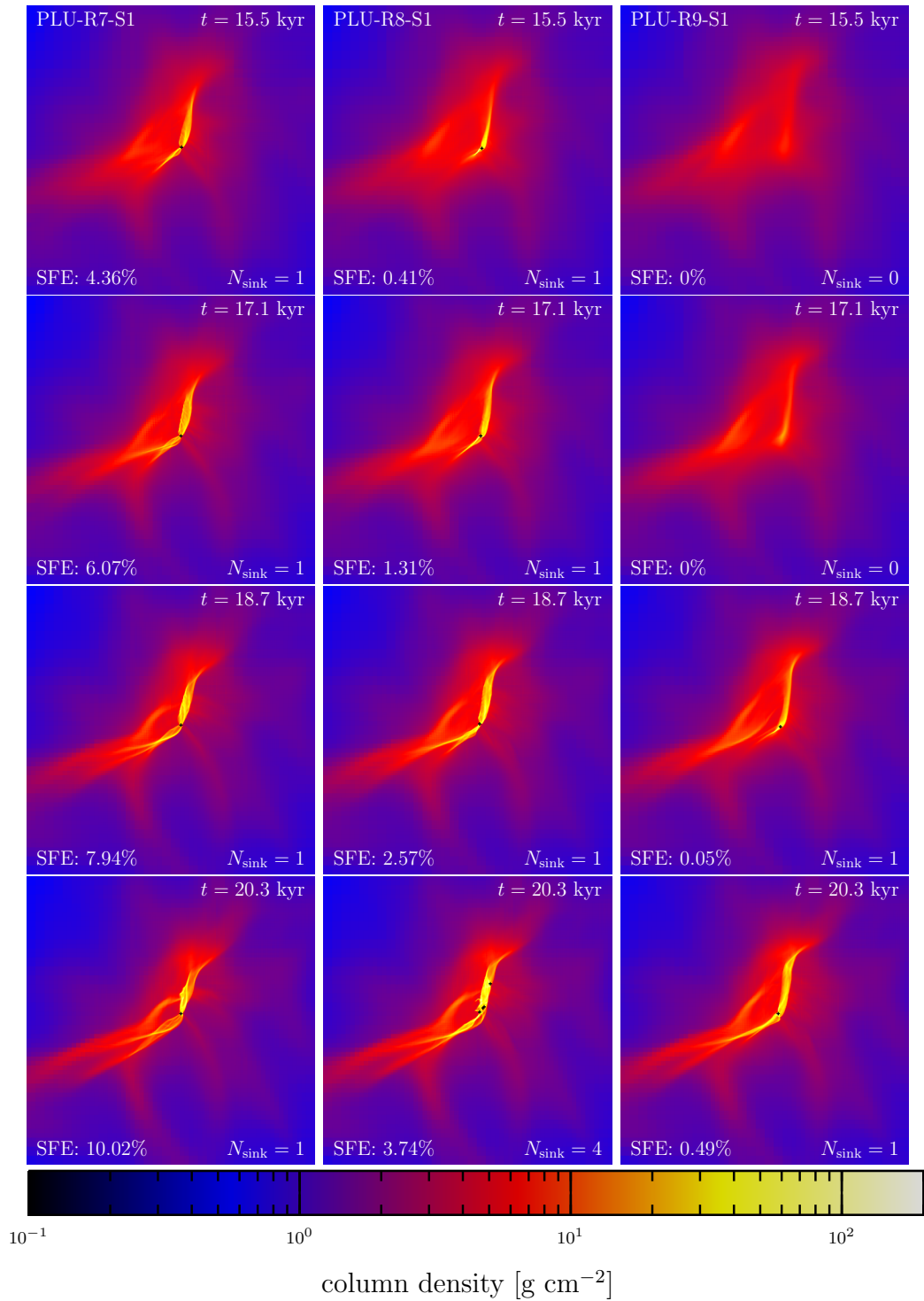


Figure 7.6: Column density plots for the runs PLU-R7-S1, PLU-R8-S1 and PLU-R9-S1. Each rows shows the evolution at the same time. In all cases the box spans  $2 \times 10^{17}$  cm in  $x$  and  $y$  direction.

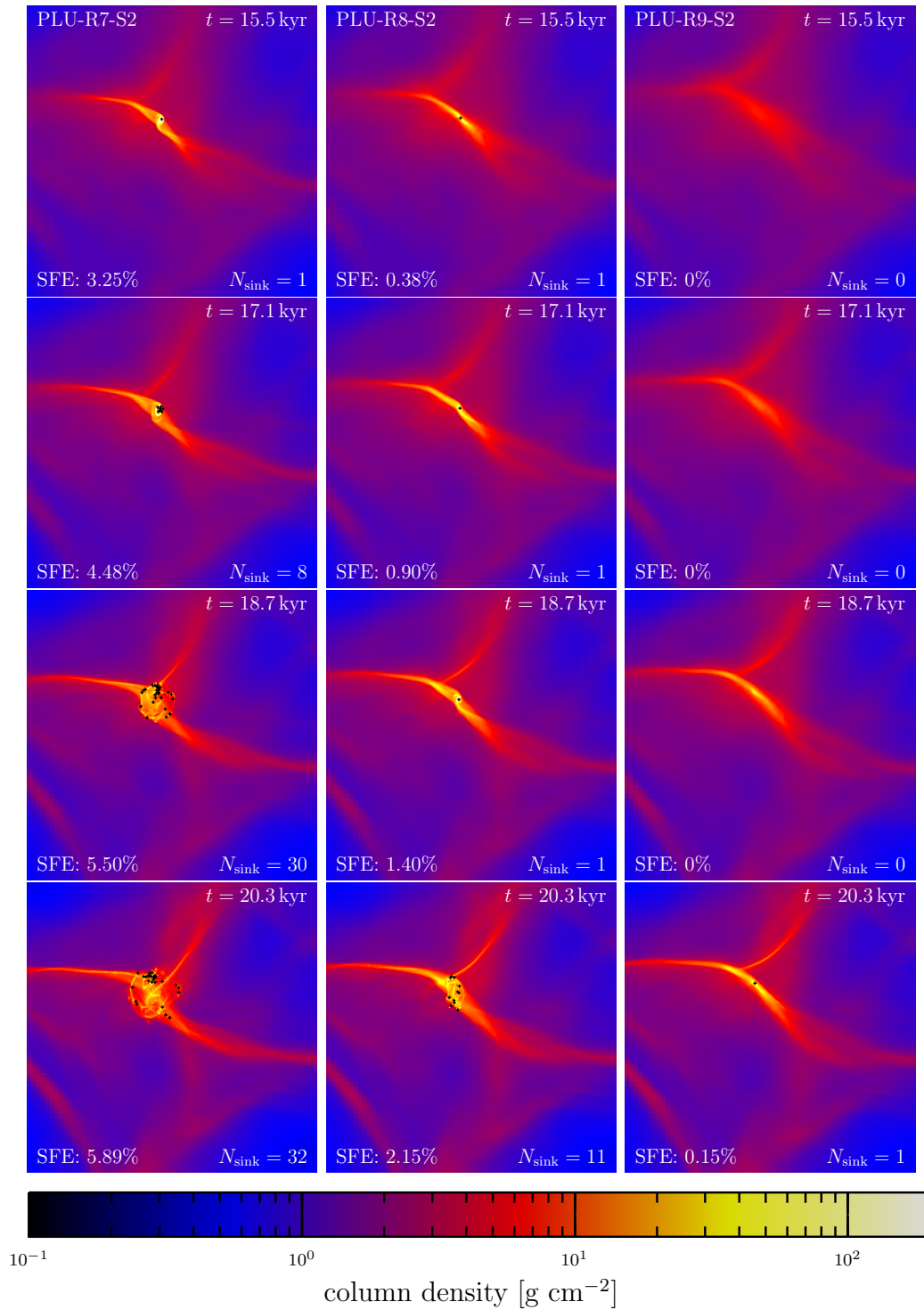


Figure 7.7: Column density plots for the runs PLU-R7-S2, PLU-R8-S2 and PLU-R9-S2. Each rows shows the evolution at the same time. In all cases the box spans  $2 \times 10^{17}$  cm in  $x$  and  $y$  direction.

start to collapse as well. The mass evolution in plot (b) follows exactly the number of collapsed objects, which indicates that the star formation rate can directly be transformed to the global accretion rate. This is not necessarily the case for a dense cluster environment where the formation rate of stars might drop while the total accretion rate onto the existing stars remains high. Plot (c) shows the accretion rate as a function of time, which reaches a high value of  $\sim 2 \times 10^{-3} M_{\odot} \text{yr}^{-1}$  at the end of the simulation. Finally, plot (e) shows the mass evolution of the individual protostars for the run with random seed S1. It is easy to see that the formation time is not necessarily related to the final mass of the protostar. Some particles accrete gas at high rates during the simulation independent of the formation time, for other objects the accretion is completely cut off or occurs in jumps. These differences can be explained by the different surroundings in which the protostars evolve. Objects that form in isolation can accrete material at a smooth and high accretion rate, where the evolution of the accretion rate only depends on the surrounding density profile. Protostars that form next to already existing neighbours in an elongated filament need to compete with them for the available gas. The special geometry of a string-like gaseous structure only allows the stars inside it to accrete material from two opposite channels along the filament. If other protostars form along this channel the accretion onto the central protostars is almost entirely shielded. This results in protostars with nearly constant masses for long periods of the simulation. Particle-particle interactions influence the position inside the filament which leads to accretion jumps every now and then. The influence of close neighbours can be seen in plot (d), where we show the average accretion rate,  $\langle \dot{M} \rangle$ , as a function of distance to the nearest neighbour  $d$ . All particles with a large distance to their nearest neighbour have high average accretion rates. If particles are close to neighbours their accretion rate strongly depends on the exact position and the accretion flow.

### 7.4.3 Turbulence with central collapse

In the simulations *with* central collapse we apply the described initial density profile and choose isolated boundary conditions for the gravitational potential and outflow boundary conditions for the hydrodynamics.

#### Tidal forces and the evolution of overdensities

As shown in section 7.3.2, equation (7.13), the necessary over-density at  $r$  in comparison to the average density inside  $r$  needs to be up to 8 to resist tidal disruption. We measure the fraction of total mass that is in tidally

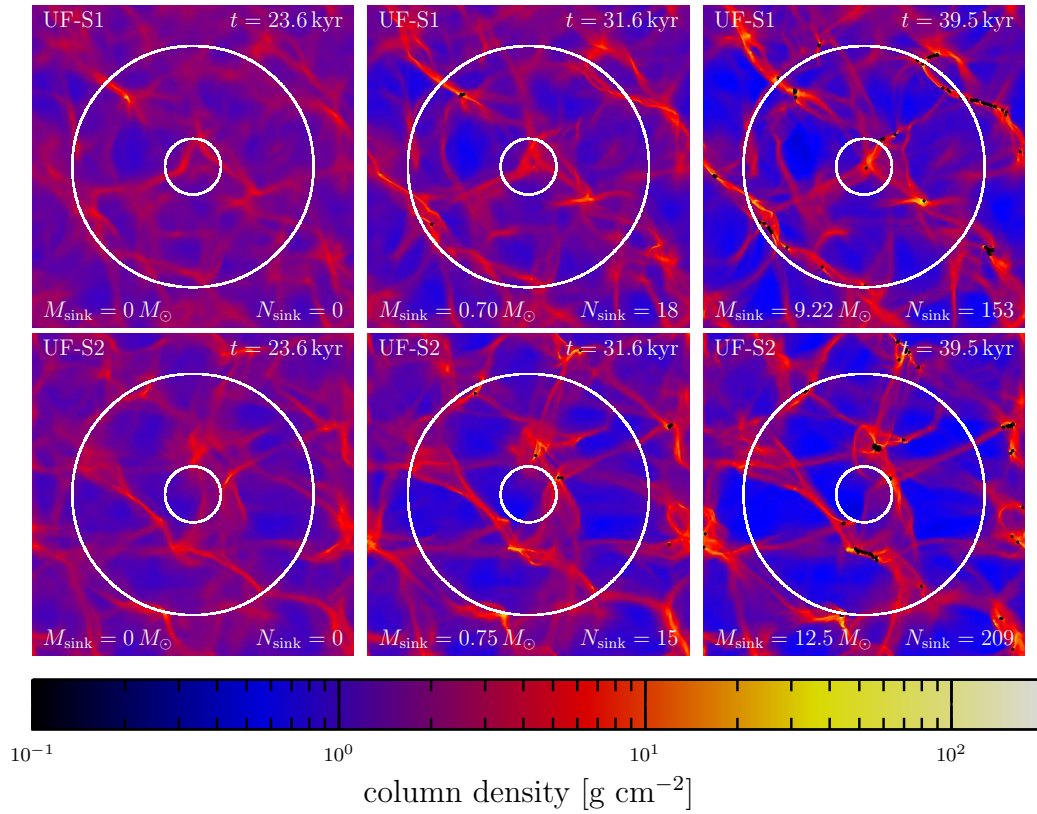


Figure 7.8: Column density plots for the simulations with initially uniform density. The upper panel shows the time evolution for the run with seed 1, the lower for the run with seed 2. The large circle indicates the cloud size of the corresponding runs with density profiles R1-R9 ( $R = 0.1$  pc), the inner circle has diameter of a Jeans length. In all cases the box spans  $8 \times 10^{17}$  cm in  $x$  and  $y$  direction.

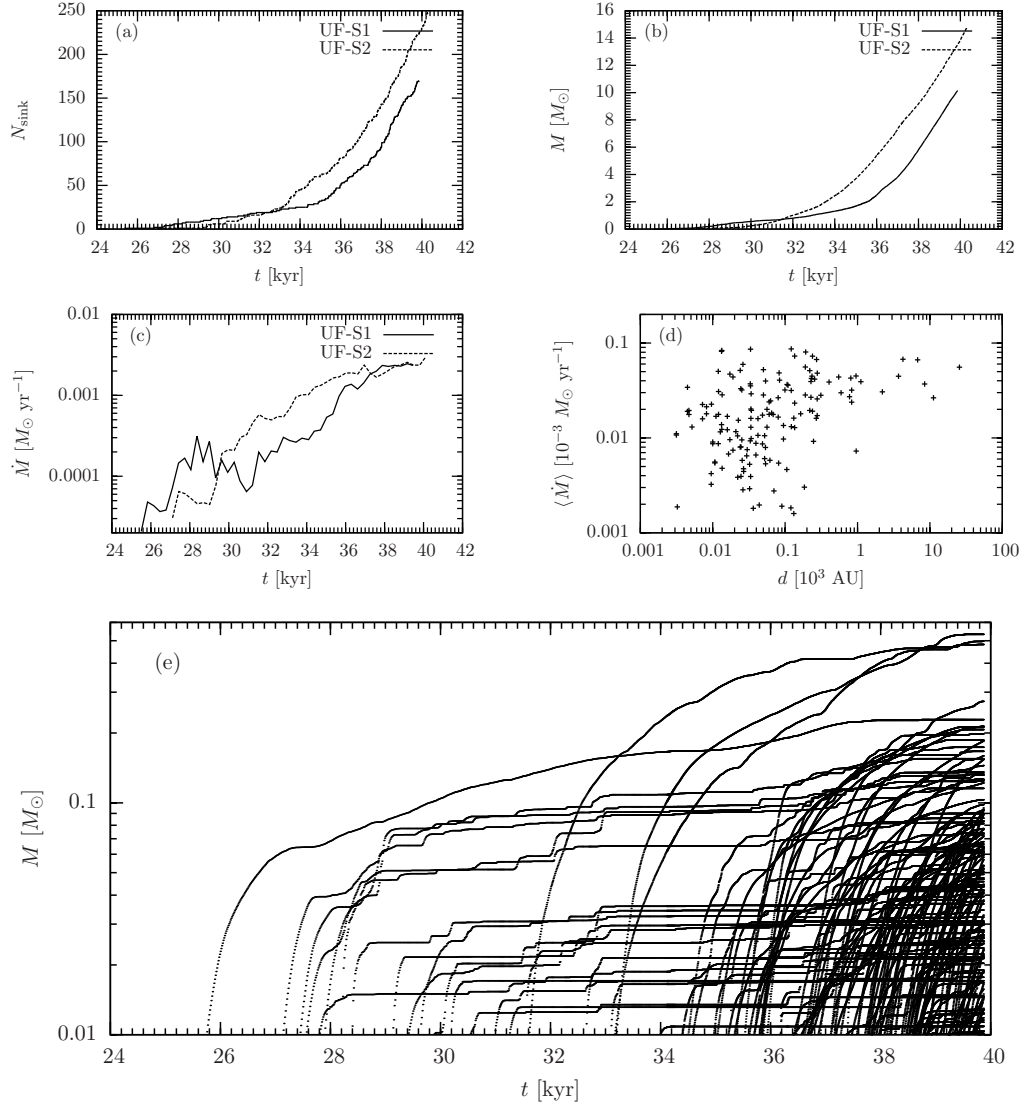


Figure 7.9: Protostellar properties and evolution for the uniform density runs. Plot (a) shows the number of protostars, plot (b) the total mass captured in particles. Both simulations show a systematically similar evolution. However, the box with velocity seed 2 forms protostars earlier. Plot (c) shows the accretion rate onto all particles, (d) the relation between the distance to the nearest neighbour and the average accretion rate and (e) the mass evolution of every single protostar for the uniform profile with seed 1. The corresponding plot (e) for seed 2 does not show systematic differences.

stable regions with a density contrast of more than 10 as a function of radius from the centre of the cloud. Figure 7.10 shows that fraction for different times for the simulations R5 to R9. The runs with smaller core radii are very similar to the setups with R5 and are omitted to keep the plots readable. The left hand plot corresponds to runs with random seed 1, the right hand panel shows runs with random seed 2. Overall the runs with seed 1 evolve faster. Therefore, the left panel shows snapshots at smaller times than the right panel. In the last snapshot the simulations with strong central mass concentrations have already reached a SFE of 10% and are therefore not plotted. For both random seeds a large amount of the total mass is located in regions with  $\rho(r) > 10 \langle \rho(r) \rangle$ . These regions extend to larger radii as the simulation advances. As a result the total amount of tidally stable gas increases for all simulations. In the first panel for seed S1 ( $t = 8$  kyr), only the simulations up to core radius R6 have developed tidally stable over-densities. The setups with initially lower central density need more time to collapse and to form overdensities. Once overdensities have formed, all simulations show very similar fractions of tidally stable mass. The longer the simulation evolves, the larger is the radius up to which a significant fraction of mass is tidally stable. A generally similar behaviour can be seen with random seed S2 in the right panel. In contrast to the setups with random seed S1, the turbulence causes a strong second peak at 2000 AU from the centre of the cloud. Hence, the fraction of total mass located in stable regions is higher by a factor of a few for the entire cloud. At  $t = 20$  kyr a gap at  $r \sim 500$  AU develops which is due to the numerous protostars that form close to the centre. In all cases the overall amount of mass located in regions that are dense enough to prevent tidal disruption is fairly large and does not strongly depend on the initial mass concentration, taken the different collapse times into account. Therefore, we conclude that (a) the effects of tidal disruption are generally rather small and (b) do not significantly depend on the initial density distribution. A different random velocity seed, however, may change the effect of tidal forces noticeably. Note that the existence of tidally stable regions is just a necessary but not a sufficient criterion for the formation of protostars.

### Evolution of angular momentum

For both random seeds, the cloud as a whole does not have any net rotation. The initial ratio of rotational over gravitational energy is of the order of  $10^{-3}$ . Nevertheless, the turbulent motions cause local regions to have higher angular momenta. In case of uniform initial density and without global central collapse, local angular momenta play a minor role. In contrast, a dense core

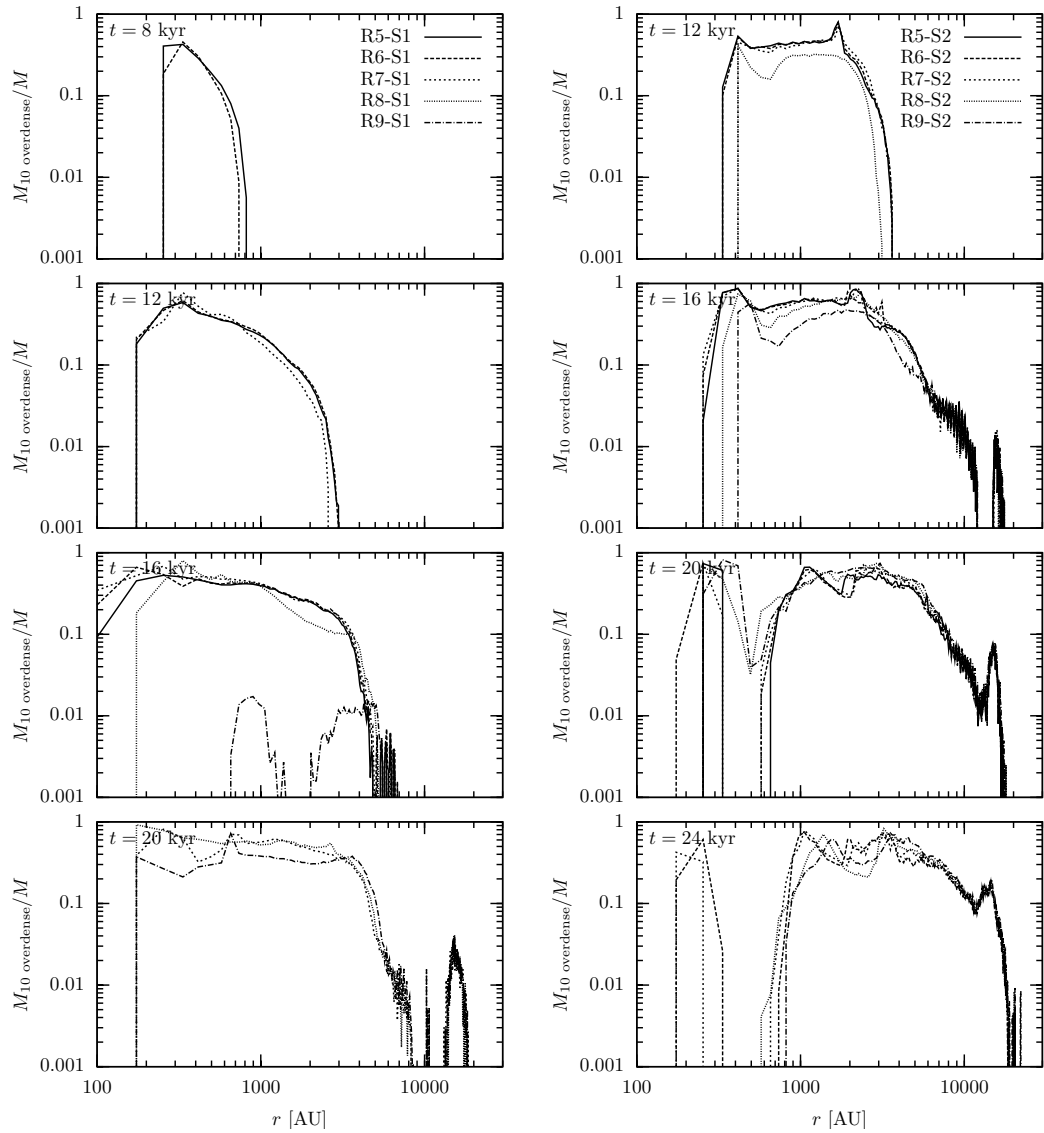


Figure 7.10: Fraction of mass that is located in overdense regions to the total mass at radius  $r$  for different times.

that collapses globally is more influenced by the turbulence-induced angular momentum with respect to the centre of the collapse. Different turbulent patterns in the velocity field are therefore expected to influence the local angular momentum with respect to the centre of the collapse. Given a turbulent velocity field, the different initial density profiles do not show a significant evolution of the angular momentum. Figure 7.11 shows the specific angular momentum with respect to the centre of the collapse for density profile R5 and both seeds. Each plot shows the radial distribution for different times in the simulation. In both cases, the distribution varies during the collapse with a different evolution for the two seeds. In the run with seed S1, the specific angular momentum first increases in the centre and decreases in the region of a few times  $10^3$  AU, i.e., within a sphere with a radius of a Jeans length. Then the values gradually increase until the end of the simulation. The single central star in this simulation does not disturb the evolution of the angular momentum visibly. The setup with random seed S2 shows slightly stronger variations and a strong enhancement between  $t = 12$  kyr and  $t = 16$  kyr at a radius of  $\lesssim 10^3$  AU. This is the time and the radial distance at which the setup with random seed 2 starts to form secondary protostars. The impact of their formation induces further fluctuations in the subsequent evolution. Figure 7.12 shows the ratio of the specific angular momentum at two different times to the distribution at the beginning of the simulation as a function of radius. The reference distribution is taken at  $t = 2$  kyr rather than the actual initial configuration because initially the adaptive mesh in the centre is not yet refined down to the smallest scales. For random seed 2, the growth of specific angular momentum at scales around  $10^3$  AU is larger than for seed 1. Although the angular momentum is smaller than the Keplerian values in all cases, the redistribution of angular momentum closer to the centre, i.e., a net amplification of the angular momentum, retards the the collapse leaving more time for the gas to form collapsing overdensities.

Only the very concentrated profiles (R1–R3) with random seed S2 form a transient disc-like structure that quickly fragments and forms stars. However, the disc-like accumulation of gas around the first protostar is strongly disturbed by the dense filament, in which it forms and constantly reshaped by strong accretion flows. The structure therefore does not deserve to be called disc and a proper analysis with disc-specific quantities fails or gives misleading results.

Whether the first central star remains the only one in the simulation is mainly determined by the initial density profile and the nature of the turbulent velocity field. Once subsequent stars form, their formation rate also depends on the density profile. Stronger mass concentrations lead to a slightly earlier collapse of filaments but lower stellar formation rates within these fila-

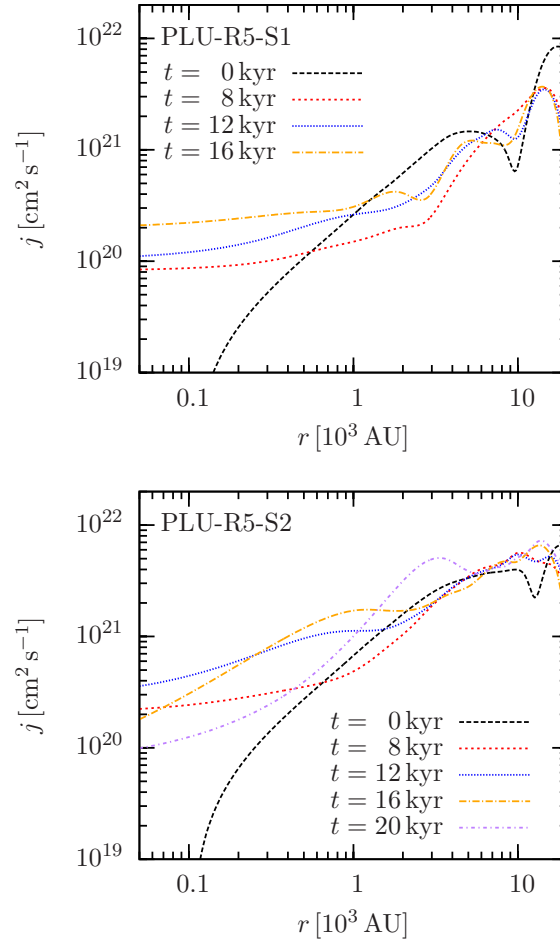


Figure 7.11: Specific angular momentum for the density profile R5 for both random seeds with respect to the centre of the collapse. The total values are higher for random seed 2 than for random seed 1.

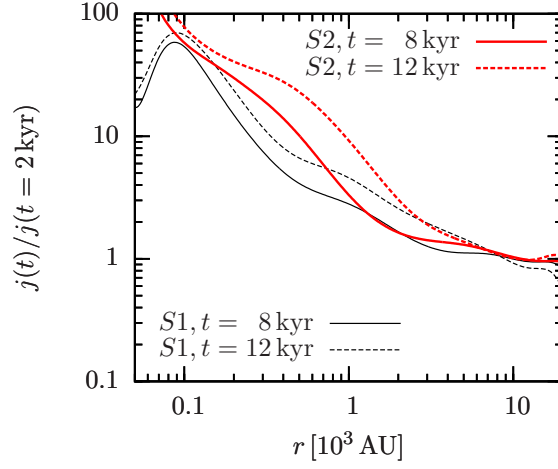


Figure 7.12: Specific angular momentum for the density profile R5 for both random seeds with respect to the centre of the collapse. The total values are higher for random seed 2 than for random seed 1.

ments ranging from  $\sim 5 (\text{kyr } 100 M_{\odot})^{-1}$  for R2-S2 up to  $\sim 20 (\text{kyr } 100 M_{\odot})^{-1}$  for R9-S2. The comparison run with uniform density and random seed 2 forms  $\sim 10 (\text{kyr } 100 M_{\odot})^{-1}$ . The extended filamentary structures in the setups with large core radii abet the formation of filamentary stars. In contrast, the very strong mass concentrations in setups with small core radii lowers the formation rate of subsequent stars. This is consistent with the effects of tidal forces on the cloud. The strong mass concentrations maintain a density profile with a slope  $p \gtrsim 1.5$ , which tends to shear condensations apart. The initially large flat cores favour the tidally-induced formation of condensations. As the turbulence is the dominant driver in the formation of overdensities, the tidal effects are only of second-order and may change the formation rate of stars by only a factor of a few. The comparison runs with uniform density lie between the formation rates of the extreme cases, consistent with the additional tidal effects.

### Formation time of protostars

The central collapse and the resulting formation of a protostar in the centre of mass is mainly determined by the initial central density. Figure 7.13 shows the formation time of the first protostar for all density profiles and both random seeds. As expected, the time needed to form the first protostar decreases with increasing central density (crosses and circles). The influence of the random seed of the turbulent motion is relatively small. Both runs

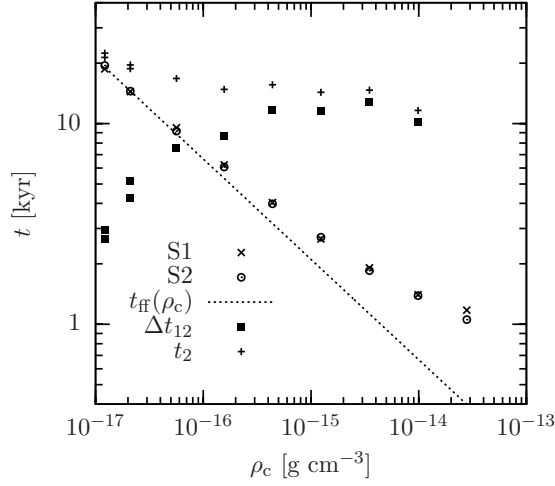


Figure 7.13: Overview of various times as a function of the initial central density  $\rho_c$ . The plot shows the formation time for the first protostar (crosses for runs with S1, circles for S2), the free-fall time, and the time delay between the first and second protostar ( $\Delta t_{12}$ ), and the formation of the second one ( $t_2$ ). The free-fall time of the initial central density serves as a useful estimate for the formation of the first protostar.

(S1, S2) only show small differences for the same central density, indicating that the collapse is dominated by gravitational central infall rather than turbulent flows. The comparison with the free-fall time,  $t_{\text{ff}}$ , reveals that cores with larger core radii form the central protostar very close to the free-fall time evaluated at the initial central density. For the very dense cores, the formation time is delayed compared to the local free-fall time. This is not surprising because the strongly concentrated core covers only a small volume and contains a mass significantly smaller than the Jeans mass (see table 7.1). The central region therefore needs to accrete some gas before becoming unstable. Nevertheless, the initial central density serves as a rough estimate for the formation time of the first protostar.

How dominant the first protostar is in comparison to subsequent protostars depends on its mass evolution and therefore primarily on the time difference between its formation and the formation of further objects as well as on the accretion processes after the formation of subsequent protostars. The larger the time gap, the more gas can be accreted on to the first protostar and the stronger is its gravitational impact. After the formation of other protostars the evolution of the accretion rate will be important. Figure 7.14 shows the time difference between the formation of protostars (see also ta-

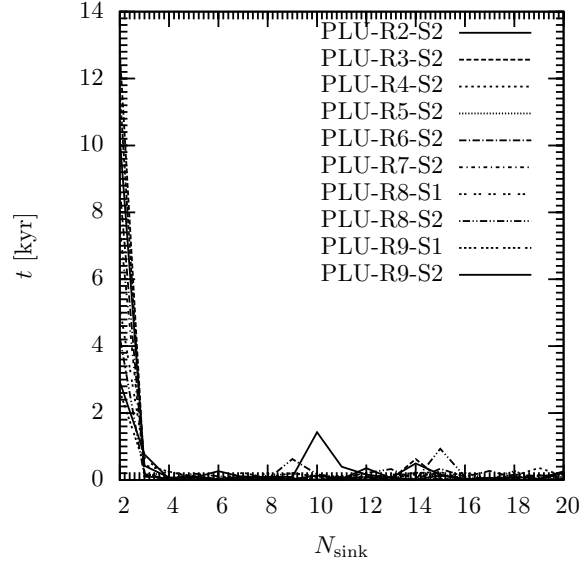


Figure 7.14: Time gap between the formation times of the first 20 protostars. The plotted time is the difference between the formation of protostar  $n$  and the previous one  $n - 1$ . The lower the initial density the smaller is the time gap to the formation of the second protostar. As soon as more objects form, they form in very short time intervals.

ble 7.2.2). The formation of the second protostar indicates the beginning of the filamentary collapse. Therefore, the second and all further protostars form shortly one after another, showing the uniform collapse of the filaments. However, the speed at which filaments form and collapse is significantly influenced by the density profile and the central collapse. In figure 7.15 we plot the absolute formation time of the protostar and the distance of their location of formation to the point where the first protostar was formed. This first object of course forms with a distance of 0 to itself, which is marked with an arrow. There is a clear correlation between the formation of the first protostar and the subsequent collapse of filamentary condensations. A simulation with an early formation of the first protostar also shows an early collapse of filaments. The distances however do not seem to show systematic behaviour. Note that in this figure only the first 20 protostars of each setup are shown in order to keep the plot readable. The appearance of filamentary protostars shows that a strong central mass concentration and a resulting fast collapse do not delay the condensation of filaments but accelerate it. The density enhancements and the resulting increase in gravitational attraction is stronger than disrupting tidal effects, especially in the dense region at small distances from the centre.

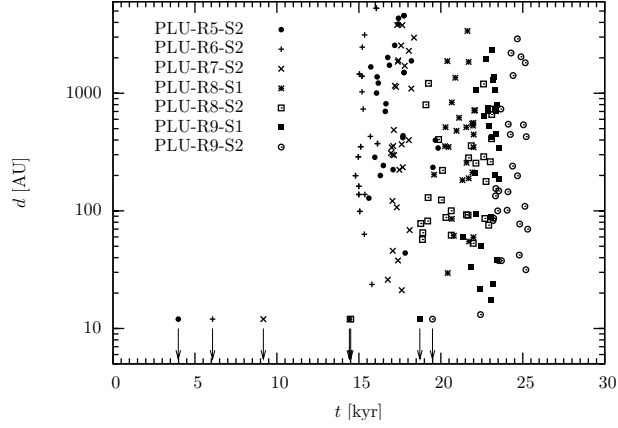


Figure 7.15: Formation time and distance to the location where the first protostar was formed. The first protostars are indicated with arrows. The earlier the first object is created the earlier filaments collapse forming numerous stars.

### Accretion rates and dominant central protostar

In order to determine the transition between a cloud collapse with dominant central protostar and one with many protostars formed in filaments, the mass evolution of the first protostar is important. If the accretion rate onto the first collapsed object is very high, it may grow to the most massive star before other protostars form in its neighbourhood. After the formation of neighbours, the further accretion process strongly depends on how efficient the accretion flow can reach the central star.

Figure 7.16 shows the time evolution of protostars for selected setups. We show the simulations with a core radius R5 or larger and multiple protostars. Setups with smaller core radius have very large time gaps between the formation of the first and the subsequent protostars. Because of the high accretion rates, the first collapsing object can grow to a massive protostar before other neighbours form. Hence, up to the end of the simulation, they are always the dominant protostar. Plot (a) in figure 7.16 shows the total mass of all formed protostars, in part (b) we plot the total accretion rate onto all stars. The mass evolution of the first protostar can be seen in panel (c) and the lower part presents the number of stars in the setup. The time axis is shifted to the formation time of the first protostar in each run. The total mass enclosed in all objects increases rapidly during the entire simulation time, which reflects the high total accretion rate (b). Although the accretion strongly varies with time, the values are above  $10^{-4} M_{\odot} \text{yr}^{-1}$  during the entire simulation. The mass of the first protostar increases rapidly at the beginning and at roughly

constant accretion rate until other companions form (d). In all cases the mass accretion onto the first protostar decreases significantly at this point in the evolution, while the total accretion rate onto all protostars remains high. Hence, we can conclude that the accretion onto the central object is shielded very efficiently and that its final mass is mainly determined by the time gap between its formation and the formation of subsequent stars.

## 7.5 Tidal effects – summary and conclusions

We performed three-dimension simulations of a dense turbulent molecular cloud core with a diameter of 0.2 pc containing a total mass of  $100 M_{\odot}$ . The gas is assumed to be isothermal at a temperature of 20 K. All clouds have supersonic turbulent velocity fields with an average rms Mach number  $\mathcal{M} = 3.3$ . We varied the initial density profile of the cloud with different Plummer-like distributions as well as the random seed of the turbulent motion. In total 9 different density realisations with 2 random velocity fields each were set up.

With this study we aim to answer under what condition the evolution of the cloud is dominated by an early formed central protostar that grows to the most massive one in the cluster and dominates the dynamical evolution of the nascent cluster rather than many protostars that form along collapsing filaments induced by the turbulence. In addition, we analysed the impact of tidal forces on the fragmentation of the cloud. We can summarise our conclusion as follows:

- A strong central density concentration accelerates the star formation process. This applies to both the first star that forms in the centre of a highly concentrated cloud as well as stars that form subsequently in collapsing filaments.
- The collapse of filaments proceeds uniformly, even in extreme density concentrations. Once filamentary stars start to form, they form one by one with short time gaps in between.
- Overall, tidal effects do not play an important role in the presence of the applied supersonic turbulence. The formation of overdense regions that can resist tidal disruption is fairly independent of the initial density profile. In all cases there are large radial ranges where (far) more than 20% of the total mass is located in tidally stable regions. However, tidal forces may have a second-order effect on the formation rate of protostellar objects, which shows a consistent dependency of the

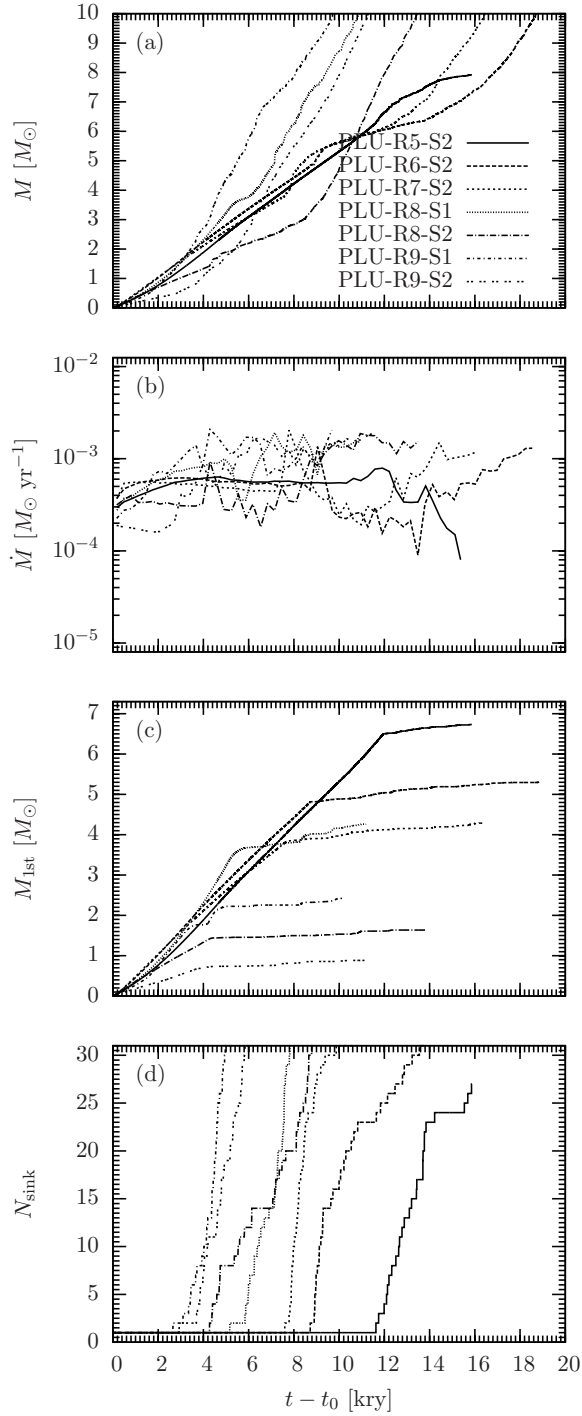


Figure 7.16: Protostellar evolution of the setups. From the top to the bottom the panels show the total mass captured in all protostars (a), the total accretion rate (b), the mass of the first protostar (c) and the number of collapsed objects (d). As soon as filamentary protostars formed the accretion onto the first one is shielded efficiently.

tidal effects on the density profile. For flat density distributions, tidal forces can amplify local overdensities leading to a higher protostellar formation rate for the filamentary condensations. Steeper density profiles, i.e., profiles with a small flat inner core, result in tidal forces that attenuate overdensities and reduce the formation rate.

The random realisation of the turbulent motions has a noticeable impact on the individual locations of tidally stable gas and thus may abet or retard the effect of tidal disruption perceptibly.

- The transition between initial density profiles that form one dominant central protostar and an initial setup that forms a cluster of stars from subsequently collapsing filaments is indicated by two quantities: (a) a vanishing time gap between the formation of the first and other stars, i.e., a sufficiently flat central core in the density distribution and (b) equal time scales for the free-fall time of the flat core and the turbulence crossing time for the core radius. Case (a) is an important condition, because accretion onto the first central star is efficiently shielded after the formation of other stars in our setups.
- In case of a dominant central star, the later formation of further stars strongly depend on the impact of the turbulent velocity field on the gas flow towards the centre of the cloud. Centrally converging flows push the material into the central region where it is efficiently accreted onto the central star, retarding the formation of filaments and inhibiting collapsing condensations within them. Diverging central flows act against the gravitational central collapse, and delay the infall of the gas. As a result, the gas in the central region has more time to form dense filaments and protostars. This delay is additionally supported by a larger specific angular momentum, which is likely to arise from the slightly longer collapse time and the accumulated angular momentum from a larger amount of gas. However, the angular momentum is always significantly smaller than the Keplerian value.



# Chapter 8

## Cluster properties

This chapter is published in parts in Girichidis et al. 2012, MNRAS 420, 3264.

### 8.1 Introduction

In the current paradigm of star formation, most of the stars form in a clustered environment (Lada et al., 2003). Concerning massive stars, studies by de Wit et al. (2004, 2005) show that only  $\sim 20\%$  of the their selected O-stars are field stars. Of these, about half can be traced back to a cluster or association origin, and only about 5 – 10% of them can not be assigned to any grouped formation manner and are thus true field stars.

Over a huge spatial range of astrophysical objects and thus also during the collapse of a molecular cloud and the formation of a stellar cluster, the observed kinetic energy shows a robust scaling with the size of the object (Larson, 1981; Solomon et al., 1987; Ossenkopf and Mac Low, 2002; Heyer and Brunt, 2004; Hily-Blant et al., 2008; Roman-Duval et al., 2011). This global analysis, however, does not take into account the spatial and dynamical substructure of small-scale collapsing regions with sizes below 0.1 pc. The energy balance and virial state of the star-forming region may vary during the formation of the cluster and for different degrees of substructure in a cloud. Local changes in the dynamics may lead to different formation modes of the cluster and alter the stellar distribution and the accretion process in a nascent cluster.

Within a cluster, the distribution of stars is generally not uniform, but shows signatures of mass segregation with a tendency of more massive stars to be located closer to the centre of the cluster. This phenomenon is observed in many young clusters (Hillenbrand and Hartmann, 1998; Stolte et al., 2005,

2006; Kim et al., 2006; Harayama et al., 2008; Espinoza et al., 2009; Bon-temps et al., 2010; Gennaro et al., 2011). However, the detailed definitions of mass segregation and the regions where they apply lead to controversies. Kirk and Myers (2011) find mass segregation in small groups in Taurus, Parker et al. (2011) find more massive stars to be inversely mass segregated, concentrating on the complex as a whole. In addition, there is a strong debate, whether the observed mass segregation in young clusters is primordial or due to dynamical interactions via two-body relaxation. One fundamental problem of that debate lies within the definition of mass segregation and the methods and tools to determine the segregation state. Allison et al. (2009) define mass segregation as massive stars located close to other massive stars. Kirk and Myers (2011) base their mass segregation on the distance of the more massive stars to the centre of the local association. Maschberger and Clarke (2011) investigated mass segregation of a collection of smaller cores and modified the model by Allison et al. (2009) to be more robust in case of outlier stars. In addition, they also used local surface density as a measure of mass segregation. Generally, the substructure of the region in question plays a significant role in the explanation of the origin of mass segregation. Whereas the global system might not have enough time to dynamically relax, the small individual subclusters might well be able to reach a relaxed segregated state. In addition, the final mass segregation may crucially depend on how much degree of mass segregation is preserved during the merger of small subclusters, i.e. how much mass segregation the merged structure can inherit from its constituents. Consequently, a combined investigation of the degree of substructure as a function of time, the energetic state of the cloud, the formation mode of stars within the cluster, and the formation of the clusters themselves is absolutely crucial to understand the mass segregation process.

In this study we analyse the dynamical evolution of collapsing cloud cores and their virial state before and during the formation of protostars. In addition, we investigate the resulting substructure during the collapse and the possible degree of dynamical mass segregation for dense collapsing cloud cores in numerical simulations. We vary the initial density profile as well as the initially imposed turbulent motions and analyse their impact on the later cluster structure. The simulations follow the collapse of the core and the formation of protostars. We find that the initial conditions have a large impact on the degree of substructure in a cluster and that the clusters show strong dynamical interactions between the protostars. As a result, the individual subclusters are very likely to have enough time for dynamical mass segregation. In contrast, for the global cloud, the time scales for dynamical relaxation are too long in comparison to the time scale at which stars form in these dense cores. Due to the strong dynamical interactions in the cen-

tral region of the (sub)clusters from their formation onwards, it is basically impossible to define primordial mass segregation in the simulated cores.

The chapter is organised as follows. In section 8.2 we introduce the methods that we use to analyse the energy state, the degree of substructure, and the mass segregation. Section 8.3 presents our results, separately for the global cloud and the central or main subclusters. Section 8.4 and 8.5 comprise the discussion of the obtained results and the conclusions, respectively.

## 8.2 Cloud and cluster analysis

In this section we briefly motivate and summarise the methods we used to analyse our simulation data.

### 8.2.1 Energy analysis

The global energy partitioning of a gas cloud can be quantified by the ratio of kinetic to the potential energy  $E_{\text{kin}}/|E_{\text{pot}}|$ , where a value of 0.5 corresponds to a virialised cloud. During the collapse of the cloud and the collapse of fragments into protostars, potential energy is converted into kinetic energy and transferred from the smooth gas to relatively compact protostars. In order to investigate the energy evolution of the collapse, we analyse the energy budget for the gas and the protostars separately.

The total kinetic energy of the gas is calculated by simply summing over all cells in the cloud

$$E_{\text{kin,gas}} = \frac{1}{2} \sum_i m_i (v_{i,x}^2 + v_{i,y}^2 + v_{i,z}^2). \quad (8.1)$$

The kinetic energy of the protostars,  $E_{\text{kin,sink}}$ , is found analogously. For the potential energy of the gas we integrate numerically over radial bins around the centre of mass, yielding

$$E_{\text{pot,gas}}(r) = - \int \frac{G M(r) dm(r)}{r}, \quad (8.2)$$

where  $G$  is Newton's constant,  $M(r)$  the enclosed mass inside radius  $r$ , and  $dm(r)$  the mass in the radial shell with thickness  $dr$ . The potential energy of the protostars can be calculated by summing over the point masses

$$E_{\text{pot,sink}} = - \sum_{i \neq j} G \frac{m_i m_j}{|r_i - r_j|}. \quad (8.3)$$

However, in order to avoid the formation of hard binary systems and resulting very small time steps, we apply a softening term in the computation of the gravitational force between the protostars. For the softening we use the energy-conserving formalism described in [Price and Monaghan \(2007\)](#) which yields a potential energy of

$$E_{\text{pot,sink}} = \sum_{i \neq j} G m_i m_j \phi(r_i - r_j, h), \quad (8.4)$$

with a kernel function  $\phi$  (see [Appendix C.1](#)).

The internal motions of the gas and the protostars are quantified using the mass-weighted velocity dispersion

$$\sigma_k^2 = \frac{\sum_i m_i (u_{k,i} - \langle u_k \rangle)^2}{\sum_i m_i} \quad (8.5)$$

where  $k \in \{x, y, z\}$  and  $\langle u_k \rangle$  is the mean velocity in dimension  $k$ ,

$$\langle u_k \rangle = \frac{\sum_i m_i u_{k,i}}{\sum_i m_i}. \quad (8.6)$$

The three-dimensional velocity dispersion is then given by

$$\sigma_{3D} = \sqrt{\sum_k \sigma_k^2}. \quad (8.7)$$

In the simulations we calculate  $\sigma_{3D}$  using each component of the velocity. For the one-dimensional velocity dispersion we assume the same value for all three components and thus use  $\sigma_{1D} = \sigma_{3D}/\sqrt{3}$ . So far we have only considered the turbulent contribution to the velocity dispersion. Including the thermal contribution, the total dispersion along the line of sight is

$$\sigma_{\text{tot}} = \sqrt{\sigma_{1D}^2 + c_s^2}. \quad (8.8)$$

### 8.2.2 Subclustering

Depending on the interplay between turbulent motions and the central collapse of a cloud, the spatial distribution of protostars may vary significantly (see [chapter 5](#)). In order to analyse the clustering properties of our protostars, we use the  $Q$  value ([Cartwright and Whitworth, 2004](#))

$$Q = \frac{\langle s \rangle_n}{\langle m \rangle_n} \quad (8.9)$$

of the clusters. Here,  $\langle s \rangle_n$  is the normalised mean separation of the protostars and  $\langle m \rangle_n$  is the normalised mean length of the edges of the minimal spanning tree (MST), where the edge is the distance between two protostars. For a detailed discussion of the motivation for this definition of  $Q$  see [Cartwright and Whitworth \(2004\)](#).

The distribution function  $p(s)$  describes the probability of two protostars to be separated by the distance,  $s$ . We discretise  $p(s)$  with  $N_{\text{bin}}$  bins for the entire cluster, leading to an equal-sized bin width of  $\Delta s = 2R_C/N_{\text{bin}}$ , where  $R_C$  is the cluster radius. The normalised number of pairs in bin  $i$  can thus be expressed with

$$p(i) = \frac{2N_i}{N_C(N_C - 1)\Delta s}. \quad (8.10)$$

Here  $N_i$  denotes the number of pairs with a distance in the range  $[i\Delta s, (i + 1)\Delta s)$  and  $N_C(N_C - 1)/2$  is the total number of separations for  $N_C$  cluster members. Multiple peaks in the distribution function are related to subcluster structure, which gives higher counts at low distances due to the small separations within each subcluster and higher counts at a larger separation due to the large distance between the subclusters. In case of no distance degeneracy between subclusters, the number of peaks equals the number of subclusters. The mean value  $\langle s \rangle$  of all  $N_C(N_C - 1)$  particle separations  $s_j$ ,

$$\langle s \rangle = \frac{2}{N_C(N_C - 1)} \sum_j s_j, \quad (8.11)$$

gives a measure for the mean distance between particles in the set.

The MST is calculated using the [Gower and Ross \(1969\)](#) description of Prim's algorithm ([Prim, 1957](#)). The more particles are confined in an observed area, the smaller is the mean edge of the tree. The resulting decrease of the mean edge due to the increasing number of nodes in the tree has to be corrected by a dimensionality factor. The correction factor for the three-dimensional cluster model with cluster volume  $V$  was set to

$$\frac{(VN_C^2)^{1/3}}{N_C - 1}, \quad (8.12)$$

taken from [Schmeja and Klessen \(2006\)](#).

For stellar clusters with a smooth radial density gradient,  $Q$  ranges from 0.8 – 1.5, corresponding to a radial density distribution of particles  $n \propto r^{-\eta}$  with  $\eta = 0$  to 2.9. Clusters with substructure have  $Q = 0.8 - 0.45$ , decreasing with increasing degree of subclustering. A detailed relation between  $Q$ ,  $\eta$  and the degree of subclustering can be found in [Cartwright and Whitworth \(2004\)](#).

### 8.2.3 Mass segregation

A set of stars or protostellar objects may show a mass-dependent spatial distribution within a cluster. In a mass-segregated cluster, massive objects tend to be located closer to the centre of the cluster, whilst low-mass objects occupy regions of larger radii. We quantify the degree of mass segregation using the MST as described in Allison et al. (2009) with the *mass segregation ratio* (MSR)

$$\Lambda_{\text{MSR}} = \frac{\langle l_{\text{norm}} \rangle}{l_{\text{massive}}} \pm \frac{\sigma_{\text{norm}}}{l_{\text{massive}}}. \quad (8.13)$$

The ratio describes, how large the spatial spread of the most massive stars is, compared to the spatial spread of a random choice of stars. How many most massive stars are counted and compared to an equal amount of random stars should not be fixed, but rather treated as a free parameter, which we name  $N_{\text{MST}}$ . In order for the MST of the random set of stars to be a good measure for the average spread, we need to pick many sets of random stars and average over the individual lengths of the MST. We set the number of sets to 500 as suggested by Allison et al. (2009). With the average length  $\langle l_{\text{norm}} \rangle$  of these 500 sets and the length of the  $N_{\text{MST}}$  most massive stars,  $l_{\text{massive}}$ , we then determine the degree of mass segregation. The error is computed with the standard deviation  $\sigma_{\text{norm}}$  of  $\langle l_{\text{norm}} \rangle$ . If  $\Lambda_{\text{MSR}}$  takes values significantly larger than unity, the  $N_{\text{MST}}$  most massive stars are located much closer to one another than the same amount of randomly picked stars. Hence the system shows mass segregation. In the opposite case ( $\Lambda_{\text{MSR}} \ll 1$ ) the most massive stars have much larger distances between one another than a set of random stars in the cluster and the system shows inverse mass segregation.  $N_{\text{MST}}$  is basically a free parameter that we loop over starting from 2 up to half of the total number of sink particles, in order to determine the number  $N_{\text{MST}}$  up to which the system is mass segregated, i.e.,  $\Lambda_{\text{MSR}} > 1$ .

Mass segregation can either originate from dynamical  $N$ -body relaxation or is primordial in nature, where the latter case means the more massive stars form closer to the centre. In order to analyse whether mass segregation is primordial or due to dynamical processes, we use the mass segregation time (Spitzer, 1969),

$$t_{\text{seg}}(M) \approx \frac{\langle m \rangle}{M} t_{\text{relax}}, \quad (8.14)$$

with  $\langle m \rangle$  being the average mass of all stars in the cluster and  $M$  the mass of the star in question. The relaxation time  $t_{\text{relax}}$  can be expressed in terms of the number of stars  $N$ , the radius of the cluster  $R_C$ , and the stellar velocity dispersion  $\sigma$ , yielding for the mass segregation time (e.g. Binney and

Tremaine, 1987),

$$t_{\text{seg}}(M) \approx \frac{\langle m \rangle}{M} \frac{N}{8 \ln N} \frac{R_C}{\sigma}. \quad (8.15)$$

By setting the time according to different stages in the simulation, one can obtain the minimum mass down to which stars had enough time to dynamically mass segregate. Care must be taken when applying the mass segregation time to hydrodynamic collapse simulations. In contrast to old stellar clusters, where there is no or very little interstellar gas left and consequently  $N$ ,  $\langle m \rangle$  and  $M$  do not vary with time, hydrodynamic collapse simulations follow the formation of protostars from the beginning of the collapse. Not only do protostars form at different times, they also accrete further gas from the surrounding dense medium in which they were born and are subject to gas drag forces. The number of protostellar objects  $N$ , their individual masses  $M$ , their mean mass  $\langle m \rangle$ , and the cluster radius  $R$  are therefore strongly varying with time. Consequently, the mass segregation and the minimum segregated mass for a given time can not be calculated for the total set of objects as a whole. Instead, the possibility of being segregated within the cluster has to be estimated for each star individually by taking into account the formation time and the growing mass of the star due to accretion.

## 8.3 Cluster properties – results

### 8.3.1 Overview

We follow the cloud collapse until 20% of the mass is accreted by sink particles. The simulation time, the number of formed protostars, the mass of the most massive protostar and the key parameters of the substructure of the cluster are listed in table 8.1. A column density plot at the end of each simulation is shown in chapter 5, figures 5.4 and 5.5.

The TH profile takes the longest time to form gravitationally collapsing regions and to capture 20  $M_{\odot}$  in sink particles. During this time, approximately 45 – 50 kyr, the turbulent motions can compress the gas in locally disconnected areas, leading to distinct subclusters of sink particles. The stronger mass concentration in the centre of the BE setups and the resulting shorter collapse and sink particle formation time suppresses the formation of disconnected subclusters in favour of one main central cluster. The corresponding PL15 profiles show a very similar overall cloud structure to the BE runs, but significantly different stellar properties. Due to the much stronger gas concentration in the centre of the cloud, all PL15 setups form a protostar very early in the simulation. This initial central protostar accretes the

Table 8.1: List of the runs and their main properties

name	$\mathcal{M}$	total $\frac{E_{\text{kin}}}{ E_{\text{pot}} }$	total $\frac{E_{\text{therm}}}{ E_{\text{pot}} }$	$t_{\text{sim}}$ [kyr]	$t_{\text{sim}}/t_{\text{ff}}$	$N_{\text{sink}}$	$M_{\text{max}}$ [ $M_{\odot}$ ]	$n_{*}^{\text{glob}}$ [ $\text{pc}^{-3}$ ]	$\langle s \rangle$ [ $10^3 \text{ AU}$ ]	$\langle s \rangle_n$	$\langle m \rangle_n$	$Q$
TH-m-1	3.3	0.075	0.047	48.0	0.96	311	0.86	$5.50 \times 10^4$	6.51	0.42	0.11	0.26
TH-m-2	3.6	0.090	0.047	45.5	0.91	429	0.74	$8.00 \times 10^4$	8.51	0.65	0.14	0.21
BE-c-1	3.3	0.058	0.039	27.5	0.55	305	0.94	$1.70 \times 10^6$	3.11	0.16	0.09	0.53
BE-c-2	3.6	0.073	0.039	27.5	0.55	331	0.97	$3.60 \times 10^4$	5.68	0.31	0.08	0.27
BE-m-1	3.3	0.053	0.039	30.1	0.60	195	1.42	$3.20 \times 10^6$	1.10	0.13	0.13	1.03
BE-m-2	3.6	0.074	0.039	31.9	0.64	302	0.54	$2.48 \times 10^6$	1.46	0.13	0.09	0.74
BE-s-1	3.3	0.055	0.039	30.9	0.62	234	1.14	$3.70 \times 10^7$	0.52	0.11	0.14	1.30
BE-s-2	3.5	0.074	0.039	35.9	0.72	325	0.51	$3.20 \times 10^6$	1.43	0.21	0.14	0.68
PL15-c-1	3.3	0.056	0.038	25.7	0.51	194	8.89	$2.42 \times 10^6$	1.99	0.11	0.06	0.71
PL15-c-2	3.6	0.068	0.038	25.8	0.52	161	12.3	$1.66 \times 10^4$	7.82	0.45	0.09	0.21
PL15-m-1	3.3	0.050	0.038	23.8	0.48	1	20.0	—	—	—	—	—
PL15-m-2	3.6	0.071	0.038	31.1	0.62	308	6.88	$2.66 \times 10^6$	1.21	0.11	0.11	0.99
PL15-s-1	3.3	0.053	0.038	24.9	0.50	1	20.0	—	—	—	—	—
PL15-s-2	3.5	0.069	0.038	36.0	0.72	422	4.50	$1.11 \times 10^7$	1.01	0.16	0.19	1.20
PL20-c-1	3.3	0.042	0.029	10.7	0.21	1	20.0	—	—	—	—	—

The acronym for the run is shown in the first column, where the first part indicates the density profile, the middle letter the turbulent mode ('c' for compressive modes, 's' for solenoidal modes and 'm' for a natural mix of both), and the number at the end of each name the random seed for the turbulence. The initial energetic state is given by the Mach number  $\mathcal{M}$ , and the ratios of kinetic and thermal energy to the potential energy.  $t_{\text{sim}}$  and  $t_{\text{sim}}/t_{\text{ff}}$  show the simulation time,  $N_{\text{sink}}$  the total number of protostars, and  $M_{\text{max}}$  the mass of the most massive protostar. The stellar number density is shown in column  $n_{*}^{\text{glob}}$ . The global cluster properties are given as the mean separation between the protostars  $\langle s \rangle$ , the normalised mean separation  $\langle s \rangle_n$ , the normalised mean length of the minimal spanning tree  $\langle m \rangle_n$ , and the ratio  $Q$ .

surrounding gas at a high rate and can grow to a massive protostar before the turbulent motions eventually form collapsing filaments and trigger fragmentation. The PL15 setups with turbulent fields m-1 and s-1 (PL15-m-1, PL15-s-1) do form dense filaments, but no further sink particles until the first protostar reaches a mass of  $20 M_{\odot}$ . In case of multiple sink particles, the clusters are more compact than in the corresponding BE case. The PL20 profile only forms one single sink particle due to the very strong mass concentration. The central protostar forms very early and accretes gas at an almost constant rate of  $\approx 2 \times 10^{-3} M_{\odot} \text{ yr}^{-1}$ , close to the analytical value of a highly unstable singular isothermal sphere (Shu 1977). This results in a total simulation time of only 11 kyr, which is not enough for turbulent motions to form filaments and further sink particles.

The following discussion of the cluster properties therefore abstains from a detailed description of the setups PL15-m-1, PL15-s-1 and PL20-c-1.

### 8.3.2 Energy evolution of the global cloud

In order to better understand the energy evolution, we separately analyse the gas and sink particle contributions to the total energy.

All setups are gravitationally very unstable and start to collapse immediately. As a result, the initial random velocities of the gas are reoriented towards the direction of the central acceleration. The total kinetic energy strongly increases with time due to the infall motion. Figure 8.1 shows a representative example of the kinetic over the potential energy of the gas as a function of radius for different times in the simulation. The cloud starts in a strongly sub-virial state and exceeds a ratio of kinetic to gravitational energy of 0.5 for the entire cloud after roughly 20 kyr. Within a radius of  $10^4$  AU the ratio reaches values greater than unity and diverges in the very central region. This behaviour can be explained by a simple estimate using a singular isothermal sphere, which is characterised by an initial density profile  $\rho \propto r^{-2}$  and approaches a free-fall density profile  $\rho \propto r^{-3/2}$  inside the head of the rarefaction wave (Shu, 1977; Whitworth and Summers, 1985). The corresponding velocity field scales as  $v \propto r^{-1/2}$ . The resulting potential energy scales as  $E_{\text{pot}} \propto r^2$ , while the kinetic energy follows a relation  $E_{\text{kin}} \propto r^{1/2}$ . Consequently, the ratio  $E_{\text{kin}}/|E_{\text{pot}}|$  scales as  $r^{-3/2}$  and diverges for small radii, indicating that the innermost part of the cloud is dominated by kinetic energy.

The different initial density profiles as well as the different formation modes of protostars lead to different radial distributions during the collapse. A comparison of  $E_{\text{kin,gas}}/|E_{\text{pot,gas}}|$  for all setups at the end of the simulation is shown in figure 8.2. A significant difference is found between the simulations

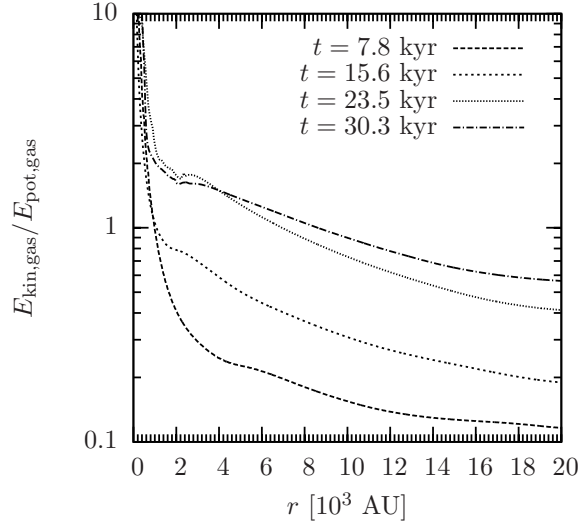


Figure 8.1: Ratio of kinetic over potential energy of the gas for the BE-m-1 setup as a function of radius for different times. The cloud evolves from a strongly gravitationally dominated state to an energy state with  $E_{\text{kin,gas}}/|E_{\text{pot,gas}}| > 0.5$  at the end of the simulation.

with only one protostar (dotted lines) and the ones that form many protostars (solid lines). The three setups with only one protostar show much higher values for most of the cloud and a steeper slope. This is not surprising because the gas in the central region can fall towards the central particle without being disturbed by other sink particles and their  $N$ -body interactions. In case of multiple protostars the ratio  $E_{\text{kin,gas}}/|E_{\text{pot,gas}}|$  shows a large scatter close to the central region ( $R \lesssim 4 \times 10^3$  AU), which can be explained by the local variations in the sink particle positions and motions, and the resulting impact on the gas. The scatter in the energy ratio is significantly lower in the outskirts of the cluster.

The average value as well as the spread of  $E_{\text{kin,tot}}/|E_{\text{pot,tot}}|$  increase when the sink particles' mass is included in the virial analysis (see figure 8.3). There is no systematic correlation between the various initial conditions and the ratio of the energies. The fact that including the protostars leads to higher values, shows that the cluster contributes more to the kinetic rather than the potential energy. A comparison of the kinetic energy of the sink particles and the gas ( $E_{\text{kin,sink}}/E_{\text{kin,gas}}$ ) is plotted in figure 8.4. The ratio is above unity for all simulations with many protostars (solid lines). Although the protostars account for only 20% of the total mass at the end of the simulation, their kinetic energy dominates the total kinetic energy budget of the cloud. Again,

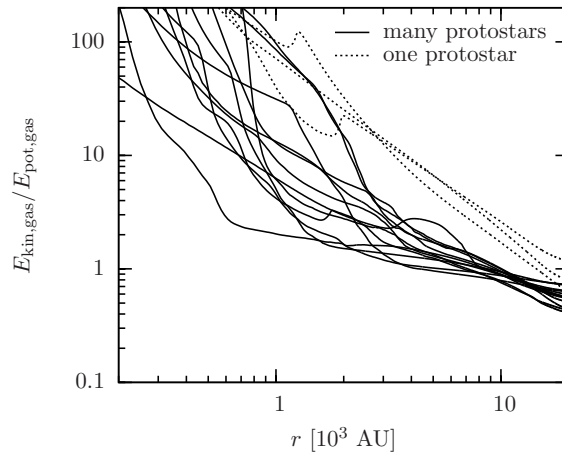


Figure 8.2: Ratio of kinetic over potential energy of the gas for all profiles at the end of the simulation at 20% star formation efficiency. The dotted lines indicate the runs with only one protostar, the runs with multiple protostars are shown with solid lines. Note that the physical times differ strongly between 11 and 48 kyr for the different setups, see table 6.1.

the setups with only one protostar constitute an exception (dotted lines). In these cases, the kinetic energy of the protostar is significantly lower, which can be explained by accretion flows from opposite directions that result in an almost vanishing net momentum transfer onto the protostar (see figure 8.4). The dashed-dotted line shows  $E_{\text{kin, sink}}/E_{\text{kin, gas}}$  for the TH-m-2 setup. As the cloud in this run forms two distinct subclusters with a central void between them (see right part of figure 8.9) the total kinetic energy of the few protostars between the subclusters is relatively low.

As a link to observable properties of star-forming regions we calculate the velocity dispersion for the entire cloud as a function of time. Here we assume isotropy of the motions of the gas and restrict our analysis to the one-dimensional velocity dispersion  $\sigma_{1D}$ . Because of the initial random turbulence, the velocity dispersion of the gas shows anisotropies, which tend to reduce during the simulation. Initially, the deviation from isotropy is of the order of 10 – 20%. During the simulation the value shows variations but decreases to about half of the initial value ( $\Delta\sigma/\sigma \sim 5 - 10\%$ ), averaged over all simulations. There is no clear trend with the varied initial conditions and the number of protostars. Figure 8.5 shows the turbulent velocity dispersion  $\sigma_{1D}$  for the gas for all runs. Initially,  $\sigma$  just reflects the initial turbulent velocity, the increasing values correspond to the additional infall motion. The significantly lower values for the TH profiles are simply due

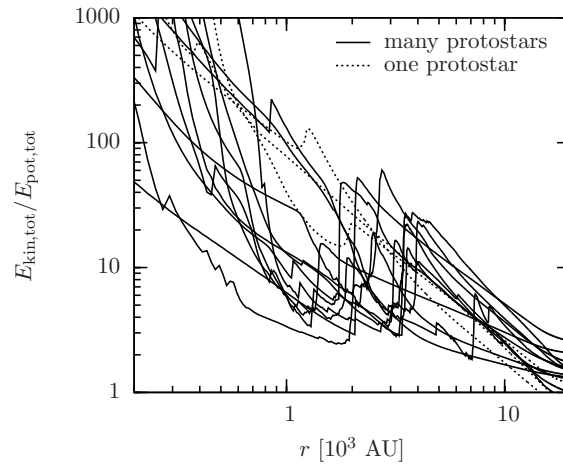


Figure 8.3: Same as figure 8.2 but for the total energies (protostars and gas).

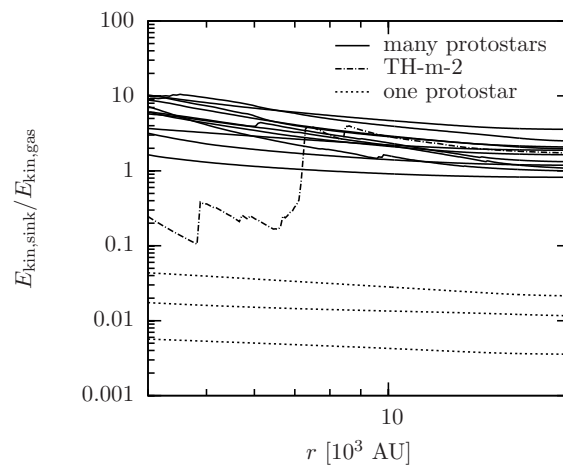


Figure 8.4: Ratio of kinetic energy of the sink particles to the kinetic energy of the gas for all profiles at the end of the simulation. The inner region ( $R_C < 4$  AU) varies extremely because of the slight offsets of the centre of mass and the centre of the cluster and is not shown.

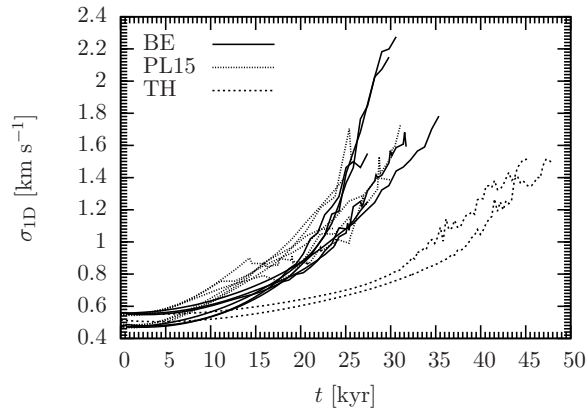


Figure 8.5: Velocity dispersion for the gas for all runs. The values increase over time due to the increasing infall motion.

to the delayed dominant central collapse. The formation of disconnected subclusters reduces the global infall speed in comparison to the other setups with one central cluster. The combined velocity dispersion for gas and sink particles can be seen for the TH profiles in figure 8.6. The plots for the other setups look similar. As shown in figure 8.4, the protostars contain a significant fraction of the kinetic energy. Therefore, the total value including sink particles is remarkably higher. None of the curves saturates during the simulated time, which can be explained by a simple free-fall approximation. The maximum speed that can be reached by free-falling gas is of the order of  $R_0/t_{\text{ff}} \approx 2 \text{ km s}^{-1}$ , where  $R_0$  is the cloud radius and  $t_{\text{ff}}$  the global free-fall time. None of the setups needs more than a free-fall time to convert 20% of the gas mass into stars when we stop the simulation, so no setup had enough time to reach the limiting free-fall velocity dispersion of  $2 \text{ km s}^{-1}$ .

With a focus on the nascent cluster as an  $N$ -body system, we also analyse the virial state of the sink particles without including the contributions of the surrounding gas. To do so, we treat the protostars as point masses and we calculate the gravitational potential via direct summation (equation 8.4). The corresponding ratio of kinetic to potential energy for the sink particles is shown in figure 8.7, excluding the runs with only one protostar. The time axis in the plot is adjusted to the time when the first condensation was created. In the case of all PL15 profiles with multiple sink particles, the second and further sink particles formed with a large delay after the first sink particle. Therefore, the curves for the PL15 profiles start at times  $t - t_0 > 10 \text{ kyr}$  (see  $\Delta t_{12}$  in table 8.2). The first protostars form with the velocity that the collapsing condensation inherits from the gas motion. The positions at which

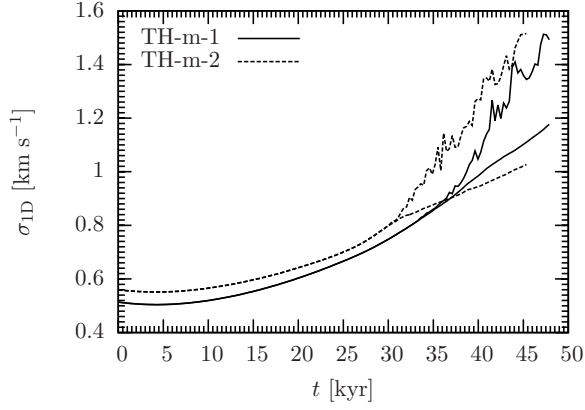


Figure 8.6: Velocity dispersion for the TH setups. The lower curves correspond to the gas only, the higher curves include the turbulent contribution of the sink particles. As the sink particles contain a significant fraction of the kinetic energy, the curves including sink particles are remarkably higher.

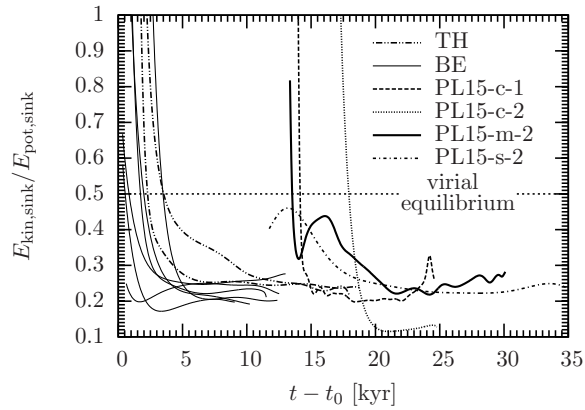


Figure 8.7: Ratio of kinetic to potential energy as a function of time for the sink particles only. The time was adjusted to the formation of the first sink particle in the setup.

they form is determined by the structure of the filaments or the fragmenting disc. As they form independent from one another, sometimes even in separate subclusters, their kinetic and potential energies are uncorrelated. As the protostars form with the velocity of the parental gas cloud and because they are usually separated by a large distance, the initial values of  $E_{\text{kin,sink}}/|E_{\text{pot,sink}}|$  are very high. Soon after their formation, the protostars dynamically decouple from the gas and move towards the central region of the nascent cluster. The system begins to virialise, leading to decreasing values of  $E_{\text{kin,sink}}/|E_{\text{pot,sink}}|$ . Without the formation of subsequent protostars, the system would quickly reach a virialised state. However, as this process continues, the energy ratio of the total cluster is influenced by the virial state of the newly formed objects. If they form at time  $t_i$  at position  $r_i$  with velocities  $v_i$  smaller than the virial velocity  $v_{\text{virial}}(r_i, t_i)$ , they lead to a decreasing energy ratio. A quick analytical estimate illustrates, why this behaviour is expected. The virial velocity is given by

$$v_{\text{virial}} = \left( \frac{GM_{\text{Cl}}}{R_{\text{Cl}}} \right)^{1/2}, \quad (8.16)$$

with the mass and radius of the cluster  $M_{\text{Cl}}$  and  $R_{\text{Cl}}$ . As a lower limit, we can assume a constant stellar density in the cluster over time,  $\rho_*$ , which relates the cluster radius to the cluster mass like  $R_{\text{Cl}}(t) = (3M_{\text{Cl}}(t)/(4\pi\rho_*))^{1/3}$  and thus the virial velocity in this lower limit follows  $v_{\text{virial,low}} \propto M_{\text{Cl}}^{1/3}$ , increasing with time as the total mass of the cluster increases. Of course, the velocity of the gas is also increasing over time due to the collapse of the cloud. However, as shown in figure 8.5, the velocity dispersion of the gas increases over time by a factor of only 3 at most. In addition, figure 8.6 illustrates that the kinetic contribution of the protostars is remarkably larger than that of the gas. In order for the lower limit virial velocity,  $v_{\text{virial,low}}$ , to be higher than the average gas velocity, the cluster mass must grow by a factor of 27 during the entire simulation, which can be achieved. Considering the fact, that the stellar density also increases, the virial velocity will be even higher. Consequently, the newly formed stars, which inherit the low gas velocity, tend to decrease the energy ratio.

The larger the cluster, the lower is the available mass in the central region of the cluster (see chapter 6). Therefore, new protostars must form at increasingly larger radii. In order to show that these new stars are the ones that push the ratio  $E_{\text{kin,sink}}/|E_{\text{pot,sink}}|$  to lower than virialised values, we calculate the ratio as a function of the fraction of total protostars. Figure 8.8 shows the energy ratio with the protostars sorted by their distance from the centre of the cluster. In all cases, only the innermost  $\sim 10 - 30\%$  have a

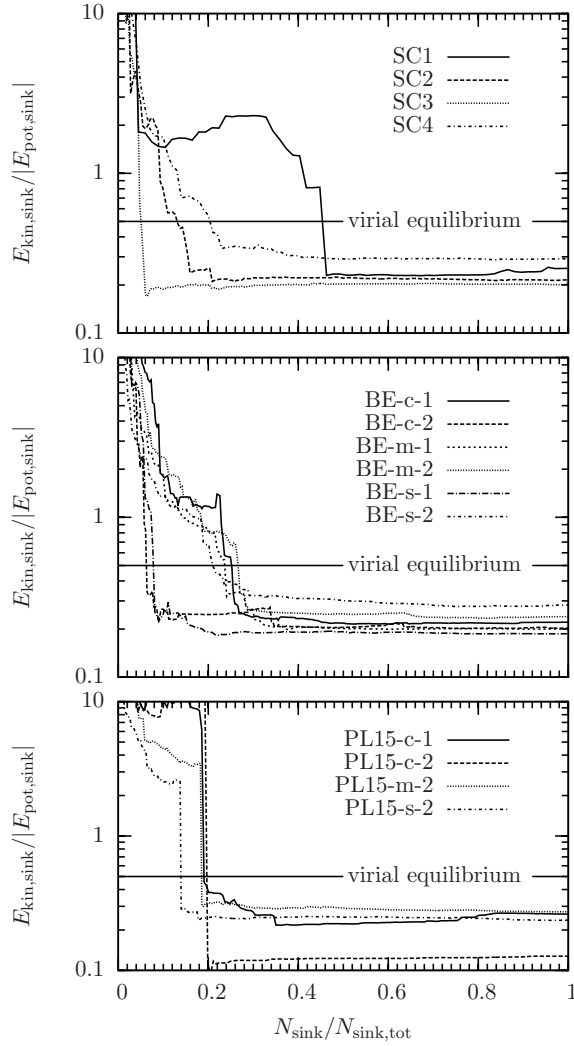


Figure 8.8: Energy balance  $E_{\text{kin,sink}}/|E_{\text{pot,sink}}|$  as a function of normalised number of protostars,  $N_{\text{sink}}/N_{\text{sink,tot}}$ . The protostars were sorted by their distance from the centre of the cluster. In all cases, only the innermost  $\sim 10 - 30\%$  of the stars form a cluster with virial or super-virial energy balance.

virial or super-virial energy balance. The majority of the nascent cluster has an overall sub-virial energy partition (see, e.g., [Offner et al., 2009](#)). But we expect that the ensemble virialises on a dynamical time scale as soon as star formation stops in the cluster region.

From our simulations we conclude that a detailed energy analysis can only be performed properly, if both protostars and gas are included in a self-consistent way. In turn, the remaining gas is essential to the virial state of the nascent cluster.

### 8.3.3 Global cluster properties

In this section we discuss the spatial distribution of the protostars in the simulated cloud. We begin with an analysis of all protostars in the simulations in order to measure the cluster properties of the cloud as a whole. A detailed investigation of individual subclusters without outlier protostars is presented in section [8.3.4](#) and below.

#### TH runs

Both setups with initially uniform density distribution show distinct subclusters as illustrated in figure [8.9](#). We selected the four biggest subclusters for further analysis and named them SC1-SC4. The other subclusters have too few protostars for a statistical analysis. Note that subcluster SC1 is not very compact in the centre. Therefore, our reduction algorithm does not exclude the outliers, which yields the relatively large radius.

The distribution function of the separations between the particles as well as the  $Q$ -value (equation [8.9](#)) of the entire cloud is shown in figure [8.10](#). TH-m-1 shows three different peaks in the distribution function: the one at 9,000 AU corresponds to the distance of SC2 to SC1, the peak at 13,000 AU to the degenerate distance of SC2 to SC5 and SC6, and the last peak describes the distance from the upper subcluster SC1 to SC5 and SC6, which is also degenerate within the width of the distance bin. TH-m-2 shows two main subclusters corresponding to the peak at 15,000 AU in the plot. The degenerate distance between SC3 and SC7 as well as SC4 and SC7 can be seen as small peak in the distribution at 13,000 AU. The  $Q$  value of the entire cloud shows strong variations at the beginning of stellar formation due to the different regions of the cloud where the sink particles are created. Having established the subclusters,  $Q$  shows roughly constant behaviour at a value of  $Q \sim 0.2$  for both runs.

The key properties for the subclusters SC1–SC4 are listed in table [8.3](#). The protostars in SC1 have significantly larger mean separations between

Table 8.2: Reduced cluster properties for the simulations with many sink particles

Cluster	$N_{\text{sink}}$	$M_C$ [ $M_\odot$ ]	$\langle M \rangle$ [ $M_\odot$ ]	$R_C$ [kAU]	$n_*^{\text{red}}$ [ $\text{pc}^{-3}$ ]	$t_1$ [kyr]	$\Delta t_{12}$ [kyr]	$\sigma_{\text{1D}}$ [km/s]	$t_{\text{relax}}$ [kyr]	$t_{\text{avail}}$ [ $t_{\text{relax}}$ ]	$N_{\text{seg}}$	$f_{\text{seg}}$	seg?
SC1 (TH-m-1)	67	4.2	0.063	2.74	$6.82 \times 10^6$	32.0	0.008	1.86	8.01	2.00	19	0.28	0
SC2 (TH-m-1)	182	10.4	0.057	0.97	$4.18 \times 10^8$	29.9	0.776	2.90	4.02	4.31	72	0.40	++
SC3 (TH-m-2)	232	9.4	0.041	1.00	$4.86 \times 10^8$	26.5	0.709	2.82	5.17	3.53	82	0.35	+
SC4 (TH-m-2)	100	5.7	0.057	0.45	$2.30 \times 10^9$	28.5	0.933	3.00	1.12	14.31	77	0.77	++
BE-c-1	192	11.4	0.060	0.64	$1.53 \times 10^9$	14.9	0.279	3.61	2.21	5.58	81	0.42	0
BE-c-2	275	15.0	0.055	5.05	$4.47 \times 10^6$	15.1	0.764	2.43	34.93	0.33	8	0.03	0
BE-m-1	99	11.9	0.121	0.24	$1.50 \times 10^{10}$	19.6	0.052	5.91	0.30	34.66	84	0.85	++
BE-m-2	255	15.7	0.061	1.39	$1.99 \times 10^8$	20.2	0.086	3.20	6.81	1.71	67	0.26	+
BE-s-1	190	16.1	0.085	0.50	$3.18 \times 10^9$	21.5	0.083	4.64	1.35	6.92	100	0.53	++
BE-s-2	288	16.7	0.058	2.12	$6.33 \times 10^7$	22.3	0.004	2.85	12.97	1.05	43	0.15	-
PL15-c-1	170	17.0	0.100	1.46	$1.14 \times 10^8$	1.1	13.5	4.02	4.11	2.69	37	0.22	++
PL15-c-2	79	14.8	0.187	1.64	$3.75 \times 10^7$	1.0	15.5	2.50	1.45	6.43	13	0.16	0
PL15-m-2	240	15.6	0.065	1.00	$5.03 \times 10^8$	1.0	13.3	4.47	3.34	5.03	68	0.28	-
PL15-s-2	396	18.5	0.047	1.46	$2.67 \times 10^8$	0.9	10.3	3.45	9.64	2.57	82	0.21	0

The table shows the properties for the reduced cluster with the number of protostars  $N_{\text{sink}}$ , the total cluster mass  $M_C$ , the average protostellar mass  $\langle M \rangle$ , the radius  $R_C$ , and the protostellar number density  $n_*^{\text{red}}$ . Column  $t_1$  indicates the time of the formation of the first protostar,  $\Delta t_{12}$  the time difference between the formation of the first and the second protostar.  $\sigma_{3D}$  and  $\sigma_{1D}$  show the stellar velocity dispersion of the cluster. The key values for the mass segregation are the relaxation time  $t_{\text{relax}}$ , the available lifetime of the cluster  $t_{\text{avail}}$  in units of the relaxation time, and the total and normalised number of protostars that had enough time to relax dynamically  $N_{\text{seg}}$  and  $f_{\text{seg}} = N_{\text{seg}}/N_{\text{sink}}$ . The column “seg?” indicates the segregation state of the cluster: significantly mass segregated (+++), marginally mass segregated (+), not mass segregated (0), and inversely mass segregated (-).

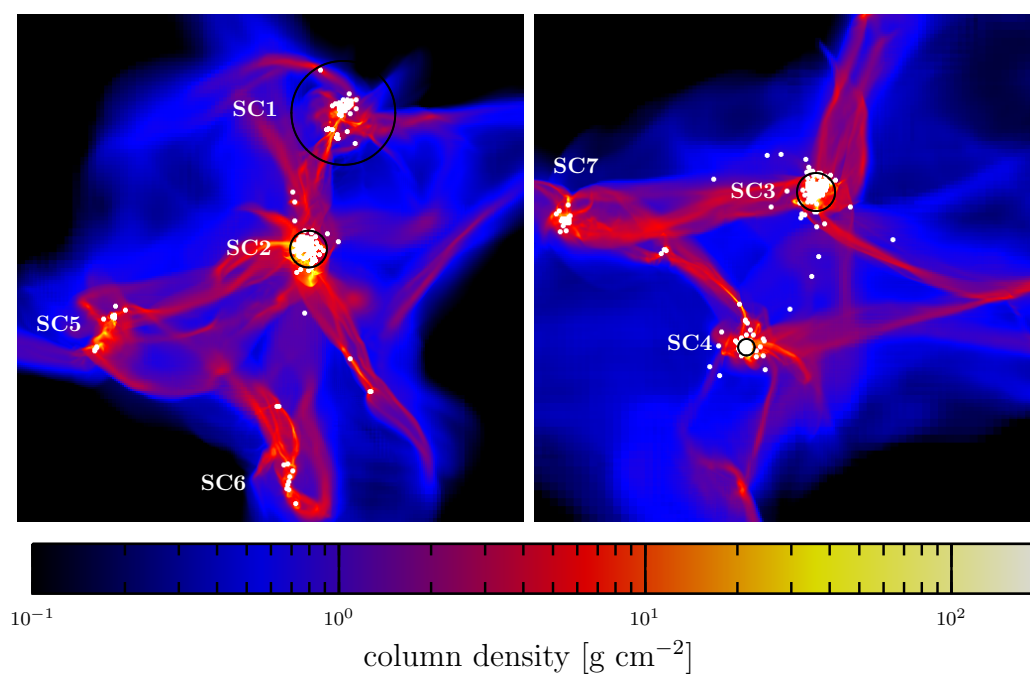


Figure 8.9: Subclusters in the TH runs. The left picture shows TH-m-1 with the subclusters SC1 and SC2. The two largest subclusters in TH-m-2 on the right are labelled SC3 and SC4. The circles indicating the subclusters' diameter are to scale. The total size of the plot is 0.13 pc in both x and y direction.

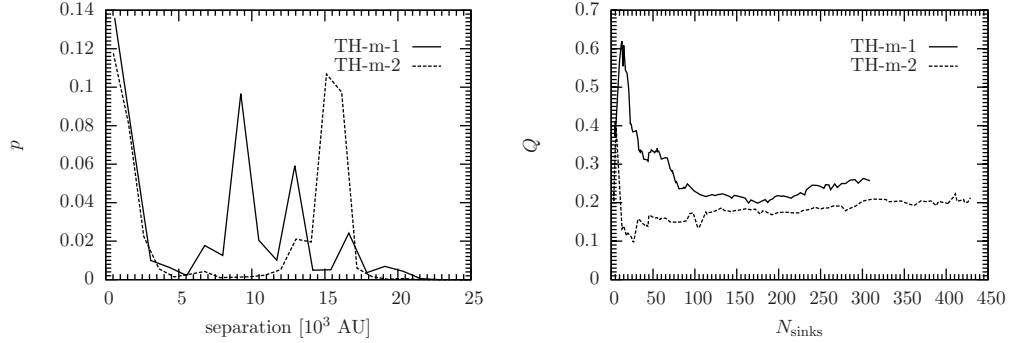


Figure 8.10: Global cluster values for the TH runs. Left plot: TH-m-1 shows three different peaks in the distribution function: the one at 9,000 AU corresponds to the distance of SC2 to SC1 (see figure 8.9), the peak at 13,000 AU to the degenerate distance of SC2 to the lower and left one and the last peak describes the distance from the upper to the lower and left subcluster, which is also degenerate within the width of the distance bin. TH-m-2 shows two main subclusters, whose distance corresponds to the peak at 15,000 AU. Right plot: After roughly 100 sink particles have formed, the  $Q$  value approaches a constant value which is similar for both of the runs, indicating a high degree of substructure in both clouds.

one another and a  $Q$  value of  $\sim 0.7$ , slightly lower than the threshold value to sub-structure of 0.8. The other three subclusters have very similar  $Q$ , indicating a smooth stellar distribution.

## BE runs

The effects of the much more dominant central infall during the collapse of the BE setups can be seen in the average distance between the sink particles and the  $Q$ -value in figure 8.11. The separation distribution shows only one significant maximum for all simulations. However, the peak for the BE-c-2 run is at a much larger distance. There, the sink particles form along large elongated filaments and lead to larger mean separations than in the other BE setups. Here, the strong effects of the compressive turbulent motions have a major impact. The mean separation for both runs with compressive turbulence is significantly larger than for the other runs (see  $\langle s \rangle$  in table 6.1). The  $Q$  values and the resulting degree of substructure are very different and strongly change with time (and consequently  $N_{\text{sink}}$ ) depending on where the sink particles form. BE-c-2 shows strong substructure from the very beginning, BE-c-1 forms protostars at larger radii at a later stage in the

Table 8.3: Subcluster properties from the TH setups

subcluster	$N_{\text{sink}}$	$\langle s \rangle$ [ $10^3$ AU]	$\langle m \rangle$ [ $10^3$ AU]	$Q$
SC1	67	1.13	0.31	0.69
SC2	182	0.49	0.19	1.36
SC3	232	0.51	0.16	1.19
SC4	100	0.23	0.10	1.27

For each subcluster the number of sink particles  $N_{\text{sink}}$ , the mean separation  $\langle s \rangle$ , the mean MST length  $\langle m \rangle$  and the  $Q$  value are shown. SC1 shows signs of sub-structure indicated by a  $Q$  value slightly below the critical transition value of 0.8. SC2, SC3 and SC4 have values of  $Q \gtrsim 1.2$  which indicates a smooth internal structure.

simulation, leading to a decrease of  $Q$  at around  $N_{\text{sink}} \sim 170$ . The two runs with the lower number of sink particles (BE-s-1 and BE-m-1) have the highest values, revealing a rather smooth cluster without much substructure.

### PL15 runs

The even stronger mass concentration in the PL15 profiles shows a systematic influence on the mean distance between the sink particles. The mean particle separation for the PL15-c-1, PL15-m-2 and PL15-s-2 runs is roughly 15–35% smaller than in the corresponding BE runs (see table 6.1). The fact that the mean separation in PL15-c-2 is larger than in BE-c-2 is just due to the fact that the former one forms fewer sink particles; the positions of the distant sink particles at large radii are similar. Figure 8.12 shows the separation function and the  $Q$  values. The distribution function on the left shows one main peak for all setups. The peak for PL15-c-2 is much wider, reflecting the larger central cluster. In addition, the setup forms more protostars further out than other setups. In combination with the lower total number of particles than in the BE-c-2 case, this yields the large value of  $\langle s \rangle$  and result in the lowest  $Q$  value for PL15-c-2. PL15-c-1 and PL15-m-2 are around the threshold value to substructure ( $Q = 0.8$ ), PL15-s-2 is smooth over almost all the simulated time.

### Comparison

There are some general trends of the subclustering properties. The flatter the initial density profile is, the more impact has the turbulent velocity field. This causes collapsing regions to form at larger separations from each other. The observed relation  $\langle Q_{\text{TH}} \rangle \lesssim \langle Q_{\text{BE}} \rangle \lesssim \langle Q_{\text{PL15}} \rangle$  supports this intuitive

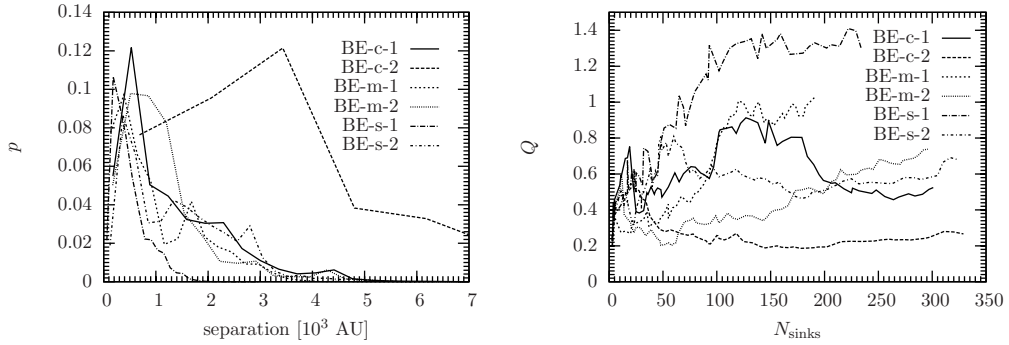


Figure 8.11: Cluster properties for the protostars in the BE runs. The plot of the separations (left figure) clearly shows the formation of only one main cluster for all runs, indicated by only one main peak in the distribution of protostellar separations. However, the cluster structure varies significantly (right figure). The  $Q$  value differs by a factor of more than 5 for the individual runs and shows a correlation with the turbulent modes. Compressive modes show more substructure than mixed and solenoidal modes.

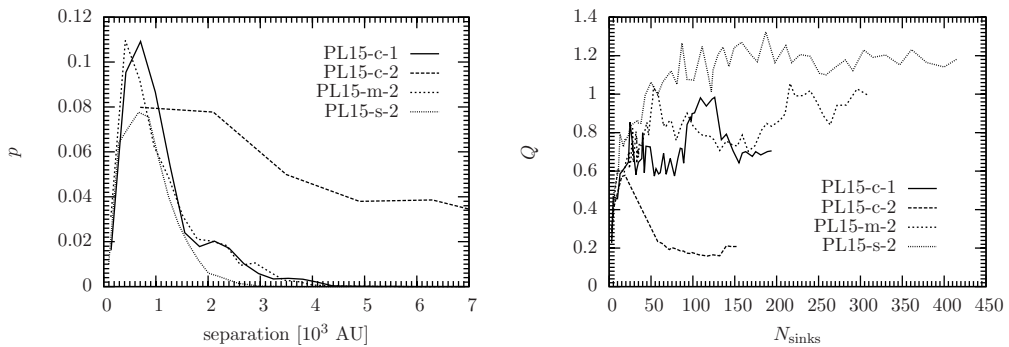


Figure 8.12: Cluster properties for the protostars in the PL15 runs. The plot of the separations (left figure) clearly shows the formation of only one main cluster for all runs. However, the cluster structure varies significantly (right figure).

picture. In a similar manner, compressive turbulent modes lead to collapsing filaments more quickly, not allowing the gas to assemble as close to the centre as in solenoidal turbulent cases. Therefore, within one density profile, the impact of turbulent modes shows  $\langle Q_{\text{comp}} \rangle \lesssim \langle Q_{\text{mix}} \rangle \lesssim \langle Q_{\text{sol}} \rangle$ .

### 8.3.4 Properties of the reduced clusters

Having analysed the total set of protostars in the entire cloud, we now focus on the central regions of the main clusters in each setup, ignoring the outliers that do not belong to the main cluster. In order to find the individual compact clusters, we iteratively exclude outlier protostars until we reach a converged cluster configuration. We first select the main region by eye. In the two TH runs we select the already mentioned subclusters (see figure 8.9), in all other setups with many sink particles we chose the central cluster. The particle reduction method works as follows. We find the centre of mass of the set of particles. Then we compute the average separation  $\langle s \rangle$  between protostars and remove all objects that are located at radii larger than three times the mean separation from the centre of mass. We then recalculate the centre of mass and repeat the exclusion until no further particle is excluded from the set of objects. The radius of the cluster  $R_C$  is set to  $3\langle s \rangle$ , ensuring that all selected particles are within the cluster radius. The factor three is somewhat arbitrary, but after some tests it turned out to be a useful distance factor that does exclude all very distant particles, but no or very few particles that could be dynamically important for the cluster within the simulated time. The key values for the reduced clusters are listed in table 8.2, their velocity dispersion as a function of stellar density is shown in figure 8.13. For the following discussion we focus on the reduced clusters.

As the motions in the forming cluster are highly chaotic and the number of protostars is constantly growing, the time evolution of the reduced cluster properties fluctuates, i.e., every time step, the reduction algorithm chooses different protostars to belong to the reduced cluster. It is therefore impossible to follow single protostars within the reduced clusters. In the further analysis we thus concentrate on the clusters at the end of the simulation.

### 8.3.5 Mass segregation

We address the mass segregation problem in two ways. Firstly, we investigate the time that each protostar had for dynamical mass segregation after its formation, and secondly, we analyse the reduced cluster at the end of the simulation with the minimal spanning tree, neither taking into account the

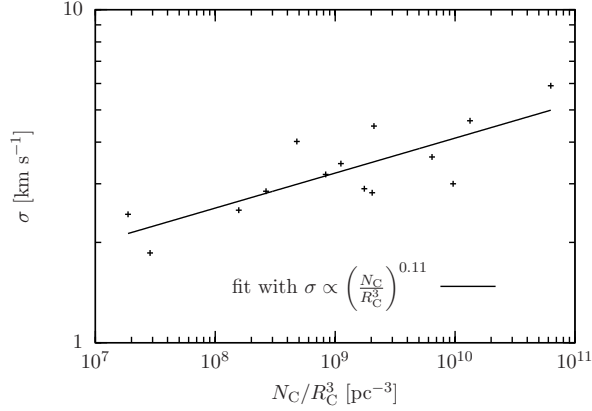


Figure 8.13: Velocity dispersion of the selected main (sub)clusters as a function of stellar density. The data points represent the clusters at the end of the simulation. The clusters show a weak correlation with a significant scatter.

different formation times of the particles nor the change in mass during the accretion process.

Although the degree of mass segregation can not be calculated for a single particle but has to be seen as a global cluster property, we analyse the possibility to dynamically mass segregate via two-body relaxation for every single protostar. According to equation (8.15) we set the time  $t_{\text{seg}}$  to the time that the sink particle had for mass segregation, i.e., the difference between the end of the simulation and the creation time of the protostar in question. From that we infer the threshold mass  $M_{\text{seg}}$  with the given final values of  $R_C$  and  $\sigma$ . If the mass of this particular protostar is larger than the threshold mass, we count it for possible mass segregation. The quantity  $N_{\text{seg}}$  in table 8.2 refers to the total number of possibly mass-segregated objects;  $f_{\text{seg}}$  denotes the fraction  $N_{\text{seg}}/N_C$ . The strong dynamical effects during the formation of the cluster result in significantly varying values for  $R_C$ ,  $N_C$ , and  $\sigma$ . However, the combined quantity in equation (8.15) differs much less and serves as a remarkably stable estimate. With a roughly constant formation rate of protostars, a strong correlation between the protostellar number density ( $N_C/R_C^3$ ) and  $f_{\text{seg}}$  as found in the simulated clusters is not surprising (see figure 8.14). The segregation fraction  $f_{\text{seg}}$  covers a very large range (0.03 – 0.85), indicating that in some setups almost all objects had enough time to dynamically mass segregate, while in others hardly any protostar can relax in the cluster.

For the second approach, we analyse the mass segregation at the end of the simulation according to equation (8.13). The values for  $\Lambda_{\text{MST}}$  as a function

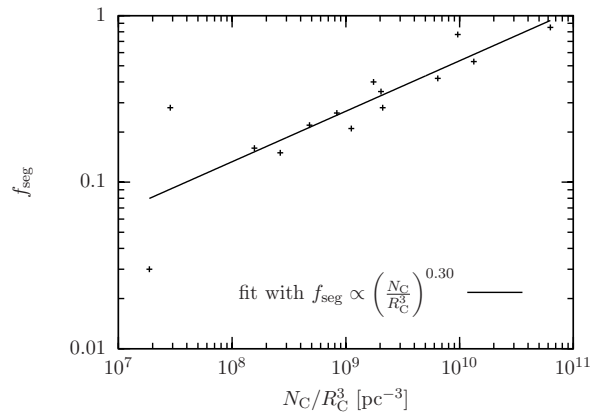


Figure 8.14: Possible fraction of dynamically mass-segregated stars as a function of protostellar number density of the cluster. The data points represent the reduced clusters at the end of the simulation and show a strong correlation with only little scatter.

of  $N_{\text{MST}}$  for all clusters are plotted in figure 8.15. In order to keep the plots readable, most of the curves are shown without errorbars; we included errorbars for the lowest curves that still differ from unity within a  $1\text{-}\sigma$  error in order to give some indication of the uncertainties involved. In order for mass segregation to be eminent,  $\Lambda_{\text{MST}}$  needs to be significantly above unity for mass segregation and significantly below unity for inverse mass segregation. The upper panel shows  $\Lambda_{\text{MST}}$  for the TH runs. All subclusters except for SC1 show mass segregation up to at least  $N_{\text{MST}} \sim 30$ , i.e., the 30 most massive protostars form a compact subset of the cluster members around the centre of the cluster. Including more than the 30 most massive objects to the subset enlarges the spatial extent such that the position of the chosen subset is hardly distinguishable from a random subset of the same number of cluster members. SC3 and SC4 show a significantly higher degree of mass segregation below  $N_{\text{MST}} \sim 20$  and  $N_{\text{MST}} \sim 12$ , respectively. This corresponds to a minimum segregated sink mass of  $0.074 M_{\odot}$  in SC3 and  $0.11 M_{\odot}$  in SC4 and contains roughly 40% and 37% of the total cluster mass. Even higher values for  $\Lambda_{\text{MST}}$  can be found in the BE setups (middle panel). Here the central clusters in BE-m-1 and BE-s-1 show  $\Lambda_{\text{MST}} > 1.5$  below  $N_{\text{MST}} \sim 35 - 45$  and  $N_{\text{MST}} \sim 20$ , respectively. The minimum segregated mass in BE-m-1 is  $M_{\text{seg}} \approx 0.1 M_{\odot}$ , the total confined mass down to this mass is about 75%, in the latter case  $M_{\text{seg}} = 0.17 M_{\odot}$ , containing around 40% of the cluster mass. If one includes the second bump of  $\Lambda_{\text{MST}}$  between  $20 < N_{\text{MST}} < 40$  in BE-s-1, the measured contained mass that is segregated is roughly 58%. Among

the PL15 density profile only one cluster shows significant mass segregation, PL15-c-1.  $\Lambda_{\text{MST}}$  is greater than 1.5 for  $N_{\text{MST}} \lesssim 19$ . This gives a minimum segregated mass of  $M_{\text{seg}} = 0.11 M_{\odot}$  and corresponds to a fraction of about 72% of the cluster mass.

There is a weak correlation between the actual measured mass segregation and the theoretically possible fraction of segregated protostars ( $f_{\text{seg}}$ ). The actual number of segregated stars  $N_{\text{MST,max}}$  with  $\Lambda_{\text{MST}}(N \leq N_{\text{MST,max}}) \gtrsim 1.5$  is lower in almost all cases, but follows a consistent trend with  $N_{\text{seg}}$ . Taking into account that the protostars form at different positions and need some time to dynamically relax within the cluster, the relation  $N_{\text{MST,max}} < N_{\text{seg}}$  seems reasonable in comparison to an initially spherical cluster with a constant number of members.

The actual mass segregation can also be compared to the total time that the cluster as a whole has for mass segregation. As the number of protostars changes with time, we count the *available* time starting at the point where two sink particles are formed until the end of the simulation. The ratio  $t_{\text{avail}}/t_{\text{relax}}$  in table 8.2 indicates how many mass segregation times the cluster evolved, again assuming that  $t_{\text{relax}}$  at the end of the simulation is representative for the entire cluster evolution. There is again a weak correlation between this ratio and the degree of mass segregation.

## 8.4 Cluster properties – discussion

In all simulations we set up cores with a very low ratio of kinetic to gravitational energy, i.e., the clouds are strongly bound. As the cores are isolated, they are disconnected from any potential dynamical impact from the surrounding environment. The initially imposed supersonic turbulent motions result in a global velocity dispersion for the gas of  $\sim 0.5 \text{ km s}^{-1}$ . Given the diameter of the core, 0.2 pc, this is close to the velocity dispersion we expect from Larson’s relation (Larson, 1981; Solomon et al., 1987; Ossenkopf and Mac Low, 2002; Heyer and Brunt, 2004; Roman-Duval et al., 2011). However, it is lower than the observed turbulent velocity component of the massive dense cores in Cygnus X (Bontemps et al., 2010; Csengeri et al., 2011). The observed cores with very similar key properties to our cores, i.e., mass, size, and temperature, show velocity dispersions from  $\sim 0.5 - 3.5 \text{ km s}^{-1}$ , higher than the turbulent velocity dispersions in our numerical setups. Observations of massive, dense filaments show supersonic infall motions (Schneider et al., 2010), which may easily lead to a much more dynamical formation of the cores. We do not impose an initial net rotation to the core, however, the random turbulent pattern of high and low-velocity regions in different

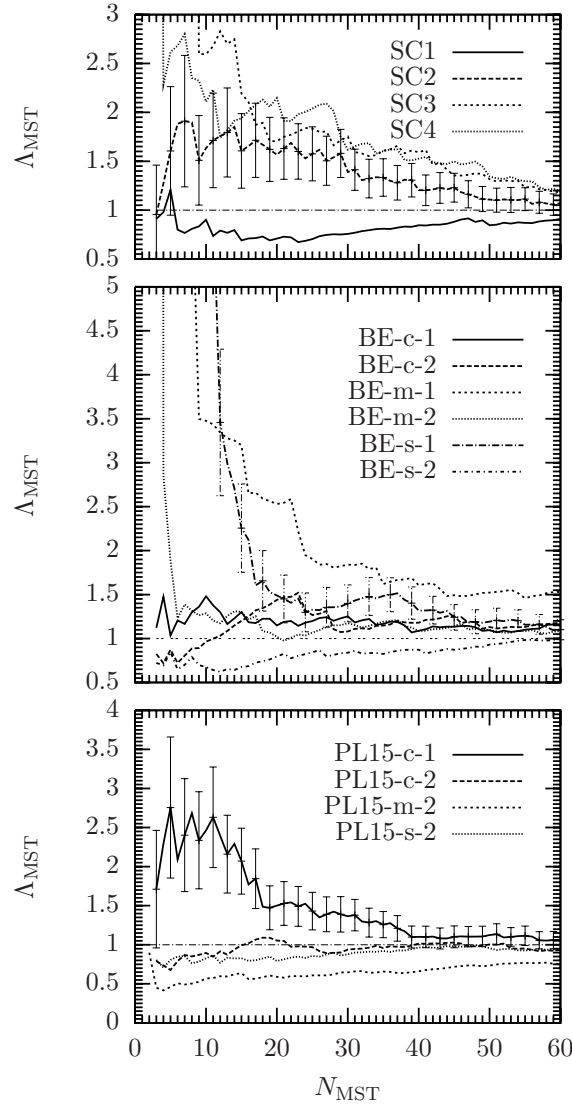


Figure 8.15: Mass segregation  $\Lambda_{\text{MST}}$  for all setups at the end of the simulation. For the setups where the deviation from unity is not obvious,  $\Lambda_{\text{MST}}$  is plotted with errorbars.

density environments results in a net rotation of the cores with a ratio of rotational to gravitational energy ranging from  $10^{-10} - 10^{-3}$ , in agreement with the values for the dense cores in Cygnus X (Bontemps et al., 2010; Csengeri et al., 2011). During the simulation, the velocity dispersion increases significantly due to the strong global infall and reaches values that are more consistent with the observed ones. After some  $\sim 10 - 40$  kyr, depending on the initial density profile, the cores as a whole reach or exceed a virialised energy budget  $E_{\text{kin}}/|E_{\text{pot}}| \geq 0.5$ . The final energy balance is in agreement with the theoretical virial analysis in Shetty et al. (2010). They investigated the scaling relations between mass, size, and virial state of clumps of different sizes that formed self-consistently in turbulent flows. The virial state of their clumps with similar sizes and masses to our setups is consistent with our energy analysis. Also the measured line widths of our cores is consistent with the analysis in Shetty et al. (2010). The increasing values for  $\sigma_{1D}$  are dominated by the gas motions in the dense central region, which is also observed. Csengeri et al. (2011) notice small-scale turbulent motions with high velocities (a few  $\text{km s}^{-1}$ ) in high-resolution studies of the central region of the cores.

As soon as protostars form, the question of early substructure and mass segregation arises. These two properties of young stellar clusters can not be disentangled and analysed separately. In particular, the determination whether a cluster shows primordial or dynamical mass segregation sensitively depends on the definition of mass segregation and spatial demarcation of the region in question.

The theoretical analysis of a self-gravitating  $N$ -body system predicts dynamical mass segregation via two-body relaxation and dynamical friction that an object experiences while moving through a sea of other objects. For different properties of the cluster, the dynamical friction and the resulting dynamical relaxation time of the total cluster differs (Chandrasekhar, 1943; McMillan and Portegies Zwart, 2003; Spinnato et al., 2003; Fellhauer and Lin, 2007). The global relaxation time, defined as a statistical quantity with only global cluster properties and thus not reflecting any substructure, therefore only serves as a rough estimate. Depending on how well these global quantities fit the observed or simulated system, the relaxation time might differ significantly from the time scale of local dynamical interactions.

The question whether dynamical mass segregation can be excluded based on a time-scale argument, can therefore only be answered for a specific definition of mass segregation and for a well-defined cluster or subcluster region. Traditionally, numerical work started without initial mass segregation and investigated the purely dynamical aspect of the  $N$ -body system, without taking into account the dynamical changes of the individual  $N$ -body objects,

like mass accretion in the early phase of cluster formation and the mass loss due to winds. Recently, several prescriptions of initial mass segregation have been developed (Baumgardt et al. 2008, Šubr et al. 2008, Vesperini et al. 2009), still investigating the cluster as a whole without local substructure.

One basic problem with the analysis of mass segregation is the definition of what mass segregation actually means. Allison et al. (2009) use the minimal spanning tree (MST) of the most massive stars in comparison to the MST of random stars and thus define mass segregation as the most massive stars being located closer to each other than the same number of randomly picked stars. As long as a single cluster or a conglomeration of several individual clusters does not show massive outliers, this method works stably. In case of massive outliers, this method needs to be slightly modified (Maschberger and Clarke, 2011; Olczak et al., 2011). In observational studies, mass segregation is mostly defined as more massive stars being located closer to the centre of the cluster (e.g. Hillenbrand 1997, Hillenbrand and Hartmann 1998, Fischer et al. 1998, de Grijs et al. 2002, Sirianni et al. 2002, Gouliermis et al. 2004, Huff and Stahler 2006, Stolte et al. 2006, Sabbi et al. 2008, Gennaro et al. 2011, Kirk and Myers 2011). However, the definition of the centre of a young star forming region with a large degree of substructure is not obvious.

One possibility to study mass segregation in resolved clusters is to investigate radial variations of the IMF. In unresolved clusters the different inferred radii in different wavelengths may indicate mass segregation. However, in both cases, mass segregation is difficult to identify given the observational difficulties (e.g., Ascenso et al., 2009; Portegies Zwart et al., 2010).

Even more difficult is the answer to the question about primordial versus dynamical mass segregation. In order for *global* mass segregation to be primordial in nature, it is required that stars with a given mass  $m$  must be more centrally concentrated than stars with the average stellar mass  $\langle m \rangle$  and that the cluster must be younger than the dynamical friction time scale for that given mass  $m$ , i.e., the more massive stars must have formed closer to the centre. This global picture is consistent with numerical simulations (e.g., Klessen and Burkert, 2000; Bonnell and Bate, 2006). However, this time scale argument only holds for spherical clusters in virial equilibrium. If clusters form through mergers of smaller subclusters, these subclusters might have enough time to dynamically relax and mass segregate because of the much smaller size and the higher number of stellar encounters. The degree of mass segregation in merged clusters is significantly higher than would be expected from a global time scale analysis (McMillan et al., 2007; Moeckel and Bonnell, 2009). In addition Allison et al. (2010) show that dynamical mass segregation is very fast even without mergers of partially mass segregated substructures. Therefore, a detailed analysis of the formation of substructure

ture and the collapse of stars within them is crucial to fully understand the mass segregation process. The analysis of our reduced clusters and subclusters with their own dynamical and orbital centre shows that there is a weak correlation between the possible degree of segregation  $f_{\text{seg}}$  and the actual mass segregation. Given the fact that we follow the evolution of our clusters for only a very short time, it seems very likely that dynamical mass segregation can provide a significant contribution to the mass segregation within the subclusters. If, in addition, the bigger stellar cluster that formed by mergers of smaller subsystems, can inherit a reasonable degree of mass segregation of the progenitors, it becomes very difficult to exclude dynamical effects on different spatial and dynamical levels to be responsible for mass segregation of a cluster.

The total cluster including all protostars shows a sub-virial energy budget, indicating that the relaxation time is larger and thus the dynamical mass segregation process of the total cloud is slower than in a virialised case. However, the central regions, where the crossing times are much smaller and stellar encounters more frequent, the  $N$ -body system is virialised. The central region therefore does not suffer from a dynamical delay concerning the mass segregation process. In addition, the simple analysis of dynamical mass segregation does not include the effects of gas, but only the dynamical friction due to the other stellar objects in the sample. In addition, the gas also provides dynamical friction (Dokuchaev, 1964; Ruderman and Spiegel, 1971; Rephaeli and Salpeter, 1980; Ostriker, 1999; Lee and Stahler, 2011). Due to the turbulent motions, an analytic estimate is difficult to apply in our collapsing core. Nevertheless, this additional friction helps to increase the dynamical cross sections and thus makes stellar encounters more frequent, resulting in an acceleration of the dynamical mass segregation.

An interesting aspect that weakens the effect of dynamical mass segregation is presented in recent work by Converse and Stahler (2011), where they argue that low- $N$  systems with an even higher number of objects than in our clusters do not relax dynamically. If this also applies to accreting stellar systems with gaseous background, a large degree of mass segregation might not be possible in the smallest subclusters but only later after some merger events. We nevertheless do not expect dynamical relaxation to become completely irrelevant because of the low number of protostars in our clusters and subclusters.

As a remark, we want to point to recent studies by Kruijssen et al. (2012). They analysed the substructure within clusters as well as the dynamical state of the stellar cluster when gas expulsion becomes important, i.e., at a slightly later stage of the evolution of the cluster. Analysing the simulations of Bonnell et al. (2003, 2008), they find that the stellar system quickly reaches a

globally virialised state if the gas potential is excluded and the stellar system is followed with pure  $N$ -body dynamics. Their results support the evolutionary picture of the formation of protostars that we see in our simulations. New protostars that form at larger radii from the centre of the cluster in gas dominated regions have sub-virial velocities. As soon as they decouple from the gas motion and move to the central gas-poor environment, they quickly virialise.

Note that the number density of protostars in the central region of the clusters is high enough for protostellar collisions to become important (Baumgardt and Klessen, 2011). This could indeed lead to changes in the stellar initial mass function.

## 8.5 Cluster properties – summary and conclusions

We analysed the simulations with the focus on the properties of the embedded young stellar clusters. We analysed the energy evolution of the gas and the nascent cluster, computed the degree of subclustering, and quantified the mass segregation in the continuously growing clusters. Our main conclusions can be summarised as follows.

In all setups, the collapsing cloud virialises within the simulated time, which corresponds to a star formation efficiency of 20%. Just considering the gas, all clouds have a virial or super-virial energy budget  $E_{\text{kin}} \gtrsim 0.5|E_{\text{pot}}|$ , the runs with only one protostar have significantly higher ratios of kinetic to gravitational energy. Although the total mass of all protostars is only 20% of the total cloud mass, their total kinetic energy is larger than that of the gas in the cases with multiple protostars. In contrast, the three runs with only one protostar show a smaller ratio of kinetic energy of the protostar to kinetic energy of the gas, which can be explained by the vanishing momentum impact of opposite accretion flows. Analysing the entire stellar clusters as pure  $N$ -body systems, we find an overall sub-virial energy balance with  $E_{\text{kin}} \sim 0.2|E_{\text{pot}}|$ , independent of the varied initial conditions. If we concentrate on the central regions of the clusters (innermost  $\sim 10 - 30\%$  of the protostars), we find virialised conditions. This difference can be explained by the formation history of the cluster. New protostars continue forming at increasing radii from the centre of the cloud due to the lack of available gas in the central region. These protostars inherit the kinetic energy from their parental gas region, which is relatively low in comparison to their gravitational contribution, i.e., new stars form at sub-virial velocities. Soon after

their formation, the protostars decouple from the gas and agglomerate in the central region, where they virialise.

The degree of subclustering strongly depends on the initial density profile. Initially uniform density allows for turbulent motions to form distinct subclusters before the global collapse can confine the gas in one cluster in the central region. With a  $Q$  value of  $\sim 0.2$ , these clouds show considerable substructure with distinct conglomeration of protostars. The stronger the initial mass concentration around the centre of the cloud, the less subclustering is found. Bonnor-Ebert-like spheres show mainly one dominant central cluster with some substructure. The considered power-law density distributions form more compact protostellar clusters with less internal structure, if they form clusters at all. In three strongly condensed setups the cloud does not fragment and forms only one protostar. In general, we find that the  $Q$  parameter, used to quantify subclustering, shows the following trend:  $\langle Q_{\text{TH}} \rangle \lesssim \langle Q_{\text{BE}} \rangle \lesssim \langle Q_{\text{PL15}} \rangle$ , where lower  $Q$  means more substructure. We also note different subclustering trends with different turbulent modes. For a given density profile, compressive modes lead to a higher degree of substructure than mixed modes, which in turn lead to more substructure than solenoidal modes, i.e.,  $\langle Q_{\text{comp}} \rangle \lesssim \langle Q_{\text{mix}} \rangle \lesssim \langle Q_{\text{sol}} \rangle$ .

Focusing on the central region of the clusters, where outliers are removed from the set of protostars, roughly half of the clusters show mass segregation. The degree of mass segregation varies strongly between the clusters, however, no cluster with significant inverse mass segregation is found. Except for one cluster (PL15-m-2), the mass segregation ratio does not drop below 0.5. The mass segregation is consistent with the time for dynamical mass segregation, so all the clusters had enough time for dynamical relaxation of the most massive objects in the cluster. In the simulated collapsing cores, primordial mass segregation is not necessarily required to achieve a significant mass segregation at the end of the simulation. However, due to the ongoing formation of protostars and the increase in protostellar mass due to accretion, the cluster is exposed to continuous momentum and energy impact from the surrounding gas, which may modify the actual mass segregation behaviour in comparison to the idealised process of dynamical mass segregation via two-body relaxation. A contribution that may have a significant influence is the episodic accretion of gas as well as the fact that the protostars follow the global flow pattern of the gas they form from, before they dynamically decouple from the gas. Overall, there is no clear correlation between the initial conditions and the mass segregation in our simulated clusters.

We conclude that the kinetics of young stellar clusters do not strongly depend on the initial density profile, nor on the initial structure of the turbulent modes. This is because the nascent protostars quickly decouple dynamically

from the parental filament in which they were formed. The interactions as an  $N$ -body system dominate the cluster motions. Continuous formation of subsequent protostars with initially sub-virial velocities lead to a globally sub-virial ( $E_{\text{kin}}/|E_{\text{pot}}| < 0.5$ ) state for the majority of the protostars. Taken into account the dynamics of small subclusters with dynamical times much smaller than the dynamical time of the entire cloud, the measured degree of mass segregation is fully consistent with dynamical mass segregation, there is no need for primordial mass segregation in our simulations.



# Chapter 9

## Conclusion and outlook

### 9.1 Summary

In this thesis we analysed the influence of the initial conditions for star formation in the case of massive dense prestellar cores. With three-dimensional numerical simulations, the impact of different density distributions and varying turbulent motions on the fragmentation and energetics of the cloud, the formation of stars as well as the dynamical processes and the statistical properties within young stellar clusters were investigated. All simulated systems contain a total mass of  $100 M_{\odot}$  within a radius of 0.2 pc and are kept isothermal at a temperature of 20 K. The initial turbulent motions are supersonic with Mach numbers of the order of  $\mathcal{M} \approx 3.5$ . We distinguished between compressive, solenoidal and mixed turbulence modes.

### 9.2 Main conclusions

To what extent initial conditions matter strongly depends on the quantity in question. Some properties of the collapsing cloud are solely determined by the initial conditions, others are only marginally influenced, if at all.

**Cloud morphology** The morphology of the cloud shows significant deviations for different initial conditions, among which the density profile seems to be the most important parameter. Flat density profiles collapse on time scales that turbulence motions need to compress material above the threshold density for star formation. These clouds are therefore shaped by the turbulent motions and form disconnected protostellar clusters according to the random pattern of the turbulence. The stronger the initial central mass

concentration in the cloud, the more is the collapse determined by the free-fall conditions of the central regions. High central densities result in free-fall times of the region under consideration that is significantly smaller than the turbulent crossing time for that part of the cloud. The impact of turbulent motions is therefore drastically reduced in these setups. In the case of one central overdensity, the cloud only forms one central cluster.

**Accretion mode in clusters** Almost independent of the initial conditions is the accretion mode in the formed clusters. All clusters from the fluffy disconnected clusters to the compact central clusters show an efficient accretion shielding, starving the central region of the cluster of gas. This is in contrast to the competitive accretion picture, in which the central stars can profit from the deep gravitational potential and accrete more gas than the stars in the outskirts of the cluster. Interestingly, an apparent measure for the competitive accretion model that relates the mass of the most massive star to the total mass in stars is also found in the accretion shielding model presented in this work. Whether the accretion behaviour in this thesis is result of the global parameters, which are the same for all setups, e.g., the total number of Jeans masses, can not be determined without further studies.

**Number of protostars** Apart from the extreme density profiles like a uniform density distribution or a steep power-law profile, the number of formed stars is significantly influenced by the realisation of the turbulent velocities. Slightly converging flows towards the centre may efficiently push the gas onto already existing objects, which accrete the gas. Less converging flows, in contrast, can delay the gravitational collapse sufficiently, so that the individual overdensities can collapse themselves before being accreted by the central protostar. One caveat of the simulations shown in this thesis is definitely the artificially created turbulence, which may cause extreme cases of converging and diverging flows that are not created self-consistently with the density structures. However, in unstable cores like the ones in our setups, small differences in the turbulent motions can already be enough to completely alter the result, showing the sensitivity of the collapsing cores to turbulent motions.

**Tidal effects** Overall, a significant fraction of the total mass is located in tidally stable regions of the cloud, so star formation is not delayed or suppressed by tidal forces. The supersonic turbulence quickly creates regions that are dense enough to resist tidal disruption.

**Properties of protostellar clusters** In all protostellar clusters the total kinetic energy of the protostars is larger than that of the gas, although the total mass in protostars is only 20% at the end of the simulation. The protostellar clusters as a whole show a sub-virial energy budget ( $E_{\text{kin}} < 0.5|E_{\text{pot}}|$ ) quickly after the formation of the first protostars. Subsequent stars form in filaments, inheriting the motions of the gas, which is sub-virial. In all cases the innermost 10 – 30% of the stars form a cluster in virial equilibrium and above. Overall, the energy balance does not systematically depend on the initial conditions. In contrast, the degree of subclustering shows a trend with the modes of the turbulence. Compressive motions lead to a higher degree of subclustering than solenoidal motions. Roughly half of the simulated clusters show mass segregation with the more massive stars located closer to the centre than low-mass stars. There is no systematic trend of the mass segregation with the initial conditions. In all cases of mass segregation, the protostars have enough time, i.e., enough two-body encounters, to mass segregate dynamically via two-body relaxation. There is no need for primordial mass segregation in the presented simulations.

## 9.3 Extensions and outlook

The studies on the prestellar in this thesis should be extended in two different branches, which mark the main caveats of the present work. One aspect is the impact of magnetic fields, the other covers feedback from the young stellar objects, in particular radiative feedback and outflows.

### 9.3.1 Magnetic fields

Focusing on the early phases of the collapse, magnetic fields are likely to play a role by shaping the filamentary structures that form and therefore the formation mode of stars, including the degree of subclustering and mass segregation as well as the accretion mode within a cluster. Overall, magnetic fields tend to reduce the degree of fragmentation and retard the collapse of the cloud. On the one hand, that gives turbulent motions more time to shape the structures of the gas, which might allow star formation at larger separations than in the non-magnetised case. On the other hand, the longer it takes to form individual stars, the more impact might the global collapse of the cloud have, which would allow stars to form closer to the centre. The closer to each other stars form, the shorter is their dynamical time scale for relaxation. As a result, the ensemble of stars is very likely to show signs of dynamical mass segregation. In the case of compact clusters the total

number of stars in a cluster and their mean separation might significantly alter the accretion mode in clusters. Less stars might allow the central stars to accrete much more gas than surrounding companions because the gas flow might not be shielded efficiently.

Including magnetic fields of course includes the additional parameter of the field strength, which will have an impact on the effects. Additionally, the spatial structure of the magnetic field might be very important. So far, mostly homogeneous magnetic fields were used as initial conditions for simulations. However, considering the fact, that the interstellar medium is turbulent, the assumption of homogeneous magnetic fields might not be justified. Instead one should also consider tangled magnetic fields, similar to the turbulent velocities of the gas. One focus of the analysis including magnetic fields should be the relative importance of the field strength to the structure of the field.

### 9.3.2 Stellar feedback

The second important aspect of additional physics that is missing the current simulations are feedback processes. Including outflows from young stellar objects might change the morphology of the innermost part of the protostellar cluster and thereby alter the accretion processes within the cluster. Expelled gas from the outflows might starve more regions in the cluster, thereby reducing the number of unstable fragments that lead to a smaller number of total stars in the cluster. On the contrary, the additional turbulence induced by the outflows might trigger more marginally unstable regions to collapse and thus form more stars. Depending on the range of influence of the outflows, they may significantly alter the dynamical state of the cluster and the relaxation processes as well as the mass segregation within the cluster. Ideally, one would like to include magnetic fields and follow the resulting self-consistent launch of magnetically driven outflows. However, numerically this task is extremely challenging. In order to launch outflows self-consistently, one need significantly higher resolution than in the work presented here. A higher resolution itself results in significantly smaller computational time steps. In addition, the fast outflow velocities again reduce the time step in the simulation, which easily stalls the run as soon as the first outflow begins to form. The evolution of a cluster with many protostars forming at different times is impossible to follow self-consistently. Therefore, semi-analytical solutions of outflows need to be included in the numerical model of sink particles with parameterised outflow descriptions.

At later times stellar radiation is likely to heat the central region of the cluster, thereby inhibiting further fragmentation and subsequent star forma-

tion. The total amount of stars might be reduced significantly. At the same time, the formation radius of stars might increase out to regions that are thermally less influenced and thus fragment and collapse quicker. In this case, the accretion rate onto the central stars is might be significantly higher than in the case without radiative feedback.



# Appendix A

## Resolution Study

### A.1 Resolution study

We test the influence of the numerical effective resolution of the code on the collapse by simulating the different cloud setups with different resolutions. The order of the numerical resolution was chosen such that the isothermal approximation for the equation of state is appropriate and the computational effort is acceptable. The different resolutions have acronyms corresponding to the maximum refinement level (RL) in the code:  $l_{\max} = 7$  (RL07),  $l_{\max} = 8$  (RL08),  $l_{\max} = 10$  (RL10) and  $l_{\max} = 12$  (RL12). Due to the different sizes of the smallest cell, the maximum gas density before creating sink particles, as well as the accretion radius vary. A comparison of the parameters can be seen in table [A.1](#).

As the computational time for the BE and the TH profile are very large (i.e., more than an order of magnitude larger than for the PL20 profile, because of the quite space-filling refinement in the evolution of these profiles), these setups have only been compared in an early evolutionary stage. The highly concentrated PL20 cloud has been investigated in more detail: for a longer evolution time, for more different resolutions and analytically.

#### A.1.1 BE profile

Due to the flat inner core of this profile, refinement is initiated in a rather large volume of the core, which makes the computational effort for this profile much larger than for the other profiles, and thus the resolution test was done only for a short simulation time. In figure [A.1](#) we compare the total accretion rate,  $\dot{M}$ , and the number of sink particles  $N$  of the Bonnor-Ebert profiles BE-c-1 and BE-s-1 for resolutions RL10 and RL12. The accretion rates are comparable and give roughly the same star formation efficiency with

Table A.1: Main simulation parameters for different resolutions

refinement	eff. res.	$\Delta x$ [AU]	$r_{\text{accr}}$ [AU]	$\rho_{\text{max}}$ [g cm $^{-3}$ ]	$n_{\text{max}}$ [cm $^{-3}$ ]
RL07	512 $^3$	104.4	313.3	$3.85 \times 10^{-16}$	$1.01 \times 10^8$
RL08	1024 $^3$	52.2	156.7	$1.54 \times 10^{-15}$	$4.03 \times 10^9$
RL10	4096 $^3$	13.1	39.2	$2.46 \times 10^{-14}$	$6.45 \times 10^9$
RL12	16384 $^3$	3.3	9.8	$3.94 \times 10^{-13}$	$1.03 \times 10^{11}$

Main simulation parameters for different effective resolutions. The accretion radius of the sink particles  $r_{\text{accr}}$  is set to 3 times the minimum cell size  $\Delta x$ .

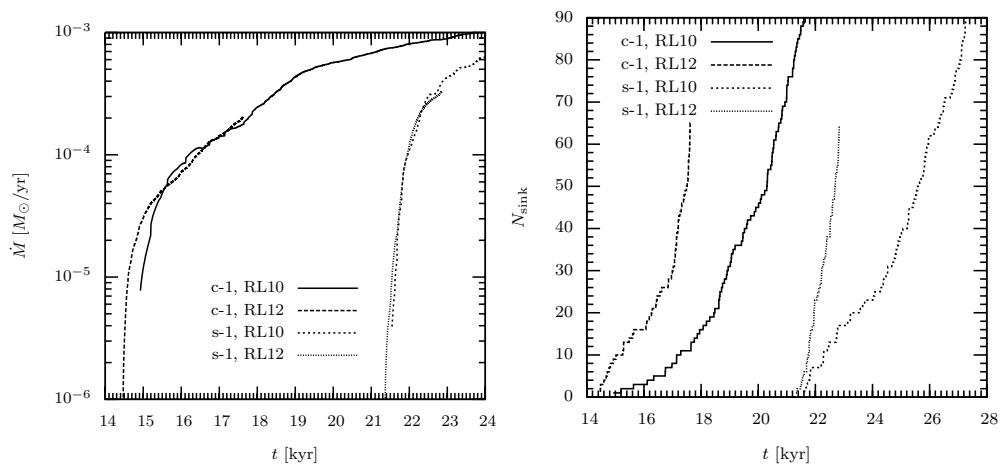


Figure A.1: Comparison of the Bonnor-Ebert profiles BE-c-1 and BE-s-1 for resolutions RL10 and RL12. The mass accretion as a function of time (left plot) shows only small differences between the two resolutions. The number of sink particles, however, differs strongly (right plot).

time. However, the number of particles varies significantly with resolution. This is expected, since we use an isothermal equation of state, which does not introduce a physical length scale or density threshold to the problem, i.e., the problem remains scale-free. Changes in the equation of state, in particular if the gas becomes optically thick, will break the scale-free collapse (e.g., Jappsen et al., 2005; Krumholz et al., 2007; Bate, 2009c).

### A.1.2 PL20 profile

For the concentrated density profile with  $\rho \propto r^{-2}$  and the turbulence profile c-1, detailed simulations were run for four different maximum refinement levels: RL07, RL08, RL10, RL12. In all cases only one sink particle was created in

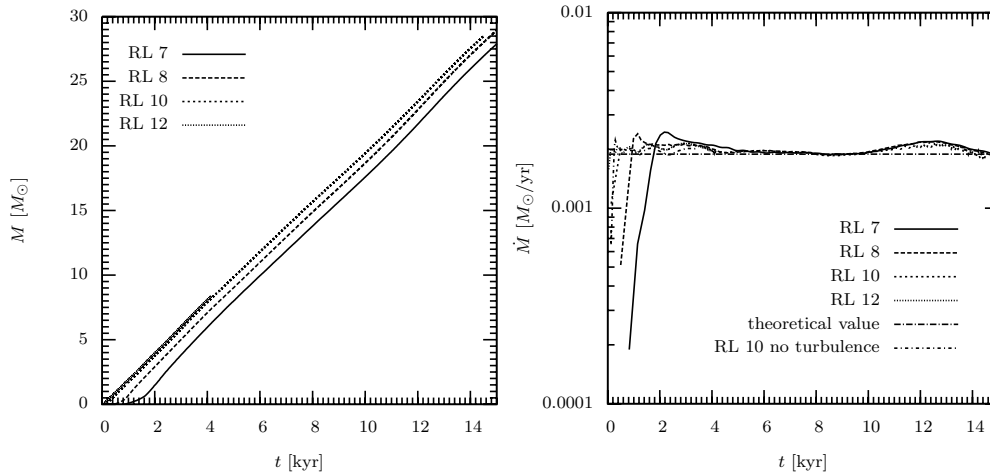


Figure A.2: Resolution comparison for the PL20 runs with turbulence field c-1. After an initial evolution time the accretion rates approach the same value for all setups. The differences at the beginning of the simulation are due to different maximum central resolutions. The flattened density function at the centre of the box is much shallower for lower resolutions resulting in larger times for a central collapse.

the centre of the cloud after a few steps of hydrodynamical evolution.

The results for the PL20 runs can be seen in figure A.2. The accretion rate onto the protostar  $\dot{M}$  does not differ significantly, resulting in the same slope of the mass  $M$  as a function of time. The different evolution of the accretion rate at the very beginning of the simulation is due to the different geometrical setup conditions (see sec. 5.2.1). The larger size of the smallest cell for lower refinement levels results in a much coarser density distribution in the centre of the cloud and needs more evolution time in order to develop a sink particle with constant accretion rate. The theoretical value for the accretion rate fits the simulated values very well (see sec. 5.2.1). The comparison with a simulation without turbulent velocities only shows minor differences.

## A.2 Tidal forces

The tidal acceleration in a spherically symmetric setup at distance  $r$  from the centre with an enclosed mass  $M$  is given by

$$a_{\text{tidal}}(r) = GM \left( \frac{1}{(r + \Delta r)^2} - \frac{1}{(r - \Delta r)^2} \right), \quad (\text{A.1})$$

where  $G$  is the gravitational constant and  $\Delta r \ll r$ . The enclosed mass can then be considered to be constant within the variation  $\Delta r$ . Given a density profile of the form  $\rho(r) \propto r^{-p}$  yields a mass function  $M(r) \propto r^{3-p}$ , and the tidal acceleration scales as

$$a_{\text{tidal}}(r) \propto r^{1-p}. \quad (\text{A.2})$$

The derivative with respect to  $r$ ,

$$\frac{\partial a_{\text{tidal}}}{\partial r}(r) \propto (1-p)r^{-p}, \quad (\text{A.3})$$

changes sign at  $p = 1$ . For  $p < 1$ ,  $a_{\text{tidal}}$  increases with radius ( $\partial a_{\text{tidal}}/\partial r > 0$ ) and therefore compresses material at radius  $r$ . For  $p > 1$ ,  $\partial a_{\text{tidal}}/\partial r < 0$  and shears condensations apart.

# Appendix B

## Angular Momentum

### B.1 Angular momentum

In order to see the time evolution of the angular momentum, we show the specific angular momentum as a function of enclosed mass for the setups PL15-m-2 and BE-m-2 (figures B.1 and B.2). In both cases the angular momentum distribution is exposed to variations of the order of a few up to almost an order of magnitude due to the turbulent interactions and the gas accretion onto protostars. Due to the unstructured motions of the protostars and the random character of the turbulence, the variations do not show systematic changes over time, i.e., the gas in the cluster can quickly gain angular momentum due to accretion streams or lose it via shocks and dissipation.

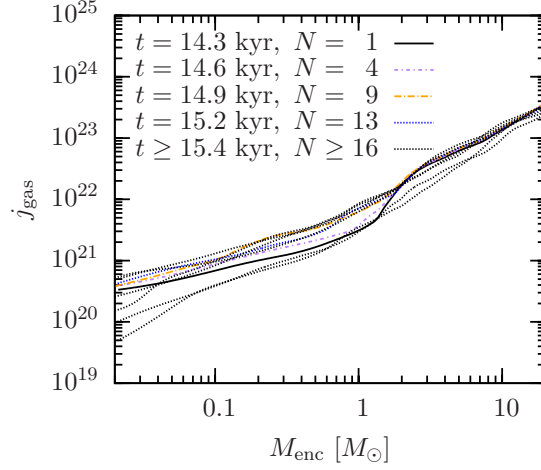


Figure B.1: Specific angular momentum of the gas as a function of enclosed mass for PL15-m-2. The plot shows temporal changes of the angular momentum of the gas during the formation of the cluster.

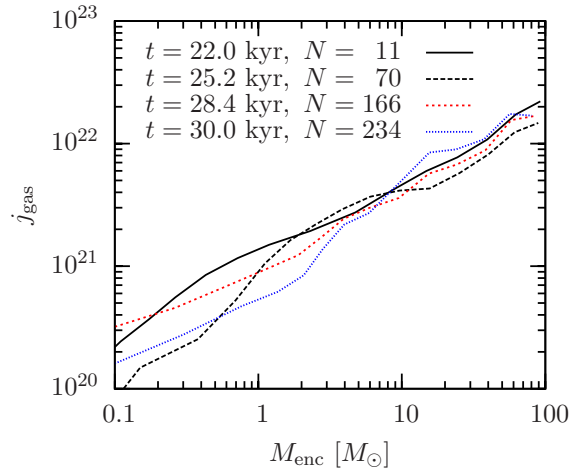


Figure B.2: Same as figure B.1 but for setup BE-m-2.

# Appendix C

## Gravitational Softening

### C.1 Gravitational force softening

We used the gravitational softening for the sink particles as described in [Price and Monaghan \(2007\)](#). The potential energy can be written as

$$E_{\text{pot}} = \sum_{i \neq j} G m_i m_j \phi(r_i - r_j, h), \quad (\text{C.1})$$

where  $h$  is the smoothing length, which is set to the accretion radius of the sink particles  $h = r_{\text{accr}}/2$ , and  $\phi(r, h)$  is given by ( $q = r/h$ )

$$\phi(r, h) = \begin{cases} h^{-1} \left( \frac{2}{3}q^2 - \frac{3}{10}q^4 + \frac{1}{10}q^5 - \frac{7}{5} \right), & 0 \leq q < 1 \\ h^{-1} \left( \frac{4}{3}q^2 - q^3 + \frac{3}{10}q^4 - \frac{1}{30}q^5 - \frac{8}{5} + \frac{1}{15q} \right), & 1 \leq q < 2 \\ -1/r, & 2 \leq q. \end{cases} \quad (\text{C.2})$$

Note that the function  $\phi$  is defined such that the potential energy is negative.



# Bibliography

- Abbasi, R. U., Abu-Zayyad, T., Allen, M., Amman, J. F., Archbold, G., Belov, K., Belz, J. W., Ben Zvi, S. Y., Bergman, D. R., Blake, S. A., Brusova, O. A., Burt, G. W., Cannon, C., Cao, Z., Connolly, B. C., Deng, W., Fedorova, Y., Finley, C. B., Gray, R. C., Hanlon, W. F., Hoffman, C. M., Holzscheiter, M. H., Hughes, G., Hüntemeyer, P., Jones, B. F., Jui, C. C. H., Kim, K., Kirn, M. A., Loh, E. C., Maestas, M. M., Manago, N., Marek, L. J., Martens, K., Matthews, J. A. J., Matthews, J. N., Moore, S. A., O'Neill, A., Painter, C. A., Perera, L., Reil, K., Riehle, R., Roberts, M., Rodriguez, D., Sasaki, N., Schnetzer, S. R., Scott, L. M., Sinnis, G., Smith, J. D., Sokolsky, P., Song, C., Springer, R. W., Stokes, B. T., Thomas, S. B., Thomas, J. R., Thomson, G. B., Tupa, D., Westerhoff, S., Wiencke, L. R., Zhang, X., and Zech, A.: 2008, *Physical Review Letters* **100**(10), 101101
- Abraham, J., Abreu, P., Aglietta, M., Aguirre, C., Allard, D., Allekotte, I., Allen, J., Allison, P., Alvarez-Muñiz, J., Ambrosio, M., and et al.: 2008, *Physical Review Letters* **101**(6), 061101
- Allison, R. J., Goodwin, S. P., Parker, R. J., Portegies Zwart, S. F., and de Grijs, R.: 2010, *MNRAS* **407**, 1098
- Allison, R. J., Goodwin, S. P., Parker, R. J., Portegies Zwart, S. F., de Grijs, R., and Kouwenhoven, M. B. N.: 2009, *MNRAS* **395**, 1449
- Alves, J., Lada, C. J., Lada, E. A., Kenyon, S. J., and Phelps, R.: 1998, *ApJ* **506**, 292
- Andrews, S. M. and Williams, J. P.: 2007, *ApJ* **659**, 705
- Arnett, D.: 1996, *Supernovae and Nucleosynthesis*
- Arzoumanian, D., André, P., Didelon, P., Könyves, V., Schneider, N., Men'shchikov, A., Sousbie, T., Zavagno, A., Bontemps, S., di Francesco, J., Griffin, M., Hennemann, M., Hill, T., Kirk, J., Martin, P., Minier,

- V., Molinari, S., Motte, F., Peretto, N., Pezzuto, S., Spinoglio, L., Ward-Thompson, D., White, G., and Wilson, C. D.: 2011, *A&A* **529**, L6
- Ascenso, J., Alves, J., and Lago, M. T. V. T.: 2009, *A&A* **495**, 147
- Balbus, S. A. and Hawley, J. F.: 1991, *ApJ* **376**, 214
- Ballesteros-Paredes, J., Hartmann, L., and Vázquez-Semadeni, E.: 1999, *ApJ* **527**, 285
- Ballesteros-Paredes, J., Klessen, R. S., Mac Low, M., and Vazquez-Semadeni, E.: 2007, *Protostars and Planets V*, *Univ. Arizona Press, Tuscon* pp 63–80
- Banerjee, R. and Pudritz, R. E.: 2006, *ApJ* **641**, 949
- Banerjee, R., Vázquez-Semadeni, E., Hennebelle, P., and Klessen, R. S.: 2009, *MNRAS* **398**, 1082
- Bartko, H., Martins, F., Trippe, S., Fritz, T. K., Genzel, R., Ott, T., Eisenhauer, F., Gillessen, S., Paumard, T., Alexander, T., Dodds-Eden, K., Gerhard, O., Levin, Y., Mascetti, L., Nayakshin, S., Perets, H. B., Perrin, G., Pfuhl, O., Reid, M. J., Rouan, D., Zilka, M., and Sternberg, A.: 2010, *ApJ* **708**, 834
- Bastian, N., Covey, K. R., and Meyer, M. R.: 2010, *ARA&A* **48**, 339
- Bate, M. R.: 2009a, *MNRAS* **392**, 590
- Bate, M. R.: 2009b, *MNRAS* **397**, 232
- Bate, M. R.: 2009c, *MNRAS* **392**, 1363
- Bate, M. R. and Bonnell, I. A.: 2005, *MNRAS* **356**, 1201
- Bate, M. R., Bonnell, I. A., and Bromm, V.: 2003, *MNRAS* **339**, 577
- Bate, M. R., Bonnell, I. A., and Price, N. M.: 1995, *MNRAS* **277**, 362
- Baumgardt, H., De Marchi, G., and Kroupa, P.: 2008, *ApJ* **685**, 247
- Baumgardt, H. and Klessen, R. S.: 2011, *MNRAS* **413**, 1810
- Beatty, J. J. and Westerhoff, S.: 2009, *Annual Review of Nuclear and Particle Science* **59**, 319
- Beck, R.: 2009, *Astrophysics and Space Sciences Transactions* **5**, 43

- Bergin, E. A. and Tafalla, M.: 2007, *ARA&A* **45**, 339
- Bertoldi, F.: 1989, *ApJ* **346**, 735
- Bertoldi, F. and McKee, C. F.: 1990, *ApJ* **354**, 529
- Beuther, H., Churchwell, E. B., McKee, C. F., and Tan, J. C.: 2007, *Protostars and Planets V, Univ. Arizona Press, Tuscon* pp 165–180
- Beuther, H., Schilke, P., Sridharan, T. K., Menten, K. M., Walmsley, C. M., and Wyrowski, F.: 2002, *A&A* **383**, 892
- Beuther, H., Vlemmings, W. H. T., Rao, R., and van der Tak, F. F. S.: 2010, *ApJ* **724**, L113
- Bhattacharjee, P., Hill, C. T., and Schramm, D. N.: 1992, *Physical Review Letters* **69**, 567
- Binney, J. and Tremaine, S.: 1987, *Galactic dynamics*, Princeton, NJ, Princeton University Press, 1987, 747 p.
- Bisnovatyi-Kogan, G. S.: 2011, *Stellar Physics 2: Stellar Evolution and Stability*
- Blandford, R. D. and Payne, D. G.: 1982, *MNRAS* **199**, 883
- Bondi, H.: 1952, *MNRAS* **112**, 195
- Bondi, H. and Hoyle, F.: 1944, *MNRAS* **104**, 273
- Bonnell, I. A. and Bate, M. R.: 2002, *MNRAS* **336**, 659
- Bonnell, I. A. and Bate, M. R.: 2005, *MNRAS* **362**, 915
- Bonnell, I. A. and Bate, M. R.: 2006, *MNRAS* **370**, 488
- Bonnell, I. A., Bate, M. R., Clarke, C. J., and Pringle, J. E.: 2001a, *MNRAS* **323**, 785
- Bonnell, I. A., Bate, M. R., and Vine, S. G.: 2003, *MNRAS* **343**, 413
- Bonnell, I. A., Clark, P., and Bate, M. R.: 2008, *MNRAS* **389**, 1556
- Bonnell, I. A., Clarke, C. J., Bate, M. R., and Pringle, J. E.: 2001b, *MNRAS* **324**, 573
- Bonnell, I. A., Vine, S. G., and Bate, M. R.: 2004, *MNRAS* **349**, 735

- Bonnor, W. B.: 1956, MNRAS **116**, 351
- Bontemps, S., Motte, F., Csengeri, T., and Schneider, N.: 2010, A&A **524**, A18+
- Brandenburg, A. and Subramanian, K.: 2005, Phys. Rep. **417**, 1
- Braun, H. and Schmidt, W.: 2012, MNRAS **421**, 1838
- Bressert, E., Bastian, N., Gutermuth, R., Megeath, S. T., Allen, L., Evans, II, N. J., Rebull, L. M., Hatchell, J., Johnstone, D., Bourke, T. L., Cieza, L. A., Harvey, P. M., Merin, B., Ray, T. P., and Tothill, N. F. H.: 2010, MNRAS **409**, L54
- Bürzle, F., Clark, P. C., Stasyszyn, F., Greif, T., Dolag, K., Klessen, R. S., and Nielaba, P.: 2011, MNRAS **412**, 171
- Cartwright, A. and Whitworth, A. P.: 2004, MNRAS **348**, 589
- Castor, J. I., Abbott, D. C., and Klein, R. I.: 1975, ApJ **195**, 157
- Chabrier, G.: 2003, PASP **115**, 763
- Chandrasekhar, S.: 1943, ApJ **97**, 255
- Chandrasekhar, S. and Münch, G.: 1952, ApJ **115**, 103
- Chiosi, C. and Maeder, A.: 1986, ARA&A **24**, 329
- Clark, P. C., Bonnell, I. A., and Klessen, R. S.: 2008a, MNRAS **386**, 3
- Clark, P. C., Glover, S. C. O., and Klessen, R. S.: 2008b, ApJ **672**, 757
- Clark, P. C., Klessen, R. S., and Bonnell, I. A.: 2007, MNRAS **379**, 57
- Colella, P. and Woodward, P. R.: 1984, *Journal of Computational Physics* **54**, 174
- Commerçon, B., Hennebelle, P., Audit, E., Chabrier, G., and Teyssier, R.: 2010, A&A **510**, L3+
- Converse, J. M. and Stahler, S. W.: 2011, MNRAS **410**, 2787
- Crutcher, R. M., Nutter, D. J., Ward-Thompson, D., and Kirk, J. M.: 2004, ApJ **600**, 279

- Crutcher, R. M., Troland, T. H., Lazareff, B., Paubert, G., and Kazès, I.: 1999, *ApJ* **514**, L121
- Csengeri, T., Bontemps, S., Schneider, N., Motte, F., and Dib, S.: 2011, *A&A* **527**, A135+
- Dame, T. M., Elmegreen, B. G., Cohen, R. S., and Thaddeus, P.: 1986, *ApJ* **305**, 892
- de Grijs, R., Gilmore, G. F., Johnson, R. A., and Mackey, A. D.: 2002, *MNRAS* **331**, 245
- de Wit, W. J., Testi, L., Palla, F., Vanzi, L., and Zinnecker, H.: 2004, *A&A* **425**, 937
- de Wit, W. J., Testi, L., Palla, F., and Zinnecker, H.: 2005, *A&A* **437**, 247
- Dokuchaev, V. P.: 1964, *Soviet Ast.* **8**, 23
- Draine, B. T. and Lee, H. M.: 1984, *ApJ* **285**, 89
- Ebert, R.: 1955, *ZAp* **37**, 217
- Elmegreen, B. G.: 2000, *ApJ* **530**, 277
- Elmegreen, B. G.: 2007, *ApJ* **668**, 1064
- Elmegreen, B. G. and Lada, C. J.: 1977, *ApJ* **214**, 725
- Elmegreen, B. G. and Scalo, J.: 2004, *ARA&A* **42**, 211
- Espinoza, P., Selman, F. J., and Melnick, J.: 2009, *A&A* **501**, 563
- Eswaran, V. and Pope, S. B.: 1988, *Computers and Fluids* **16**, 257
- Federrath, C., Banerjee, R., Clark, P. C., and Klessen, R. S.: 2010a, *ApJ* **713**, 269
- Federrath, C., Klessen, R. S., and Schmidt, W.: 2008, *ApJ* **688**, L79
- Federrath, C., Klessen, R. S., and Schmidt, W.: 2009, *ApJ* **692**, 364
- Federrath, C., Roman-Duval, J., Klessen, R. S., Schmidt, W., and Mac Low, M.: 2010b, *A&A* **512**, A81+
- Federrath, C., Sur, S., Schleicher, D. R. G., Banerjee, R., and Klessen, R. S.: 2011, *ApJ* **731**, 62

- Fellhauer, M. and Lin, D. N. C.: 2007, MNRAS **375**, 604
- Fischer, P., Pryor, C., Murray, S., Mateo, M., and Richtler, T.: 1998, AJ **115**, 592
- Fleck, Jr., R. C.: 1981, ApJ **246**, L151
- Frisch, U.: 1995, *Turbulence. The legacy of A. N. Kolmogorov*.
- Frisch, U. and Bec, J.: 2001, in M. Lesieur, A. Yaglom, & F. David (ed.), *New Trends in Turbulence*, p. 341
- Fryxell, B., Olson, K., Ricker, P., Timmes, F. X., Zingale, M., Lamb, D. Q., MacNeice, P., Rosner, R., Truran, J. W., and Tufo, H.: 2000, ApJS **131**, 273
- Gennaro, M., Brandner, W., Stolte, A., and Henning, T.: 2011, MNRAS **412**, 2469
- Goldsmith, P. F. and Langer, W. D.: 1978, ApJ **222**, 881
- Goodman, A. A., Bastien, P., Menard, F., and Myers, P. C.: 1990, ApJ **359**, 363
- Gouliermis, D., Keller, S. C., Kontizas, M., Kontizas, E., and Bellas-Velidis, I.: 2004, A&A **416**, 137
- Gower, J. C. and Ross, G. J. S.: 1969, *Appl. Stat.* **18**, 54
- Grasso, D. and Rubinstein, H. R.: 2001, Phys. Rep. **348**, 163
- Hansen, C. J., Kawaler, S. D., and Trimble, V.: 2004, *Stellar interiors : physical principles, structure, and evolution*
- Harayama, Y., Eisenhauer, F., and Martins, F.: 2008, ApJ **675**, 1319
- Hartmann, L., Ballesteros-Paredes, J., and Bergin, E. A.: 2001, ApJ **562**, 852
- Heger, A., Fryer, C. L., Woosley, S. E., Langer, N., and Hartmann, D. H.: 2003, ApJ **591**, 288
- Heiles, C. and Crutcher, R.: 2005, in R. Wiełebinski & R. Beck (ed.), *Cosmic Magnetic Fields*, Vol. 664 of *Lecture Notes in Physics*, Berlin Springer Verlag, p. 137

- Heiles, C. and Troland, T. H.: 2005, *ApJ* **624**, 773
- Heitsch, F., Mac Low, M., and Klessen, R. S.: 2001, *ApJ* **547**, 280
- Hennebelle, P. and Chabrier, G.: 2008, *ApJ* **684**, 395
- Hennebelle, P. and Ciardi, A.: 2009, *A&A* **506**, L29
- Hennebelle, P., Commerçon, B., Joos, M., Klessen, R. S., Krumholz, M., Tan, J. C., and Teyssier, R.: 2011, *A&A* **528**, A72+
- Hennebelle, P. and Fromang, S.: 2008, *A&A* **477**, 9
- Hennebelle, P. and Teyssier, R.: 2008, *A&A* **477**, 25
- Heyer, M. H. and Brunt, C. M.: 2004, *ApJ* **615**, L45
- Hill, C. T., Schramm, D. N., and Walker, T. P.: 1987, *Phys. Rev. D* **36**, 1007
- Hill, T., Motte, F., Didelon, P., Bontemps, S., Minier, V., Hennemann, M., Schneider, N., André, P., Men'shchikov, A., Anderson, L. D., Arzoumanian, D., Bernard, J.-P., di Francesco, J., Elia, D., Giannini, T., Griffin, M. J., Könyves, V., Kirk, J., Marston, A. P., Martin, P. G., Molinari, S., Nguyen Luong, Q., Peretto, N., Pezzuto, S., Roussel, H., Sauvage, M., Soubie, T., Testi, L., Ward-Thompson, D., White, G. J., Wilson, C. D., and Zavagno, A.: 2011, *A&A* **533**, A94
- Hillas, A. M.: 1984, *ARA&A* **22**, 425
- Hillenbrand, L. A.: 1997, *AJ* **113**, 1733
- Hillenbrand, L. A. and Hartmann, L. W.: 1998, *ApJ* **492**, 540
- Hily-Blant, P., Falgarone, E., and Pety, J.: 2008, *A&A* **481**, 367
- Huff, E. M. and Stahler, S. W.: 2006, *ApJ* **644**, 355
- Iben, Jr., I.: 1967, *ARA&A* **5**, 571
- Jappsen, A.-K., Klessen, R. S., Larson, R. B., Li, Y., and Mac Low, M.-M.: 2005, *A&A* **435**, 611
- Jeans, J. H.: 1902, *Royal Society of London Philosophical Transactions Series A* **199**, 1
- Johnstone, D., Matthews, H., and Mitchell, G. F.: 2006, *ApJ* **639**, 259

- Johnstone, D., Wilson, C. D., Moriarty-Schieven, G., Joncas, G., Smith, G., Gregersen, E., and Fich, M.: 2000, *ApJ* **545**, 327
- Kandori, R., Nakajima, Y., Tamura, M., Tatematsu, K., Aikawa, Y., Naoi, T., Sugitani, K., Nakaya, H., Nagayama, T., Nagata, T., Kurita, M., Kato, D., Nagashima, C., and Sato, S.: 2005, *AJ* **130**, 2166
- Kim, S. S., Figer, D. F., Kudritzki, R. P., and Najarro, F.: 2006, *ApJ* **653**, L113
- Kirk, H. and Myers, P. C.: 2011, *ApJ* **727**, 64
- Kirk, J. M., Ward-Thompson, D., and André, P.: 2005, *MNRAS* **360**, 1506
- Kirk, J. M., Ward-Thompson, D., and Crutcher, R. M.: 2006, *MNRAS* **369**, 1445
- Kitamura, Y., Momose, M., Yokogawa, S., Kawabe, R., Tamura, M., and Ida, S.: 2002, *ApJ* **581**, 357
- Klessen, R. S.: 2001, *ApJ* **556**, 837
- Klessen, R. S. and Burkert, A.: 2000, *ApJS* **128**, 287
- Klessen, R. S. and Burkert, A.: 2001, *ApJ* **549**, 386
- Klessen, R. S., Burkert, A., and Bate, M. R.: 1998, *ApJ* **501**, L205+
- Klessen, R. S., Heitsch, F., and Mac Low, M.: 2000, *ApJ* **535**, 887
- Klessen, R. S., Krumholz, M. R., and Heitsch, F.: 2009, *ASL*, in press (arXiv:0906.4452)
- Kolesnik, I. G.: 1973, *Astrometriia i Astrofizika* **18**, 45
- Kolmogorov, A.: 1941, *Akademiia Nauk SSSR Doklady* **30**, 301
- Könyves, V., André, P., Men'shchikov, A., Schneider, N., Arzoumanian, D., Bontemps, S., Attard, M., Motte, F., Didelon, P., Maury, A., Abergel, A., Ali, B., Baluteau, J., Bernard, J., Cambrésy, L., Cox, P., di Francesco, J., di Giorgio, A. M., Griffin, M. J., Hargrave, P., Huang, M., Kirk, J., Li, J. Z., Martin, P., Minier, V., Molinari, S., Olofsson, G., Pezzuto, S., Russeil, D., Roussel, H., Saraceno, P., Sauvage, M., Sibthorpe, B., Spinoglio, L., Testi, L., Ward-Thompson, D., White, G., Wilson, C. D., Woodcraft, A., and Zavagno, A.: 2010, *A&A* **518**, L106+

- Kratter, K. M. and Matzner, C. D.: 2006, MNRAS **373**, 1563
- Kroupa, P.: 2001, MNRAS **322**, 231
- Kroupa, P.: 2002, *Science* **295**, 82
- Kruijssen, J. M. D., Maschberger, T., Moeckel, N., Clarke, C. J., Bastian, N., and Bonnell, I. A.: 2012, MNRAS **419**, 841
- Krumholz, M. R. and Bonnell, I. A.: 2009, *Models for the formation of massive stars*, pp 288–+, Cambridge University Press
- Krumholz, M. R., Cunningham, A. J., Klein, R. I., and McKee, C. F.: 2010, ApJ **713**, 1120
- Krumholz, M. R., Klein, R. I., and McKee, C. F.: 2007, ApJ **656**, 959
- Krumholz, M. R., Klein, R. I., McKee, C. F., Offner, S. S. R., and Cunningham, A. J.: 2009, *Science* **323**, 754
- Krumholz, M. R., McKee, C. F., and Klein, R. I.: 2004, ApJ **611**, 399
- Lada, C. J.: 1985, ARA&A **23**, 267
- Lada, C. J., Bergin, E. A., Alves, J. F., and Huard, T. L.: 2003, ApJ **586**, 286
- Lada, C. J. and Lada, E. A.: 2003, ARA&A **41**, 57
- Lada, C. J., Lada, E. A., Clemens, D. P., and Bally, J.: 1994, ApJ **429**, 694
- Lada, C. J., Muench, A. A., Rathborne, J., Alves, J. F., and Lombardi, M.: 2008, ApJ **672**, 410
- Larson, R. B.: 1969, MNRAS **145**, 271
- Larson, R. B.: 1973, Fund. Cosmic Phys. **1**, 1
- Larson, R. B.: 1981, MNRAS **194**, 809
- Lee, A. T. and Stahler, S. W.: 2011, MNRAS pp 1280–+
- Li, H., Griffin, G. S., Krejny, M., Novak, G., Loewenstein, R. F., Newcomb, M. G., Calisse, P. G., and Chuss, D. T.: 2006, ApJ **648**, 340
- Li, P. S., Norman, M. L., Mac Low, M., and Heitsch, F.: 2004, ApJ **605**, 800

- Lilley, A. E.: 1955, *ApJ* **121**, 559
- Löckmann, U., Baumgardt, H., and Kroupa, P.: 2010, *MNRAS* **402**, 519
- Lombardi, M. and Alves, J.: 2001, *A&A* **377**, 1023
- Mac Low, M.-M.: 2003, in E. Falgarone & T. Passot (ed.), *Turbulence and Magnetic Fields in Astrophysics*, Vol. 614 of *Lecture Notes in Physics*, Berlin Springer Verlag, pp 182–212
- Mac Low, M.-M. and Klessen, R. S.: 2004, *Reviews of Modern Physics* **76**, 125
- Maness, H., Martins, F., Trippe, S., Genzel, R., Graham, J. R., Sheehy, C., Salaris, M., Gillessen, S., Alexander, T., Paumard, T., Ott, T., Abuter, R., and Eisenhauer, F.: 2007, *ApJ* **669**, 1024
- Maschberger, T. and Clarke, C. J.: 2011, *MNRAS* **416**, 541
- Mathis, J. S.: 1990, *ARA&A* **28**, 37
- McKee, C. F. and Ostriker, E. C.: 2007, *ARA&A* **45**, 565
- McKee, C. F. and Tan, J. C.: 2002, *Nature* **416**, 59
- McKee, C. F. and Tan, J. C.: 2003, *ApJ* **585**, 850
- McMillan, S. L. W. and Portegies Zwart, S. F.: 2003, *ApJ* **596**, 314
- McMillan, S. L. W., Vesperini, E., and Portegies Zwart, S. F.: 2007, *ApJ* **655**, L45
- Men'shchikov, A., André, P., Didelon, P., Könyves, V., Schneider, N., Motte, F., Bontemps, S., Arzoumanian, D., Attard, M., Abergel, A., Baluteau, J., Bernard, J., Cambrésy, L., Cox, P., di Francesco, J., di Giorgio, A. M., Griffin, M., Hargrave, P., Huang, M., Kirk, J., Li, J. Z., Martin, P., Minier, V., Miville-Deschênes, M., Molinari, S., Olofsson, G., Pezzuto, S., Roussel, H., Russeil, D., Saraceno, P., Sauvage, M., Sibthorpe, B., Spinoglio, L., Testi, L., Ward-Thompson, D., White, G., Wilson, C. D., Woodcraft, A., and Zavagno, A.: 2010, *A&A* **518**, L103+
- Mestel, L.: 1965, *QJRAS* **6**, 265
- Mestel, L. and Spitzer, Jr., L.: 1956, *MNRAS* **116**, 503

- Meynet, G., Maeder, A., Schaller, G., Schaerer, D., and Charbonnel, C.: 1994, *A&AS* **103**, 97
- Miller, G. E. and Scalo, J. M.: 1979, *ApJS* **41**, 513
- Miville-Deschênes, M.-A., Martin, P. G., Abergel, A., Bernard, J.-P., Boulanger, F., Lagache, G., Anderson, L. D., André, P., Arab, H., Baluteau, J.-P., Blagrove, K., Bontemps, S., Cohen, M., Compiègne, M., Cox, P., Dartois, E., Davis, G., Emery, R., Fulton, T., Gry, C., Habart, E., Huang, M., Joblin, C., Jones, S. C., Kirk, J., Lim, T., Madden, S., Makiwa, G., Menshchikov, A., Molinari, S., Moseley, H., Motte, F., Naylor, D. A., Okumura, K., Pinheiro Gonçalves, D., Polehampton, E., Rodón, J. A., Russeil, D., Saraceno, P., Schneider, N., Sidher, S., Spencer, L., Swinyard, B., Ward-Thompson, D., White, G. J., and Zavagno, A.: 2010, *A&A* **518**, L104
- Moeckel, N. and Bonnell, I. A.: 2009, *MNRAS* **400**, 657
- Motte, F., Andre, P., and Neri, R.: 1998, *A&A* **336**, 150
- Mouschovias, T. C. and Spitzer, Jr., L.: 1976, *ApJ* **210**, 326
- Myers, P. C.: 1983, *ApJ* **270**, 105
- Nagano, M., Teshima, M., Matsubara, Y., Dai, H. Y., Hara, T., Hayashida, N., Honda, M., Ohoka, H., and Yoshida, S.: 1992, *Journal of Physics G Nuclear Physics* **18**, 423
- Nakamura, F. and Li, Z.: 2005, *ApJ* **631**, 411
- Nakano, T.: 1998, *ApJ* **494**, 587
- Nakano, T. and Nakamura, T.: 1978, *PASJ* **30**, 671
- Nayakshin, S. and Sunyaev, R.: 2005, *MNRAS* **364**, L23
- Newton, I.: 1687, *Royal Society London*
- Noether, E.: 1918, *Nachr. D. König. Gesellsch. D. Wiss. Zu Göttingen, Math-phys. Klasse 1918: p. 235-237* pp 235–237
- Offner, S. S. R., Hansen, C. E., and Krumholz, M. R.: 2009, *ApJ* **704**, L124
- Offner, S. S. R., Klein, R. I., and McKee, C. F.: 2008, *ApJ* **686**, 1174

- Olczak, C., Spurzem, R., Henning, T., Kaczmarek, T., Pfalzner, S., Harfst, S., and Portegies Zwart, S.: 2011, *ArXiv e-prints*
- Olson, K. M., MacNeice, P., Fryxell, B., Ricker, P., Timmes, F. X., and Zingale, M.: 1999, *Bulletin of the American Astronomical Society* **31**, 1430
- Ossenkopf, V. and Mac Low, M.-M.: 2002, *A&A* **390**, 307
- Ostriker, E. C.: 1999, *ApJ* **513**, 252
- Ostriker, E. C., Gammie, C. F., and Stone, J. M.: 1999, *ApJ* **513**, 259
- Padoan, P. and Nordlund, Å.: 2002, *ApJ* **576**, 870
- Parker, R. J., Bouvier, J., Goodwin, S. P., Moraux, E., Allison, R. J., Guieu, S., and Güdel, M.: 2011, *MNRAS* **412**, 2489
- Peretto, N., André, P., and Belloche, A.: 2006, *A&A* **445**, 979
- Peters, T., Banerjee, R., Klessen, R. S., Mac Low, M., Galván-Madrid, R., and Keto, E. R.: 2010a, *ApJ* **711**, 1017
- Peters, T., Banerjee, R., Klessen, R. S., and Mac Low, M.-M.: 2011, *ApJ* **729**, 72
- Peters, T., Klessen, R. S., Mac Low, M., and Banerjee, R.: 2010b, *ApJ* **725**, 134
- Peters, T., Mac Low, M., Banerjee, R., Klessen, R. S., and Dullemond, C. P.: 2010c, *ApJ* **719**, 831
- Pineda, J. E., Goodman, A. A., Arce, H. G., Caselli, P., Longmore, S., and Corder, S.: 2011, *ApJ* **739**, L2
- Pirogov, L. E.: 2009, *Astronomy Reports* **53**, 1127
- Portegies Zwart, S. F., McMillan, S. L. W., and Gieles, M.: 2010, *ARA&A* **48**, 431
- Predehl, P. and Schmitt, J. H. M. M.: 1995, *A&A* **293**, 889
- Price, D. J. and Bate, M. R.: 2007, *Ap&SS* **311**, 75
- Price, D. J., Federrath, C., and Brunt, C. M.: 2011, *ApJ* **727**, L21+
- Price, D. J. and Monaghan, J. J.: 2007, *MNRAS* **374**, 1347

- Prim, R. C.: 1957, *Bell Systems Tech. J.* **36**, 1389
- Pudritz, R. E.: 2004, *Ap&SS* **292**, 471
- Pudritz, R. E. and Norman, C. A.: 1983, *ApJ* **274**, 677
- Rephaeli, Y. and Salpeter, E. E.: 1980, *ApJ* **240**, 20
- Roman-Duval, J., Federrath, C., Brunt, C., Heyer, M., Jackson, J., and Klessen, R. S.: 2011, *ApJ* **740**, 120
- Ruderman, M. A. and Spiegel, E. A.: 1971, *ApJ* **165**, 1
- Sabbi, E., Sirianni, M., Nota, A., Tosi, M., Gallagher, J., Smith, L. J., Angeretti, L., Meixner, M., Oey, M. S., Walterbos, R., and Pasquali, A.: 2008, *AJ* **135**, 173
- Salpeter, E. E.: 1955, *ApJ* **121**, 161
- Scalo, J.: 1990, in R. Capuzzo-Dolcetta, C. Chiosi, and A. di Fazio (eds.), *Physical Processes in Fragmentation and Star Formation*, Vol. 162 of *Astrophysics and Space Science Library*, Dordrecht, Netherlands, Kluwer Academic Publishers, pp 151–176
- Scalo, J.: 1998, in G. Gilmore & D. Howell (ed.), *The Stellar Initial Mass Function (38th Herstmonceux Conference)*, Vol. 142 of *Astronomical Society of the Pacific Conference Series*, pp 201–+
- Scalo, J. M.: 1986, *Fundamentals of Cosmic Physics* **11**, 1
- Scheck, F.: 1990, *Mechanik. Von den Newtonschen Gesetzen zum deterministischen Chaos.*
- Schmeja, S. and Klessen, R. S.: 2004, *A&A* **419**, 405
- Schmeja, S. and Klessen, R. S.: 2006, *A&A* **449**, 151
- Schmidt, W., Federrath, C., Hupp, M., Kern, S., and Niemeyer, J. C.: 2009, *A&A* **494**, 127
- Schmidt, W., Kern, S. A. W., Federrath, C., and Klessen, R. S.: 2010, *A&A* **516**, A25+
- Schmidt, W., Niemeyer, J. C., and Hillebrandt, W.: 2006, *A&A* **450**, 265
- Schneider, N., Csengeri, T., Bontemps, S., Motte, F., Simon, R., Hennebelle, P., Federrath, C., and Klessen, R.: 2010, *A&A* **520**, A49+

- Seifried, D., Banerjee, R., Klessen, R. S., Duffin, D., and Pudritz, R. E.: 2011a, *MNRAS* **417**, 1054
- Seifried, D., Schmidt, W., and Niemeyer, J. C.: 2011b, *A&A* **526**, A14
- Shepherd, D. S. and Churchwell, E.: 1996, *ApJ* **472**, 225
- Shetty, R., Collins, D. C., Kauffmann, J., Goodman, A. A., Rosolowsky, E. W., and Norman, M. L.: 2010, *ApJ* **712**, 1049
- Shu, F. H.: 1977, *ApJ* **214**, 488
- Shu, F. H.: 1992, *The physics of astrophysics. Volume II: Gas dynamics.*
- Sirianni, M., Nota, A., De Marchi, G., Leitherer, C., and Clampin, M.: 2002, *ApJ* **579**, 275
- Smith, R. J., Clark, P. C., and Bonnell, I. A.: 2008, *MNRAS* **391**, 1091
- Smith, R. J., Longmore, S., and Bonnell, I.: 2009, *MNRAS* **400**, 1775
- Solomon, P. M., Rivolo, A. R., Barrett, J., and Yahil, A.: 1987, *ApJ* **319**, 730
- Spinnato, P. F., Fellhauer, M., and Portegies Zwart, S. F.: 2003, *MNRAS* **344**, 22
- Spitzer, Jr., L.: 1969, *ApJ* **158**, L139+
- Spruit, H. C.: 1996, *ArXiv Astrophysics e-prints*
- Stolte, A., Brandner, W., Brandl, B., and Zinnecker, H.: 2006, *AJ* **132**, 253
- Stolte, A., Brandner, W., Grebel, E. K., Lenzen, R., and Lagrange, A.-M.: 2005, *ApJ* **628**, L113
- Teixeira, P. S., Lada, C. J., and Alves, J. F.: 2005, *ApJ* **629**, 276
- Testi, L. and Sargent, A. I.: 1998, *ApJ* **508**, L91
- Tomisaka, K., Ikeuchi, S., and Nakamura, T.: 1988, *ApJ* **335**, 239
- Toomre, A.: 1964, *ApJ* **139**, 1217
- Toro, E. F.: 2009, *Riemann Solvers and Numerical Methods for Fluid Dynamics: A Practical Introduction*, Springer, 3rd edition

- Truelove, J. K., Klein, R. I., McKee, C. F., Holliman, J. H., Howell, L. H., and Greenough, J. A.: 1997, *ApJ* **489**, L179+
- Šubr, L., Kroupa, P., and Baumgardt, H.: 2008, *MNRAS* **385**, 1673
- Vázquez-Semadeni, E., Gazol, A., and Scalo, J.: 2000, *ApJ* **540**, 271
- Vázquez-Semadeni, E., Kim, J., and Ballesteros-Paredes, J.: 2005a, *ApJ* **630**, L49
- Vázquez-Semadeni, E., Kim, J., Shadmehri, M., and Ballesteros-Paredes, J.: 2005b, *ApJ* **618**, 344
- Vesperini, E., McMillan, S. L. W., and Portegies Zwart, S.: 2009, *ApJ* **698**, 615
- von Hoerner, S.: 1951, *ZAp* **30**, 17
- von Weizsäcker, C. F.: 1951, *ApJ* **114**, 165
- Wang, P., Li, Z., Abel, T., and Nakamura, F.: 2010, *ApJ* **709**, 27
- Ward-Thompson, D., André, P., Crutcher, R., Johnstone, D., Onishi, T., and Wilson, C.: 2007, *Protostars and Planets V, Univ. Arizona Press, Tuscon* pp 33–46
- Ward-Thompson, D., Kirk, J. M., Crutcher, R. M., Greaves, J. S., Holland, W. S., and André, P.: 2000, *ApJ* **537**, L135
- Ward-Thompson, D., Motte, F., and Andre, P.: 1999, *MNRAS* **305**, 143
- Ward-Thompson, D. and Whitworth, A. P.: 2011, *An Introduction to Star Formation*
- Weidner, C. and Kroupa, P.: 2006, *MNRAS* **365**, 1333
- Weidner, C., Kroupa, P., and Bonnell, I. A. D.: 2010, *MNRAS* **401**, 275
- Whitworth, A. and Summers, D.: 1985, *MNRAS* **214**, 1
- Whitworth, A. P., Bhattal, A. S., Chapman, S. J., Disney, M. J., and Turner, J. A.: 1994, *MNRAS* **268**, 291
- Whitworth, A. P. and Ward-Thompson, D.: 2001, *ApJ* **547**, 317
- Widrow, L. M.: 2002, *Reviews of Modern Physics* **74**, 775

- Wu, Y., Wei, Y., Zhao, M., Shi, Y., Yu, W., Qin, S., and Huang, M.: 2004, A&A **426**, 503
- Wuchterl, G. and Klessen, R. S.: 2001, ApJ **560**, L185
- Yorke, H. W. and Sonnhalter, C.: 2002, ApJ **569**, 846
- Ziegler, U.: 2005, A&A **435**, 385
- Zinnecker, H. and Yorke, H. W.: 2007, ARA&A **45**, 481
- Zuckerman, B. and Evans, II, N. J.: 1974, ApJ **192**, L149

# Danksagung

Allen voran bedanke ich mich bei Ines Kühn und meiner Familie, die mich immer tatkräftig unterstützt haben. Die vergangenen Jahre ohne sie kann und möchte ich mir nicht vorstellen.

Zudem danke ich meinen Betreuern Robi Banerjee und Ralf Klessen für ihre Unterstützung während meiner Zeit als Doktorand. Die vielseitigen Diskussionen haben mir einen breiten Einblick in die Thematik der Sternentstehung verschafft. Insbesondere möchte ich mich bei Robi Banerjee für die flexible Betreuung nach seinem Wechsel nach Hamburg bedanken, die es mir erlaubten, meine Doktorarbeit in Heidelberg zu beenden.

Für die Betreuung an der Cardiff University bedanke ich mich herzlich bei Anthony Whitworth. Seine besonnenen und gründlichen Überlegungen haben mein Verständnis der relevanten Physik deutlich erweitert.

Weiterhin gilt mein Dank meinen Bürokollegen in Heidelberg und Cardiff. Ich danke Daniel Seifried für ein angenehmes Arbeitsklima in unserem Büro und die tatkräftige Unterstützung in physikalischer, programmiertechnischer und auch weniger arbeitsrelevanter Hinsicht. In Cardiff haben mir Steffi Walch, Oliver Lomax und Dimitris Stamatellos eine schöne und erfolgreiche Zeit beschert. Mein letztes Jahr in Heidelberg verbrachte ich zusammen mit Jennifer Schober, Christoph Federrath sowie Erik Bertram in einem Büro, was mir immer ein großes Vergnügen war. Ein besonderer Dank gebührt Lukas Konstandin für die täglichen Diskussionen u.a. zur Physik der Turbulenz, zur Strukturentstehung in astrophysikalischen Systemen sowie zu strukturierter und nachhaltiger Programmierung von wissenschaftlicher Software.

Ebenso bedanke ich mich bei Matthias Bartelmann, Kees Dullemond, Anna Zacheus und Silvia Matyssek für eine angenehme Zeit am ITA und die zahlreichen Hilfestellungen.

Besondere Freude haben mir die Diskussionen mit Johannes Schönke bereitet. Seine Überlegungen zur numerischen Betrachtung der Sternentstehung sowie seine entspannte Art haben mich sehr beeindruckt.

Für die technische Unterstützung bei der Administration der Rechner bedanke ich mich bei Emanuel Ziegler und Julian Merten.

